A Computational Study of Aspects of ZnO Nanorod Film Electro-Crystallisation

Jade River Mackay

A thesis
submitted to the Victoria University of Wellington
in fulfilment of the
requirements for the degree of
Doctor of Philosophy
in Physics.

Victoria University of Wellington
2009

Abstract

A new generation of material technologies is being produced by tuning the properties of an existing material through control of the size and shape on the nanoscale. Zinc oxide is an excellent candidate for such an approach due to its possession of a plethora of useful properties, both mechanical and electronic, and a fantastically rich family of morphologies accessible on the nanoscale.

A more detailed control over the nano-structure of these materials requires a more detailed understanding of the events that control the growth. We have undertaken computational studies of the electrodeposition of zinc oxide nano-rod films to open up and improve the understanding of the pathways, and events that facilitate the controlled selection of desired structures and therefore properties. We have applied methods that span vastly different scales to provide insight on the continuum and atomistic regimes. Specifically, we have developed a macroscopic transport model to track the evolution of crystallite shape, surrounding concentration distributions, and electric field variation. The macroscopic view is complemented with a classical description of crystal growth, in which we obtain the key parameters using quantum mechanical calculations.

For Karen, Justine, and Rudy

♡

Acknowledgments

I wish to thank my supervisor, Shaun Hendy, for his advice and guidance throughout this work. I also wish to thank Steve White, who introduced me to the numerical approach to electrochemical systems, and who sadly passed away during the early stages of this work. I am grateful to Brent Walker for his friendship, and many discussions in the areas of DFT, numerics, and computation. I am also indebted to Peter McGavin for introducing me to the Linux way of life, and demonstrating that the best things in computing are free. I thank Mary Ryan and Benoît Illy for doing great experiments and providing me with the data. I also thank Kate McGrath for her advice and assistance. Finally I wish to thank my family and friends for their support, without which I couldn't have finished this work: Justine, Rudy, Layla, Omar, Kaja, Allan, Dee, Pam, Jorgen, Terasa, Benjamin, Kathleen and Terry. Put yo' hands in the air.

Contents

1 Introduction **1**

1.1 Background 2

1.2 Overview of Work 2

1.3 Chapter Overview 4

1.3.1 Chapter 2: Electrochemistry and Zinc Oxide 4

1.3.2 Chapter 3: The Electrochemical Model 4

1.3.3 Chapter 4: Numerical Method and Implementation . 5

1.3.4 Chapter 5: Electrochemical Model Results 5

1.3.5 Chapter 6: DFT: Theory and Method 5

1.3.6 Chapter 7: A Study of ZnO Using DFT 6

2 Electrochemistry and Zinc Oxide **7**

2.1 ZnO Electrodeposition 7

2.2 Electrochemistry and Oxide Growth 10

2.2.1 Electrodeposition Results and Observations 14

2.3 Summary 21

3 The Electrochemical Model **23**

3.1 System Composition 23

3.1.1 Essential Reactions 25

3.1.2 The Electrostatic Potential 30

3.1.3 The Thin Double Layer Approximation 31

3.2 Macroscopic Electrolyte Tranport Model 34

3.3 Time Evolution 37
3.4 The Electroneutrality Constraint 39
3.5 Approximate Approaches to Solving NPEN 42
3.5.1 Similar Diffusivities (NPEN-β) 42
3.5.2 Nernst-Planck-Laplace (NPEN-γ) 43
3.6 Simple Study 44
3.6.1 Case 1: Fixed Flow Area, Free Aspect Ratio 47
3.6.2 Case 2: Free Flow Area, Fixed Aspect Ratio 49
3.6.3 Results 53
3.6.4 Comments 54
3.7 Summary 54

4 Numerical Method and Implementation **55**
4.1 System Geometry 55
4.2 Discrete Formulation 56
4.3 Iterative Method 61
4.4 Calculation Scheme Objects 63
4.4.1 The Solution Vector, $\mathbf{u}$ 63
4.4.2 The Function Vector, $\mathbf{F}(\mathbf{u})$ 64
4.4.3 The Jacobian Matrix, $\mathbf{F}'(\mathbf{u})$ 66
4.5 Meshing 71
4.6 Boundaries 73
4.7 Model Comparisons 76
4.7.1 System Parameter Convergence 76
4.7.2 Output Comparison 78
4.7.3 Numerical Convergence 80
4.8 Summary 81

5 Electrochemical Model Results **84**
5.1 Experimental Results 84
5.2 System Behaviour and Electrolyte Dynamics 87
5.2.1 Coarse Parameter Search 89

5.2.2 The Standard Case 91
5.2.3 The Oxygen Reduction Reaction (ORR) and Electrolyte Dynamics 94
5.3 Basic Variation of System Parameters 98
5.3.1 Zn^{2+} Concentration 99
5.3.2 Crystallite Density 100
5.3.3 The Surface Potential 102
5.3.4 Growth Rate Anisotropy 105
5.3.5 The ORR Rate, α 106
5.3.6 Minimum Inter-Crystallite Gap 109
5.4 Summary 111

6 DFT: Theory and Method 115
6.1 The Calculus of Variations 115
6.1.1 The Stationary Value of a Functional 116
6.1.2 Variational Calculus with Constraints 119
6.2 Quantum Mechanics 121
6.2.1 Schrödinger's Wave Equation 121
6.2.2 The Variational Principle of Quantum Mechanics . . 122
6.2.3 A First Application of Calculus of Variations 124
6.2.4 The Wave Function Method(s) 125
6.3 Electronic Density Functional Theory (DFT) 128
6.3.1 Kohn-Sham DFT 133
6.3.2 The Exchange-Correlation Functional(s) 135
6.4 DFT Techniques 136
6.4.1 Plane Waves 137
6.4.2 Pseudopotentials 139
6.4.3 Structure Optimisation 141
6.4.4 Supercells 141
6.4.5 VASP DFT Code 142
6.4.6 Computing 142

6.5 Summary 144

7 A Study of ZnO Using DFT **145**
7.1 Introduction 145
7.2 Zinc Oxide 146
7.3 DFT and Thermodynamics 151
7.4 DFT and Crystal Growth 156
7.4.1 The Equilibrium Shape 156
7.4.2 The Kinetic Models 157
7.5 ZnO Bulk Structure Convergence 165
7.6 Surface Energy calculations 172
7.6.1 Bare Non-Polar Surfaces 173
7.6.2 Bare Polar Surfaces 174
7.7 Hydrated Surfaces 182
7.7.1 Hydrated Non-Polar Surfaces 182
7.7.2 Hydrated Polar Surfaces 184
7.7.3 Summary of Hydrated Polar and Non-Polar Surface Studies 196
7.8 Stepped Surfaces 196
7.9 Summary 199

8 Conclusions **203**

List of Figures

2.1 Bar graphs showing interest in ZnO and nanoscale ZnO as indicated by the number of English language articles returned by Web of Science for the period 1998 - 2008. 8

2.2 Illustration of the Experimental rig used by Benoît Illy, Dr Mary Ryan and Dr Bridget Ingham of Imperial College, London 9

2.3 The fundamental results obtained from x-ray absorption measurements of growth with variation of cathodic potential 2.3a and Zn^{2+} concentration 2.3b. 16

2.4 (a) Current density (black) and X-ray absorption intensity at 9720 eV from repeated scans (red) as a function of time, (b) Repeated Synchrotron XANES across the Zn K-edge. Courtesy of BI and MR 17

2.5 SEM images of electrodeposited ZnO films (in all images the red scale bar represents 100 nm): (a) Cathodic potential of -770 mV (Ag/AgCl), 5 mM $Zn(NO_3)_2$, and 0.1 M KCl, (b) cathodic potential -370 mV (Ag/AgCl), otherwise the same as (a). (c) Same as (a) but with 1 mM $Zn(NO_3)_2$. (d) Profile image under same conditions as (a), aspect ratio approximately 6. (e) Plan view of sample used in (d) showing tapered tip, and islands suggestive of layer growth. 18

2.6 Growth behaviour of morphological outcomes. 19

2.7 Film morphology and XANES signal intensity evolution over time. SEM images were acquired at 15, 60, 120, 240 and 600 seconds. 21

3.1 Schematic of computational domain in which the transport region is white, the crystallite is grey, the black line indicates the boundaries (dotted lines indicate mirror boundaries). the polar (P) surface is the upper grey edge, and the non-polar (NP) surface is the lateral grey edge. Also shown are the reactions considered at various boundaries. 24

3.2 The constrained transport-reaction scheme for the species involved in ZnO formation with Zn^{2+}/OH^{-} reaction fixed at the electrode. Again (bulk) refers to the solution composition at great distance from the growing film, (el) is the electrode region, (rxn) is the region where Zn^{2+} and OH^{-} meet, and (hkl) refers to a particular ZnO crystal facet. Transport is denoted with horizontal arrows and chemical reactions with horizontal arrows. 25

3.3 Schematic of the electric double layer. 32

3.4 Illustration of approximate length scales associated with electrochemical systems. 33

3.5 Plots of the variation of potential away from the electrode in 0.1 M 2:1 electrolyte ($CaCl_2$), calculated using (3.23), with $\lambda_D = 0.6$ nm. 34

3.6 Equivalent diffusion limited growth scenarios. (a) Growth limited by the transport of Zn^2+ or OH^{-} to the substrate (electrode). (b) Growth limited by the steady state transport of OH^{-} formed at the electrode by conversion of O_2. (c) Growth limited by the steady state transport of zinc hydroxide species formed at the electrode by reaction of Zn^{2+}. 48

3.7 The two real branches of the Lambert W function. 51

3.8 Ideal rod arrangement used to investigate the free area, fixed aspect ratio model. The filled hexagons represent the unit rods, and the white hexagonal shells represent the flow area associated with each unit rod. 52
3.9 Diffusion limited growth behaviour obtained using a rod spacing of 1 per 100 nm: (a) vertical-only growth at a variety of rod widths (w), and (b) vertical and lateral growth for a variety of aspect ratios (Γ). 53

4.1 Schematic showing how 2-dimensional model is derived and relates to the 3-dimensional system. Images (a) and (b) emphasise the hexagonal nature of the nanorods. The purple line represents a 2D plane representative of the interrod 3D space. Image (c) shows the 2D plane in perspective, and (d) shows the smallest by symmetry 2D plane used to represent the 2D model domain. 56
4.2 Five point centred FD stencil used for spatial derivatives. . . 57
4.3 Finite difference stencils used to march forward in time. . . . 60
4.4 Schematic representation of convergence using Newton's method. 62
4.5 (a) Schematic representation of computational domains. As the crystal (red) grows the solution vector is dominated by the internal area of the crystal. (b) Schematic representation of compressed computational domain in which the crystal interior is omitted. As the crystal (red) grows the solution vector becomes smaller, requiring less computational resources and allowing the calculation to proceed faster. . . 65
4.6 The compressed and non-compressed solution array sizes for a typical simulation. 65
4.7 Finite difference stencils for the each variable. From top to bottom: ϕ, Zn^{2+}, O_2, OH^-, Ca^{2+}, the central index i, j is black, ϕ is red, and chemical species are coloured blue. . . . 67

4.8 Schematic showing relation between the 2-dimensional model domain, and the 1-dimensional analogue used in the calculational scheme. 68
4.9 (a) Illustration of a non-uniform mesh. Here the outer orange boundary corresponds to the virtual x+1 and y+1 points used to evaluate Neumann boundary conditions, the blue rectangle is the NP domain boundary, the black box represents the crystal, and the red lines indicate the crystal boundaries. The dark gridlines are the present grid, and the fainter grey lines indicate the grid belonging to the previous interpolant. (b) An example of a non-uniform finite difference grid used in this work (c.a. 5 seconds). The crystallite is represented by the bold black rectangle. 72
4.10 Boundary domains: I - electrode directly below rod, II - inter-rod electrode area, III - inter-rod mirror boundary, IV - bulk boundary, V - upper central mirror boundary, VI - crystal upper boundary, VII - crystal upper corner, VIII - crystal lateral boundary, IX - crystal lower corner, X - crystal lower boundary, XI - lower central mirror boundary. 74
4.11 Convergence study of key code numeric parameters. 77
4.12 Comparison of the three models NPEN (3.45-3.46), NPEN-β (3.67-3.68), and NPEN-γ (3.71-3.72), over a range of isotropic rate constants, β, and surface potentials, $\phi_\circ$. 79
4.13 The delta (δ_k) variation of the NPEN models (a) over an entire simulation, (b) the first 500 iterations, and (c) the first 100 iterations. The response to a grid update for (d) NPEN (3.45-3.46), (e) NPEN-β (3.67-3.68), and (f) NPEN-γ (3.71-3.72). The convergence behaviour for 3 consecutive sets of five iterations in which the legend denotes the change in scale, (g) NPEN (3.45-3.46), (h) NPEN-β (3.67-3.68), and (i) NPEN-γ (3.71-3.72). 82

4.14 Jacobian build times ((a) and (c)) and System solve times ((b) and (d)) using Intel Pentium(R) Dual CPU (2.80 Giga-Hertz) processors which share 2 Gigabytes of memory. 83

5.1 (a) The effect of concentration variation on deposition with an applied potential of -770 mV (Ag/AgCl). (b) A plot emphasising the similarity of early growth in [Zn^{2+}]= 5 mM, and [Zn^{2+}] = 20 mM depositions. (c) Emphasis of early growth behaviour of [Zn^{2+}]= 5 mM, and [Zn^{2+}] = 20 mM. . 86

5.2 The effect of concentration on deposition at E = -670,-770,-970 mV is illustrated by (a) [Zn^{2+}] = 5 mM, and (c) [Zn^{2+}] = 10 mM. The effect of increased Zn^{2+}concentration on the deposition at a given potential is shown in (b) E = -670 mV, (d) E = -770 mV, and (e) E = -970 mV. 88

5.3 Model growth results with isotropic variation of rate constant, β, and electrode surface potential $\phi^{el}_{\circ}$, with mirror conditions for ϕ_P, and ϕ_{NP}. 90

5.4 The growth curve obtained using the standard conditions ([Zn^{2+}] = 5 mM, $\phi = -50$ mV, $\beta = 0.25 \times 10^{-31}$ mols^{-1}) (a), and profiles at characteristic times along the system height (from the electrode to the upper boundary) of (b) ϕ (c) [Zn^{2+}] (d) [O_2] (e) [OH^-]. The crystallite heights are highlighted with red squares. 92

5.5 The growth curve obtained using [Zn^{2+}] = 0.5 mM with otherwise standard conditions ($\phi = -50$ mV, $\beta = 0.25 \times 10^{-30}$ mols^{-1}) (a), and profiles at characteristic times along the system height (from the electrode to the upper boundary) of (b) ϕ (c) [Zn^{2+}] (d) [O_2] (e) [OH^-]. The crystallite heights are highlighted with red squares. 93

5.6 Simulated growth curves obtained using the standard conditions with the ORR occurring at the electrode, ORR(el), the electrode and polar facet, ORR(el,P), the electrode and the non-polar facet, ORR(el,NP), and all surfaces, ORR(el,P,NP). 95

5.7 Profiles of the key variables [Zn^{2+}], [O_2], and [OH^-]. The left column was obtained using standard conditions ($\phi_{el} = -50$ mV, [Zn^{2+}]$_\infty$ = 5 mM, $\beta = 0.25 \times 10^{-31}$ mols^{-1}) with the ORR occurring on the electrode and the polar crystallite surface, ORR(el,P), and the right column was obtained with the ORR occurring on the electrode only, ORR(el). The large red squares indicate the crystal height. 97

5.8 Plots showing the efficiency of OH^- contribution to growth under the characteristic ORR regimes: electrode only (green), and electrode and crystallite polar surface (blue line). The kinks are an artefact of the grid update an interpolation procedure and require further development. 98

5.9 Plots showing the efficiency of OH^- contribution to growth in terms of the amount of OH^- exiting the system, under the characteristic ORR regimes: electrode only (green), and electrode and crystallite polar surface (blue line). Again, the kinks in the flux ratios are numerical artefacts. 99

5.10 Plots illustrating the effect of Zn^{2+} concentration variation on the simulated growth curves. The upper plot was by permitting the ORR to occur at the electrode only, and the lower figure permitted the ORR on all surfaces. 101

5.11 Simulations probing the possibility of a relationship between concentration and crystallite seed density. (a) High concentration at high and low density, (b) high concentration-high density with low concentration-low density, and (c) high concentration-low density with low concentration-high density, (d) inset of (c) illustrating slower initial growth rate at higher concentration. 103
5.12 Simulated growth curves obtained using standard conditions (c.f. Table 5.1) with varied ϕ_P° and ϕ_{el}° and ϕ_{NP}° fixed at -50 mV. 105
5.13 Comparison of the growth curves at the various ORR configurations using (a) standard conditions (b) $\beta_P = 0.20 \times 10^{-30}$ mols^{-1}. 107
5.14 Variation of ad hoc rate dependence of the ORR (a) at the polar crystallite surface, (b) at the electrode, and (c) at both the electrode and the polar crystallite surface. 110
5.15 Plots of the simulated volume (a), length (b), and width (c), obtained for a range of enforced crystallite maximum widths. The minimum inter-crystallite gap is denoted by d. . 112
5.16 Zn^{2+}concentration map at the mode one - mode two transition, obtained using ORR(el,P,NP). 113

6.1 Schematic of the pseudo wavefunction (upper), and the pseudopotential (lower). 140
6.2 Aperiodic structures can be expressed as a 'crystal' of supercells containing empty space in the aperiodic directions. . 143

7.1 Schematics showing the typical parameters used to characterise the ZnO wurtzite crystal structure. (a) ZnO wurtzite unit cell in terms of fractional coordinates and angles α,β,γ. Red - oxygen, blue - zinc. (b) ZnO wurtzite unit cell showing R_1 and R_2. 147

7.2 Ball and stick representations of the wurtzite low index facets (here the small red circles represent O and the larger blue circles represent Zn): (a) Top view where dashed line indicates the unit cell, (b) perspective view illustrating the hexagonal prism structure, (c) profile view of a lateral facet, (d) planar view of a lateral facet, (e) perspective of lateral facet (here the dashed line is used to emphasise perspective). 148
7.3 Morphological difference observed in electrochemical deposition: (a) An SEM image showing the two extreme morphologies (b) the large aspect ratio, and (c) the small aspect ratio. 149
7.4 Schematic representations of atom arrangement in ZnO wurtzite. Zn - blue, O - red. (a) illustrates the atom arrangement in terms of the hexagonal prism, (b) emphasises high index polar planes (b) indicates the polar nature of the basal planes. 150
7.5 Schematic showing layered structure and surface charge modification required to cancel macroscopic dipole. Here $\sigma' = 0.25\sigma$. 151
7.6 A two dimensional depiction of surface (red blocks) growth by incorporation of growth unit (blue) into a kink site on a (a) rough surface, and a (b) Smooth surface. 158
7.7 Schematics depicting facet growth by propagation of steps . 161
7.8 Schematic showing how a kink can be formed from a step. (a) Shows a step with energy ϕ_S^1 per characteristic area (yellow), while (b) shows a kink forms by extrusion of part of the step with energy $2\phi_K \approx \phi_S^1 + \phi_S^2$ (red). At the kink two differently oriented step fronts meet. 163

7.9 (a) Illustration of the symmetrically independent faces required to describe a coarse average kink energy on hexagonal columnar ZnO. The beige face is the only symmetrically independent step on the $\{0001\}$ faces, whilst the $\{10\bar{1}0\}$ require three steps due to the polar nature of ZnO in the $\vec{c}$ direction. The green step points in the $[10\bar{1}0]$ direction, red in the $[0001]$, and purple in the $[000\bar{1}]$ direction. Sections of the unique steps considered in our studies to calculate the average kink energy from the lowest index step orientations are represented in (b)-(f), in which the first indice is denotes the facet whilst the second denotes the step rise direction. The basal steps (b) $(0001) - (10\bar{1}0)$, and (c) $(000\bar{1}) - (10\bar{1}0)$, and the lateral steps (d) $(10\bar{1}0) - (000\bar{1})$, (e) $(10\bar{1}0) - (0001)$, and (f) $(10\bar{1}0) - (10\bar{1}0)$. 166

7.10 k-point convergence for ZnO 167

7.11 Isotropic volume scan with structural relaxation at each volume using LDA (Ceperley-Alder [144]), and GGA functionals (Perdew-Wang 91 [145]). The curves are offset by their respective minimum total energies: E_{min}(ZnO), -10.63 eV for the LDA, and -9.087 eV for the GGA. 168

7.12 Contour plots (in eV) showing the various (c, a) convergence tests performed using either electron-only relaxation or fixed volume, free shape atom position, structural relaxation (ISIF=4) at each (c, a). (a) Electron-only using literature cell. (b) Structural relaxation of literature cell (c) Electron-only relaxation of the unit cell obtained using the conventional isotropic energy-volume convergence, and (c) Structural relaxation executed at each (c, a). 170

7.13 (a) Contour map of $\gamma_{relax} - \gamma_{\circ}$, the γ angle in the relaxed structure versus the un-relaxed cell. (b) A plot of $\gamma_{relax} - \gamma_{\circ}$, the γ angle in the relaxed structure versus the un-relaxed cell, against the cell anisotropy for a specific $|a|$. 171
7.14 The largest and smallest supercells used to investigate convergence of supercell parameters for the non-polar $(10\bar{1}0)$ surface. 174
7.15 Non-polar bare surface supercell convergence using full relaxations (electron and atom), displayed as a surface energy (eV/Å^2) contour plot. 175
7.16 Supercell parameter electron-only convergence behaviour (in eV/Å^2) of the polar $\{0001\}$ surfaces, surface energy, $E_{\{0001\}} = (E_{slab} - N_{Zn}E_{ZnO})/2A_{\{0001\}}$, versus $N_c = N_{Zn}$ and N_v 176
7.17 Supercell parameter electron and all atom convergence behaviour (in eV/Å^2) of the polar $\{0001\}$ surfaces, surface energy, $E_{\{0001\}} = (E_{slab} - N_{Zn}E_{ZnO})/2A_{\{0001\}}$, versus $N_c = N_{Zn}$ and N_v 176
7.18 The deviation from bulk of the core R_1's plotted against the slab centre for ZnO layers from 6 to 11. 177
7.19 (N_a, N_c) convergence surfaces (in eV/Å^2) for (a) fixed atoms (cleavage), (b) fixed core, free outer two layers, and (c) all atoms free to move. 178
7.20 Relaxation energies per surface area (eV/Å^2). 179
7.21 Surface total energy (eV), $E_{surf}(N_c)$, as a function of N_c for the $9, 5$-slab using fixed and non-fixed core slabs. 179
7.22 Bar plots showing the deviation from bulk structure upon relaxation of the (9,5)-slab, in terms of R_1 and R_2 (a), and atom position (b). Full, all atoms realxations are coloured blue, outer 3 layer relaxations are red, and outer 2 layer relaxations are coloured green. 180

7.23 $N_v = 5$ series, $(6,5)$-slab (red), $(7,5)$-slab (green), $(8,5)$-slab (blue), $(9,5)$-slab (purple), $(10,5)$-slab (black), $(11,5)$-slab (cyan). The left column (a, c, e) shows the movement of the individual atoms (Zn = filled, O = non-filled), and the right column shows the change in the layer distance (R_1 = filled, and R_2 = non-filled). 181
7.24 Ball and stick models of the $(10\bar{1}0)$ supercells where Zn is blue, O is red, and H is white. (a) The bare supercell, and (b) the hydrated supercell created by replacement of a terminal Zn with H and the complementary O with OH. 183
7.25 Ball and stick models of the $(10\bar{1}0)$ supercells where Zn is blue, O is red, and H is white. (a) The bare supercell, and (b) the hydrated supercell created by addition of H on one face and OH on the other. 183
7.26 (a) The surface free energy and, (b) the water binding energy, of singly (blue) and doubly (green) hydrated non-polar slabs in the vicinity of the ideal gas state of H_2O. 184
7.27 Ball and stick (Zn=blue, O=red, H=white) models of the supercells used to study the energetic influence of surface hydration. (a) Full hydration, (b) 50% hydration, (c) 25% hydration, (d) 50% hydration on (0001)-Zn and full hydration of $(000\bar{1})$-O, (e) 50% hydration on $(000\bar{1})$-O and full hydration of (0001)-Zn, and (f) full protonation of $(000\bar{1})$-O and 75% protonation of the oxylated (0001)-Zn surface. Slabs (a)-(c) are neutral and (d)-(f) are charged. 185
7.28 (a) Surface free energy, and (b) water binding energy, of the neutrally hydrated polar surface. 187

7.29 (a) Surface free energy, plotted against the deviation from the chemical potential of the ideal gas state of water, of the hydrated non-polar surface (red), and the hydrated polar surface (blue). (b) The expected aspect ratio of a hexagonal prism shape rod based on the minimum surface free energies of the non-polar and polar surface models. The vertical red lines indicate changes in minimum energy surface termination. 188
7.30 Surface free energy against μ_{H_2O} and μ_H of method 1 hydration of the polar surface. 190
7.31 The minimum surface free energy against μ_{H_2O} and μ_H of method 1 hydration of the polar surface: (a) The complete method 1 set, and (b) only the positive surfaces. 191
7.32 The minimum surface free energy against μ_{H_2O} and μ_H of method 2 hydration of the polar surface: (a) 3d plots (b) scatter plot. All slab models have negative free energy in some part of the domain. 192
7.33 (a) The minimum surface free energy surfaces of all (method 1 & 2) hydrated slab models against μ_{H_2O} and μ_{H_2}, and (b) the resulting minimum energy surface. 193
7.34 The minimum positive surface free energy against μ_{H_2O} and μ_{H_2} of method 1 & 2 hydration of the polar surface. 194
7.35 Surface free energy, γ versus pH for the surface hydration states. 195
7.36 The step models used to model the the lowest-index steps on the polar and non-polar surfaces illustrated in Figure 7.9. (a) $(10\bar{1}0) - (10\bar{1}0)$ and (b) hydrated, (c) The average of $(10\bar{1}0) - (0001)$ and $(10\bar{1}0) - (000\bar{1})$, and (d) hydrated, (e) the average of $(0001) - (10\bar{1}0)$ and $(000\bar{1}) - (10\bar{1}0)$, and (f) hydrated. 198

7.37 (a) Step free energy, plotted against the deviation from the chemical potential of the ideal gas state of water, of the hydrated non-polar surface (red), and the hydrated polar surface (blue). (b) The ratio of non-polar to polar growth rates based on a layer growth mechanism. 199

Chapter 1

Introduction

In the context of materials science, nanotechnology is concerned with tuning the the properties of a given material by controlling its size and shape on the nanoscale. Zinc oxide (ZnO) has an abundance of useful properties [1, 2], and forms a commensurate variety of shapes at the nanometer scale [1]. The useful properties include piezoelectricity [3, 4], pyroelectricity [5], and large band-gap semi-conductivity (~ 3.2 eV) [2]. The breadth of nanostructures formed by ZnO is breathtaking, and includes rods [6], needles [7, 8], plates [9], flowers [10], belts [1], and helices [11]. Examples of reported nanodevices include field emission transistors [12, 13], ultrasensitive gas sensors [14], cantilevers [15], resonators [16, 17], transducers [18], actuators [19], LEDs [20], and lasers [21]. Studies have found the properties of ZnO crystals to be intricately related to their size and shape [22]. The importance of size and shape on the material behaviour emphasises the importance of the ability to predict growth behaviour, or understand why growth proceeds in a particular way. Our goal is to investigate ways in which the growth of ZnO nanorod films can be controlled using computational means.

1.1 Background

Only a handful of papers have focused on aspects of simulation and modelling of ZnO crystallite formation. It was found by Viswanatha *et al* [23] that solution growth of ZnO proceeded through an intricate balance of diffusion and reaction kinetics. Another group achieved 'semi-quantitative' success in predicting ZnO nanorod formation of a patterned surface from a supersaturated aqueous solution using a 2-dimensional numerical diffusion-reaction model [24]. The only report pertaining to the influence of surface energy on ZnO growth and morphology focused on the formation of ZnO nanobelts [25]. A thermodynamic model, parameterised with quantum mechanically calculated surface energies, applicable to isolated structures of size $\sim 3 - 100$ nm was used. The model assumed growth limited by the rate of nucleation and the surface energy was used as the nucleation activation energy. Finally, a leading group in the laboratory study of electrochemical deposition of ZnO, has published work on the simulation of ZnO-organic hybrid film electrodeposition [26], and work that couples hydrodynamic, electrochemical, and chemical phenomena with a Monte Carlo substrate simulation [27]. In both cases the films were amorphous rather than nanocrystalline.

1.2 Overview of Work

The aim of this work is to develop a prototype model or set of models that describe a macroscopic sized crystal growth achieved experimentally. The physics and mathematics required to solve such a system occur over a variety of time and length scales that require distinct physical descriptions for each scale. The value of simulation methods is two-fold, one can use a model to make predictions of how a system will behave given a set of conditions. Such a model can be considered an *extrapolation*. Alternatively one can use a model to find, or 'back-out', details of the system that

are too difficult or expensive to do experimentally. This type of work resembles *interpolation*. The first approach reduces the need for experiment and is the development of fundamental theory, method two compliments experiment.

In this work we present the development and results of two different models that focus on different aspects of ZnO nano-rod film growth. The first model is a macroscopic electrolyte transport model that centres around the solution of a system of non-linear partial differential equations (PDE). The part of an electrical system in which the charge carriers are ions, rather than electrons, is called an electrolyte. Thus a model that seeks to capture the transport, formation, and reaction of charged species within an electric field must treat electrolytic transport. Determination of the boundary conditions associated with the crystal growth are used to make inferences about the mechanisms that produce the experimentally observed growth dependence on the experimental variables.

The development and results of a second model that focuses on the microscopic dynamics and energetics of the crystal surfaces is also presented. This model depends on parameters that we obtain using *ab initio* quantum mechanical calculations on models that represent surface features required for crystal growth. The use of quantum mechanical calculations to predict the macroscopic growth behaviour of a crystal is very ambitious, but in our opinion, is necessary for the advancement of materials simulation.

Treatment of both the macroscopic and microscopic aspects of the ZnO electrodeposition constitutes the first steps of a multi-scale approach. The development of a fully fledged multi-scale model is a very large undertaking. It requires an understanding not only of many aspects of the specific system of interest, but also requires expertise in a wide variety of simulation and analysis tools, as well as access to, and ability to use, a variety of computational resources.

Clearly the project scope on the simulation side is very large, even the narrowed aims here constitute a very large undertaking. However, it is

only half of the story. Part of the challenge for large multi-scale projects is the requirement for, and acquisition of, vast amounts of accurate data. The data is required to ensure consistency of the model over the scales it spans. In this context a multiscale approach to a typical laboratory experiment is truly daunting. However, this is part of the challenge to bring such techniques to the benchtop, to begin applying simulation and modelling techniques and approaches not only to highly sophisticated and expensive long-terms projects but to the "everyday" laboratory situation. Given the sometimes fuzzy and uncertain nature of laboratory experimentation, it is potentially a major advantage for the experimenter to have simulation results to help give direction to experimental investigations.

In this work we endeavour to bring computational modelling, at both the conventional macroscopic scale, and the more exotic electronic scale to the typical laboratory benchtop.

1.3 Chapter Overview

The presentation of our work has the following structure.

1.3.1 Chapter 2: Electrochemistry and Zinc Oxide

In this chapter we outline the basic thermodynamic concepts used to describe electrochemical systems. We also outline the experimental methods used by our collaborators at Imperial College (London) to obtain film growth behaviour, and introduce the experimental results which our simulation will focus upon.

1.3.2 Chapter 3: The Electrochemical Model

Here we discuss the structure of the electrochemical system from a modelling point of view. We discuss the treatment of chemical reactions and

derive the transport equations that govern concentration and electric field variation in the electrolyte. We also introduce two simpler approximate forms of the transport model equations to ease numerical solution. Finally we perform some simple analytic case studies.

1.3.3 Chapter 4: Numerical Method and Implementation

This chapter outlines the numerical details used to solve the system of transport and boundary equations that constitute the model described in Chapter 3. The effect of the system parameters (such as grid size, and maximum time step), the output variation, and numerical convergence of the three transport models is also investigated.

1.3.4 Chapter 5: Electrochemical Model Results

Here we make direct comparison between simulated growth behaviour and experimentally observed behaviour. We use the simulation results to infer effects of experimental conditions on the way the nanocrystalline film grows. Our findings include: evidence for OH^- limited crystallite growth, anisotropic crystallite surface growth rate constants, a growth mode transition due to electrode coverage, and behaviour that suggests that the oxygen reduction reaction (ORR) occurs at the electrode and the growing crystallites, at a rate dependent on the applied potential.

1.3.5 Chapter 6: DFT: Theory and Method

In this chapter we introduce the basics of electronic Density Functional Theory (DFT), the method used to perform detailed surface energy calculations which form the basis of our first principles crystal growth model.

1.3.6 Chapter 7: A Study of ZnO Using DFT

In the first part of this chapter we describe how total energies are related to macroscopic thermodynamic variables. We then introduce a basic classical theory of crystal growth, and propose a way in which key parameters, step and kink energies, can be parameterised using total energies obtained from quantum mechanical calculations. The second part demonstrates the method used to obtain the the step and kink free energies using electronic density functional theory (DFT) calculations, and the morphological prediction of nanorod formation under conditions of high and low humidity.

Chapter 2

Electrochemistry and Zinc Oxide

In this chapter we introduce the fundamental concepts of electrochemistry, give an overview of the electrodeposition of ZnO, and present the most relevant experimental results from a modelling and simulation perspective.

2.1 ZnO Electrodeposition

ZnO forms a wide variety of nanostructures that show promise for applications in optoelectronics [28], sensors [14] and piezoelectronics [29]. Such promise has led to a tremendous increase in the scientific literature over the last decade, particularly in the field of nanotechnology, as shown in Figure 2.1. As aqueous electrochemical deposition techniques often allow precise control of the morphology of oxide nanostructures, there is interest in applying these methods to ZnO [9]. Indeed there is evidence that electrochemical parameters such as the substrate lattice parameter [30], the electrolyte [31, 32, 33], the amount of oxygen dissolved in the electrolyte [34], the applied potential across the cell [35], and electrode pre-treatment [32] can all influence the morphology of electrochemically deposited ZnO [9, 6]. Electrochemical synthesis is also attractive because it has the scope for large scale industrial application [36] while being low-cost and readily accessible to researchers.

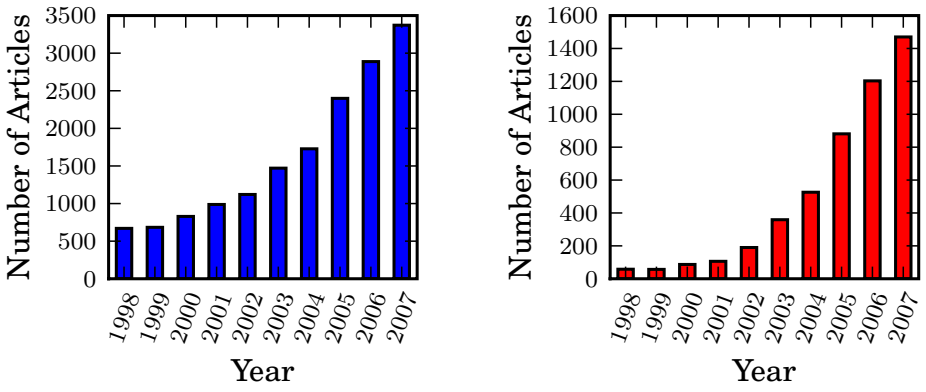

(a) (Zinc Oxide OR ZnO).

(b) (Zinc Oxide OR ZnO) AND (nano).

Figure 2.1: Bar graphs showing interest in ZnO and nanoscale ZnO as indicated by the number of English language articles returned by Web of Science for the period 1998 - 2008.

In Ref. [9], Illy *et al* deposited ZnO nanostructured films by applying a cathodic potential bias to an electrode substrate immersed in an electrolyte solution at 80° C (see Figure 2.2a and 2.2b for image of the experimental rig). The electrolytic solution was composed of a small amount (5 mM) of zinc chloride ($ZnCl_2$), 100 mM calcium chloride ($CaCl_2$), and dissolved molecular oxygen. The concentration of dissolved molecular oxygen under such conditions was determined by Lincot *et al* [37] to be 0.8 mM. Typically, the resulting films consisted of an array of columnar hexagonal prismatic crystallites each with a radius between 80 to 200 nm and length greater than 1000 nm, depending on the deposition conditions. The crystal structure of the crystallites was determined as wurtzite [6].

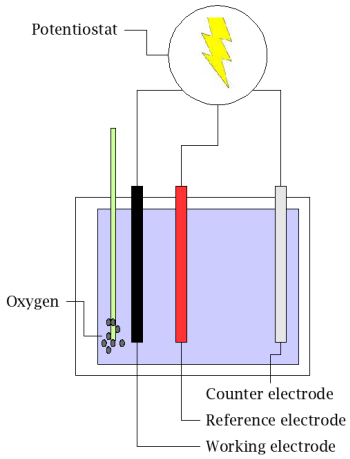

(a) A schematic of the electrochemical rig used to grow the ZnO nanocrystalline thin films.

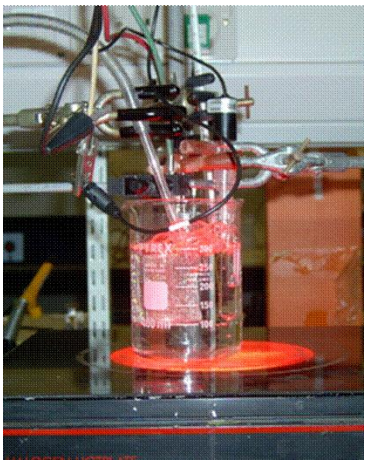

(b) A photograph of the electrochemical rig used to grow the ZnO nanocrystalline thin films.

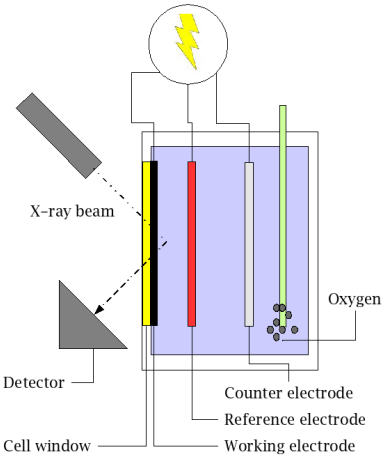

(c) A schematic of the electrochemical rig used to perform X-ray Absorbance Near Edge Spectroscopy (XANES) measurements during the electrochemical thin film growth

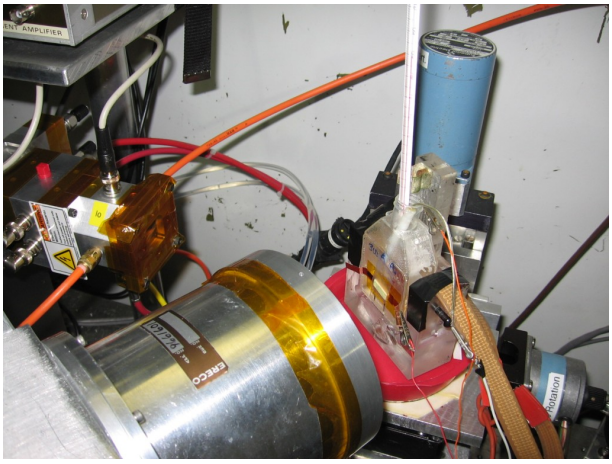

(d) A photograph of the electrochemical rig used to perform X-ray Absorbance Near Edge Spectroscopy (XANES) measurements during the electrochemical thin film growth

Figure 2.2: Illustration of the Experimental rig used by Benoît Illy, Dr Mary Ryan and Dr Bridget Ingham of Imperial College, London

2.2 Electrochemistry and Oxide Growth

Oxide films can be formed by either oxidation of metal (as in the case of metallic corrosion), or precipitation of dissolved precursors. Oxidation of solid metal is limited in that it requires the passage of ions through an oxide layer. Ionic diffusion through an oxide lattice is very slow ($D \sim 10^{-16}\text{cm}^2\text{s}^{-1}$ [38]). Precipitation of dissolved reactants can proceed in one of two ways. One involves electrochemically oxidising or reducing a dissolved metal oxide from a soluble oxidation state to one that is insoluble. This method requires a soluble metal oxide with multiple oxidation states. The second way depends on an electrochemical reaction involving oxygen. Cathodic deposition of ZnO is the second type of reaction [39]. Dissolved Zn ions react with hydroxide that is generated at the electrode by reduction of oxygen with water to form the insoluble metal oxide ZnO.

The electrodic production of OH^-, the *oxygen reduction reaction* (ORR), is defined by

$$O_2 + 2H_2O + 4e^- \rightarrow 4OH^- \qquad E = 0.4 \text{ V (NHE)}. \tag{2.1}$$

The OH^- then reacts with dissolved Zn ions to form the insoluble oxide or hydroxide according to,

$$Zn^{2+} + 2OH^- \rightarrow ZnO + H_2O, \tag{2.2}$$

on the electrode. The overall electrochemical reaction is obtained by adding reaction 2.1 (multiplied by a half to maintain stoichiometry) and reaction 2.2 to yield

$$Zn^{2+} + \tfrac{1}{2}O_2 + 2e^- \rightarrow ZnO \qquad E = 0.89 \text{ V (NHE)}. \tag{2.3}$$

The procedure must avoid the deposition of pure zinc metal from solution,

$$Zn^{2+} + 2e^- \rightarrow Zn \qquad E = -0.76 \text{ V (NHE)}. \tag{2.4}$$

From these electrochemical reactions and their reduction potentials (obtained from standard data tables [40]) we can calculate the potential boundaries within which ZnO can be successfully and exclusively deposited.

The thermodynamic quantity of interest is the electrochemical reduction potential E. Determination of the potential boundaries is demonstrated by the following argument. The electrochemical reduction potential E is related to the Gibbs free energy of formation by $\Delta G = -nFE$, where n is the number of electrons transfered and F is Faraday's constant (96485 Cmol^{-1}). Here E is the *reduction* potential. This is obtained when we split a complete electrochemical reaction into its constituent electron donating (oxidation or anodic) and electron accepting (reduction or cathodic) reactions (electron transfer reactions):

$$A^{z+} + ye^- \rightarrow A^{(z-y)+} \qquad \text{reduction half reaction} \tag{2.5}$$

$$D \rightarrow D^{y+} + ye^- \qquad \text{oxidation half reaction.} \tag{2.6}$$

A reduction half reaction is simply the reverse of an oxidation half reaction and likewise the reduction potential is simply the negative of the oxidation potential. Any electrochemical half reaction can be expressed as anodic or cathodic. However, the convention is to use the cathodic (reduction) reaction. Thus $E > 0$ is spontaneous and $E < 0$ is not. Like the Gibbs free energy, the cell potential can be taken as the sum of the basis reactions i, which by convention are defined in the direction of reduction,

$$E_{tot} = \sum_{i}^{N} E_i^{red}. \tag{2.7}$$

In other words, the total reduction potential (the electrochemical potential corresponding to the reaction of interest defined in the direction of reduction) is the sum of the contributing reactions (oxidation and reduction) expressed in terms of their reduction potentials (i.e. in the direction of reduction). We include the applied potential by noting that the net electron transfer represented by equation (2.7) must be balanced by a charge

conserving oxidation reaction at another electrode with a known reduction potenial, a reference electrode. The applied potential, E_{app}, set on the potentiostat is that of the reference electrode, and in the convention used here, is anodic (oxidation). Thus we subtract its potential from the summation,

$$E_{tot} = \sum_{i}^{N} E_i^{red} - E_{app}. \tag{2.8}$$

The condition to ensure spontenaeity of the cathodic reaction is,

$$E_{tot} > 0 \quad \text{i.e.} \quad E_{app} < \sum_{i}^{N} E_i^{red}. \tag{2.9}$$

Conversely, the condition for reaction in the anodic direction is

$$E_{tot} < 0 \quad \text{i.e.} \quad E_{app} > \sum_{i}^{N} E_i^{red}. \tag{2.10}$$

The two cases above, (2.9) and (2.10), correspond to a cathodic and anodic working elctrode respectively.

For the ZnO system

$$\mathrm{Zn}^{2+} + \tfrac{1}{2}\mathrm{O}_2 + 2e^- \rightarrow \mathrm{ZnO} \qquad E = 0.89 \text{ V (NHE)}, \tag{2.11}$$

the condition is written

$$E_{tot} = E_{red}(\mathrm{ZnO}) - E_{app} > 0. \tag{2.12}$$

Hence for spontaneous ZnO formation

$$E_{app} < 0.89 \text{ V (NHE)}. \tag{2.13}$$

The applied potential must be less than 0.89 V/NHE, giving us a possible upper bound to ensure ZnO formation. We must also ensure that formation of the OH^- precursor is spontaneous,

$$\mathrm{O}_2 + 2\mathrm{H}_2\mathrm{O} + 4e \rightarrow 4\mathrm{OH}^- \qquad E = 0.4 \text{ V (NHE)} \tag{2.14}$$

in which case

$$E_{tot} = E_{red}(\mathrm{O_2}) - E_{app} > 0, \tag{2.15}$$

giving

$$E_{app}(cathode) < 0.4 \text{ V (NHE)}, \tag{2.16}$$

which is our (lowest) upper bound for applied potential. To prohibit Zn precipitation we require the condition

$$E_{tot} = E_{red}(Zn) - E_{app} < 0 \qquad \text{(non-spontaneous)} \tag{2.17}$$

which yields

$$E_{app} > -0.76V/NHE \tag{2.18}$$

and this is our lower bound. The resulting potential boundaries are

$$-0.76 < E_{app} < +0.4 < +0.89 \text{ V (NHE)} \tag{2.19}$$

and using E V (AgCl) = +0.20 V (NHE)

$$-0.96 < E_{app} < +0.20 \text{ V (AgCl)}. \tag{2.20}$$

Where AgCl denotes the silver chloride reference electrode, which will be used in the throughout the remainder of this work.

Although we have been able to define a region of applied potential where ZnO will be thermodynamically preferred, the rate at which the reaction will proceed has not been considered. Such a consideration is a kinetic consideration, and involves an understanding of the structure of the electrode-electrolyte interface, and the transport properties of the surrounding medium. The kinetics of the ZnO/ORR system have been investigated by Lincot and co-workers [39], and the ORR was found to be occurring at the mass transport limited regime under the conditions (applied potential and concentration) we are interested in. The main focus in the present work is the transport within the surrounding medium.

2.2.1 Electrodeposition Results and Observations

Our goal is to model the growth of ZnO nanorod films under conditions as close as possible to the experiments described in Ref. [41], to predict the growth rate and morphology of the nanorods as a function of time. The information produced should then allow interpretation of the observed growth dependence on the electrochemical conditions and the identification of critical parameters that control film morphology.

Here we summarise the key experimental data to aid in model development, and conditions that must be met or replicated in order to validate our modelling. We begin by outlining the fundamental data we wish to replicate: the growth behaviour represented by X-ray Absorbance Near Edge Spectroscopy (XANES) intensity change with time. Synchrotron radiation has been used to measure the rate of ZnO deposition *in situ* under various electrochemical conditions [41, 9], using the apparatus shown in Figure 2.2c. The XANES technique measures the amount of Zn in a crystalline environment per area. If the deposited film is monolithic, the film volume per area can be obtained by multiplication by the molar volume of ZnO. Even though we are not working with monolithic ZnO films, our preferred measure of nano-rod film growth is that of volume per area of an equivalent monolithic film, and the unit is used throughout this work.

The variation of the observed growth rates with the cathodic potential, and Zn^{2+} concentration is shown in Figure 2.3. These curves are representative of the growth dependence on the experimental variables, concentration and applied potential, at values that produce the preferred nano-rod films. The preferred nano-rod films have high density of nanorods with a uniform diameter of 100 nm or less, and height on the order of a micron. The results show a clear difference between the effect of varying the potential and that of varying concentration of zinc ions. A striking feature of many of the measured growth curves is the presence of two distinct growth rates. During the early growth stage, which we refer to as 'mode one', there is larger growth rate than the later stage growth, referred to as

'mode two'. The transition from the first growth mode to the second is abrupt.

Two observations can be made about the effect of potential variation. The first observation is that the mode one growth rates obtained at potentials -670, -770, and -970 mV (Ag/AgCl) are the same, and greater than that obtained for potential of -370 mV (Ag/AgCl). The reason for this difference is attributed to the amount of OH^- present. For applied potential more positive than -420 mV (Ag/AgCl) the ORR reaction proceeds more slowly, according to the reaction [37, 42, 43],

$$O_2 + 2H_2O + 2e^- \rightarrow H_2O_2 + 2OH^-. \tag{2.21}$$

At potentials more negative than -420 mV (Ag/AgCl), the mode one growth curves have almost identical slope and duration. The effect of the potential is manifested in the slope of the second growth phase, with more negative potential resulting in a greater mode two growth rate.

The effect of increasing the Zn^{2+} concentration at a particular applied potential is shown in Figure 2.3c. Overall the growth is increased, however, the rate of early growth is decreased by increasing the concentration. The 10 mM curves also lack the abrupt growth mode transition observed for the 5 mM curves.

We can supplement the growth behaviour described above with a variety of auxiliary observations. A relation between the potentiostatic current measured by the electrochemical equipment, and the growth behaviour, measured by the *in situ* X-ray measurements was observed. During the deposition the current profile, associated with the ORR, exhibits a sharp rise and decline over a period identical to the duration of the first growth phase measured by synchrotron radiation (see Figure 2.4a), and then settles to a steady value. Given that the rods are growing in height and to a lesser extent width, eventually we would expect to see a diminishing current due to the increasing distance the O_2 must travel in order for the ORR to occur solely at the electrode. However, the current settles to a

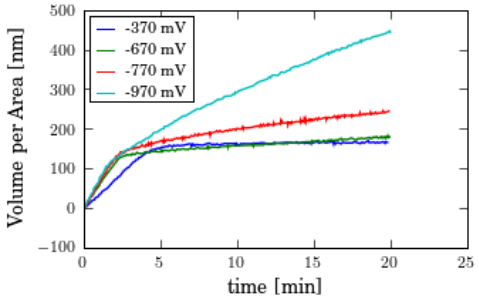

(a) Growth curves obtained at various potentials, and solution composition: 5 mM $ZnCl_2$, and 0.1 M $CaCl_2$.

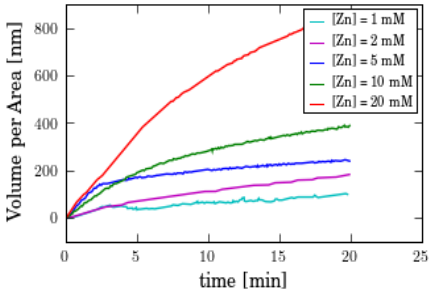

(b) Growth curves obtained at potential of -770 mV (Ag/AgCl) for Zn^{2+} concentration ranging from 1 to 20 mM.

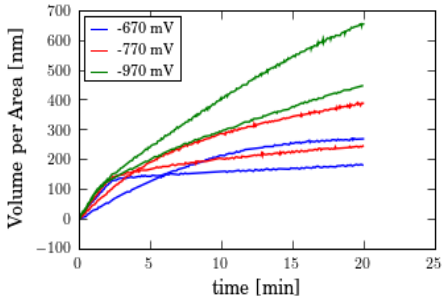

(c) Growth curves obtained for Zn^{2+} concentration of 5 and 10 mM, at potentials -670 (blue), -770 (red), -970 (green) mV (Ag/AgCl). For each coloured pair, the lower curve corresponds to a Zn^{2+} concentration of 5 mM.

Figure 2.3: The fundamental results obtained from x-ray absorption measurements of growth with variation of cathodic potential 2.3a and Zn^{2+} concentration 2.3b.

steady value, thus it seems likely the ORR is occurring on some or all of the nano-crystallite film faces.

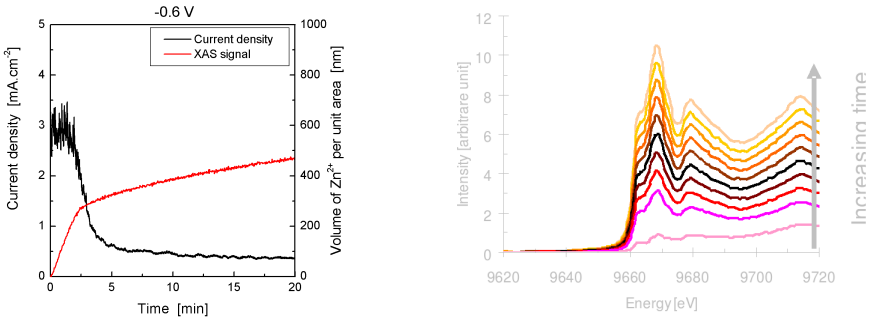

(a) (b)

Figure 2.4: (a) Current density (black) and X-ray absorption intensity at 9720 eV from repeated scans (red) as a function of time, (b) Repeated Synchrotron XANES across the Zn K-edge. Courtesy of BI and MR

The crystal environment of the Zn was investigated using synchrotron X-ray absorption near edge spectroscopy (XANES) of the Zn K-edge. The data shows (Figure 2.4b) that throughout the deposition, although there are two growth phases, the Zn bonding environment remains the same. Thus no significant chemical changes are occurring with growth over the duration of the deposition.

Scanning Electron Microscope (SEM) images give an impression of the actual morphology and appearance of the deposited film, and individual crystallites. The influence of the potential on morphology is shown by Figures 2.5a & 2.5b. An applied cathodic potential below -420 mV (AgCl) (Figure 2.5a) yields larger rod diameter, and a lower rod density per area, than that obtained from a cathodic potential greater than -420 mV (AgCl) (Figure 2.5b). Such a result suggests competition between rod growth, slowed due to diminished OH^- at higher applied potential, and seed nucleation.

The measured growth curves and final film morphologies for the standard Zn^{2+} concentration (5 mM) at applied potential of -770 mV and -370 mV (AgCl) are shown in Figure 2.6. The growth curves indicate that the same amount of material has been deposited during the mode one growth, yet the rod diameters and densities are different. It appears that slower growth produces higher density films, and therefore greater nucleation, or less coalescence. Conversely, higher nucleation (or less coalescence) produces slower growth.

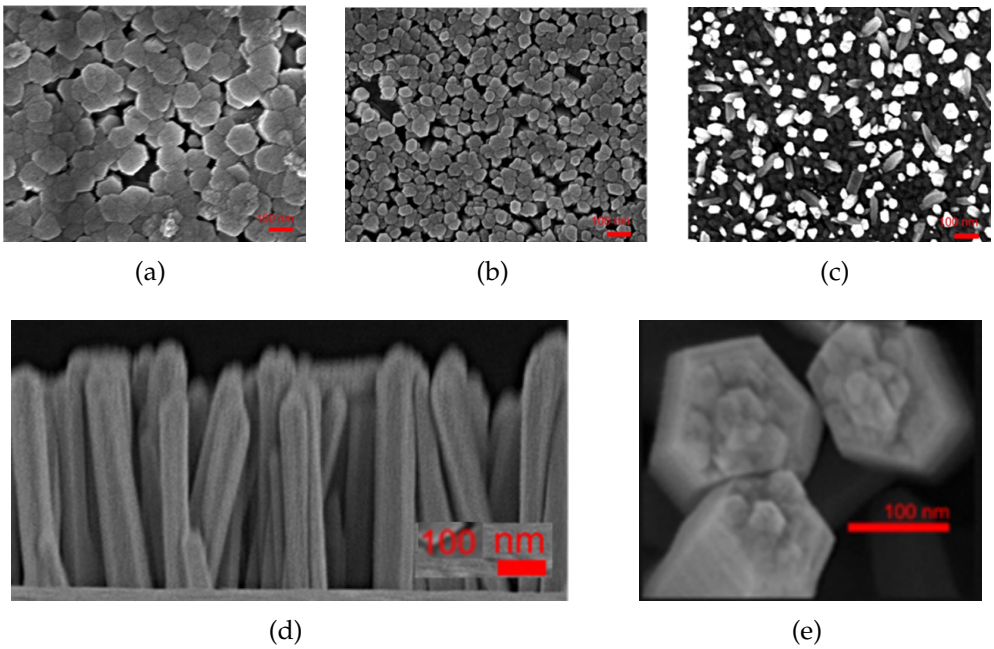

(a) (b) (c)

(d) (e)

Figure 2.5: SEM images of electrodeposited ZnO films (in all images the red scale bar represents 100 nm): (a) Cathodic potential of -770 mV (Ag/AgCl), 5 mM $Zn(NO_3)_2$, and 0.1 M KCl, (b) cathodic potential -370 mV (Ag/AgCl), otherwise the same as (a). (c) Same as (a) but with 1 mM $Zn(NO_3)_2$. (d) Profile image under same conditions as (a), aspect ratio approximately 6. (e) Plan view of sample used in (d) showing tapered tip, and islands suggestive of layer growth.

The effect of dramatically decreasing the Zn^{2+} concentration is illustrated by comparison of Figures 2.5a & 2.5c. We see that decreasing the concentration by a factor of five leads to poorly aligned rods, with small radii, and an increased density. As with the case of applied potential variation, the increased density is likely to be a result of slower (lateral) growth, due to diminished Zn^{2+}, thus allowing more time for nucleation of new rods. Alternatively, it is possible that at higher Zn^{2+} concentration and growth rates, the small crystals coalesce to form bigger crystals.

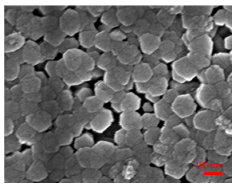

(a)

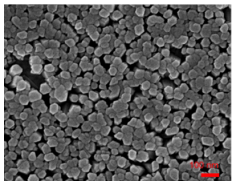

(b)

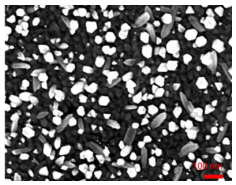

(c)

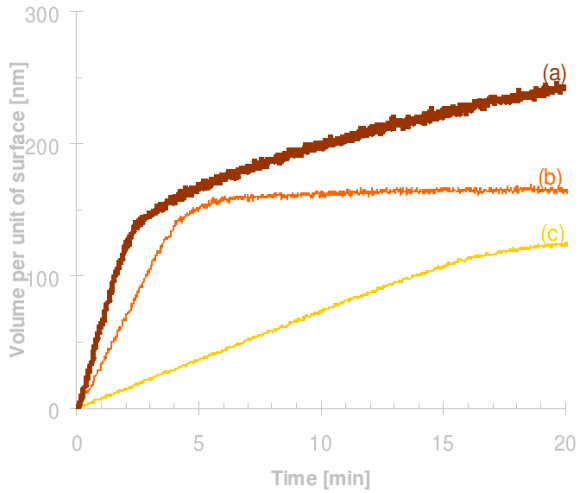

(d) The growth curves corresponding to (a) left-top, cathodic potential of -770 mV (Ag/AgCl), 5 mM $Zn(NO_3)_2$, and 0.1 M KCl, (b) left-middle, cathodic potential -370 mV (Ag/AgCl), 5 mM $Zn(NO_3)_2$, and 0.1 M KCl, and (c) left-bottom, same as (a) but with 1 mM $Zn(NO_3)_2$.

Figure 2.6: Growth behaviour of morphological outcomes.

The growth curves associated with the morphological outcomes shown in Figure 2.5 are shown in Figure 2.6. We see that the nano-rods formed at the lowest Zn^{2+} concentration grow much more slowly, and exhibit a more subtle transition to the second growth mode after about fifteen min-

utes. The XANES intensity at the transition is lower than that with equal applied potential but greater Zn^{2+} concentration. Thus, for cases in which the growth rates are very different the XANES intensity gives an indication of the rod packing, however for similar growth rates, a clear distinction cannot be made.

The above observations indicate that the early rod growth rate depends on the concentration of Zn^{2+}, and the applied potential through its effect on OH^- production. We also observe that slower initial growth rate, due to lower concentration of Zn^{2+} or OH^-, is always accompanied by increased nano-rod density. The effect of variation of applied potential on mode one growth vanishes for potential less than -420 mV (AgCl), suggesting that the rate of OH^- production has reached a maximum. It also implies that under conditions in which the applied potential is less than -420 mV (AgCl), variation of the Zn^{2+} concentration has sole influence on variation of nucleation and mode one growth rate.

The two mode growth behaviour is consistent with unhindered initial growth until lateral growth is spatially hindered, at which stage the second growth stage, dominated by vertical growth dominates. The idea of lateral growth blocking due to closing of the inter-rod gap is supported by the results shown in Figure 2.7. The data was obtained by carrying out the electrochemical deposition over a variety of times, followed by SEM observation. We see that the transition between first and second growth modes is coincident with the closing of the interrod gap.

Our final observation from the SEM images pertains to the growth mechanism of the ZnO nanorods. Figure 2.5e shows the top face of three nanorods. All three faces are covered in coarsely faceted rises ('steps') and islands which are co-oriented with the lateral facets of the nanorod. The presence of steps and islands strongly suggests the existence of a layer growth mechanism [44]. The presence of a tapering towards the top of the rod, and the striation on the lateral faces also suggest layer growth in which steps formed on the interior of the top facet propagate out to the

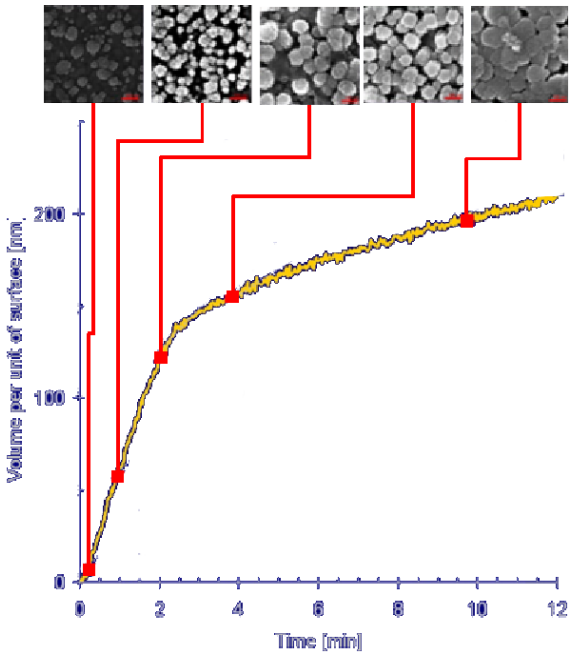

Figure 2.7: Film morphology and XANES signal intensity evolution over time. SEM images were acquired at 15, 60, 120, 240 and 600 seconds.

edge of the facet [44]. The presence of many islands and the tapered shape suggests that the multiple layers are growing at the same time. Similar angular island structures have been observed on the $(000\bar{1})$ face of ZnO discs formed using a vapour phase transport (VPT) technique. In this case a layer growth mechanism was also proposed [45].

2.3 Summary

We wish to emphasise the most important inferences made from the experimental data. Firstly, under the standard conditions the growth exhibits two growth modes separated by an abrupt transition. The cause of the transition appears to be due to inhibition of lateral growth due to crowding. The most abrupt transitions are observed when the first growth mode is rapid. The films that characterise this behaviour are composed of nanorods with a diameter around 100 nm and are densely packed.

The magnitude of the mode one growth depends on both the concen-

tration of Zn^{2+} and the applied potential. The most obvious contribution of the applied potential on the mode one growth rate is in the production of OH^-. This is demonstrated by the observation of a significantly slower mode one growth rate at applied potentials that are known to produce OH^- by a less efficient reaction. Thus the mode one growth depends on the concentration of both Zn^{2+} and OH^-. We also note that slower mode one growth, due to lower Zn^{2+} concentration or less cathodic potential, is always associated with increased nucleation.

Variation of the potential in the region where the ORR occurs most efficiently (< -420 mV (AgCl)) has no effect on the mode one growth rate, but does affect mode two growth rate in a continuous fashion. Thus, at these potentials, the rate of mode one growth is mediated solely by the Zn^{2+} concentration. Observation of steady mode two growth that is not diminished by increased rod height suggests the ORR occurs on the growing crystallite, as otherwise growth retardation would be expected due to an increasing diffusion length. Although, if OH^- is in significant excess to Zn^{2+}, such growth retardation may not be observed in the twenty minute duration of the film depositions. The continuous effect of the potential on second phase growth suggests the potential mediates a growth rate determining process.

Chapter 3

The Electrochemical Model

In the first part of this chapter we review the phenomena thought to characterise the experimental system, and develop a schematic model. Our emphasis is on the examination of transport models for the treatment of our zinc oxide system. We also consider the nature of the solid-electrolyte interfaces in the context of boundary conditions. We treat transport as the most important description, the basis, or fundamental model upon which any other more exotic or fine-grained model must be built. Electrolyte transport is what connects us to the microscopic aspects of the film growth, such as chemical reaction and surface dynamics. We present the development of the fundamental transport equations for electrolytic systems, and finally, we investigate the behaviour of a simplified 1-dimensional transport limited model.

3.1 System Composition

The phenomena that dictate the film growth belong to either growth kinetics or transport, depicted in Figure 3.1. The kinetics includes that of chemical species formation and consumption at an interface (electrodics), as well as inclusion into the crystal (crystal growth). In Figure 3.1 chemical reactions are depicted on all three crystallite surfaces. This is because there

is no evidence indicating an epitaxial bonding between the nanorods and the substrate. In Ref [6] Illy *et al* emphasise that nanorod film coverage on the polycrystalline substrate is much greater than the area of a particular epitaxially oriented grain ($\sim 1\ \mu m^2$), indicating that epitaxial bonding is unlikely. Thus it is possible that chemical reactions and growth can occur at the bottom, side, and top faces of the nano-rods. First we give an overview of our treatment of the surface kinetics.

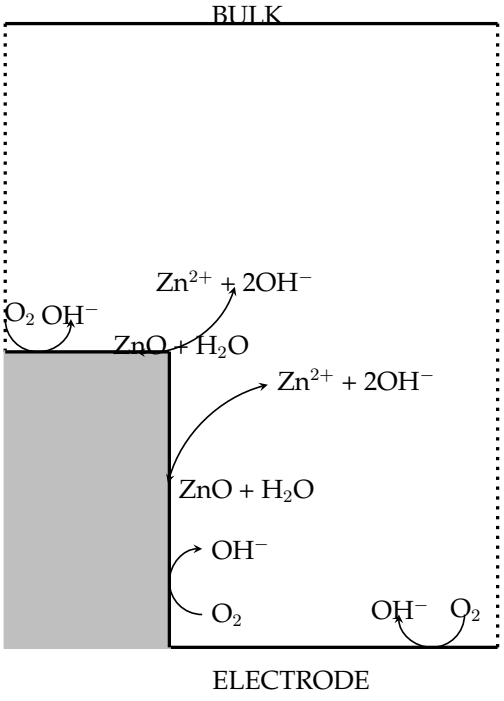

Figure 3.1: Schematic of computational domain in which the transport region is white, the crystallite is grey, the black line indicates the boundaries (dotted lines indicate mirror boundaries). the polar (P) surface is the upper grey edge, and the non-polar (NP) surface is the lateral grey edge. Also shown are the reactions considered at various boundaries.

The electrolyte consists of millimolar amounts of Zn^{2+}, O_2, OH^-, and molar amounts of ionic buffer (Ca^{2+}, Cl^-). With regard to crystal formation the buffer is regarded as a spectator as it does not directly contribute

to the film growth. It is possible that the Ca^{2+} or Cl^{-} could affect the crystal growth, a process called 'poisoning'. However, depositions performed using potassium chloride (K^{+} and Cl^{-}), and calcium nitrate (Ca^{2+} and NO_3^{-}), exhibited the same behaviour as that obtained using $CaCl_2$ [46]. The behaviour of the participating species, Zn^{2+}, O_2, OH^{-}, is of paramount importance in the description of the film growth.

3.1.1 Essential Reactions

The precise mechanistic details of how the ZnO forms and the solution composition ($Zn_xO_yH_z$ complexes are known to exist) are still only known for a few specific conditions [47]. The model transport-reaction scheme is shown in Figure 3.2. The scheme depicts fluxes with vertical arrows, electrochemical reactions with horizontal arrows and summarises the paths that the bulk species must take for ZnO to be formed. The chemical reac-

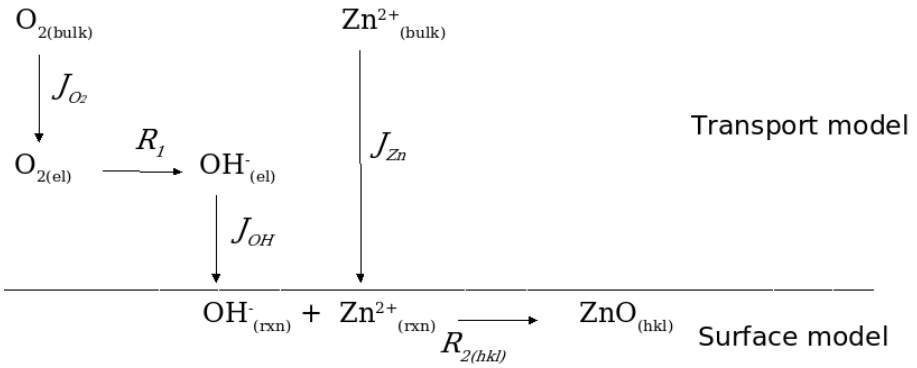

Figure 3.2: The constrained transport-reaction scheme for the species involved in ZnO formation with Zn^{2+}/OH^{-} reaction fixed at the electrode. Again (bulk) refers to the solution composition at great distance from the growing film, (el) is the electrode region, (rxn) is the region where Zn^{2+} and OH^{-} meet, and (hkl) refers to a particular ZnO crystal facet. Transport is denoted with horizontal arrows and chemical reactions with horizontal arrows.

tions described above lead to crystal growth via

$$Zn^{2+} + 2OH^- \rightleftharpoons ZnO + H_2O, \tag{3.1}$$

at the crystal facets, where OH^- is generated by the oxygen reduction reaction

$$O_2 + 2H_2O + 4e^- \rightarrow 4OH^- \tag{3.2}$$

at both the electrode and the crystal facets. The details of both these reactions can be quite complex.

The Oxygen Reduction reaction (ORR)

The oxygen reduction reaction is an electrode reaction, and therefore is influenced by the electrode overpotential. The most appropriate treatment of this reaction under conditions in which both transport and applied potential can contribute to the rate is the current-overpotential equation [48],

$$i = i_\circ \left[\frac{C_{O_2}}{C^\infty_{O_2}} e^{-pnf\eta} - \frac{C_{OH}}{C^\infty_{OH}} e^{(1-p)nf\eta} \right]. \tag{3.3}$$

The equilibrium exchange current density, $i_\circ$, represents the rate of the electrode reaction, the overpotential, η, is the deviation from the potential at which current flow is zero. The location of the kinetic barrier is denoted by the "symmetry factor" p, n is the number of electrons being transfered, f is Faraday's number divided by the thermal energy, RT, and the bulk and electrode concentrations are denoted by C^∞ and C respectively.

To simplify the treatment we consider the case in which the second term is small. Such a case exists when the kinetic barrier is higly assymmetrical, $p \rightarrow 1$, or when the surface overpotenial is increasingly cathodic, $\eta << 0$. Under such conditions we have,

$$i = i_\circ \left[\frac{C_{O_2}}{C^\infty_{O_2}} e^{-pnf\eta} \right]. \tag{3.4}$$

To qualitatively investigate the relationship between applied potential and the ORR rate we write (3.4) in terms of the O_2 boundary flux, J_{O_2},

$$i_{ORR} = FnJ_{O_2}, \tag{3.5}$$

where, as above, n is the number of electrons transfered, F is Faraday's number, and J_{O_2} is the flux of O_2 at the boundary. Rearrangement gives,

$$J_{O_2} = \left[\left(\frac{i_\circ}{nFC^\infty_{O_2}}\right)\exp(-npf\eta)\right]C_{O_2}, \tag{3.6}$$

which is recast as a flux-reaction balance in which the reaction is first order in terms of O_2 concentration, and the term inside the square brackets constitutes the rate constant, α,

$$J_{O_2} = \alpha C_{O_2} \qquad \text{where} \qquad \alpha = \left(\frac{i_\circ}{nFC^\infty_{O_2}}\right)\exp(-npf\eta). \tag{3.7}$$

We can qualitatively represent variation in applied potential by variation of α because a cathodic applied potential corresponds to a negative overpotential, η, and therefore α is positive, i.e. E_{app} and the ORR rate contant, α, vary monotonically.

In the ZnO system at the potentials we are investigating the oxygen reduction reaction proceeds very close to the mass transport limited regime [37]. Under the mass transport limited regime, the consumption of O_2 at the electrode occurs at a greater rate than it can be delivered by diffusive transport processes. Thus there is no O_2 net accumulation, the O_2 is effectively instantaneously consumed in the diffusion timescale, $\alpha >> J_{O_2}$. We implement this scenario with,

$$C_{O_2} = 0 \tag{3.8}$$

as the electrode boundary condition for O_2. Clearly, if periods of oxygen limited growth exist, this scenario will make the system sensitive to the amount of dissolved oxygen in the system. However, the system is considered to be O_2 saturated. The mass transport limited boundary condition is useful in the search for system parameters because it reduces the degrees of freedom.

ZnO Formation and Incorporation into the Crystallite

The reaction and incorporation of ZnO units into the growing crystal is also a complex process which involves the surface charge of the growing crystal, the electric double layer, the dynamics of the crystal surface features (such as steps and kinks), and the multitude of intermediate steps between adsorption and inclusion. In this study we use a simple scaling rate law to describe the formation of ZnO,

$$R_{hkl} = \beta_{hkl}\left(1 - \frac{Q}{K}\right) \tag{3.9}$$

where β_{hkl} is the surface specific reaction-inclusion rate constant, Q is the reaction quotient corresponding to the reverse of reaction (3.1)

$$Q = [\mathrm{Zn}^{2+}][\mathrm{OH}^{-}]^2$$

where square brackets denote concentrations. The magnitude of the rate coefficients β_{hkl} can be estimated to match the experimental growth rates in Ref. [41]. Note the alternative forward form

$$Q' = \frac{1}{[\mathrm{Zn}^{2+}][\mathrm{OH}^{-}]^2}$$

is problematic if $[i] = 0$. Finally K is the equilibrium (dissolution) constant. It is easy to see that when $Q > K \Rightarrow R < 0$ the rate of production of Zn^{2+} and OH^{-} is negative i.e. ZnO is produced. Conversely when $Q < K \Rightarrow R > 0$ the rate of production of Zn^{2+} and OH^{-} is positive and ZnO dissolution is favoured.

The scaling law described above is often used in corrosion science [49, 50, 51, 52], in which corrosion processes are considered to proceed isotropically. In the context of crystal growth we re-cast the scaling law into a form more familiar to crystal growth theory [53, 44, 54, 55, 56],

$$R_{hkl} = \beta_{hkl}\left(1 - \frac{Q}{Q_\circ}\right), \tag{3.10}$$

and rearrange to,

$$R_{hkl} = \beta_{hkl}\left(\frac{Q_\circ - Q}{Q_\circ}\right). \tag{3.11}$$

The bracketed quantity is easily recognised as the supersaturation of ZnO, σ. Thus,

$$R_{hkl} = \beta_{hkl}\sigma, \tag{3.12}$$

and from the crystal growth literature we know,

$$\sigma = (\mu_C - \mu_\circ)/kT = \Delta\mu/kT \tag{3.13}$$

where μ_C is the chemical potential of the bulk crystal and $\mu_\circ$ is that of the crystal surface. In Chapter 7 we elaborate on how Equations 3.12 and 3.13 relate to crystal growth mechanisms.

In the Wurtzite structure, ZnO predominantly exhibits two families of crystal facets: the $\{0001\}$ (which is polar) and the $\{01\bar{1}0\}$ (which is non-polar). The anisotropy of the different crystal surfaces is modelled here by assigning different values of β_{hkl} for each facet. Furthermore, changes in the applied potential will also alter the reaction rates at the different crystal facets, an effect we mimic by varying the rate constants β_{hkl}. The boundary conditions for the ionic flux, $\vec{J}_i$, of species i at the (hkl) crystal facet are then given by:

$$A_{hkl}\vec{n}_{hkl} \cdot \left(\vec{J}_i + c_i\vec{v}_{hkl}\right) = R_{hkl} \tag{3.14}$$

where $\vec{n}_{hkl}$ is the unit normal to the facet, v_{hkl} is the velocity of the facet, R_{hkl} is the rate of ZnO formation and A_{hkl} is the facet area.

The model parameters D_i and K, the solubility constant, can be found in the literature. The ZnO solubility constant K was found in the literature to be 2.2×10^{-17} mol^{3}L^{-3} [57]. The diffusion coefficients (see Table 3.1) of Zn^{2+} (1.4×10^{-9} m^{2}s^{-1}) and OH^- (5.3×10^{-9} m^{2}s^{-1}) were obtained from the reference literature [58] and D_{O_2} (2.4×10^{-9} m^{2}s^{-1}) was obtained from the electrochemical literature [37]. The magnitude of the β_{hkl} parameters were chosen so that the simulations grew at approximately the rates observed

in experiments, and were also varied in order to understand their effect on the growth regimes. We discuss the selection and variation of β in Chapter 5.

Table 3.1: Diffusion coefficients [58, 37]

Species (i)	Diffusion coefficient (D_i / $\mathrm{m^2 s^{-1}}$)
Zn^{2+}	1.41×10^{-9}
O_2	2.42×10^{-9}
OH^-	$5.27 \times 10{-}9$
Ca^{2+}	1.58×10^{-9}
Cl^-	2.03×10^{-9}

3.1.2 The Electrostatic Potential

The focus of our work is ostensibly on the behaviour of mass: crystal growth, mass transport. However, an essential part of the *electro*chemical system are the forces associated with the electrostatic potential and its spatial variation. The electric force, $\mathbf{f}$, experienced by a test charge, q, is used to introduce the electric field $\mathbf{E}$,

$$\mathbf{f} = q\mathbf{E}. \tag{3.15}$$

In the absence of a changing magnetic field, the curl of the electric field is zero,

$$\nabla \times \mathbf{E} = 0. \tag{3.16}$$

Given that the curl of the gradient of a scalar field is zero, the electrostatic potential Φ, is now introduced as,

$$\mathbf{E} = -\nabla\Phi \tag{3.17}$$

which satisfies (3.16). The variation on the electric field as a function of a charge distribution, ρ_e, is given by Poisson's Equation,

$$\nabla \cdot (\epsilon\mathbf{E}) = \rho_e, \tag{3.18}$$

where ϵ, the dielectric constant, represents the ability of the field to propagate through the medium. For a medium of uniform dielectric constant, ϵ,

$$\nabla^2 \Phi = -\frac{\rho_e}{\epsilon}. \tag{3.19}$$

3.1.3 The Thin Double Layer Approximation

Our discussion so far has neglected the microscopic structure of the solid-electrolyte interface. Before we discuss the development of our transport based growth model we elaborate on the nature of the electric double layer. The charge on the electrode (or any surface susceptible to a charging mechanism) induces structure on the surrounding electrolyte by electrostatic interaction with the charged species. The size (thickness) of the region is mediated by the balance of the strength of the electrostatic interaction (effectively the electrode polarity) against randomisation by thermal jostling. The electric force is greatest near the electrode and becomes progressively weaker away from the electrode. The result is a fixed layer of charge near the electrode and a diffuse cloud of charge away from the electrode. This is called the diffuse interface model [59]. The closeness of the fixed layer, called the Outer Helmholtz Plane (OHP), is determined by the size of the charged species, and their associated hydration shells. The region between the surface and the OHP has fixed charge, and therefore by (3.19), is a region of linear electric field.

The electrode structure model (illustrated in Figure 3.3) is called the Gouy-Chapman-Stern model [48], in which the double charge layer part is described as a conventional capacitor (called the Stern layer), and the diffuse part (beyond the OHP) is described by the (independent) work of Gouy and Chapman. The capacitance of the Stern layer is effectively independent of electric potential and electrolyte concentration, whereas the capacitance of the diffuse layer is sensitive to both. In the context of our bulk transport model, the Stern layer can be considered as part of the

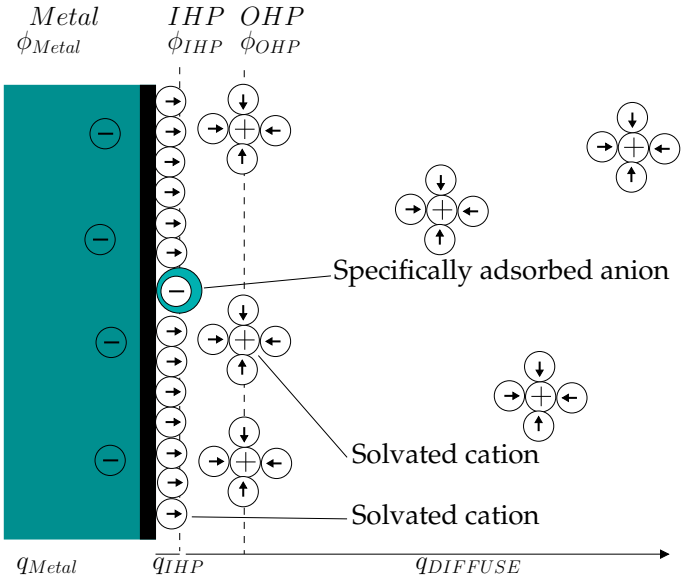

Figure 3.3: Schematic of the electric double layer.

electrode, however, this is not necessarily the case for the diffuse layer.

To quantify the extent of the diffuse layer Gouy and Chapman combined Poisson's Equation with Boltzmann's distribution to yield the Poisson-Boltzmann equation [59], given here in 1 dimension,

$$\frac{d^2\phi}{dx^2} = -\frac{q}{\epsilon}\sum z_i \rho_{\infty i} \exp\left(\frac{-z_i q\phi}{kT}\right), \tag{3.20}$$

where ρ_∞ is the bulk concentration, z_i is the valence of species i, and q is the elementary charge. Noting that far from the electrode, the potential and electric field vanish,

$$\phi_\infty = 0 \quad \text{and} \quad \left(\frac{d\phi}{dx}\right)_\infty = 0, \tag{3.21}$$

results in the relation,

$$\frac{\epsilon}{2kT}\left(\frac{d^2\phi}{dx^2}\right) = \sum \rho_i - \sum \rho_{\infty i}, \tag{3.22}$$

between electrostatic potential and charge density in the diffuse layer. For a 2:1 electrolyte, such as $CaCl_2$ the dominant electrolyte in our system, the

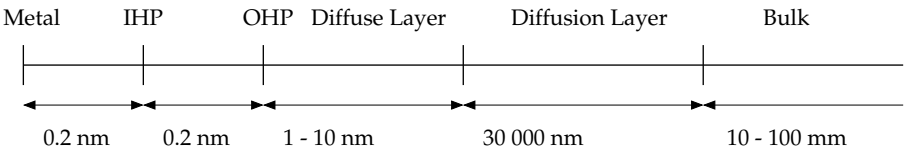

Figure 3.4: Illustration of approximate length scales associated with electrochemical systems.

relation between the surface potential $\phi_\circ$ and ϕ is [60],

$$\left(\frac{\sqrt{1+2e^{q\phi/kT}}-3}{\sqrt{1+2e^{q\phi/kT}}+3}\right)=\left(\frac{\sqrt{1+2e^{q\phi_\circ/kT}}-3}{\sqrt{1+2e^{q\phi_\circ/kT}}+3}\right)e^{-\lambda_D^{-1}x} \tag{3.23}$$

where $\phi_\circ$ denotes the potential at the OHP, and

$$\lambda_D=\left(\frac{\epsilon RT}{F^2\sum_i z_i^2 c_{i\infty}}\right)^{1/2}. \tag{3.24}$$

where ϵ is the permittivity, RT the proper thermal energy, F is Faraday's constant, z_i is the valence of i, and $c_{i\infty}$ is the bulk equilibrium concentration of i. At high electrode surface potentials the potential drops rapidly (plotted in Figure 3.5) and therefore the diffuse double layer is very compact. The overall electrochemical system has a structure like that shown in Figure 3.4 [61], in which the diffuse layer is separated from the bulk by a diffusion layer with length, L, over which the electrolyte composition differs from the bulk due to diffusive transport. For low potentials, $\phi_\circ <$ 25 mV, 3.23 reduces to

$$\phi \approx \phi_\circ e^{-\lambda_D^{-1}x}, \tag{3.25}$$

and the quantity, λ_D, known as the Debye length, characterises the decay length of the potential. According to Equation 3.24 the Debye length of the ZnO electrochemical system, in which [$CaCl_2$] = 0.1 M, is not greater than $\approx$ 0.6 nm. Thus, any charge separation, or macroscopic deviation from electroneutrality, is considered as part of the boundary, and does not affect the bulk electrolytic transport. In dynamic studies it is typical to ignore the details of the charge distribution and treat the electrode-electrolyte region

as a sharp interface [62, 63]. This is called the thin double layer approximation and is justified when the diffusion length, L, is much greater than the Debye length, λ_D, i.e. $\lambda_D/L << 1$.

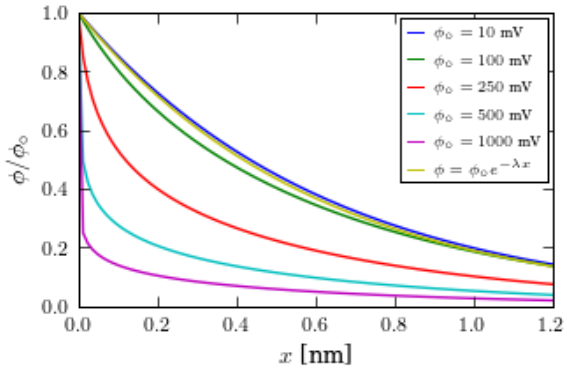

Figure 3.5: Plots of the variation of potential away from the electrode in 0.1 M 2:1 electrolyte ($CaCl_2$), calculated using (3.23), with $\lambda_D = 0.6$ nm.

3.2 Macroscopic Electrolyte Tranport Model

We begin our mathematical description from the macroscopic thermodynamic potential X. The common thermodynamic potentials are the Helmholtz potential F, the enthalpy, H, and the Gibbs potential, G [64]. The potential X depends on a combination of the basic variables, $\{x\}$, including entropy, S, temperature, T, pressure, P, volume, V, and amount, n. The condition for spontaneity and equilibrium of a given thermodynamic potential $X(\{x\})$, is $(dX)_{\{x\}} \leq 0$ [65]. In order to use the condition to model the process of spontaneous change, local thermodynamic equilibrium (LTE) is assumed. The LTE treats a non-equilibrium system by dividing it into a set of sub-regions in which each sub-region is at thermodynamic equilibrium and therefore the thermodynamic equations hold within each sub-region [66]. Thermodynamic parameters are now described as fields, $f(\mathbf{r}, t)$, in which each coordinate is in local equilibrium. The assumption is justified

because the spatial variation of the fields is slow compared to molecular dimensions and the timescale of molecular motion is so small that the molecular motions are fully relaxed compared to the temporal variation of the field. The thermodynamic driving forces are obtained by taking the partial derivative of the thermodynamic potential with respect to the extensive (natural) variable of interest - the solute number - whilst the other variables are fixed,

$$\left(\frac{\partial X}{\partial n_i}\right)_{x\neq\{n_i\}} = \mu_i \tag{3.26}$$

Here, n_i is the total amount (in a given sub-region) of solute i and μ_i is the chemical potential of i,

$$\mu_i = \mu_\circ + RT\ln(a_i) \tag{3.27}$$

where a_i is the activity of species i. We use the ideal solution approximation in which the interaction between ions is assumed to be negligible, in which case the activity a_i is equivalent to the concentration, c_i [67]. For low Reynolds number, viscous forces dominate and the solute moves with a velocity proportional to the applied force

$$v(\mathbf{r},t) = u_i\bar{F}(\mathbf{r},t) \tag{3.28}$$

where the proportionality constant , u_i, is the *mobility* of the solute, and $\bar{F}$ is the force experienced by that solute. As usual, the force is obtained from the negative derivative of the potential, in this case, the chemical potential μ_i.

In electrochemical systems an electrostatic potential is present, thus an additional term [65, 64], $\phi_i dq_i$, is included in the internal energy. Here ϕ_i is the electrostatic potential of the phase containing i, and q_i is the charge contribution of i ($q_i = c_i z_i$). However, the natural variables of the Gibbs (or other) potential are unchanged. Thus the additional potential possessed by solutes that have charge is included in the chemical potential. The re-

sult is the *electrochemical* potential[1]

$$\tilde{\mu}_i = \mu_i^\circ + RT\ln(c_i) + z_i F\phi \tag{3.29}$$

where z_i is the molecule's charge, F is Faraday's number (the charge of 1 mole of electrons), ϕ is the (external) electrostatic potential, and μ_i° is the standard electrochemical potential of i in a phase with zero electric potential.

The flux of species i in the system is defined as

$$J_i(\mathbf{r},t) = c_i(\mathbf{r},t)v_i(\mathbf{r},t), \tag{3.30}$$

where the velocity, $v_i = u_i F_i$, is obtained from the electrochemical potential

$$F_i = -\nabla\bar{\mu}_i = -RT\nabla\ln(c_i) - z_i F\nabla\phi \tag{3.31}$$

$$= -\frac{RT}{c_i}\nabla c_i - z_i F\nabla\phi. \tag{3.32}$$

Thus the flux is

$$J_i(\mathbf{r},t) = -u_i RT\nabla c_i - z_i u_i F c_i\nabla\phi, \tag{3.33}$$

and using Einstein's relation, $u_i = D_i/RT$, we get the form for the flux called the Nernst-Planck (NP) flux for ionic *migration*,

$$J_i(\mathbf{r},t) = -D_i\nabla c_i - z_i u_i F c_i\nabla\phi. \tag{3.34}$$

When $\nabla\phi = 0$ the NP equation reduces to Fick's constituative relation between flux and concentration gradient. Equation 3.34 is the appropriate flux description for electrochemical systems in which the solute-solute interaction is negligible ('dilute' or 'ideal' systems) and convection is small or absent.

[1] which is phase independent at equilibrium

3.3 Time Evolution

A relation for the time evolution of the concentration fields is easily obtained by writing the mass continuity equation,

$$\frac{\partial c_i}{\partial t} = -\nabla \cdot J_i + R_i, \tag{3.35}$$

where t is time, c_i is the concentration of species i, J_i is the Nernst-Planck flux of i, and R_i is the *accumulation* of i. In this context, the accumulation of i is the amount produced or consumed by (homogeneous) chemical reaction in the medium. Substitution of (3.34) into (3.35) gives,

$$\frac{\partial c_i}{\partial t} = D_i \nabla^2 c_i + u_i z_i F \nabla \cdot (c_i \nabla \phi), \tag{3.36}$$

in the case of $R_i = 0$. Combination with Poisson's equation

$$\epsilon \nabla^2 \phi = F \sum_i c_i z_i = \rho \tag{3.37}$$

to determine the spatial variation of the potential, ϕ, constitutes the Poisson-Nernst-Planck (PNP) system of equations [68, 69, 70]. The PNP system is highly non-linear and very difficult to solve numerically. The reason for the numerical difficulty is an instability that arises because the F/ϵ factor is so large (10^{14} Vm/equivalent) that even very small deviation from electroneutrality results in very large electric forces. Such sensitivity leads to *stiffness*, and results in very long numerical convergence times. In order to make the problem more numerically tractable the same reasoning is used; any charge separation encounters a massive restoring electric force, thus any deviation from electroneutrality vanishes. Work by White *et al* [71] on a similar system showed the time scale of charge separation to be on the order of 10^{-13} s, which is negligible over the timescales we are interested in ($\sim 1 - 10000$ s). Thus in our work we make use of the local electroneutrality constraint

$$\sum_i z_i c_i = 0. \tag{3.38}$$

To obtain an expression for the potential under the electroneutrality constraint we write the charge continuity equation using the definition of current,

$$i = F \sum_i z_i J_i, \tag{3.39}$$

by modifying the mass continuity equation

$$\nabla \cdot i = F \sum_i z_i \nabla \cdot J_i = -F \sum_i z_i \frac{\partial c_i}{\partial t} = -F \frac{\partial}{\partial t} \left(\sum_i c_i z_i \right). \tag{3.40}$$

We then invoke the electroneutrality condition (3.38) to give

$$\nabla \cdot i = 0, \tag{3.41}$$

a divergence free charge density. Expansion gives

$$F \sum_i z_i D_i \nabla^2 c_i + F^2 \sum_i u_i z_i^2 \nabla \cdot (c_i \nabla \phi) = 0, \tag{3.42}$$

and identification of the *conductivity* as

$$\kappa = F^2 \sum_i u_i z_i^2 c_i = \frac{F^2}{RT} \sum_i D_i z_i^2 c_i \tag{3.43}$$

allows us to write the charge continuity equation for the potential compactly as

$$\nabla \cdot (\kappa \nabla \phi) = -F \sum_i z_i D_i \nabla^2 c_i. \tag{3.44}$$

Finally, the Nernst-Planck-Electroneutrality (NPEN) system of equations are collected as follows:

$$\frac{\partial c_i}{\partial t} = D_i \nabla^2 c_i + u_i z_i F \nabla \cdot (c_i \nabla \phi), \quad i = 1, ..., M \tag{3.45}$$

$$\nabla \cdot (\kappa \nabla \phi) = -F \sum_i z_i D_i \nabla^2 c_i \quad \text{where} \quad \kappa = \frac{F^2}{RT} \sum_i D_i z_i^2 c_i \tag{3.46}$$

We use this system of equations (3.45-3.46) to track the temporal evolution of the spatial distribution of the solute concentrations, and electrostatic potential.

The NPEN (3.45-3.46) is a coupled non-linear system of partial differential equations in c_i and ϕ, and its solution is non-trivial. The system consists of M mass continuity equations, known as the Nernst-Planck equations (3.45), and one charge continuity equation that enforces electroneutrality (3.46). We use the electroneutrality constraint (3.38) to eliminate one species from the mass transport sub-system, and solve only the remaining $M-1$ Nernst-Planck equations.

3.4 The Electroneutrality Constraint

We illustrate the relationship between Poissons's Equation, electroneutrality and the NP equations, by following the work of Newman [72, 73] and MacGillivray [70], both of whom used a perturbative approach. We begin by investigating the conditions in which the contribution of concentration and potential driven transport processes to the flux are comparable. The respective diffusion and electro-migration driving forces are approximated as $\Delta c/L$ and $\Delta\phi/L$. Here L is the distance between the electrode and the bulk, which we take to be the maximum length of inter-crystallite channel (~ 1000 nm). We are interested in the variation of Δc and $\Delta\phi$ within this region. If the approximate driving forces are comparable over L, then by equation 3.34,

$$-D_i\frac{\Delta c_i}{L} \approx -\frac{z_i D_i F}{RT} c_\circ \frac{\Delta\phi}{L}. \tag{3.47}$$

Here $c_\circ$ is the overall electrolyte concentration (effectively the concentration of the buffer). Thus,

$$\Delta\phi \approx \left(\frac{RT}{z_i F}\right)\left(\frac{\Delta c}{c_\circ}\right), \tag{3.48}$$

which represents the product of the ratio of thermal to electrical energy (RT/F), with the magnitude of inhomogeneity ($\Delta c/c_\circ$). We know the potential decays to zero, thus,

$$\phi \approx \left(\frac{RT}{z_i F}\right)\left(\frac{\Delta c}{c_\circ}\right). \tag{3.49}$$

All the variables can now be scaled,

$$\phi = \left(\frac{RT}{z_i F}\right)\left(\frac{\Delta c}{c_\circ}\right)\hat{\phi} \tag{3.50}$$

$$x = L\hat{x} \tag{3.51}$$

$$c_p = c_\circ \hat{c}_p \tag{3.52}$$

$$c_b = c_\circ \hat{c}_b \tag{3.53}$$

$$z = z_\circ \hat{z} \tag{3.54}$$

$$\rho = F c_\circ z_\circ \hat{\rho}, \tag{3.55}$$

where c_p represents the concentration of the participating ions (Zn^{2+}, OH^-), c_b the concentration of buffer, and ρ is the charge density. The concentration scaling constant, $c_\circ$, is taken to be of the order of the buffer concentration, which is significantly larger than the participant concentration. Substitution into Poisson's Equation gives,

$$\frac{\Delta c_p \epsilon RT}{c_\circ L^2 F}\frac{d^2\hat{\phi}}{d\hat{x}^2} = F c_\circ z_\circ \hat{\rho}, \tag{3.56}$$

which can be re-written with parameter, δ,

$$\delta \frac{d^2\hat{\phi}}{d\hat{x}^2} = \hat{\rho}, \tag{3.57}$$

where in the case corresponding to a symmetric divalent electrolyte and using $z_\circ = 2$,

$$\delta = \left(\frac{\epsilon RT/F^2 c_\circ z_\circ^2}{L^2}\right)\frac{\Delta c}{c_\circ} = \left(\frac{\lambda_D^2}{L^2}\right)\frac{\Delta c}{c_\circ}. \tag{3.58}$$

We recognise the ratio (λ_D/L) from our earlier discussion of the double layer. The quantity δ can be made small by either small λ_D^2/L^2 as we

saw earlier, or by small $\Delta c/c_\circ$, which is achieved by setting $c_\circ >> c_p$, i.e. $c_b >> c_p$. Satisfaction of the two conditions, $\Delta c/c_\circ << 1$ and $\lambda_D^2/L^2 << 1$, give appropriate conditions for perturbation analysis. Substitution of an expansion of powers of the variables,

$$\hat{\phi} = \phi_\circ + \delta\phi_1 + \delta^2\phi_2 + \delta^3\phi_3 + \cdots \tag{3.59}$$

$$\hat{\rho} = \rho_\circ + \delta\rho_1 + \delta^2\rho_2 + \delta^3\rho_3 + \cdots \tag{3.60}$$

into Poisson's Equation gives,

$$\delta\nabla^2(\phi_\circ + \delta\phi_1 + \delta\phi_2 + ...) = \rho_\circ + \delta\rho_1 + \delta\rho_2 + ... \tag{3.61}$$

Thus for very small δ, $\rho_\circ = 0$ to leading order in δ, demonstrating that electroneutrality is a consequence of Poisson's Equation. However, in considering the leading potential term, $\phi_\circ$, which is first order in δ, we see the potential depends on the first order charge density,

$$\nabla^2\phi_\circ = \rho_1. \tag{3.62}$$

Thus, the electroneutrality approximation does not mean that Poisson's Equation can be simplified to Laplace's Equation. It is for this reason that the the NPEN system (3.45-3.45) is not equivalent to the PNP (3.36-3.37) under the situation where electroneutrality holds, but is an alternative description. Electroneutrality and Poisson's equations are alternative and complementary descriptions for the potential. Therefore, the application of electroneutrality to Poisson's equation to obtain Laplace's equation for the potential, and thus a decoupled system is contradictory. However, the use of electroneutrality to derive the NP equations (3.45) is entirely consistent with Poisson's Equation, and is in fact a consequence of Poisson's Equation [70]. Finally we note that both conditions for small δ are met for large $c_\circ$, thus the use of large ionic buffer concentration, $[CaCl_2] >> [ZnCl_2]$, ensures that the Debye length is small, ensuring the validity of the electroneutrality constraint.

3.5 Approximate Approaches to Solving NPEN

The NPEN system of transport equations (3.45-3.46) constitute a system of coupled non-linear equations, and although numerically simpler than the PNP, obtaining a numerical solution is non-trivial. It is desirable to investigate and compare the full system with two models obtained by simplifying (3.45-3.46). Simpler models have advantages in terms of convergence time, and robustness with respect to a broader range of initial conditions.

3.5.1 Similar Diffusivities (NPEN-β)

An alternative mathematically soluble, yet physically viable approach is sought to track the electrochemical transport. One such approach is to assume negligible difference in the ionic mobilities [74],

$$D_i \approx D_j \approx D. \tag{3.63}$$

The ionic diffusivities (see Table 3.1) vary between 1.41×10^{-9} and 2.03×10^{-9} $\mathrm{m^2 s^{-1}}$, except that of OH^- which is 2-3 times as large as the others.

Substitution into (3.44) gives,

$$\nabla \cdot (\kappa \nabla \phi) \approx \frac{FD}{RT} \sum_i^n \nabla^2 c_i z_i \tag{3.64}$$

$$\approx \frac{FD}{RT} \nabla^2 \left(\sum_i^n c_i z_i \right). \tag{3.65}$$

The RHS vanishes due to electroneutrality, giving

$$\nabla \cdot (\kappa \nabla \phi) \approx 0. \tag{3.66}$$

Thus we can write our simplified NPEN system (3.45-3.46) as,

$$\frac{\partial c_i}{\partial t} = D_i \nabla^2 c_i + u_i z_i F \nabla \cdot (c_i \nabla \phi), \quad i = 1, ..., M \tag{3.67}$$

$$\nabla \cdot (\kappa \nabla \phi) = 0 \quad \text{where} \quad \kappa = \frac{F^2 D}{RT} \sum_i z_i^2 c_i \tag{3.68}$$

As we shall see later (c.f. Section 4.7.3), the numerical convergence behaviour of Equations (3.67-3.68) is more efficient than that of Equations (3.45-3.46), and, under the conditions used for ZnO electrodeposition assumption (3.63) produces simulation outputs in excellent agreement with the full NPEN (3.67-3.68) model (c.f. Section 4.7.2, Figure 4.12).

3.5.2 Nernst-Planck-Laplace (NPEN-γ)

A further simplification can be made by assuming negligibly different diffusivities and constant conductivity. Expansion of the NPEN-β charge continuity (potential) equation, Equation 3.66, gives

$$\nabla\kappa\nabla\phi + \kappa\nabla^2\phi = 0, \tag{3.69}$$

from which it is clear that if the spatial variation in conductivity vanishes,

$$\nabla\kappa = 0, \tag{3.70}$$

then the charge continuity equation (3.68) reduces to Laplace's Equation, resulting in the Nernst-Planck-Laplace system:

$$\frac{\partial c_i}{\partial t} = D_i\nabla^2 c_i + u_i z_i F\nabla\cdot(c_i\nabla\phi) \tag{3.71}$$

$$\nabla^2\phi = 0. \tag{3.72}$$

In this model the electrostatic potential has been decoupled from the motion of ions, resulting in a constant electric field. The solution of decoupled systems is much faster, and more stable, than coupled systems, thus requiring fewer computational resources.

The uniform conductivity assumption is valid when $\nabla c_i = 0$ for all i. When this is not the case, we must justify it as an approximation. We consider the system to be in a steady state over the diffusion layer, L, and approximate Equation 3.69 with the difference equation,

$$\left(\frac{\Delta\kappa\Delta\phi}{L^2}\right) + \kappa\left(\frac{\Delta(\Delta\phi)}{L^2}\right) = 0. \tag{3.73}$$

Rearrangement to

$$\left(\frac{\Delta\kappa}{\kappa}\right) + \frac{\Delta(\Delta\phi)}{\Delta\phi} = 0, \tag{3.74}$$

indicates that the left most term diminishes as $\Delta\kappa/\kappa \rightarrow 0$. The ratio is a measure of the relative inhomogeneity of the electrolyte,

$$\frac{\Delta\kappa}{\kappa} = \frac{\sum_i \nabla c_i z_i^2}{\sum_i c_i z_i^2}. \tag{3.75}$$

Noting that the greatest change in concentration is of the order of the participating ions, and the conductivity of the system is dominated by the buffer, we approximate the ratio as,

$$\frac{\Delta\kappa}{\kappa} \approx \frac{c_{Zn}}{c_b} \tag{3.76}$$

where c_{Zn} is representative of the maximum change in the ionic concentrations, and c_b, the buffer concentration is characteristic of the net concentration. Finally, experimental values used by Illy *et al* [6], $c_{Zn} = 5 \times 10^{-4}$ M, and $c_b = 0.1$ M, produce a small ratio of 5×10^{-3}, in support of neglecting the left most term in Equation 3.69.

The Nernst-Planck-Laplace model can be valid under conditions of high buffer concentration, or homogeneous conductivity. We shall present results in Chapter 5 that indicate the ZnO electrodeposition system to satisfy both conditions, high buffer and uniform conductivity.

3.6 Simple Study

Here we construct a simple one dimensional model of growth to understand the essential features of transport limited growth. We consider two simple cases to investigate transport limited growth. The first case describes vertical growth with fixed transport channel flow area, and rod area. The second describes transport limited growth where the rod growth is in both vertical and horizontal directions. Both models assume simple

steady state Fickian flow. We simplify the one dimensional Nernst-Planck flux

$$J_i = -D_i \frac{\partial c_i}{\partial x} - \frac{Z_i F D_i}{RT} \frac{\partial \phi}{\partial x} \tag{3.77}$$

to Fick's law

$$J_i = -D_i \frac{\partial c_i}{\partial x}. \tag{3.78}$$

The simplification is justified on the basis that the electrostatic field is assumed to vary linearly in space due to the high buffer concentration ([buffer] $\approx$ 100 [reactants]), and is therefore very small, due to the large separation between the working and counter electrode compared to the length ionic transport is occurring (centimetres versus 100's of nanometres). Fickian diffusion greatly simplifies the mathematics. We also assume that transport has reached a steady state.

In the following we consider growth limited by the steady state transport of a single species. Three equivalent scenarios can be described, shown in Figure 3.6, all of which ultimately have the same form for the growth model. The first scenario is that of growth limited by Zn^{2+} or O_2 diffusion to the electrode (see Figure 3.6(left)). Once at the electrode, it is converted to ZnO by a reaction described by a first order rate law, and incorporated into the crystal. The mechanism describes growth from the bottom of the crystal, at the film-electrode interface. In this situation we apply a flux-reaction balance at the electrode

$$JA = -kc_\circ, \tag{3.79}$$

where k is the rate constant for Zn^{2+} limited ZnO formation, $c_\circ$ is the Zn^{2+} concentration at the electrode, A is the cross-sectional area of the inter-rod gap, and J is the steady state flux defined by

$$J = -\frac{D}{l}(c_l - c_\circ), \tag{3.80}$$

where l is the rod length (film height), and c_l is the concentration at the rod tip, taken to be the same as the bulk concentration. Setting the concentration at the rod tip equal to the bulk assumes that the bulk is well

mixed (the experiment is stirred), and hence the diffusive boundary layer between the film front and the bulk is negligible. In fluid dynamics such a situation is described by a large Péclet number. The dimensionless Péclet number relates the advection of a flow to its rate of diffusion and is written

$$Pe_L = \frac{LV}{D} = Re_L Sc, \tag{3.81}$$

where L is a characteristic length, V is the flow velocity, D is the mass diffusivity, Re_L and Sc are dimensionless numbers known as the Reynolds and Schmidt numbers respectively. From Equation 3.81 we also see that because within the inter-rod gap the mixing is weak, and the characteristic length small, the Péclet number will be small and diffusive transport will dominate. The electrode flux balance is written

$$-kc_\circ = -\frac{DA}{l}(c_l - c_\circ), \tag{3.82}$$

which can be rearranged to give

$$c_\circ = \frac{c_l}{\left(1 + \frac{kl}{DA}\right)}. \tag{3.83}$$

From (3.83) we identify the dimensionless ratio kl/DA, which represents the relative magnitude of the boundary reaction to the diffusive transport of mass to the boundary (electrode). In the case of $kl/DA \gg 1$, then $c_\circ << c_l$. The flux-reaction balance (3.79) is written

$$JA = \frac{-kc_l}{\left(1 + \frac{kl}{DA}\right)}, \tag{3.84}$$

which in the limit $kl/DA \gg 1$ (or $k \to \infty$) becomes $J = -Dc_l/l$. Thus the flux of material into the crystal is limited by diffusion rather than reaction, and l is now the only dynamic variable.

A second scenario is that the growth is limited by OH^- at the top of the rod, and OH^- is formed at the electrode by conversion of O_2, delivered by steady state diffusion from the bulk (see Figure 3.6(middle)). A third scenario with the same form is obtained if growth is limited by

$Zn(OH)_x^{(2-x)}$, where $Zn(OH)_x^{(2-x)}$ is formed at the electrode by reaction of OH^-, and Zn^{2+} delivered by steady state diffusion from the bulk (see Figure 3.6(right)). Both the second and third scenarios constitute a top-growth mechanism in which material is incorporated into the tip of the growing rods. For these cases we use flux-reaction balance for consumption of the limiting species at the top. In the case of OH^- limited growth at the top we use

$$J_{OH}A_g = +k_{ORR}c_{OH}^l, \tag{3.85}$$

where k_{ORR} is the first order rate constant for the oxygen reduction reaction, and c_{OH}^l is the OH^- concentration at the rod tip. A flux balance for the production of limiting species at the electrode is used. For example, in the case of OH^- limited growth at the top we use

$$J_{OH} = -2J_{O_2}, \tag{3.86}$$

where J_{O_2} is the steady state flux of O_2 to the electrode where it is being converted to OH^- at the mass limit. We find that the flux of OH^-into the material is

$$J_{OH} = +\frac{2D_{O_2}}{l}c_{O_2}^l, \tag{3.87}$$

where, as with the first case above, l is the only dynamic variable.

3.6.1 Case 1: Fixed Flow Area, Free Aspect Ratio

In this model we consider nanorod growth starting from a fixed width, corresponding to a situation where initial lateral growth occurs very quickly, and ceases before significant vertical growth begins. This type of growth resembles the *Volmer-Weber* mechanism [55] which proceeds by spreading followed by layer growth. Such a behaviour would be expected if the lateral growth velocity greatly exceeds the normal growth velocity, and a variety of mechanisms could produce such growth anisotropy. If we consider the growth of a disc shaped seed in which lateral growth dominates during immediately and after nucleation, then the disc edges effectively act

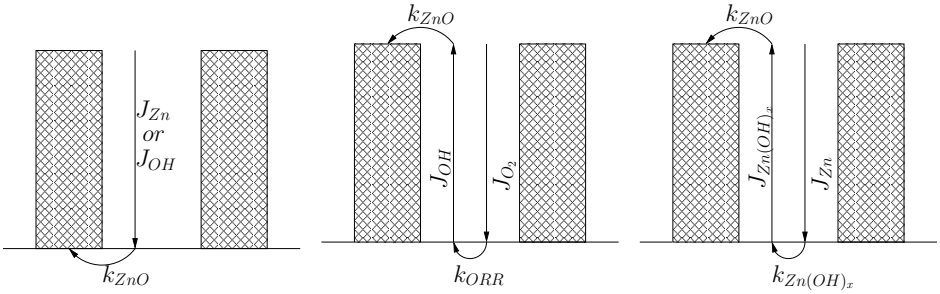

Figure 3.6: Equivalent diffusion limited growth scenarios. (a) Growth limited by the transport of Zn^2+ or OH^- to the substrate (electrode). (b) Growth limited by the steady state transport of OH^- formed at the electrode by conversion of O_2. (c) Growth limited by the steady state transport of zinc hydroxide species formed at the electrode by reaction of Zn^{2+}.

as material sinks. As the disc grows the edge sinks become close and their diffusion fields overlap, causing the amount of material fuelling growth to be greatly diminished about the edges and lateral growth is slowed. Now the vertical growth begins to dominate, and because it causes both the lateral surface area to increase, and produces a long channel with a small mouth, the lateral growth is effectively suppressed. The initial rapid lateral growth required for this mechanism might be expected if there was a scarcity of growth material, (low Zn^{2+} or OH^-) and the crystallising material was stabilised by the substrate.

The growth of the crystal is proportional to the amount of material entering the crystal (passing the solution-crystal interface) per unit time, thus

$$A_r \frac{dl}{dt} \propto JA_g = -DA_g c_l / l, \tag{3.88}$$

where A_r is the fixed cross-sectional rod area, and A_g is the fixed flux channel cross-sectional area. More clearly,

$$\frac{dl}{dt} = al^{-1}, \tag{3.89}$$

where a is a constant. Noting the equivalent form,

$$l\frac{dl}{dt} = \frac{1}{2}\frac{d}{dt}(l^2) = a, \tag{3.90}$$

substituting $x = l^2$, and using the initial condition, $x(0) = 0$, permits the simple solution

$$x(t) = 2at \tag{3.91}$$

or

$$l(t) = bt^{1/2}. \tag{3.92}$$

For the case of Zn^{2+} reaction at the electrode

$$b = \frac{2D_{Zn}c_{Zn}^{x=0}M_{ZnO}}{\rho_{ZnO}}\left(\frac{A_g}{A_r}\right), \tag{3.93}$$

and for OH^- reaction at the rod top

$$b = \frac{4D_{O_2}c_{O_2}^{x=l}M_{ZnO}}{\rho_{ZnO}}\left(\frac{A_g}{A_r}\right). \tag{3.94}$$

Here D_{Zn} and D_{O_2} are the diffusion coefficients for Zn^{2+} and O_2 respectively, M_{ZnO} is the molar mass of ZnO, ρ_{ZnO} is the density of ZnO, $c_{O_2}^{x=l}$ is the concentration of O_2 at the rod tip, $c_{Zn}^{x=0}$ is the Zn^{2+} concentration at the electrode, A_g and A_r are the cross-sectional area of the flux region and the rod respectively.

3.6.2 Case 2: Free Flow Area, Fixed Aspect Ratio

In this model we consider growth where the area of the flow channel, and rod, vary, but are constrained by a fixed aspect ratio. The purpose of this model is to capture the growth behaviour associated with both the increasing diffusion layer, and the effect of flow area constriction. Unlike the first case, this is consistent with normal growth greatly exceeding, but not eclipsing, lateral growth. Normal oriented growth domination is expected in conditions of excess reactant (high Zn^{2+}, and OH^- concentration), and also facet growth rate anisotropy.

We treat the fixed aspect ratio by considering the rod volume as the product,

$$V(t) = A_r(t)l(t), \tag{3.95}$$

where A_r is the rod cross-sectional area, and l is its height. Because the aspect ratio fixes the ratio of height to the width, we may write the area as a function of length

$$A_r(t) = \gamma l(t)^2 \tag{3.96}$$

where γ is a geometric factor. We imagine the area of an average rod-gap unit to be

$$A_T = \frac{\text{Total Area}}{\text{Number of rods}} = A_g + A_r \tag{3.97}$$

where A_T is the area associated with a single rod-gap unit, A_g is the gap area, and A_g is the nanorod area. Using the fixed aspect ratio relation (3.96) we can write the flux area as

$$A_g = A_T - \gamma l(t)^2. \tag{3.98}$$

The rod growth equation

$$\frac{dV}{dt} = -V_m J A_g, \tag{3.99}$$

where V_m is the *proper* volume defined by $V_m = M_{ZnO}/\rho_{ZnO}$, M_{ZnO} and ρ_{ZnO} are the molar mass and density of ZnO respectively, is now expressed in terms of a single independent variable, l,

$$\frac{d}{dt}(\gamma l^3) = +\frac{V_m D c_l}{l}(A_t - \gamma l^2). \tag{3.100}$$

The left hand side is expanded by the chain rule,

$$3\gamma l^2 \frac{dl}{dt} = +V_m D c_l A_T l^{-1} - V_m D c_l \gamma l, \tag{3.101}$$

and rearranged to give

$$3\gamma l \frac{dl}{dt} = +V_m D c_l A_T l^{-2} - V_m D c_l \gamma, \tag{3.102}$$

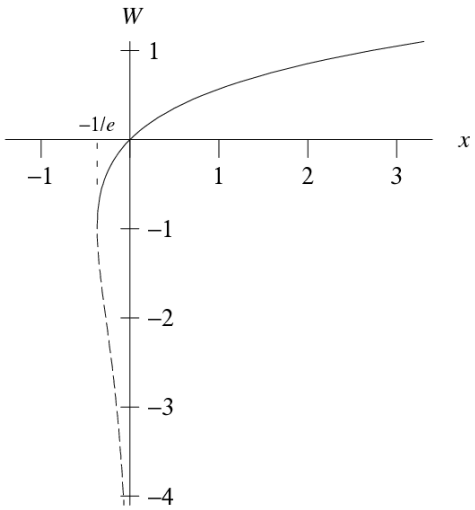

Figure 3.7: The two real branches of the Lambert W function.

which is the same as

$$\frac{3\gamma}{2}\frac{d}{dt}(l^2) = +V_m D c_l A_T l^{-2} - V_m D c_l \gamma. \tag{3.103}$$

Substituting $x = l^2$, and written in terms of constants g, and h yields

$$\frac{dx}{dt} = gx^{-1} - h, \tag{3.104}$$

where

$$g = \left(\frac{2V_m D c_l A_T}{3\gamma}\right) \quad \text{and} \quad h = \left(\frac{2V_m D c_l}{3}\right). \tag{3.105}$$

The solution is found to be

$$x(t) = \left(\frac{g}{h}\right) + \left(\frac{g}{h}\right) W\left[-\mathbf{exp}\left(-\frac{g + ht^2}{g}\right)\right], \tag{3.106}$$

where W is the Lambert W function (shown in Figure 3.7). The Lambert W function is defined as the inverse of the function

$$f(x) = xe^x, \tag{3.107}$$

i.e. it is the complex valued function that satisfies [75]

$$x = W(x)e^{W(x)}. \tag{3.108}$$

The Lambert W function can be evaluated by the recurrence relation [75]

$$w_{j+1} = w_j - \frac{w_j e^{w_j} - z}{e^{w_j}(w_j + 1) - \frac{(w_j+2)(w_j e^{w_j} - z)}{2w_j + 2}}, \tag{3.109}$$

which computes the principal branch for $x > -1/e$ (see Figure 3.7). Back-substitution of $l = x^2$ into (3.106) gives the length as

$$l(t) = \left(\left(\frac{g}{h}\right) + \left(\frac{g}{h}\right) W \left[-\mathbf{exp}\left(-\frac{g + ht^2}{g} \right) \right] \right)^{1/2}. \tag{3.110}$$

We considered a specific geometric scenario to investigate the growth be-

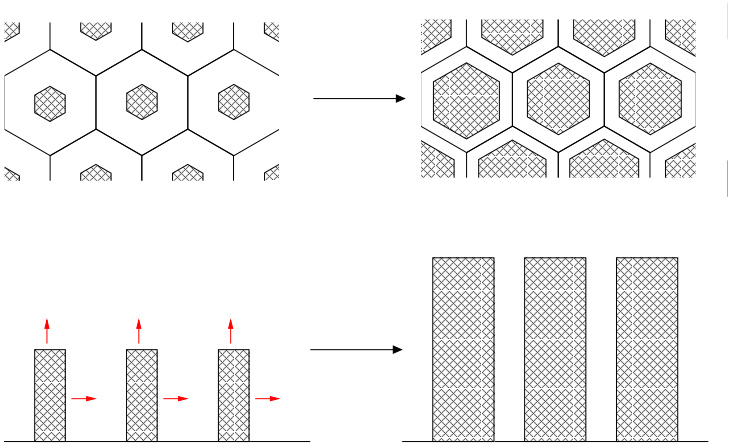

Figure 3.8: Ideal rod arrangement used to investigate the free area, fixed aspect ratio model. The filled hexagons represent the unit rods, and the white hexagonal shells represent the flow area associated with each unit rod.

haviour described by (3.110). We considered an ideal geometry in which the rods are aligned normal to the substrate, with parallel faces, and positioned on a hexagonal grid (see Figure 3.8). Under such a geometry, the constants are found to be,

$$g = \frac{16 V_m c_l D A_T}{9\sqrt{3}\Gamma^2}, \quad \text{and} \quad h = \frac{2 V_m D c_l A_T}{3}, \tag{3.111}$$

where Γ is the arbitrary fixed aspect ratio (length/width) of the crystallite, $M_{ZnO} = 81.4$ g/mol [58], D is the diffusivity of the limiting species obtained from the reference literature [58], A_T was obtained experimentally, and c_l is the bulk concentration of the limiting species.

3.6.3 Results

We investigated the vertical growth only case by using a inter-rod spacing, fixed at a typical experimentally observed value (50 nm), and varying the fixed rod width, the results are shown in Figure 3.9a. The case of fixed aspect ratio and free gap area was also investigated for an inter-rod spacing of 50 nm, and the aspect ratio was varied, the results are shown in Figure 3.9b.

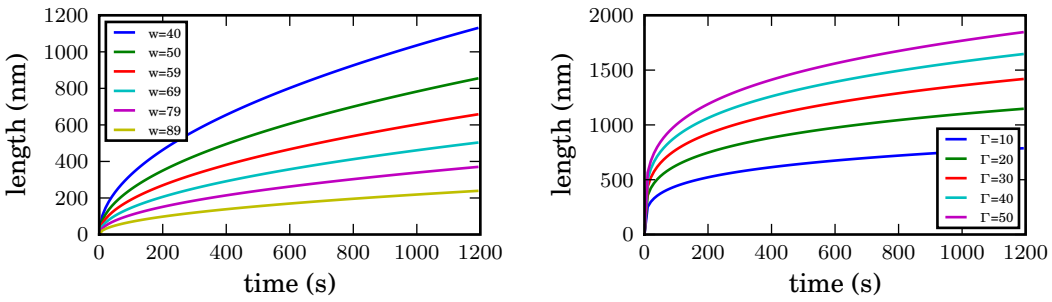

(a) (b)

Figure 3.9: Diffusion limited growth behaviour obtained using a rod spacing of 1 per 100 nm: (a) vertical-only growth at a variety of rod widths (w), and (b) vertical and lateral growth for a variety of aspect ratios (Γ).

Both growth models exhibit growth rates in the same order of magnitude as those experimentally observed, suggesting diffusion limited growth is likely, and therefore a suitable basis for further simulation. Case 1 somewhat resembles the later stages of growth observed experimentally, however, it has no resemblance to the early growth behaviour. For large aspect

ratio, case 2 looks similar to case 1 and the experimental data, suggesting that the longer growth stage (the second phase) is dominated by vertical growth. The experimental data exhibit a linear growth curve during the later growth period. Case 2 also possesses linear later stage behaviour, whereas Case 1 has a $t^{1/2}$ dependence. The sharp growth rate change indicating the end of phase one growth is best modelled by case 2 using a low aspect ratio. Low aspect ratio represents lateral growth domination, suggesting the possibility of lateral growth domination in the early stage of growth.

3.6.4 Comments

The results presented here suggest that the geometry of the rod growth environment makes a significant contribution to the diffusion dominated growth characteristics of the system. A detailed mathematical description of the transport, chemical reaction, and surface phenomena, will need to be treated independently in more than one dimension.

3.7 Summary

In this chapter we have outlined the mathematical details of a model we used to simulate the electrodeposition of ZnO nanorod films. We described the chemical reactions used to drive nanorod growth, discussed the crystal-electrolyte interface, and derived the Nernst-Planck-Electroneutrality equations and two simplified versions. We performed two case studies using simple 1D models, and concluded that investigation of the full model in two dimensions would be necessary to understand the governing processes involved in the deposition.

Chapter 4

Numerical Method and Implementation

We used a numerical approach to solve the models derived in Chapter 3. In the first part of this chapter we discuss aspects of numerical methods such as discretisation, accuracy, iterative method, meshing, data structures, and code implementation. In the second part we determine the numerical parameters required to produce consistent solutions for the NPEN (3.45-3.46), NPEN-β (3.67-3.68), and NPEN-γ (3.71-3.72) models derived in Section 3.3, 3.5.1, and 3.5.2, respectively. We also compare the numerical convergence, and the simulation results obtained from the three models, and investigate the validity of the simplified models under the initial conditions used to emulate the experimentally measured growth behaviour.

4.1 System Geometry

The first approximation we make is to assume that the system can be adequately described in two dimensions. The development of a computer code, and the resources required to evaluate the code are greatly reduced for 2D compared with 3D models. The approximation is represented schematically in Figure 4.1. We note that as the rods grow and the

film becomes more crowded, the inter-rod space become more planar in character, thus the 2D approximation improves.

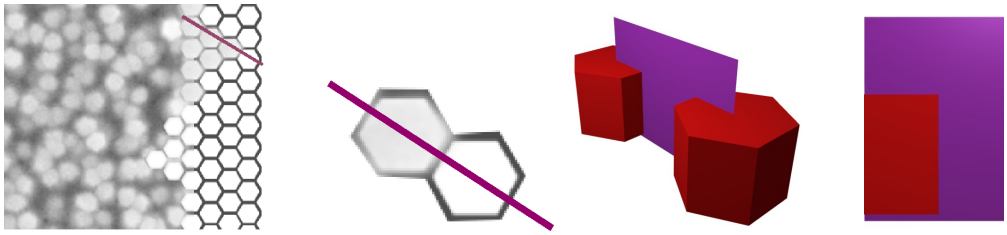

(a) (b) (c) (d)

Figure 4.1: Schematic showing how 2-dimensional model is derived and relates to the 3-dimensional system. Images (a) and (b) emphasise the hexagonal nature of the nanorods. The purple line represents a 2D plane representative of the interrod 3D space. Image (c) shows the 2D plane in perspective, and (d) shows the smallest by symmetry 2D plane used to represent the 2D model domain.

4.2 Discrete Formulation

We used the method of finite differences with a rectangular mesh to solve the system of equations for the 5 variables: Zn^{2+}, O_2, OH^-, Ca^{2+}, ϕ (Cl^- is omitted using the electroneutrality condition (3.38)). We implemented a general mixed implicit-explicit algorithm in our solver to approximate the PDE,

$$\frac{u_j^{n+1} - u_j^n}{\Delta t} = \theta(Au)^{n+1} + (1-\theta)(Au)^n \tag{4.1}$$

where $u_j^n = u(n\Delta t, j\Delta x)$, $0 \leq \theta \leq 1$, j is the space index, n is the time index, and A is the function (matrix), that, being non-linear depends on u. All spatial derivatives were discretised as centred differences (see Figure 4.2), thus first derivative finite difference equations (FDE) were written

$$\frac{\partial u_j^n}{\partial x} = \frac{u_{j+1}^n - u_{j-1}^n}{2\Delta x} + \epsilon_j^n, \tag{4.2}$$

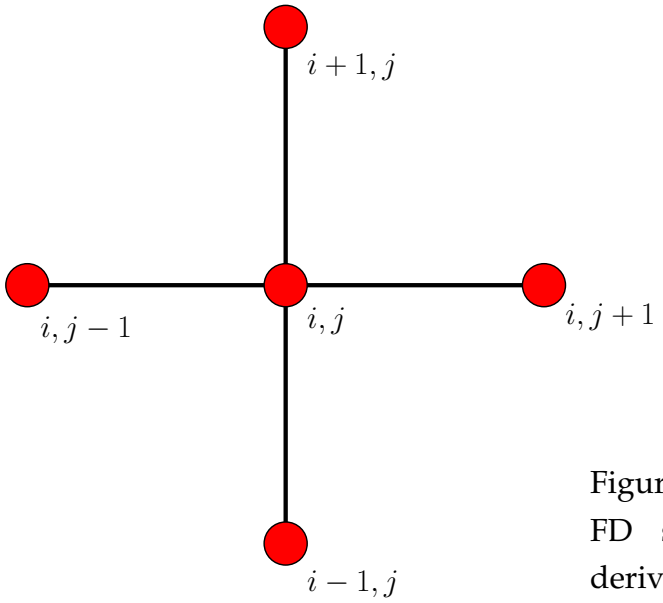

Figure 4.2: Five point centred FD stencil used for spatial derivatives.

where ϵ_j^n represents the truncation error. Similarly, spatial second derivatives were written,

$$\frac{\partial^2 u_j^n}{\partial x^2} = \frac{u_{j+1}^n - 2u_j^n + u_{j-1}^n}{\Delta x^2} + \epsilon_j^n. \tag{4.3}$$

The truncation error is obtained by substitution of a Taylor expansion of the exact solution into the FDE. The limiting case of $\theta = 0$ to Equation 4.1 yields

$$\frac{u_j^{n+1} - u_j^n}{\Delta t} = (Au)^n, \tag{4.4}$$

a fully explicit, or forward Euler, method [76]. The truncation error of the fully explicit centred first derivative is determined by,

$$\epsilon_j^{n+1} = \frac{\partial u_j^n}{\partial t} + \frac{\Delta t}{2}\frac{\partial^2 u_j^n}{\partial t^2} + \frac{\Delta t^2}{3!}\frac{\partial^3 u_j^n}{\partial t^3} + O(\Delta t^3) \tag{4.5}$$

$$- v\left(\frac{\partial u_j^n}{\partial x} + \frac{\Delta x^2}{3!}\frac{\partial^3 u_j^n}{\partial x^3} + O(\Delta x^4)\right) \tag{4.6}$$

$$= O(\Delta t, \Delta x^2), \tag{4.7}$$

and is first order in time and second order in space. Likewise the centred second derivative,

$$\epsilon_j^{n+1} = \frac{\partial u_j^n}{\partial t} + \frac{\Delta t}{2}\frac{\partial^2 u_j^n}{\partial t^2} + \frac{\Delta t^2}{3!}\frac{\partial^3 u_j^n}{\partial t^3} + O(\Delta t^3) \tag{4.8}$$

$$- v\left(\frac{\partial^2 u_j^n}{\partial x^2} + \frac{\Delta x^2}{4!}\frac{\partial^4 u_j^n}{\partial x^4} + O(\Delta x^4)\right) \tag{4.9}$$

$$= O(\Delta t, \Delta x^2), \tag{4.10}$$

is also $O(\Delta t, \Delta x^2)$. Since our FDE formulation of the NPEN system (3.67-3.68) is composed of centred spatial derivatives, the accuracy of the fully explicit case is $O(\Delta t, \Delta x^2)$. A von Neumann Fourier stability analysis on time dependent linearised equations composed of centred first and second spatial derivatives [76] indicates conditional stability. Conditional stability limits the size of our time step and grid resolution, and is therefore undesirable.

The alternative limiting case of $\theta = 1$ yields the fully implicit, or backward Euler, method,

$$\frac{u_j^{n+1} - u_j^n}{\Delta t} = (Au)^{n+1}. \tag{4.11}$$

Implicit equations are those in which the desired variable is a function of itself. Such equations require iterative solution. The truncation error is determined by,

$$\epsilon_j^{n+1} = \frac{\partial u_j^n}{\partial t} + \frac{\Delta t}{2}\frac{\partial^2 u_j^n}{\partial t^2} + \frac{\Delta t^2}{3!}\frac{\partial^3 u_j^n}{\partial t^3} + O(\Delta t^3) \tag{4.12}$$

$$- v\left(\frac{\partial u_j^n}{\partial x} + \frac{\Delta x^2}{3!}\frac{\partial^3 u_j^n}{\partial x^3} + O(\Delta x^4)\right) \tag{4.13}$$

$$= O(\Delta t, \Delta x^2) \tag{4.14}$$

which is first order in time and second order in space. Likewise for the

centred second derivative,

$$\epsilon_j^{n+1} = \frac{\partial u_j^n}{\partial t} + \frac{\Delta t}{2}\frac{\partial^2 u_j^n}{\partial t^2} + \frac{\Delta t^2}{3!}\frac{\partial^3 u_j^n}{\partial t^3} + O(\Delta t^3) \tag{4.15}$$

$$- v\left(\frac{\partial^2 u_j^n}{\partial x^2} + \frac{\Delta x^2}{4!}\frac{\partial^4 u_j^n}{\partial x^4} + O(\Delta x^4)\right) \tag{4.16}$$

$$= O(\Delta t, \Delta x^2). \tag{4.17}$$

Thus the implicit case has the same accuracy as the explicit case. However, the stability analysis finds the implicit case to be unconditionally stable [76], and thus far more useful for the investigation of the length-time regime of our electrochemical system.

Finally, we note the possibility of using a mixed, $0 < \theta < 1$, formulation. The most well known is that of Crank and Nicolson [77], where $\theta = \frac{1}{2}$. By assuming the trapezium rule holds, the truncation error for the half step can be obtained by averageing the forward and backward Euler methods

$$\epsilon_j^{n+1/2} = \frac{\epsilon_j^{n+1} + \epsilon_j^n}{2}. \tag{4.18}$$

All time dependent terms are taken as $n + \frac{1}{2}$, yielding a truncation error given by,

$$\epsilon_j^{n+1} = \frac{\partial u_j^n}{\partial t} + \frac{\Delta t^2}{3!}\frac{\partial^3 u_j^n}{\partial^3 t} + O(\Delta t^3) \tag{4.19}$$

$$- v\left(\frac{\partial^2 u_j^n}{\partial x^2} + \frac{\Delta x^2}{4!}\frac{\partial^4 u_j^n}{\partial x^4} + O(\Delta x^4)\right) \tag{4.20}$$

$$= O(\Delta t^2, \Delta x^2), \tag{4.21}$$

thus the Crank-Nicolson scheme provides second order accuracy in time and space.

The simple explicit ($\theta = 0$) finite difference formulation (as illustrated in Figure 4.3a) is first order accurate in time and second order accurate in space. However, stability (bounded or diminishing error) is only satisfied conditionally [76]. The simple implicit stencil, shown in Figure 4.3b, although it requires simultaneous solution of three unknowns (u_{j-1}^{n+1}, u_j^{n+1},

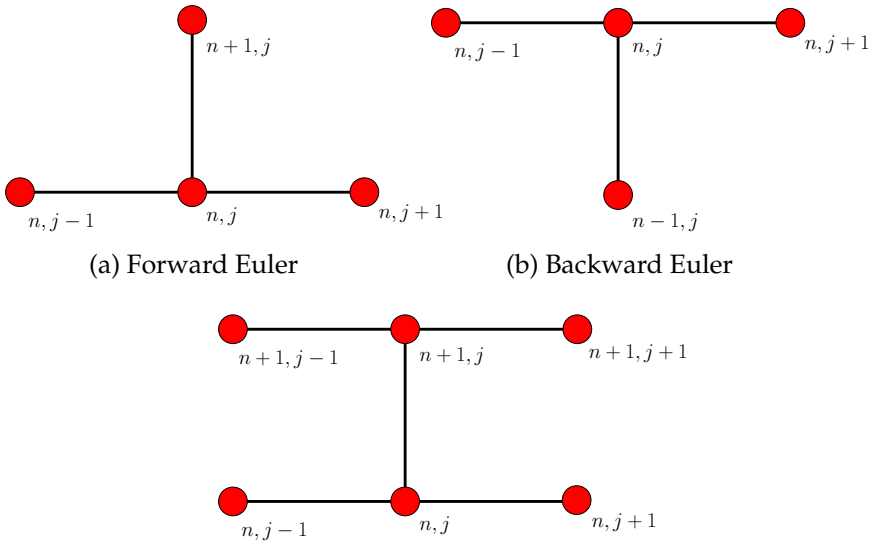

(a) Forward Euler

(b) Backward Euler

(c) Cranck-Nicolson

Figure 4.3: Finite difference stencils used to march forward in time.

and u_{j+1}^{n+1}), is found to be more favourable in a variety of ways. Firstly, a von Neumann stability analysis [76] (linearised in the case of NPEN), finds the simple implicit scheme to be unconditionally stable. Further, the time accuracy can be improved to second-order by prudential selection of the value of θ. There are, however, costs associated with the Crank-Nicolson scheme. If the timestep is too large, long lived oscillations retard or prevent convergence [78]. Hence, for systems requiring large time step and high grid resolution, the fully implicit method which is immune to oscillations is preferred [78], with the compromise of reduced time accuracy. The implicit method is also preferred for stiff equations [79]. For the solution of the NPEN system we found the Crank-Nicolson method unable to converge. However, the fully implicit method, $\theta = 1$, yielded reliable solution convergence.

4.3 Iterative Method

In the previous section we established the advantage of implicit and semi-implicit solution schemes. The use of such schemes requires an iterative method as there exist multiple unknowns in the finite difference equation [76, 78, 80]. The iterative method we have implemented is the Newton-Raphson method [81, 82], the method most commonly applied to the solution systems of non-linear equations.

Newton's method is used to find the root of a function by successively finding the root of the tangent at a succession of guesses [83], illustrated in Figure 4.4. Expressed as a recurrence relation it reads,

$$x_{k+1} = x_k - \frac{f(x_k)}{f'(x_k)}, \tag{4.22}$$

where k denotes the kth iteration.

To determine the solution of a differential equation, the function, f, is recast as a residual which when minimised with respect to u satisfies the original equation,

$$f(u) = \frac{\partial u}{\partial t} - Au. \tag{4.23}$$

Thus, for the solution u^*

$$f(u^*) = 0. \tag{4.24}$$

In the context of a finite difference solution scheme, u is a vector, and a set of residuals are minimised. The method represents a vector space search in which the search direction is determined by the first derivative of each element with respect to all other elements [81], [83]. The set of residuals is obtained by taking an n-space Taylor expansion [82] about an initial guess $\mathbf{u}_k$,

$$\begin{array}{lllll} f_1(\mathbf{u}_k) & +\frac{\partial f_1}{\partial x_1}(\mathbf{u}_k)\delta_1 & +\frac{\partial f_1}{\partial x_2}(\mathbf{u}_k)\delta_2 & +\cdots & +\frac{\partial f_1}{\partial x_n}(\mathbf{u}_k)\delta_n = 0 \\ f_2(\mathbf{u}_k) & +\frac{\partial f_2}{\partial x_1}(\mathbf{u}_k)\delta_1 & +\frac{\partial f_2}{\partial x_2}(\mathbf{u}_k)\delta_2 & +\cdots & +\frac{\partial f_2}{\partial x_n}(\mathbf{u}_k)\delta_n = 0 \\ \vdots & & & & \vdots \\ f_n(\mathbf{u}_k) & +\frac{\partial f_n}{\partial x_1}(\mathbf{u}_k)\delta_1 & +\frac{\partial f_n}{\partial x_2}(\mathbf{u}_k)\delta_2 & +\cdots & +\frac{\partial f_n}{\partial x_n}(\mathbf{u}_k)\delta_n = 0 \end{array} \tag{4.25}$$

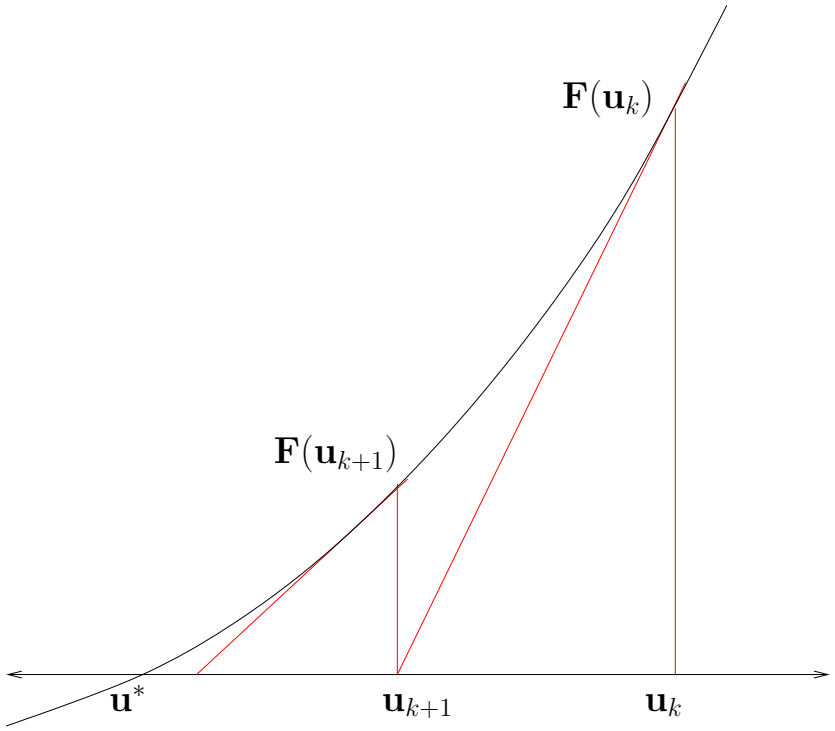

Figure 4.4: Schematic representation of convergence using Newton's method.

where k is the iteration index and $\delta = \mathbf{u}_{k+1} - \mathbf{u}_k$. Written in matrix form,

$$\mathbf{F}'_k \delta = -\mathbf{F}_k, \tag{4.26}$$

where $\mathbf{F}_k$ denotes the residual mapping, $\mathbf{F}_k = (f_1(\mathbf{u}_k), f_2(\mathbf{u}_k), \cdots, f_n(\mathbf{u}_k))^T$, and $\mathbf{F}'_k$ denotes the Jacobian matrix

$$\mathbf{F}'_k = \begin{bmatrix} \frac{\partial f_1}{\partial x_1} & \frac{\partial f_1}{\partial x_2} & \cdots & \frac{\partial f_1}{\partial x_n} \\ \frac{\partial f_2}{\partial x_1} & \frac{\partial f_2}{\partial x_2} & \cdots & \frac{\partial f_2}{\partial x_n} \\ \vdots & \vdots & \ddots & \vdots \\ \frac{\partial f_n}{\partial x_1} & \frac{\partial f_n}{\partial x_2} & \cdots & \frac{\partial f_n}{\partial x_n} \end{bmatrix}. \tag{4.27}$$

Each element in the Jacobian denotes the the partial derivative of f_j with respect to the ith variable at $\mathbf{u}$.

Perhaps the most desirable feature of Newton's method in regard to the solution of non-linear equations is that it tends to converge quadratically [81]. Provided the $\mathbf{u}_k$ are sufficiently close to the solution, $\mathbf{u}^*$, then quadratic convergence defined by,

$$||\mathbf{u}_{k+1} - \mathbf{u}^*|| \leq c||\mathbf{u}_k - \mathbf{u}^*||^2 \tag{4.28}$$

holds. Convergence is very rapid when the error at a given iteration is proportional to the square of the error at the previous iteration. In the work presented here, we have used the following criterion for convergence,

$$\frac{\max\{|\delta_i|\}}{\max\{|\mathbf{u}_i|\}} < \epsilon \tag{4.29}$$

where i denotes the solution variable ($i = \{c_{Zn}, c_{O_2}, c_{OH}, c_{Ca}, \phi\}$), and ϵ is a small number. A similar criterion was used by Buoni *et al* for the electrochemical transport and deposition of copper [84, 85, 86].

Finally, to ensure convergence, and to maximise efficiency we implemented an automatically varying time step that reduced when solution convergence was slow, and increased when convergence was fast. If convergence was achieved within three iterations the timestep was doubled, and if convergence was not achieved within ten iterations the timestep was halved.

4.4 Calculation Scheme Objects

The discussion of Newton's method introduced the use of a matrix notation. In this section we focus on the details of the nature of the algebraic objects used to seek a solution using Newton's method: the solution vector $\mathbf{u}_k$, the function mapping $\mathbf{F}_k$, and the Jacobian matrix $\mathbf{F}'_k$.

4.4.1 The Solution Vector, u

The electrochemical model devised earlier is solved in two dimensions, for the electrostatic potential, ϕ, and the concentration of four chemical

species, Zn^{2+}, O_2, OH^-, Ca^{2+}. In order to solve the system of equations represented by Equation 4.26 using conventional matrix methods, it is simpler to express the rank-2 (2D) variable array as a vector. The two dimensional variable array,

$$\begin{bmatrix} \phi_{(11)}, \mathrm{Zn}_{(11)}, \mathrm{O}_{2(11)}, \mathrm{OH}_{(11)}, \mathrm{Ca}_{(11)}, \cdots, \phi_{(1n)}, \mathrm{Zn}_{(1n)}, \mathrm{O}_{2(1n)}, \mathrm{OH}_{(1n)}, \mathrm{Ca}_{(1n)} \\ \phi_{(21)}, \mathrm{Zn}_{(21)}, \mathrm{O}_{2(21)}, \mathrm{OH}_{(21)}, \mathrm{Ca}_{(21)}, \cdots, \phi_{(1n)}, \mathrm{Zn}_{(2n)}, \mathrm{O}_{2(2n)}, \mathrm{OH}_{(2n)}, \mathrm{Ca}_{(2n)} \\ \vdots \qquad\qquad\qquad\qquad\qquad\qquad \vdots \\ \phi_{(m1)}, \mathrm{Zn}_{(m1)}, \mathrm{O}_{2(m1)}, \mathrm{OH}_{(m1)}, \mathrm{Ca}_{(m1)}, \cdots, \phi_{(mn)}, \mathrm{Zn}_{(mn)}, \mathrm{O}_{2(mn)}, \mathrm{OH}_{(mn)}, \mathrm{Ca}_{(mn)}, \end{bmatrix} \tag{4.30}$$

is transformed, or rastered, into a rank-1 vector,

$$\mathbf{u} = \left(\{\mathrm{X}\}_{(1\times1)}, \cdots, \{\mathrm{X}\}_{(2\times n)}, \cdots, \{\mathrm{X}\}_{(m\times n)}\right)^T \tag{4.31}$$

of size $m \times 5n$, where m, n indicates the grid size and X represents the set of variables at each node ($\phi, \mathrm{Zn}^{2+}, \mathrm{O}_2, \mathrm{OH}^-, \mathrm{Ca}^{2+}$). Schematically represented in Figure 4.5a.

From Figure 4.5a we can identify a computational issue associated with a solution vector containing points corresponding to the crystal interior. As the crystal grows the vector elements increasingly become those of the idle crystal interior, which yield no useful information but consume an increasing amount of computational resource for each solution iteration. In the later stages, the entire system consists of crystal interior. The problem is compounded if a higher resolution grid is used in the region immediately surrounding the crystal. To ensure efficiency we have omitted the crystal interior from our vector for computation (see Figure 4.5b and Figure 4.6). The cost of omitting the crystal interior is the introduction of additional complexity to the code implementation.

4.4.2 The Function Vector, $\mathbf{F}(\mathbf{u})$

The model Equations (3.45-3.46), (3.67-3.68), and (3.71-3.72), are represented by the residual mapping, $\mathbf{F}$. The chemical species are evaluated

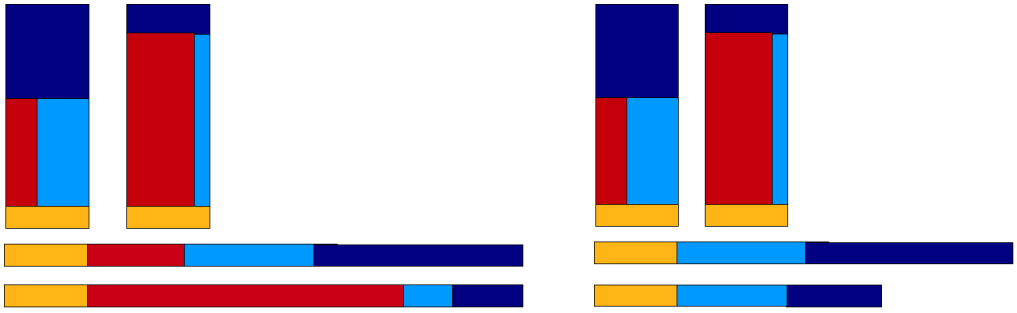

(a) (b)

Figure 4.5: (a) Schematic representation of computational domains. As the crystal (red) grows the solution vector is dominated by the internal area of the crystal. (b) Schematic representation of compressed computational domain in which the crystal interior is omitted. As the crystal (red) grows the solution vector becomes smaller, requiring less computational resources and allowing the calculation to proceed faster.

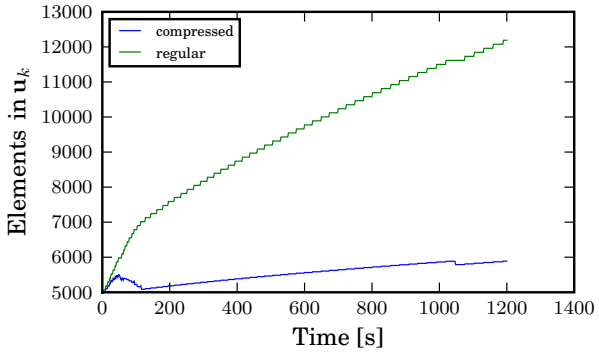

Figure 4.6: The compressed and non-compressed solution array sizes for a typical simulation.

using the mass continuity equation (first line), while the potential is varied using the charge continuity equation (the second line). The full NPEN system (3.45-3.46), results in the set of finite difference stencils shown in Figure 4.7. Our implementation solves the two coupled equations simultaneously; the mass continuity equation is applied to all $\mathbf{u}$ indices corresponding to a chemical species ($(i \times j)$ modulo $5 \neq 0$), whilst the charge continuity equation (either (3.46), (3.68), or (3.72)) is applied to all $\mathbf{u}$ indices corresponding to electrostatic potential ($(i \times j)$ modulo $5 = 0$).

Analogous to the solution vector, the function vector is transformed to a rank-1 vector. The structure of the finite difference operators is transformed such that the vertical neighbour of a given index, i is accessed by addition of the number of horizontal points (the size) in the 2D domain, $5n$. Thus on our $m \times 5n$ grid, the point (i, j) is mapped as $(i \times j)$, and the positive vertical neighbour, $(i, j+1)$, is mapped as $(i \times j + 5n)$, as illustrated in Figure 4.8a. In the situation where the the solution vector is compressed by omission of the crystal interior, the mapping is slightly more complicated, and changes as the crystal grows. In the vicinity of the crystal, the compressed mapping transforms $(i, j+1)$ to $(i \times j + 5n - 5n_{crystal})$ where $n_{crystal}$ is the size of the crystal on the computational domain, whilst away from the crystal the mapping is $(i \times j + 5n)$, as shown in Figure 4.8b.

4.4.3 The Jacobian Matrix, $\mathbf{F}'(\mathbf{u})$

The Jacobian matrix holds the first derivatives of each element of $\mathbf{F}$ with respect to each element in $\mathbf{u}$. It has size $N_{\mathbf{u}}^2$, where $N_{\mathbf{u}}$ is the size of $\mathbf{u}$, and, because our equations are discretised using 5-point centred stencils (i.e. nearest neighbour interaction) in which the largest operator has only 25 points, it is a sparse diagonal matrix. The mass continuity equation

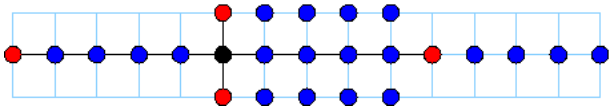

(a) ϕ (26 indices): full Equation 3.46, and half Equation 3.68

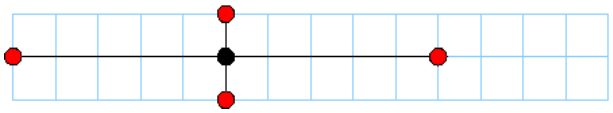

(b) ϕ (5 indices): decoupled Equation 3.72

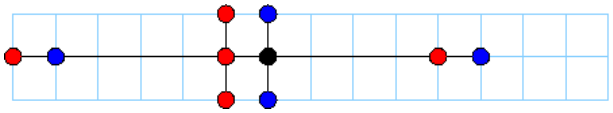

(c) Zn^{2+} (10 indices)

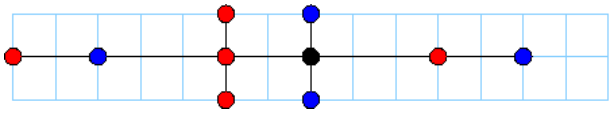

(d) O_2 (10 indices)

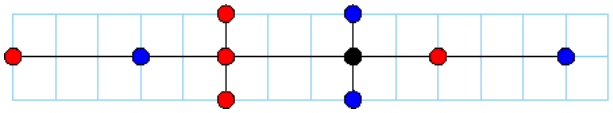

(e) OH^- (10 indices)

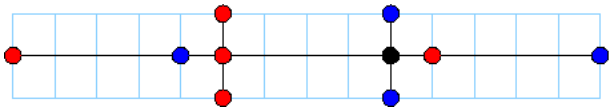

(f) Ca^{2+} (10 indices)

Figure 4.7: Finite difference stencils for the each variable. From top to bottom: ϕ, Zn^{2+}, O_2, OH^-, Ca^{2+}, the central index i, j is black, ϕ is red, and chemical species are coloured blue.

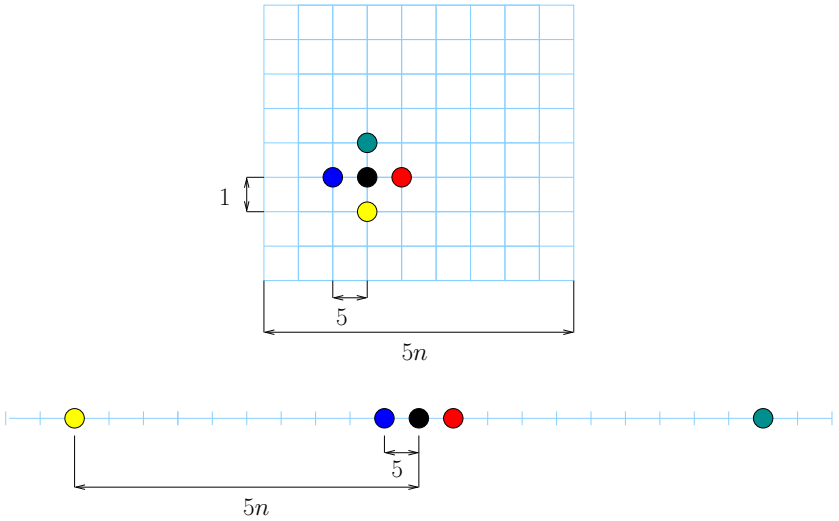

(a) Illustration of a centred FD stencil on a rank-2 array (upper), and rank-1 analogue (lower).

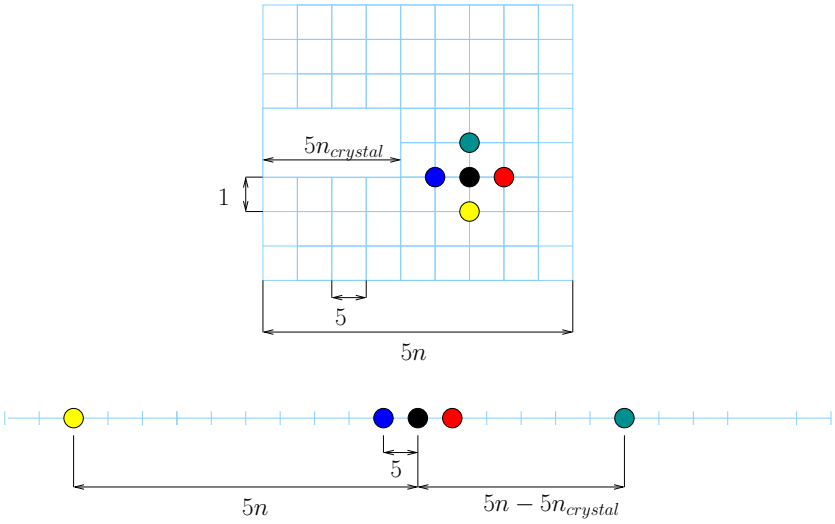

(b) Illustration of a centred FD stencil on a rank-2 array (upper) in which some points (representing crystal interior) have been omitted, and rank-1 analogue (lower).

Figure 4.8: Schematic showing relation between the 2-dimensional model domain, and the 1-dimensional analogue used in the calculational scheme.

contributes 20 diagonals indicated in parentheses,

$$\begin{aligned}\mathbf{J}_{MC}(&\text{-}5n-4,\text{-}5n-3,\text{-}5n-2,\text{-}5n-1,\text{-}5n,\\ &\text{-}4,\text{-}3,\text{-}2,\text{-}1,\\ &0,\\ &1,2,3,4,5,\\ &5n-4,5n-3,5n-2,5n-1,5n)\end{aligned} \quad . \tag{4.32}$$

while the charge continuity equation contributes 26,

$$\begin{aligned}\mathbf{J}_{CC}(&\text{-}5n,\text{-}5n+1,\text{-}5n+2,\text{-}5n+3,\text{-}5n+4,\\ &\text{-}5,\text{-}4,\text{-}3,\text{-}2,\text{-}1,\\ &0,\\ &1,2,3,4,5,6,7,8,9,10,\\ &5n,5n+1,5n+2,5n+3,5n+4)\end{aligned} \quad . \tag{4.33}$$

A total of 36 unique diagonals are present in the the full NPEN (3.45-3.46) Jacobian,

$$\begin{aligned}\mathbf{J}_{NPEN}(&\text{-}5n-4,\text{-}5n-3,\text{-}5n-2,\text{-}5n-1,\text{-}5n,\\ &\text{-}5n,\text{-}5n+1,\text{-}5n+2,\text{-}5n+3,\text{-}5n+4,\\ &\text{-}5,\text{-}4,\text{-}3,\text{-}2,\text{-}1,\\ &0,\\ &1,2,3,4,5,6,7,8,9,10,\\ &5n-4,5n-3,5n-2,5n-1,5n,\\ &5n,5n+1,5n+2,5n+3,5n+4)\end{aligned} \quad . \tag{4.34}$$

Additional diagonals arise from the unsymmetric difference stencils that result from compression. However, the trade-off between number of diagonals and system size still favours compression. The compressed Jacobian contains 56 unique diagonals, some of which are not fixed in po-

sition,

$$\begin{aligned}\mathbf{J}_Z(&\text{-}5\Delta_n-4,\text{-}5\Delta_n-3,\text{-}5\Delta_n-2,\text{-}5\Delta_n-1,\text{-}5\Delta_n,\\ &\text{-}5\Delta_n,\text{-}5\Delta_n+1,\text{-}5\Delta_n+2,\text{-}5\Delta_n+3,\text{-}5\Delta_n+4,\\ &\text{-}5n-4,\text{-}5n-3,\text{-}5n-2,\text{-}5n-1,\text{-}5n,\\ &\text{-}5n,\text{-}5n+1,\text{-}5n+2,\text{-}5n+3,\text{-}5n+4,\\ &\text{-}5,\text{-}4,\text{-}3,\text{-}2,\text{-}1,\\ &0,\\ &1,2,3,4,5,6,7,8,9,10,\\ &5n-4,5n-3,5n-2,5n-1,5n,\\ &5n,5n+1,5n+2,5n+3,5n+4)\\ &5\Delta_n-4,5\Delta_n-3,5\Delta_n-2,5\Delta_n-1,5\Delta_n,\\ &5\Delta_n,5\Delta_n+1,5\Delta_n+2,5\Delta_n+3,5\Delta_n+4)\end{aligned} \quad . \tag{4.35}$$

where the Z subscript denotes compression, and $\Delta_n = n - n_X$ where n_X denotes the crystal width. Four additional diagonals are added by the boundary equations giving a total of 60 diagonals in the full (3.45-3.46) and half (3.67-3.68) NPEN models.

Our code provides a variety of ways of solving the system of linear equations represented by Equation 4.26. The Jacobian can be built as a dense array of size $N_{\mathbf{u}}^2$ and Equation 4.26 solved using an LU decomposition implemented using the LAPACK `dgesv` routine [87]. The dense approach is not very efficient as the Jacobian has size $N_{\mathbf{u}}^2$, thus a 10 000 element vector has a corresponding Jacobian with 100 million elements. Alternatively, the Jacobian can be built using a sparse constructor. We used an implementation of the UMFPACK [88, 89, 90, 91] `spdiags` routine, which, given a list of diagonal vectors and their diagonal indices, returns a sparse matrix in compressed sparse column (CSC) format. The sparse representation of Equation 4.26 is then solved using the unsymmetric multifrontal method, and direct sparse LU factorisation routines provided by UMFPACK and collected into `spsolve`. An intermediate case

is also available in which the dense Jacobian is built and the diagonals are extracted and used to build a CSC using `spdiags`, and then solved with `spsolve`. The solve time of a sparse matrix solver scales as $O(N)$, whereas the dense solver is $O(N^2)$. The benefits, in terms of speed and memory usage, of the sparse implementation are seen in both the time required to construct the Jacobian, and the solve time of Equation 4.26. As the system gets bigger, the compression measures described above are useful, both in terms of building, as searching an array scales as $O(N^2)$, and solving the system of linear equations that arise from the iterative method.

4.5 Meshing

To reduce computational overhead we used a non-uniform mesh away from the growing crystal (shown in Figure 4.9). The mesh rules used were

$$\begin{cases} \begin{cases} x_m = (m-1)\Delta x, m < m_c \\ x_m = x_{m-1} + 2a_{m-1}\Delta x, m > m_c \end{cases} \\ \begin{cases} y_n = (n-1)\Delta y, n < n_c \\ y_n = y_{n-1} + 2a_{n-1}\Delta y, n > n_c \end{cases} \end{cases} \tag{4.36}$$

where Δx and Δy are the x and y fine grid increments, m_c and n_c are the indices after which the grid becomes non-uniform and $a_{n-1} = \sum_{k=0}^{n-2} a_k$ and $a_{m-1} = \sum_{k=0}^{m-2} a_k$ are responsible for non-uniformity. In the subsequent calculations critical indices m_c and n_c were set to 5 which corresponds to 25 nm of fine mesh surrounding the crystallite. The mesh was updated when the amount of material having crossed the boundary exceeded the amount of material encased in one fine mesh increment. The new solution vector is acquired by linear interpolation (weighted averaging) of the four bounding points from the previous mesh.

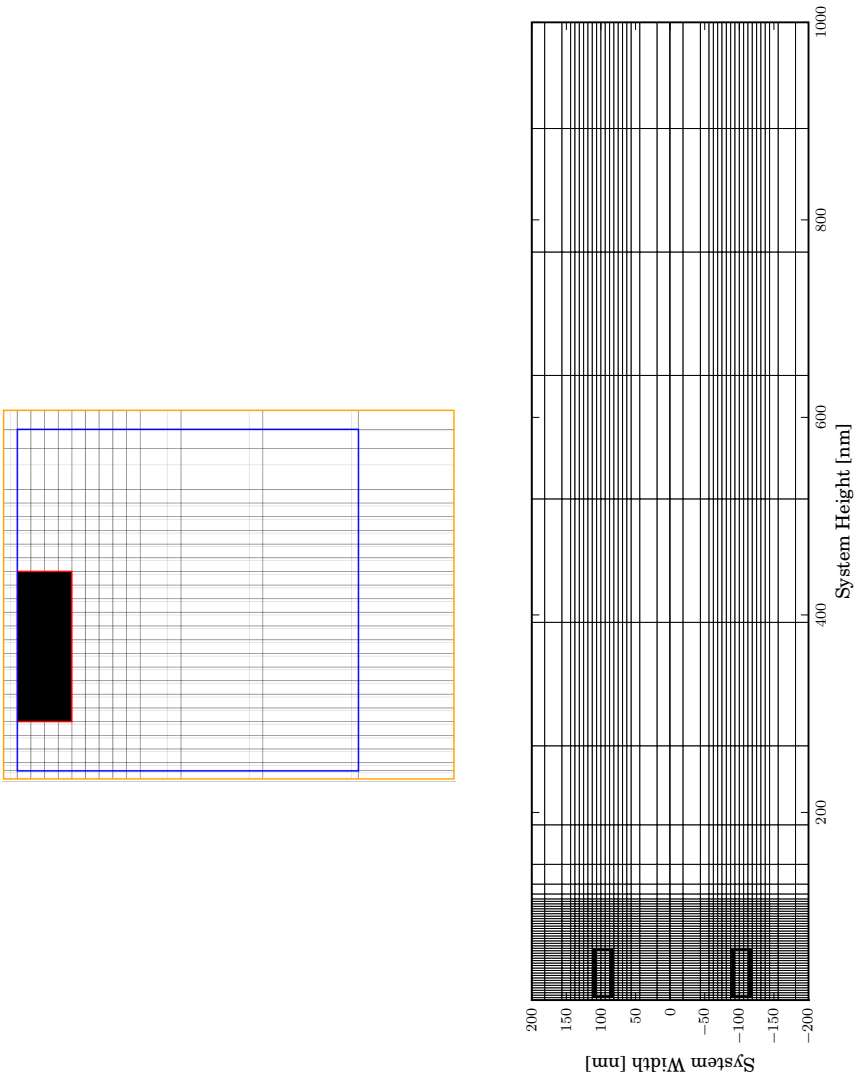

(a) (b)

Figure 4.9: (a) Illustration of a non-uniform mesh. Here the outer orange boundary corresponds to the virtual x+1 and y+1 points used to evaluate Neumann boundary conditions, the blue rectangle is the NP domain boundary, the black box represents the crystal, and the red lines indicate the crystal boundaries. The dark gridlines are the present grid, and the fainter grey lines indicate the grid belonging to the previous interpolant. (b) An example of a non-uniform finite difference grid used in this work (c.a. 5 seconds). The crystallite is represented by the bold black rectangle.

4.6 Boundaries

The system possesses 11 boundaries of varying nature, shown in Figure 4.10. There are electrode boundaries, crystal surface boundaries, bulk boundaries and symmetry boundaries. Each variable (species) behaves differently at each boundary. We have implemented 3 types of generic boundary (mirror, Neumann, and Dirichlet) and two specific boundary functions (one for Zn^{2+}, and another for OH^{-}). The generic boundaries are, Dirichlet,

$$u_i = b, \tag{4.37}$$

where b is a constant. For solutes, if $b = 0$ then transport toward the boundary occurs at the mass limit. The flux boundary,

$$J_i = b, \tag{4.38}$$

where b is a constant. And finally, the mirror boundary,

$$u_{i-1} = u_{i+1}. \tag{4.39}$$

The specific boundary condition for Zn^{2+} is,

$$J_i = R_i \tag{4.40}$$

where R_i is the reaction and inclusion rate of Zn^{2+} into the crystal as ZnO. We used a flux sum to describe the behaviour of OH^{-} on crystal boundaries,

$$J_{OH} = J_{Zn} - J_{O_2}. \tag{4.41}$$

In all cases we implemented boundaries at index $i = a$, by setting the value at a virtual or ghost index $i = a - 1$, or for upper bound, b, $i = b + 1$ was used. Thus for mirror-type boundaries

$$u_{a-1} = u_{a+1}, \tag{4.42}$$

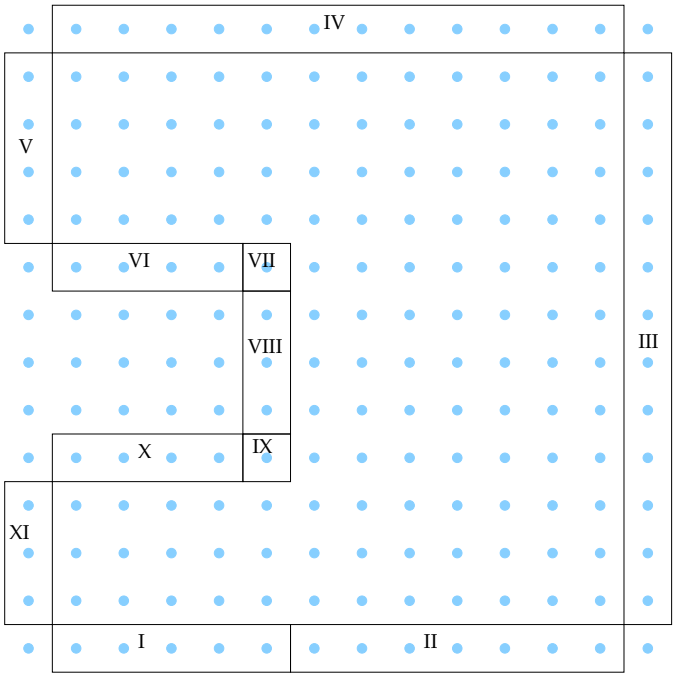

Figure 4.10: Boundary domains: I - electrode directly below rod, II - inter-rod electrode area, III - inter-rod mirror boundary, IV - bulk boundary, V - upper central mirror boundary, VI - crystal upper boundary, VII - crystal upper corner, VIII - crystal lateral boundary, IX - crystal lower corner, X - crystal lower boundary, XI - lower central mirror boundary.

we solved

$$f_{a-1} = u_{a-1} - u_{a+1}. \tag{4.43}$$

The mirror boundary condition is used for symmetrical boundaries (see Figure 4.10), and boundaries where no interaction occurs, thus a mirror boundary is used to describe the buffer at the crystal boundary. Dirichlet-type boundaries were implemented indirectly using,

$$u_{a-1} + u_{a+1} = 2u_a. \tag{4.44}$$

Thus $u_a = b$, was implemented as

$$f_{a-1} = u_{a-1} + u_{a+1} - 2b. \tag{4.45}$$

The indirect method allows evaluation of Dirichlet and Neumann conditions at the index a. Gradient (Neumann) boundary conditions were implemented using a centred finite difference,

$$\frac{du}{dx} \approx \frac{u_{a+1} - u_{a-1}}{2\Delta x} = b, \tag{4.46}$$

and solved using

$$f_{a-1} = u_{a+1} - u_{a-1} + 2\Delta x b. \tag{4.47}$$

The specific boundary function for Zn reaction (or ZnO dissolution) was constructed from a flux-reaction balance, in which a scale law (c.f. Section 3.1, Equation (3.9)) was used to describe the formation and precipitation of ZnO,

$$\vec{n}_{hkl} \cdot J_{Zn} A = \beta \left(1 - \frac{Q}{K}\right). \tag{4.48}$$

Discretised as,

$$-\frac{D_{Zn} A}{2\Delta x}(u_{a+1} - u_{a-1}) = \beta \left(1 - \frac{Q_a}{K}\right), \tag{4.49}$$

and evaluated as

$$f_a = \frac{D_{Zn} A}{2\Delta x}(u_{a+1} - u_{a-1}) + \beta \left(1 - \frac{Q_a}{K}\right), \tag{4.50}$$

where

$$Q_a = u_a(\mathrm{Zn}) u_a(\mathrm{OH})^2. \tag{4.51}$$

4.7 Model Comparisons

In the following we investigate the effect of variation of system numerical and grid parameters on the simulated growth curves and determine the configuration required to produce consistent results. We also compare the simulated growth curves produced by the three transport models derived in Chapter 3 in the vicinity of the conditions that produce growth curves resembling the experimentally measured curves. Finally we present a comparison of the numerical convergence behaviour of the three models.

4.7.1 System Parameter Convergence

We begin our discussion of the numerical investigation by presenting the convergence results for the basic numerical parameters. The basic numerical parameters, the grid settings and the size of the convergence criterion, were varied to to produce consistent and efficient simulations. The convergence studies were carried out on the full NPEN set of equations (3.45-3.46) with the initial conditions: system height 1000 nm, system width 50 nm, seed size 5×5 nm^2, maximum time step 1 s, fine grid size 2.5 nm, fine grid span 50 nm, maximum coarse grid size 50 nm, [Zn]= 5 mM, [O_2] = 0.8 mM, pH 4, [$CaCl_2$] = 100 mM, and $\phi_\circ$ = -50 mV . Such initial conditions produce a curve similar to the experimentally measured curves for [Zn] = 5 mM. The key system parameters we converged are shown in Figure 4.11, in which the total simulation times are displayed underneath the simulated growth curves. Finally we note that in order to prevent neighbouring crystallites growing together to produce a monolithic rather than nano-crystalline film, we enforced a maximum closeness of one grid unit.

Under the initial conditions described above, the cut-off criterion did not appear to have significant effect on the simulation behaviour, or the total simulation time, consistent with the rapid quadratic convergence typical of Newton's method. When convergence is fast the magnitude of the maximum allowed timestep can affect the simulated growth curves.

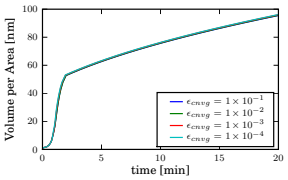

(a) Convergence criterion

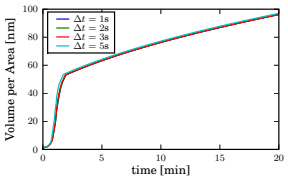

(b) Maximum time step

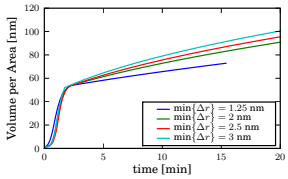

(c) Fine grid resolution ($\Delta x, \Delta y$)

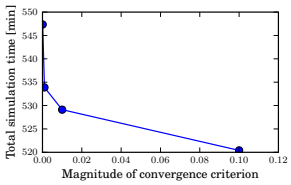

(d) Convergence criterion times

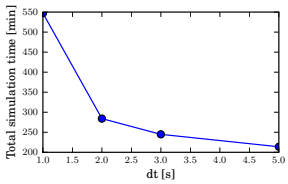

(e) Maximum time step criterion times

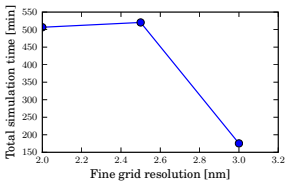

(f) Fine grid resolution times

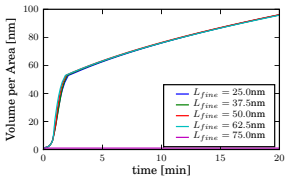

(g) Fine grid span

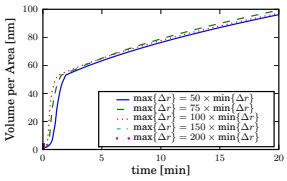

(h) Maximum coarse grid resolution

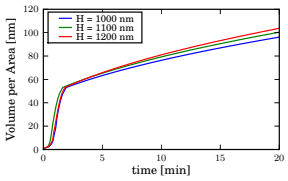

(i) System height

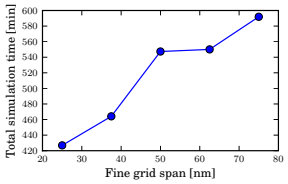

(j) Fine grid span times

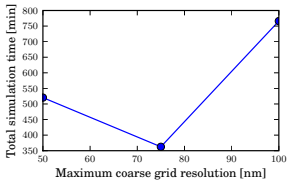

(k) Maximum coarse grid resolution times

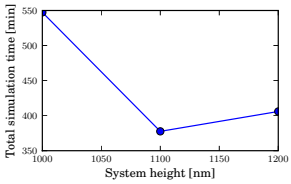

(l) System height times

Figure 4.11: Convergence study of key code numeric parameters.

Little variation in solution was observed upon increase of this parameter, although the total simulation time halves with doubling of the maximum time step. Variation of the fine grid resolution resulted in significant variation in the simulated growth curves, especially in the second growth phase. The fine grid resolution also has a profound effect on the simulation time. The fine grid span, coarse grid resolution, and system height all had very little effect on the simulated curves, and increasing the accuracy of these parameters generally resulted in a linear increase in the total simulation time. Based on the system parameter convergence study, we concluded that the above system parameter set-up is acceptable, for further studies, and is hereon referred to as the standard conditions. The system parameter configuration used in subsequent work is displayed in Table 4.1.

Table 4.1: System parameters used in this work.

Parameter	Value
Fine grid spacing	2.5 nm
Fine grid span	50 nm
Maximum coarse grid spacing	50 nm
Initial timestep	10^{-4} s
Maximum timestep	2 s
Convergence tolerance	10^{-3}

4.7.2 Output Comparison

The validity of the three models derived in Sections 3.3, 3.5.1, and 3.5.2, was investigated under conditions in the vicinity of those that produce growth curves similar to the measured curves. The growth curves, shown in Figure 4.12, find most variation between the models under conditions of small growth rate constant, and large potential. The fully decoupled model (3.71-3.72) has greater deviation from NPEN (3.45-3.46) than the NPEN-β (3.67-3.68) model.

Interestingly, the fully decoupled (3.71-3.72) and NPEN-β (3.67-3.68)

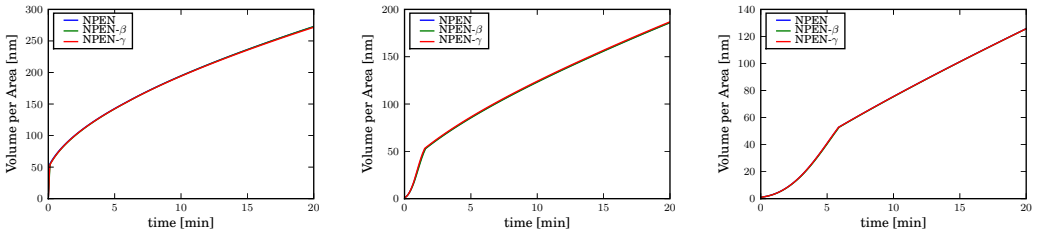

(a) $\beta, \phi_\circ^{el} = 10^{-23}$ mol/s,-100 mV (b) $\beta, \phi_\circ^{el} = 10^{-23}$ mol/s,-50 mV (c) $\beta, \phi_\circ^{el} = 10^{-23}$ mol/s,-20 mV

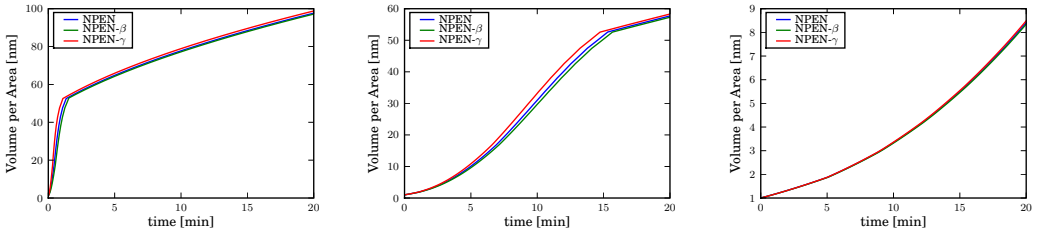

(d) $\beta, \phi_\circ^{el} = 10^{-24}$ mol/s,-100 mV (e) $\beta, \phi_\circ^{el} = 10^{-24}$ mol/s,-50 mV (f) $\beta, \phi_\circ^{el} = 10^{-24}$ mol/s,-20 mV

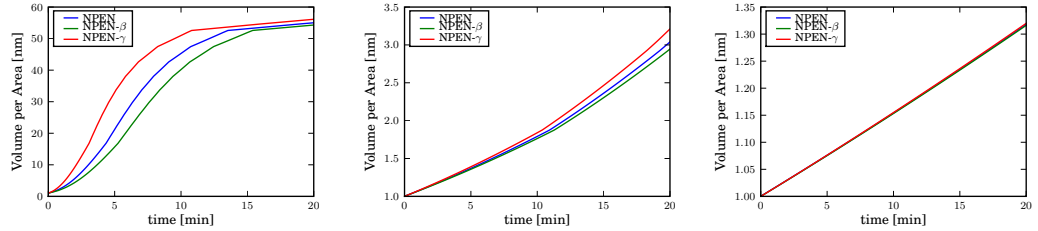

(g) $\beta, \phi_\circ^{el} = 10^{-25}$ mol/s,-100 mV (h) $\beta, \phi_\circ^{el} = 10^{-25}$ mol/s,-50 mV (i) $\beta, \phi_\circ^{el} = 10^{-25}$ mol/s,-20 mV

Figure 4.12: Comparison of the three models NPEN (3.45-3.46), NPEN-β (3.67-3.68), and NPEN-γ (3.71-3.72), over a range of isotropic rate constants, β, and surface potentials, $\phi_\circ$.

models deviate from the full NPEN (3.45-3.46) in opposite directions; NPEN-γ (3.71-3.72) produces more rapid growth, whereas NPEN-β (3.67-3.68)has marginally slower growth. The deviation is most prevalent when the reaction rate is small, and the surface potential is large. Under these conditions the field dependent migration term of equation (3.45) is the dominates driving force for transport. We see that the (3.67-3.68) system underestimates the effect of the electric field whilst the (3.71-3.72) system (the Laplacian) overestimates the electric field contribution to transport.

The lack of significant deviation between the models under conditions that best reproduce the experimental observations (see Figure 4.12b), suggests that the difference between diffusion coefficients can be considered negligible, and that the spatial variation of the conductivity is also negligible. Thus, under the conditions of growth, both simplifications are valid. In Chapter 5 we find that the concentration gradients are indeed minimal.

4.7.3 Numerical Convergence

The three transport models, a highly non-linear coupled system, a less complicated non-linear coupled system, and a less complicated decoupled system, exhibit numerical convergence behaviour commensurate with their level of complexity. Here we present some key aspects of the numerical behaviour of the three models. The convergence behaviour, in terms of the magnitude of the δ vector, over the duration of a simulation is shown for the NPEN (3.45-3.46), NPEN-β (3.67-3.68), and NPEN-γ (3.71-3.72) models in Figures 4.13a-c. The NPEN (3.45-3.46) exhibits the greatest δ magnitudes, followed by the NPEN-β (3.67-3.68), and finally the NPEN-γ. The convergence responses to an updated grid are shown in Figures 4.13d-f. The NPEN-γ (3.67-3.68) exhibits a simple spike followed by rapid decay, the NPEN-β (3.67-3.68) and NPEN (3.45-3.46) exhibit slightly more complicated behaviour. The full model has a large response followed by a gradual decrease and then smooth decay, giving it broad appearance. The

NPEN-β (3.67-3.68) has a sharp response and a clearly resolved secondary response, again, followed by smooth convergence. After the response settles, the convergence is very rapid, and quadratic convergence (sequential halving of error) is achieved. This is illustrated in Figure 4.13g-4.13i which show for each model, a set of overlaid convergence patterns for three consecutive sets of five iterates (the legend indicates the scale of each segment). Again we see the most rapid convergence for the decoupled model, moderate convergence rate for the NPEN-β model (3.67-3.68), and slowest (but still rapid) convergence for the full NPEN model (3.45-3.46).

The Jacobian build, and solve times are shown in Figure 4.14. We see that the NPEN-β (3.67-3.68) and NPEN-γ (3.71-3.72) have very similar behaviour with respect to building and solving, whereas the full NPEN (3.45-3.46) has many fluctuations, indicative of both more complicated mathematics and code implication.

4.8 Summary

In this chapter we have outlined the discretisation, and implementation into code of our numerical solver to simulate the growth model developed in Chapter 3. We have outlined our numerical method, performed convergence studies, and compared the three models derived in Chapter 3. The two simpler models are valid under the conditions used to simulate the electrochemical deposition of nanorod films in the way reported by Illy *et al* [9, 6, 41]. The fully decoupled Nernst-Planck-Laplace model (3.71-3.72), appears to be valid due to minimal variation in ionic diffusivities, and small variation in concentration, and therefore conductivities over the course of the depositions. The implementation of the solver for the full NPEN (3.45-3.46) and NPEN-β (3.67-3.68) was much more difficult than the NPEN-γ (3.71-3.72), and possess poorer convergence, yet similar overall solutions.

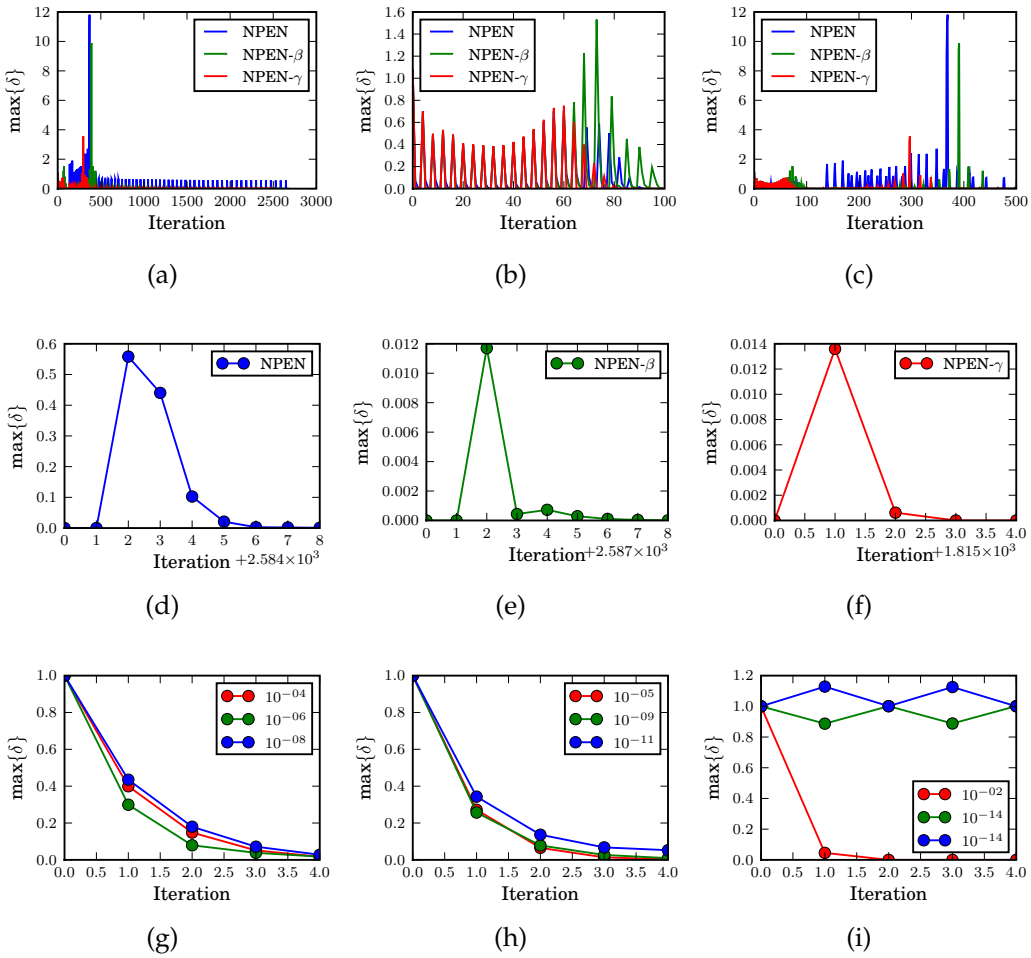

Figure 4.13: The delta (δ_k) variation of the NPEN models (a) over an entire simulation, (b) the first 500 iterations, and (c) the first 100 iterations. The response to a grid update for (d) NPEN (3.45-3.46), (e) NPEN-β (3.67-3.68), and (f) NPEN-γ (3.71-3.72). The convergence behaviour for 3 consecutive sets of five iterations in which the legend denotes the change in scale, (g) NPEN (3.45-3.46), (h) NPEN-β (3.67-3.68), and (i) NPEN-γ (3.71-3.72).

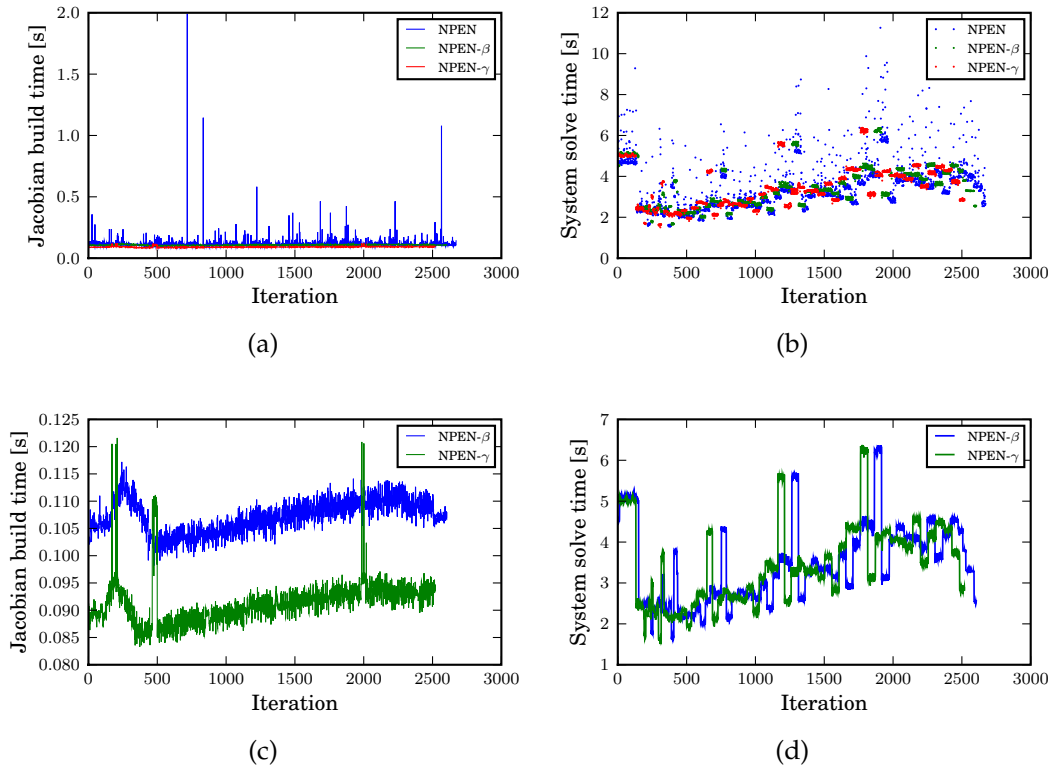

Figure 4.14: Jacobian build times ((a) and (c)) and System solve times ((b) and (d)) using Intel Pentium(R) Dual CPU (2.80 GigaHertz) processors which share 2 Gigabytes of memory. .

Chapter 5

Electrochemical Model Results

In this chapter we investigate the behaviour of the electrochemical model outlined in Chapters 3 and 4. The aim of this chapter is to elucidate some of the microscopic details that characterise the electrochemical formation of ZnO nano-rod films [6, 9, 92]. Of particular interest are the effects of variation of concentration and applied potential. We focus on conditions that produce growth curves that resemble the experimentally observed curves.

5.1 Experimental Results

Film Thickness Measure

We begin by introducing the way in which the experimental and simulation results are presented. The XANES measurements provide the amount of Zn^{2+} per area (mol/m^2),

$$I = \frac{n^f_{Zn}}{A_X}, \tag{5.1}$$

where I is the XANES intensity, n^f_{Zn} is the amount of Zn^{2+} detected, and A_X is the area sampled by the X-ray beam. The amount of Zn^{2+} in the film

can be related to the volume of the film, V^f, by

$$n_{Zn}^f = \frac{V^f}{V_m^f}, \tag{5.2}$$

where V_m^f, is the molar volume of the film. The molar volume of the film can be related to the molar volume of crystalline ZnO, V_m^{ZnO}, and the film porosity, θ, by

$$V_m^f = \theta V_m^{ZnO} \quad \text{where} \quad \theta \geq 1. \tag{5.3}$$

Here, $\theta = 1$ represents crystalline ZnO, and increased θ corresponds to increased film porosity. The XANES intensity is now written,

$$I = \frac{V^f}{A_X \theta V_m^{ZnO}}, \tag{5.4}$$

which is rearranged into a more meaningful form in terms of film deposition,

$$\frac{V^f}{A_X} = \theta I V_m^{ZnO}. \tag{5.5}$$

All data provided by Illy *et al* [6, 9, 92] is expressed as V^f/A_X for $\theta = 1$.

In this work we also present our simulated growth curves in terms of V/A. The film volume is calculated as the product of the height, width and arbitrary depth. Likewise the area per rod is taken as the product of the simulation width with arbitrary depth.

Plots of depositions performed using applied potential of -770 mV (Ag/AgCl) at varying concentration are shown in Figure 5.1a [6, 9, 92]. The general trend is that of increased deposition rate with increased Zn^{2+} concentration. However, the early growth behaviour is not so straight-forward. The lack of a clear trend is illustrated by noting that the [Zn^{2+}] = 20 mM, and [Zn^{2+}] = 5 mM, have similar growth rate, however the [Zn^{2+}] = 10 mM curve has a lower rate.

In order to clarify the data, and select a behaviour to focus the numerical investigation, we looked at the data obtained for [Zn^{2+}] = 5, and 10 mM, with applied potential E = -670, -770, and -970 (Ag/AgCl). The

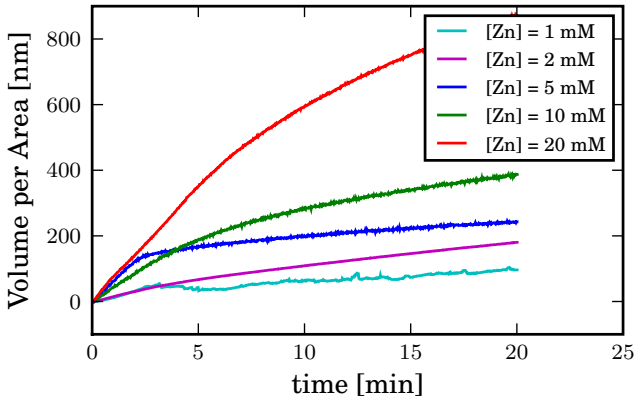

(a)

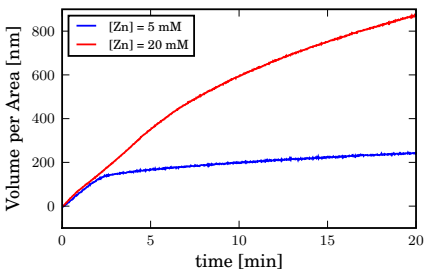

(b)

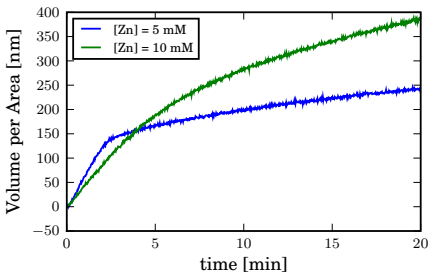

(c)

Figure 5.1: (a) The effect of concentration variation on deposition with an applied potential of -770 mV (Ag/AgCl). (b) A plot emphasising the similarity of early growth in $[Zn^{2+}]$= 5 mM, and $[Zn^{2+}]$ = 20 mM depositions. (c) Emphasis of early growth behaviour of $[Zn^{2+}]$= 5 mM, and $[Zn^{2+}]$ = 20 mM.

$[Zn^{2+}]$ = 20 mM data was not available over this applied potential range. The data is presented in Figure 5.2. The growth curves obtained at $[Zn^{2+}]$ = 5 mM (Figure 5.2a) all possess very similar early growth rates and exhibit a sharp transition in growth rate after approximately 2 minutes. The rate of the second growth phase increases with increased applied potential. Upon increasing the Zn^{2+} concentration to 10 mM (Figure 5.2c) the growth curves show an increased overall growth rate and dissappearance of the shared early stage growth rate.

The effect of increasing the Zn^{2+} concentration at a particular applied potential is shown by the right hand column of Figure 5.2. Surprisingly, the rate of early growth is decreased by increasing the Zn^{2+} concentration. The effect is greatest at the least cathodic applied potential, moderate at -770 mV, and vanishes at -970 mV.

5.2 System Behaviour and Electrolyte Dynamics

In this section we investigate the key unknown simulation variables that influence the rate of growth of the crystallite films: the electrode surface potential, ϕ°_{el} (c.f. Section 3.1.3), and the crystallite growth rate constant β, (3.9). The remaining variables were set using the reported experimental configuration and findings [6, 9, 92]. To make the parameter search more tractable we have made extensive of the mass limited boundary for O_2 transport (c.f. (3.8). The most comprehensive data set was obtained using a Zn^{2+} concentration of 5 mM, a Ca^{2+} concentration of 100 mM, with O_2 bubbled through the electrochemical cell. Lincot et al [39] determined the O_2 concentration under such conditions to be 0.8 mM. The experimental deposition was performed under acidic conditions, making the OH^- concentration of order 10^{-13} mM, which we took as zero. Finally, we used the experimentally measured inter-crystallite spacing (the crystallite density) of 100 nm in our standard set-up.

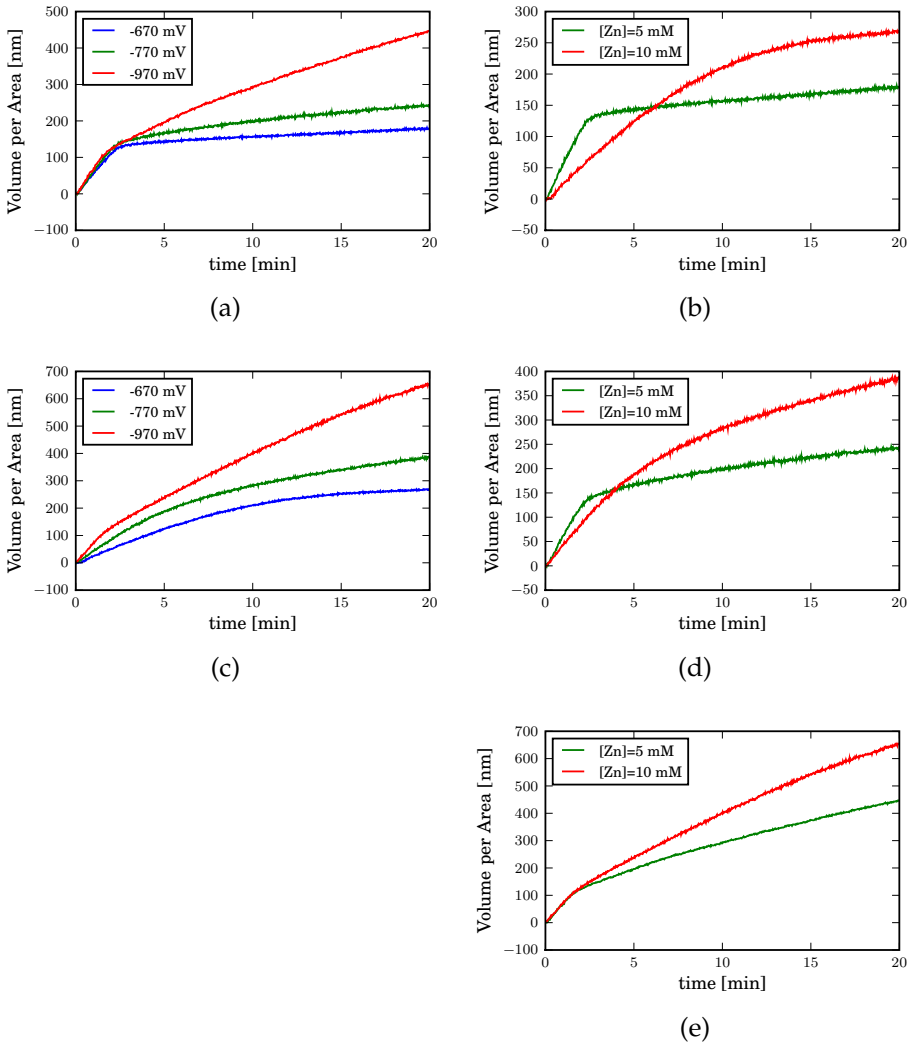

Figure 5.2: The effect of concentration on deposition at E = -670,-770,-970 mV is illustrated by (a) $[Zn^{2+}]$ = 5 mM, and (c) $[Zn^{2+}]$ = 10 mM. The effect of increased Zn^{2+}concentration on the deposition at a given potential is shown in (b) E = -670 mV, (d) E = -770 mV, and (e) E = -970 mV.

5.2.1 Coarse Parameter Search

The growth curves obtained from the coarse $\beta - \phi^\circ$ parameter scan are shown in Figure 5.3. The configuration $(\beta, \phi^\circ) = 0.25{\times}10^{-31}$ mols^{-1}, -50mV (Figure 5.3j) shows strong resemblance to the experimentally measured curves: fast initial growth, followed by slower sublinear growth, divided by an abrupt transition. The magnitude of the electrode surface potential (-50 mV) is typical of that found in electrochemical systems [48]. Other noteworthy curves that exhibit two mode growth like that observed in experiment include those shown in Figures 5.3g (same rate constant, lower electrode surface potential, $\phi_{el} = -20$ mV) and 5.3n (lower rate constant, $\beta = 0.25 \times 10^{-32}$ mols^{-1}, and larger electrode surface potential, $\phi^\circ = -100$mV). We used the $(\beta, \phi^\circ) = 0.25 \times 10^{-31}$ mols^{-1}, -50mV configuration (Figure 5.3j) as a basis for further studies because it lies between the other two possible configurations (Figures 5.3g and 5.3n). For the remainder of this Chapter we refer to the 'standard' conditions as those used to produce Figure 5.3j, listed in Table 5.1.

Table 5.1: Standard configuration. The ∞ subscript denotes the upper boundary, the el subscript denotes the electrode, and the P, and NP subscripts denote the crystallite polar and non-polar surfaces respectively.

Parameter	Setting
Zn_∞	5 mM
O_2^∞	0.8 mM
OH^-_∞	0 mM
Ca_∞	100 mM
ϕ_∞	0 mV
Crystallite density	0.01 nm^{-1}
ϕ_{el}	-50 mV
$\phi_{P,NP}$	Mirror
$\beta_{P,NP}$	0.25×10^{-31} mols^{-1}
$\alpha_{el,P,NP}$	Mass transport limit

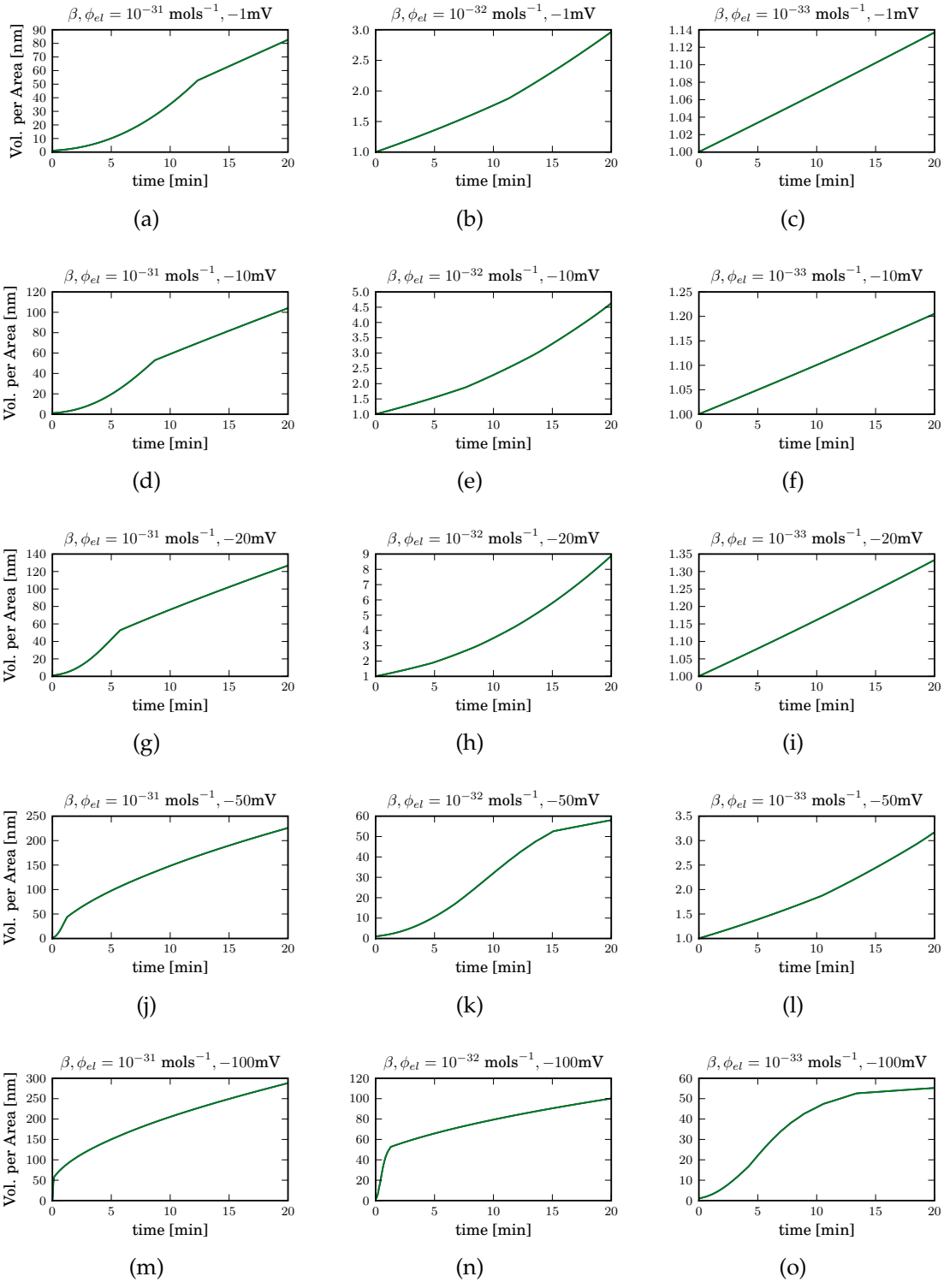

Figure 5.3: Model growth results with isotropic variation of rate constant, β, and electrode surface potential $\phi_{\circ}^{el}$, with mirror conditions for ϕ_P, and ϕ_{NP}.

5.2.2 The Standard Case

To investigate the changes in electrolyte composition, during a simulation of the system under standard conditions we looked at the profile of each variable from the electrode to the bulk boundary at the flux channel mirror boundary. The results for simulations using Zn^{2+}= 5 mM and, to enhance the expected Zn^{2+}deficiency, Zn^{2+}= 0.5 mM, are shown in Figures 5.4 and 5.5 respectively. In these plots the large red squares indicate the crystallite height, and four characteristic times are highlighted: the middle of mode one ($t \sim 0.8$ min), the transition ($t \sim 1.45$ min), shortly after the transition ($t \sim 5$ min), and mode two ($t \sim 10$ min).

The plots show that the potential decays more rapidly within the inter-rod gap than in the bulk electrolyte, the O_2 is completely consumed at the crystallite front, and there is an excess of both Zn^{2+} and OH^- surrounding the growing crystallite polar and non-polar surfaces. In fact, due to the negative electric field emanating from the electrode, the positively charged Zn^{2+} is drawn towards the electrode, and for much of the simulation the concentration of Zn^{2+} near the growing crystallite is greater than the bulk. An additional simulation in which a bulk Zn^{2+} concentration of 0.5 mM was used (ten times smaller than the standard conditions), resulted in a local concentration barely lower than the bulk (Figure 5.5). The cases in which Zn^{2+} was diminished near the crystal (large β and small ϕ) produced curves with no resemblance to the experimentally measured curves.

The stoichiometric ratio of Zn^{2+} to OH^- in the ZnO formation reaction is 1:2, and the ratio of Zn^{2+} to OH^- surrounding the crystallite during the simulations is approximately 2:1. Thus under the standard conditions that best resemble the experiment, the crystallite growth is limited by the amount of OH, which is produced by the mass-limited, or near to mass limited, transport of O_2.

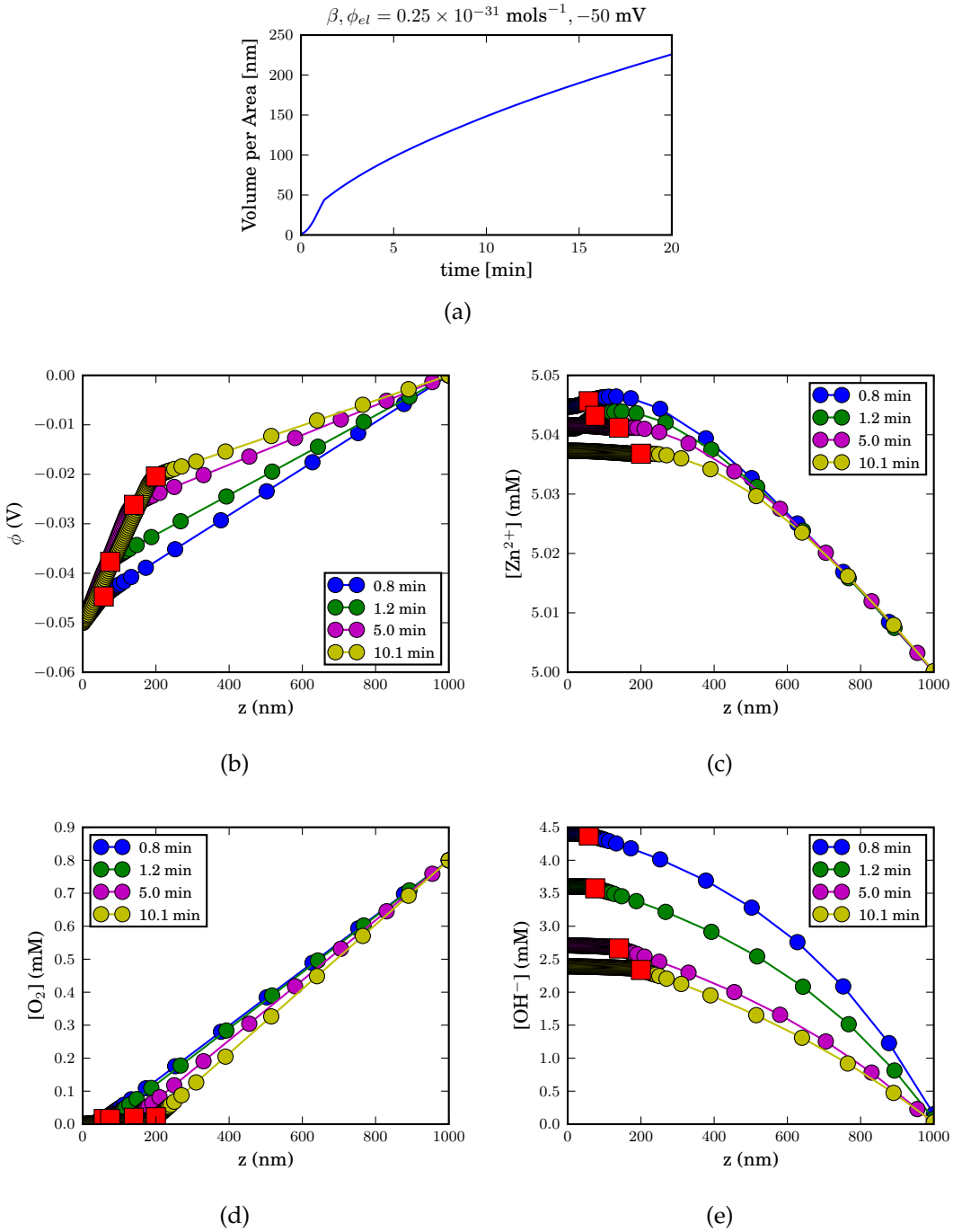

Figure 5.4: The growth curve obtained using the standard conditions ([Zn^{2+}] = 5 mM, $\phi = -50$ mV, $\beta = 0.25 \times 10^{-31}$ mols^{-1}) (a), and profiles at characteristic times along the system height (from the electrode to the upper boundary) of (b) ϕ (c) [Zn^{2+}] (d) [O_2] (e) [OH^-]. The crystallite heights are highlighted with red squares.

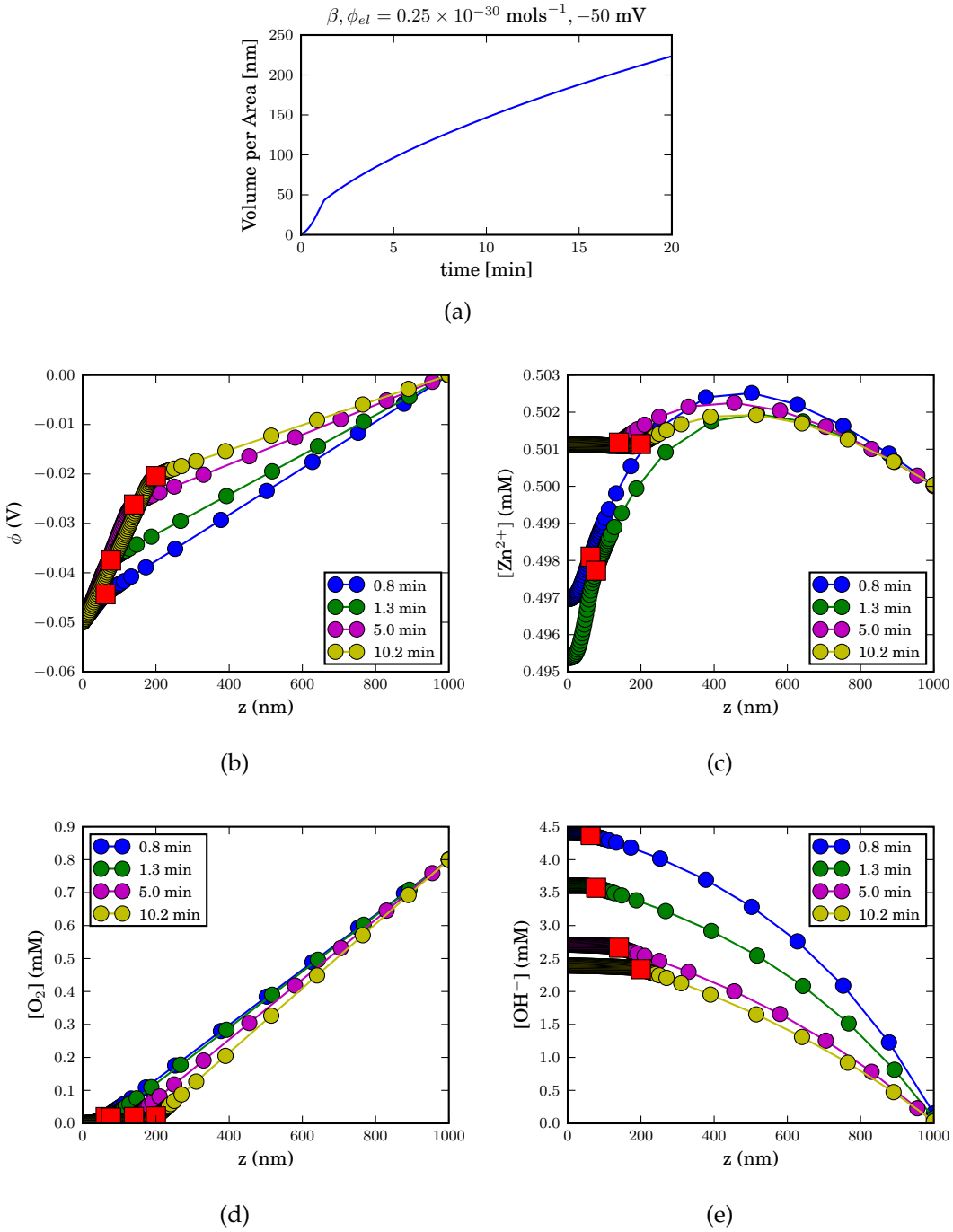

Figure 5.5: The growth curve obtained using [Zn^{2+}] = 0.5 mM with otherwise standard conditions ($\phi = -50$ mV, $\beta = 0.25 \times 10^{-30}$ mols^{-1}) (a), and profiles at characteristic times along the system height (from the electrode to the upper boundary) of (b) ϕ (c) [Zn^{2+}] (d) [O_2] (e) [OH^-]. The crystallite heights are highlighted with red squares.

5.2.3 The Oxygen Reduction Reaction (ORR) and Electrolyte Dynamics

The ORR is an essential part of the system - without it there would be no deposition. In the previous section we found the growth of the crystallite rods to be limited by the amount of OH^- surrounding the crystallite. The ORR is most likely occurring on the electrode, however, it is not obvious if, or how effectively, it occurs on the facets of the growing crystallites. In this section we investigate the standard case, and contrast the cases in which the ORR occurs (i) exclusively at the electrode, ORR(el), (ii) at the electrode and the polar crystallite surface, ORR(el,P), (iii) at the electrode and the non-polar crystallite surface, ORR(el,NP), and (iv) at the electrode, polar, and non-polar crystallite surfaces, ORR(el,P,NP).

The growth curves obtained using otherwise standard conditions are shown in Figure 5.6. Using the ORR(el,P,NP) case as a basis for comparison we notice some unexpected results. We see that within the time period of interest, growth is significantly enhanced if the ORR(P) is suppressed. The enhanced growth curve has a greater negative curvature indicating that in the longer term, the ORR(P) cases will ultimately yield greater growth rates.

The result was unexpected as generation of OH^- on all surfaces should produce more OH^- and therefore drive the ZnO formation reaction faster. However, the effect we observed was that a proportion of the OH^- generated on the polar surfaces was transported away from the growing crystal to the upper boundary, therefore much of the O_2 was simply returned to the bulk electrolyte as OH^- rather than participating in ZnO formation. Thus within the simulations, the ZnO formation reaction is limited by a balance between the O_2 transport limited production of OH^-, and the subsequent transport of OH^- away from the crystallite toward the bulk. At the higher electrode surface potentials, the effect is also present if the ORR is permitted on the non-polar crystallite surface, albeit to a far lesser de-

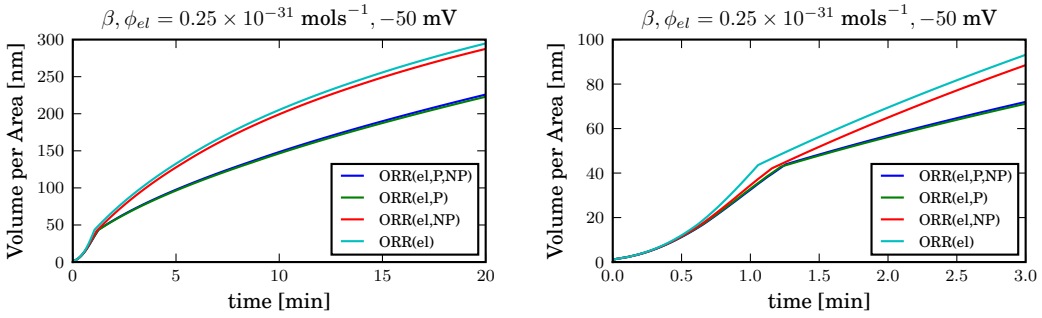

(a) (b)

Figure 5.6: Simulated growth curves obtained using the standard conditions with the ORR occurring at the electrode, ORR(el), the electrode and polar facet, ORR(el,P), the electrode and the non-polar facet, ORR(el,NP), and all surfaces, ORR(el,P,NP).

gree. This is because the larger electric field drives the negatively charged OH^-, generated at the non-polar surface, to the upper boundary more rapidly. The behaviour is reproduced at electrode surface potentials -10,-20,-40,-60, and -100 mV.

The reason for the difference in growth behaviour for differing ORR locations is illustrated clearly by comparing the electrode-to-boundary profile of the variables. The profiles of the slower growing simulations obtained when ORR(P) was permitted are shown in the left column of Figure 5.7, and those in which ORR(P) was not permitted are shown in the right column of Figure 5.7. The difference in terms of the distributions of Zn, O_2, and OH, is remarkable. At a glance we see that when the ORR(P) is suppressed, the three participating chemical species accumulate in the inter-rod space. The species concentrations and ratio of Zn^{2+} to OH^- at the crystal height (at the red squares) at the four characteristic times are collected in Table 5.2. At all timesteps there is a greater relative deficiency of OH^- to Zn^{2+} for the cases in which the ORR is allowed to proceed at the upper crystallite surface. This explains the slower simulated growth

curves when the ORR was permitted on the polar surface.

Table 5.2: ZnO formation stoichiometry about the crystallite front.

Time (s)	Variable	ORR(el,P) [mM]	ORR(el) [mM]	$[Zn^{2+}]/[OH^-]$(el,P)	$[Zn^{2+}]/[OH^-]$(el)
43	$[Zn^{2+}]$	5.048	5.045	1.1	1.0
	$[O_2]$	0	0		
	$[OH^-]$	4.5	4.9		
73	$[Zn^{2+}]$	5.045	5.040	1.4	1.1
	$[O_2]$	0	0.25		
	$[OH^-]$	3.6	4.6		
303	$[Zn^{2+}]$	5.042	5.025	1.9	1.5
	$[O_2]$	0	0.45		
	$[OH^-]$	2.7	3.4		
603	$[Zn^{2+}]$	5.032	5.018	2.1	1.8
	$[O_2]$	0	0.55		
	$[OH^-]$	2.4	2.8		

The efficiency of the ORR's contribution to crystallite growth was assessed by comparing the net flux of OH^- into the electrolyte due to the ORR, with the flux of OH^- out of the electrolyte due to crystallite formation. In Figure 5.8 we plot the ratio of the net OH^- flux into the polar surface, $J^X_{OH,P}$, with the net flux of OH^- produced by the ORR, $J^{ORR}_{OH,el} + J^{ORR}_{OH,P}$, for the ORR configurations: electrode only, ORR(el), and electrode and polar surface, ORR(el,P). We see that during mode one growth ($t < 100$ s), the OH^- efficiencies of the two ORR configurations are the same. However, for most of the mode two growth, the ORR(el) is twice as efficient as the ORR(el,P). This behaviour is a reflection of the growth curves, in which the mode one growth rate is the same, but the mode two growth rate is much larger for the ORR(el) configuration (see Figure 5.6). In the later stages of mode two growth the OH^- efficiency of the ORR(el,P) case flattens out, whereas the OH^- efficiency of the ORR(el) case remains in steady decline. Thus, as with the growth curves, we expect the ORR(el,P) to be more efficient in the long term.

Further demonstration of the diminished efficiency of the ORR growth contribution is seen by comparing the OH^- production, J^{in}_{OH}, at the electrode for ORR(el), and the crystal tip for ORR(el,P), with the OH^- exiting

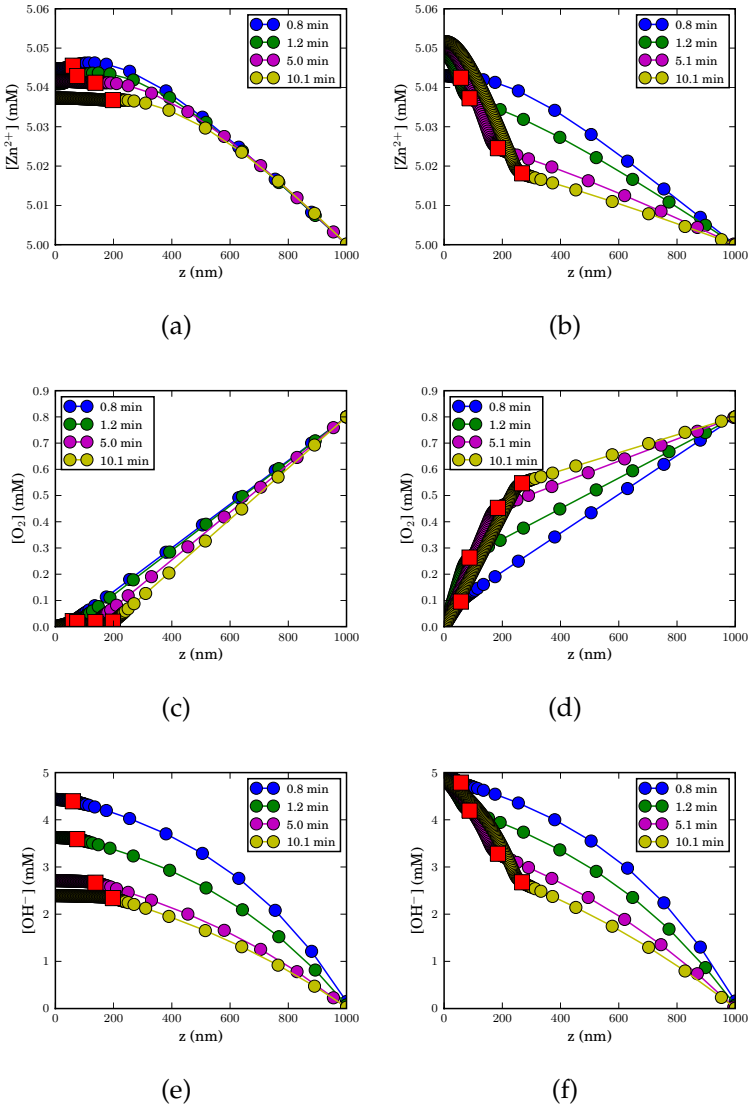

Figure 5.7: Profiles of the key variables $[Zn^{2+}]$, $[O_2]$, and $[OH^-]$. The left column was obtained using standard conditions ($\phi_{el} = -50$ mV, $[Zn^{2+}]_\infty$ = 5 mM, $\beta = 0.25 \times 10^{-31}$ mols^{-1}) with the ORR occurring on the electrode and the polar crystallite surface, ORR(el,P), and the right column was obtained with the ORR occurring on the electrode only, ORR(el). The large red squares indicate the crystal height.

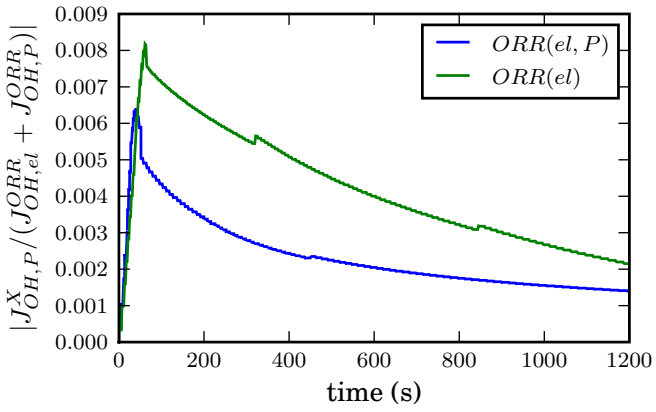

Figure 5.8: Plots showing the efficiency of OH^- contribution to growth under the characteristic ORR regimes: electrode only (green), and electrode and crystallite polar surface (blue line). The kinks are an artefact of the grid update an interpolation procedure and require further development.

the system, J^{out}_{OH}. The proportion of OH^- escaping to the bulk, J^{out}_{OH}/J^{in}_{OH}, is shown in Figure 5.9. We see that throughout the entire duration of the simulation, the proportion of OH^- lost to the bulk is greater when the ORR occurs on the crystallite.

5.3 Basic Variation of System Parameters

Our model possesses a variety of parameters that can be varied to produce a large set of growth curves. The way in which a given growth curve changes upon variation of a specific parameter gives insight into the system. The approach of this section is to vary these parameters to gain insight into the processes that determine the growth behaviour. We are particularly interested in the effect of variation of applied potential and Zn^{2+} concentration as these are the main experimental variables.

In the following, we discuss our investigations into the growth behaviour under various ORR configurations, Zn^{2+} concentrations, the crys-

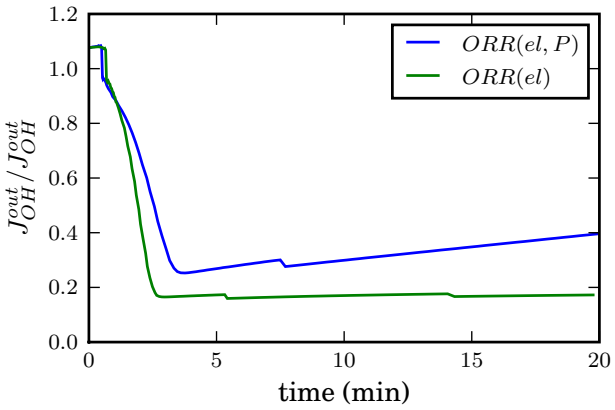

Figure 5.9: Plots showing the efficiency of OH^- contribution to growth in terms of the amount of OH^- exiting the system, under the characteristic ORR regimes: electrode only (green), and electrode and crystallite polar surface (blue line). Again, the kinks in the flux ratios are numerical artefacts.

tallite densities (centre to centre distance), the porosity (the minimum gap between adjacent crystallite faces), anisotropy in the ZnO rate constants, and surface potential.

5.3.1 Zn^{2+} Concentration

The first variation we present is that of Zn^{2+} concentration, as it is one of the important experimental variables. Increasing the concentration produced the rather predictable result of increasing growth of the crystallite. This is in very clear contrast to the experimental result in which increased concentration decreases the mode one growth rate. In the simulated results the mode one - mode two transition occurs earlier (Figure 5.10), and early mode two growth is also much greater at higher concentration. In fact, in the case of rapid growth obtained when ORR is permitted at the electrode only, the transition is barely evident due to the large vertical growth. This absence of an abrupt transition is closer to the experimen-

tal result, especially those in which the applied potential is -770 mV and -670 mV.

Also of interest is the contrast between the curves obtained with and without the ORR on the crystallite. In case of electrode-only ORR, we see that despite the large Zn^{2+} concentration, and associated growth increase, the higher concentration curve exhibits a large negative curvature and then the rate of growth flattens out to that of the lower concentration, indicative of the OH^- limited regime discussed above in Section 5.2.3.

5.3.2 Crystallite Density

It is possible that the dominant effect of Zn^{2+} concentration increase is not directly associated with transport and reaction, but the nucleation of seeds. It is conceivable that increasing the concentration may affect the frequency of seed formation to a greater extent than it increases the growth rate of existing seeds. The higher seed density in turn would result in much earlier crowding and onset of the second, and lower, growth rate, yielding a more 1-dimensional scenario. The alternative scenario is that higher concentration favours growth over nucleation, resulting in a less dense surface. The process in which larger crystals grow at the expense of smaller crystal is known as Ostwald ripening [93]. The SEM images and growth curves presented in Chapter 2 favour the latter explanation as larger diameter rods are prevalent under conditions that produce rapid growth. Rapid growth at low seed density could lead to delayed and smoothed growth mode transition.

Simulations were performed with a rod density of one crystallite per 100 nm to 20 nm, using both 5 and 10 mM Zn^{2+} concentrations. The effect of higher crystallite density on a Zn^{2+} concentration of 10 mM is shown in Figure 5.11a. We see that increased density produces a greater growth rate in the very early stages, and a much lower overall rate. This behaviour resembles the experimentally observed effect of concentration

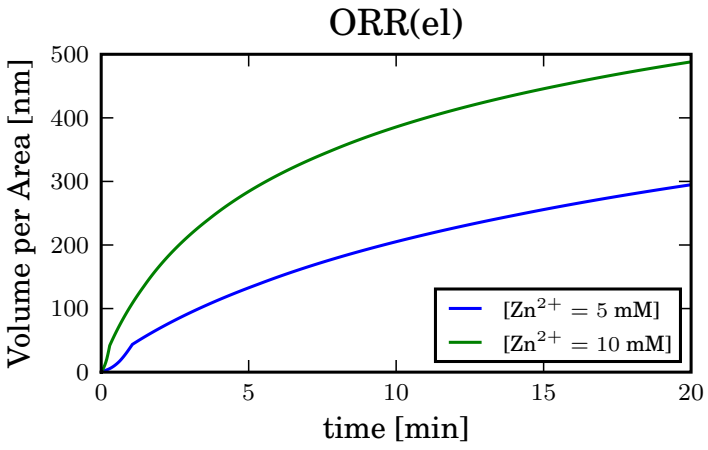

(a)

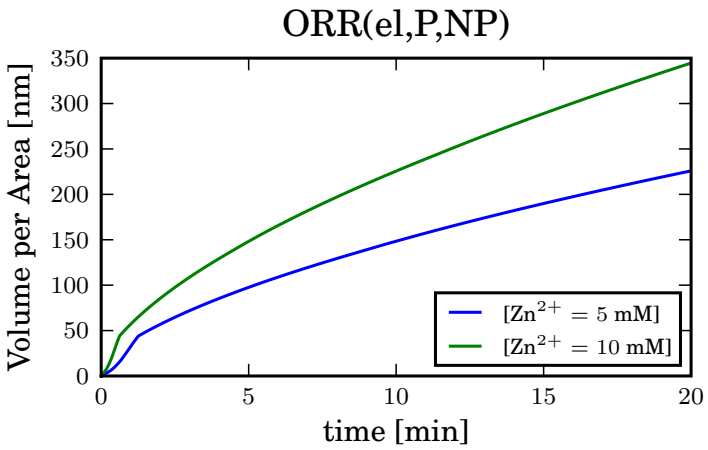

(b)

Figure 5.10: Plots illustrating the effect of Zn^{2+} concentration variation on the simulated growth curves. The upper plot was by permitting the ORR to occur at the electrode only, and the lower figure permitted the ORR on all surfaces.

increase, and indicates that the concentration variation does not simply affect the transport-reaction dynamics. Comparison of curves obtained at low crystallite density and low concentration with that obtained using high concentration and high density (corresponding to the first scenario above) are shown in Figure 5.11b. The effect of higher density as a proxy for the effect of concentration actually reduces overall the growth, in stark contrast to the experimental case in which only the initial growth is hindered while the latter growth is increased. The remaining scenario of high concentration-low crystallite density with low concentration-high crystallite density is shown in Figure 5.11c. It has the same character as the first case in which the rod density for a single concentration was varied.

A subtle, but interesting feature associated with increasing the density is not just that the mode transition occurs earlier, but that the mode one growth is greater. The reason for this is due to the efficiency of OH^- consumption described in Section 5.2.3. More OH^- escapes to the bulk when the crystallites are further apart, resulting in slower growth than when the crystallites are closer together. The simulation results suggest that if increasing the Zn^{2+} concentration influences nucleation, it does so by decreasing the crystallite density, perhaps by the process of Ostwald ripening mentioned above.

5.3.3 The Surface Potential

Up to this point we have been using a mirror boundary condition for the surface potential of the crystallite (see Table 5.1). The mirror boundary condition yields crystal surface potentials that decay with distance from the electrode resembling the behaviour of an ohmically resisting crystal, or a polarisable surface upon which the electric field does not significantly decay. The resulting curves (see for example Figure 5.13) produce growth curves with mode two growth shape much like that of the experimentally measured shape. However, in this section we discuss our investigation of

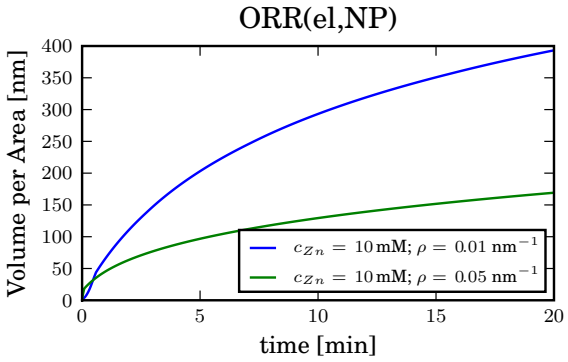

(a)

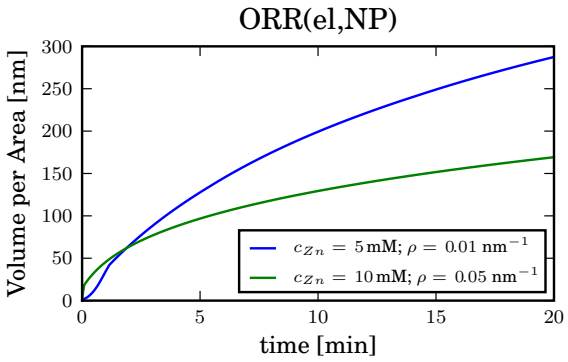

(b)

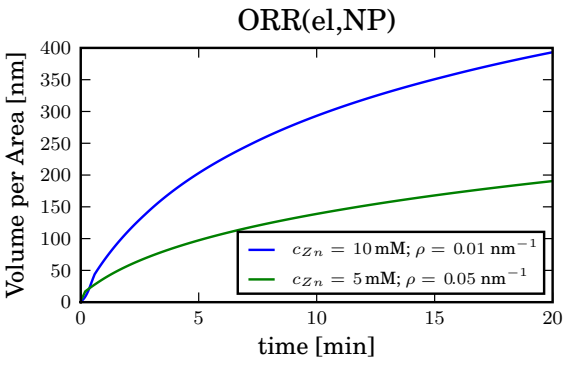

(c)

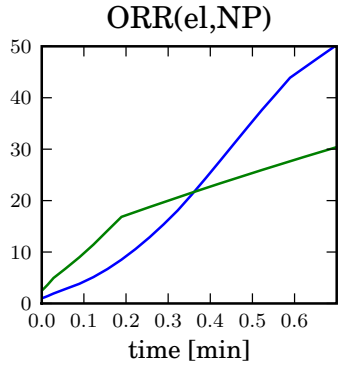

(d)

Figure 5.11: Simulations probing the possibility of a relationship between concentration and crystallite seed density. (a) High concentration at high and low density, (b) high concentration-high density with low concentration-low density, and (c) high concentration-low density with low concentration-high density, (d) inset of (c) illustrating slower initial growth rate at higher concentration.

an alternative situation in which the crystallite possesses a fixed surface potential. The scenario corresponds to the situation in which the crystallites behave as if they are part of the electrode, which is, in the data provided by Illy et al [92], also ZnO. The magnitude of the electrode surface potential is related to the applied potential through the capacitance of the electrode surface [48].

In this search, the surface potentials were set anisotropically over a range of isotropic rate constants. In general the results were uninteresting, except those in which the non-polar surface potential was fixed at -50 mV (the same as the electrode), and the polar surface was varied. These results behaved in a similar way to the experimental dependence of growth on applied potential for the [Zn^{2+}] = 5 mM case.

Table 5.3: Surface potential variation sets.

ϕ_{el} (mV)	ϕ_P (mV)	ϕ_{NP} (mV)
-50	X	Y
-50	X	50
-50	-10	X
-50	-20	X

The two mode growth behaviour is produced, and the independence of mode one and dependence of mode two on the surface potential (Figure 5.12) is analogous to the experimental response to change in applied potential (Figure 5.2a). However, the linearity of the second mode is unlike the experimental data which has a negative curvature.

The fixed potential reproduces the shared mode one rates, and the surface potential is obviously related to the applied potential. However the shape of the fixed potential simulation curves does not bear a strong resemblance to the experimentally measured curves. The mirror surface potential boundary condition produces more realistic curves but, upon variation of the electrode surface potential, does not reproduce the shared mode one growth rate observed experimentally. Both models are consistent with the cause of the termination of the first growth mode being due to abrupt

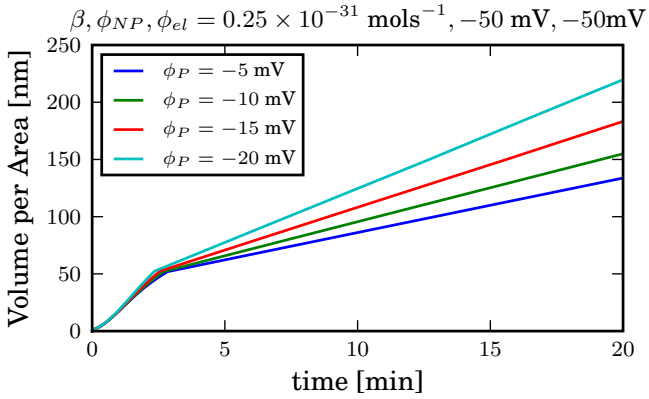

(a)

Figure 5.12: Simulated growth curves obtained using standard conditions (c.f. Table 5.1) with varied ϕ_P° and ϕ_{el}° and ϕ_{NP}° fixed at -50 mV.

cessation of the lateral growth mode due to coverage of the electrode surface. The successes associated with anisotropic surface potentials and the resulting anisotropic growth rates suggest that the use of anisotropic rate constants with the mirror potential boundary condition could yield a good reproduction of the experimental data.

5.3.4 Growth Rate Anisotropy

In the previous section, surface growth rate anisotropy, mediated through crystallite surface potential, was successful in reproducing some aspects of the effect of applied potential variation on the measured growth curves. In this section we present our findings relating to the effect of surface growth rate anisotropy mediated by variation in the surface growth rate constants. In Sections 5.3.1 and 5.3.2 we saw that decreasing rod density and increasing concentration caused earlier occurrence of the transition point. It appears that the abrupt transition is associated with a rapid cessation of lateral growth, due to the closing of the inter-crystallite gap. Thus the rate of closure of the inter-rod gap is to a large extent determined by the rate of

lateral growth. As we are satisfied with the transition time obtained under the standard conditions we kept $\beta_{NP} = 0.25 \times 10^{-31}$mols^{-1} and varied β_P only.

The effect of an order of magnitude increase in the polar growth rate constant is illustrated by Figure 5.13b. The first observation is that the amount of material (volume per area) is much closer to that of the measured data, suggesting $\beta_P \approx 10 \times \beta_{NP}$. Comparison of the effect of the ORR configuration under anisotropic rate conditions with that of isotropic rate conditions (see Figure 5.13a) shows a distinctive difference, and highlights the importance of the ORR reaction, and where it occurs.

Considering only mode one growth we see that the simulations in which the ORR is allowed to occur on the crystal (polar or non-polar surface) all exhibit the same mode one growth rate. A growth rate which is slower than that obtained when the ORR occurs exclusively on the electrode. The reason for the reduced growth rate was investigated in Section 5.2.3 and is due to loss of OH^- to the bulk electrolyte.

The differences in mode two growth are manifested between those in which the ORR is permitted on the polar surface and those in which it is not. This is because mode two growth is dominated by vertical growth. The ORR(el,P) and ORR(el,P,NP) simulations exhibit a steady mode two growth whereas the growth rate of the ORR(el), and ORR(NP) simulations diminishes with time. Thus two cases are evident; that in which vertical growth is limited by the transport of OH^- from the electrode to the tip of the growing crystallite, and that in which it is not. Late stage growth is consistent with the 'Case 1' (fixed flow area free aspect ratio) model described in section 3.6.1

5.3.5 The ORR Rate, α

Throughout the preceding sections the mass limited O_2 transport boundary condition has been effective in the determination of the system pa-

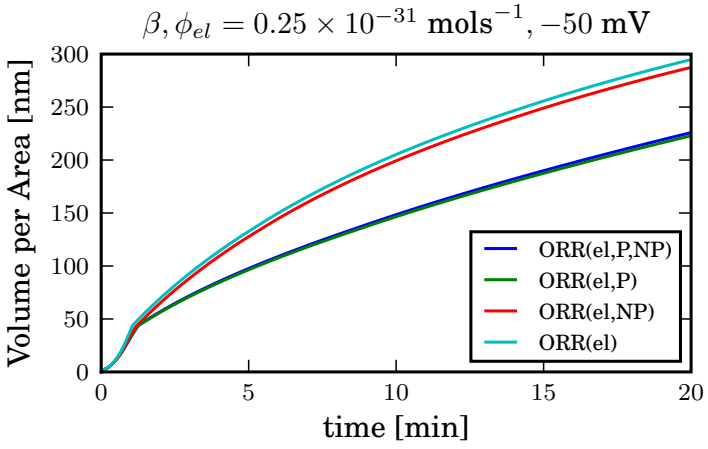

(a)

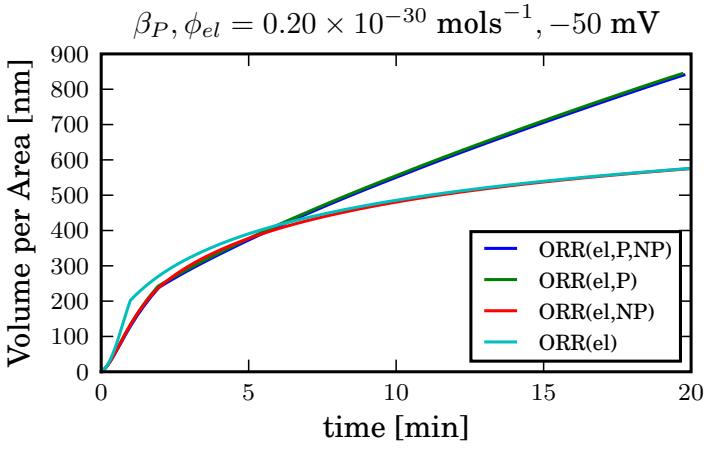

(b)

Figure 5.13: Comparison of the growth curves at the various ORR configurations using (a) standard conditions (b) $\beta_P = 0.20 \times 10^{-30}$ mols^{-1}.

rameters that produce growth curves with the same charactistics as the experimental results. However, in considering the effect of permitting the mass limited ORR at the polar crystallite surface (ORR(P)), an increase in mode two growth rate, we saw a resemblance to the effect of decreasing the applied potential (more cathodic) in the experiment. It suggests that the effect of potential might be to mediate the rate of OH^- formation on the surface boundaries. Although the O_2 mass transport limit is effective in reproducing the experimentally observed growth features such as curve shape and mode transition, it is not an optimal condition for reproduction of the behaviour associated with change in the applied potential, for which a potential dependent rate expression is more appropriate.

To explore the effect of a potential mediated ORR rate the the first order reaction-flux boundary condition (c.f. Section 3.1.1),

$$J_{O_2} = \alpha C_{O_2} \qquad \text{where} \qquad \alpha = \left(\frac{i_\circ}{nFC^\infty_{O_2}}\right)\exp(-npf\eta). \tag{5.6}$$

was evaluated at the polar crystallite boundary using an arbitrary range of α's. A greater rate constant, α, is obtained from a more negative overpotential, η, which corresponds to a more cathodic applied potential, E_{app}.

The simulation results are shown in Figure 5.14a, and comparison with Figure 5.2a indicates that increasing the rate of the ORR on the surface is qualitatively consistent with decreasing the applied potential to a more cathodic value. Thus it appears that the ORR is occurring on the growing crystallite, and exhibiting a dependence on the applied potential. However, because the divergence occurs sometime after the transition point, we suspect that not only is the ORR occurring not only at the crystallite surface with a dependence on the applied potential, but at the electrode too. Evaluation of the above boundary condition exclusively on the electrode yielded the growth curves presented in Figure 5.14b. As with experiment the curves begin to diverge at the same point, but show a clear limiting behaviour stronger than that observed experimentally (Figure 5.2a). Application of the the flux-reaction boundary condition (5.6) to both the

crystallite and the electrode produces the shared mode one growth and divergence of mode two growth from the same point. The mode two growth exhibits a very moderate downward curvature similar to that seen experimentally. The results strongly suggest that the ORR occurs on both the crystallite and elecotrode with a rate dependent on the applied potential.

5.3.6 Minimum Inter-Crystallite Gap

The minimum inter-crystallite gap, or maximum closeness, was investigated using anisotropic rate settings. Along with rod density it contributes to the porosity of the crystallite film. Investigation of the precise reasons as to why the nano-crystallite rods do not fuse together to produce a monolithic film are beyond the scope of this study. However, there are a variety of factors that could contribute to the experimentally observed spacing between crystallites such as epitaxial mismatch, or electrostatic repulsion. Epitaxial mismatch is energetically unfavourable, and occurs when facets come together with poor alignment due to a lack of alignment of the hexagonal faces of the growing crystallites. The increased energy at the mismatched contact areas would then drive dissolution, ensuring an inter-crystallite gap. Alternatively, the like nature of the crystallite chemical surface composition could lead to long-range Coulombic or low-range Van der Waals repulsion to ensure a finite inter-crystallite space. We also note that if the crystallite surfaces come close enough for their Debye layers to overlap then the electroneutrality constraint breaks down and the Nernst-Planck-Electroneutrality model (3.45-3.46) is not valid in such regions. Under such conditions the Poisson-Nernst-Planck model (3.36-3.37) would be more appropriate and might account for the spacing through transport effects. Thus, some environments may favour thinner crystallites, and others thicker. The scaling law we have used in this model does not account for such preference, so we have investigated a range of inter-crystallite spacings by enforcing a range of maximum crystallite widths.

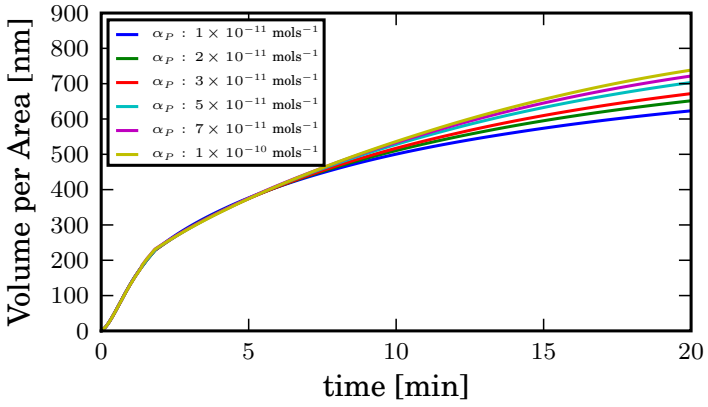

(a)

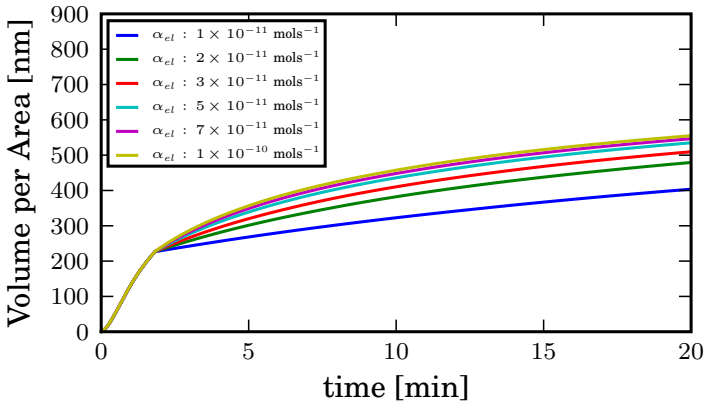

(b)

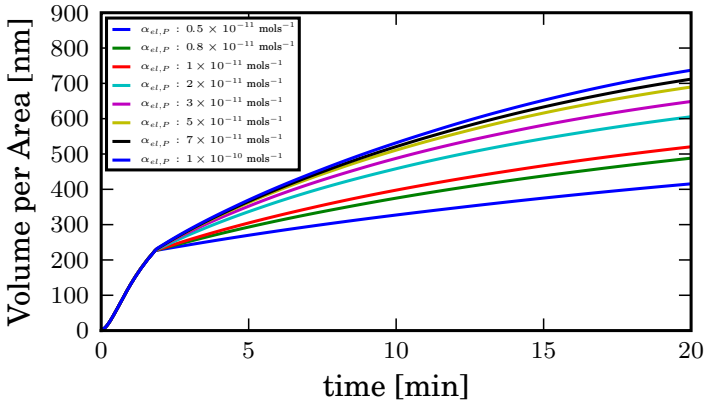

(c)

Figure 5.14: Variation of ad hoc rate dependence of the ORR (a) at the polar crystallite surface, (b) at the electrode, and (c) at both the electrode and the polar crystallite surface.

The results are particularly enlightening with regard to the nature of the mode transition point. What we see is that the distinctness of the mode transition point is determined not by the abruptness of the lateral growth cessation, or the relative growth rates of the surfaces, but the timing at which lateral growth stops. If lateral growth ceases when vertical growth is rapid, then the transition appears smooth as in the case when the maximum closeness is 25 nm (Figure 5.15). However, if this lateral growth ceases when the vertical growth rate has slowed then the transition appears very distinctly, as in the case of maximum closeness of 2.5 nm in Figure 5.15. The effect is diminished in the cases in which the ORR proceeds at the top because the vertical growth is not limited and the transition is always relatively abrupt.

5.4 Summary

Although the work presented here does not explain or replicate the experimental system in full, it does provide an impression of a variety of underlying effects that contribute to the growth behaviour. We found the growth to be limited not by Zn^{2+} , but by OH^{-} concentration. Such a result is consistent with the expectation from steady state one-dimensional transport models due to the lower concentration of O_2 compared to Zn^{2+}. The limiting effect of OH^{-} is exacerbated by the polarity of the electrode, in that it attracts Zn^{2+} and repels OH^{-}. Thus the OH^{-} limited regime is supported by two effects. First, the transport of Zn^{2+} towards the electrode is greatly accelerated by the electric field, resulting in an excess of Zn^{2+} near the electrode. The accumulation of Zn^{2+} between the growing film and the bulk, as well as its consumption by the growing rod is captured in Figure 5.16. Secondly, the $OH^{-}$is both repelled from the electrode and neutralised at the upper boundary. It is particularly interesting that excessive conversion of O_2 to OH^{-} can result in reduced growth.

Our findings with regard to the relation between the applied potential,

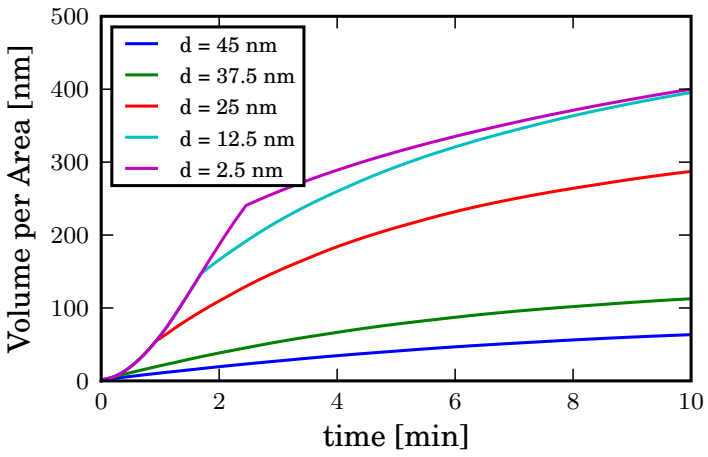

(a) ORR(el)

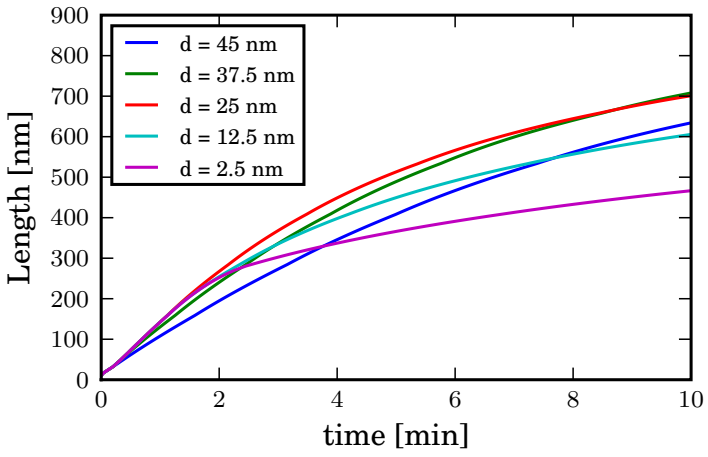

(b) ORR(el)

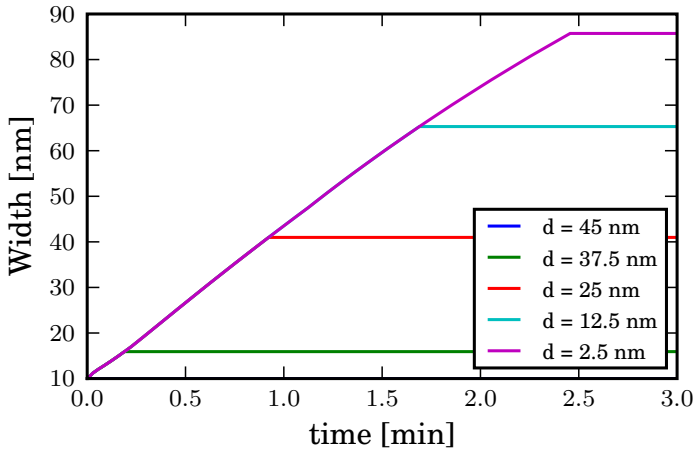

(c) ORR(el)

Figure 5.15: Plots of the simulated volume (a), length (b), and width (c), obtained for a range of enforced crystallite maximum widths. The minimum inter-crystallite gap is denoted by d.

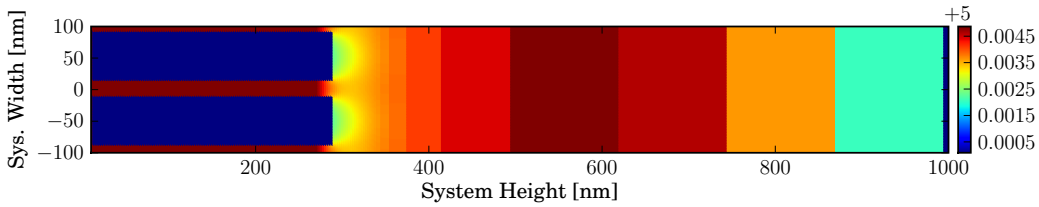

(a) ORR(el)

Figure 5.16: Zn^{2+}concentration map at the mode one - mode two transition, obtained using ORR(el,P,NP).

the ORR, and the growth curve structure is also interesting. We found two possible mechanisms for growth rate mediation through applied potential. One was that the surface potential of the crystallite varied with variation in applied potential. The increased negative potential drew more Zn^{2+} toward the crystallite surface and increased the rate of growth. However, this mechanism produced curves with a greater linearity than the experimentally observed curves. An alternative mechanism in which the applied potential drives the ORR on the crystal surfaces as well as the electrode produced growth curves that strongly resembled (see Figure 5.14) the experimentally measured curves, and their dependence on the applied potential. The results also suggest that the ORR is not proceeding at the mass transport limit but has a clear dependence on the applied potential.

Our attempts to elucidate information about the effect of concentration increase were less compelling, although two key experimentally observed features were reproduced. As with the experimental data, association of greater concentration with lower density produced an overall greater growth rate in the simulations, and lower concentration-higher density yielded a greater early growth rate. However, the simulated and experimental curves bear minimal resemblance. We believe a more detailed treatment of nucleation and very early growth phenomena would benefit our understanding of the effect of concentration.

Another aspect of the model that would benefit from a more detailed

treatment is the processes involved in ensuring the crystallites do not coalesce: crystallite-crystallite interaction. The work presented here constrained the crystal shape to be rectangular, with an aspect ratio dependent only on the reaction and migration of the electrolyte. The investigation of the minimum inter-crystallite gap emphasised the need for a treatment of the nature of the crystal surface during growth.

Finally, it seems that the structure of the growth curve is the following: rapid early growth driven by an abundance of OH^- due to an initial abundance of O_2, followed by a transition from 2-dimensional growth to 1-dimensional growth due to lateral crowding. The sharpness of this transition depends on the rate of the vertical rather than lateral growth rate. The 1-dimensional growth proceeds more slowly than the 2-dimensional growth due to a shortage of OH^-, a shortage that can be alleviated if the ORR occurs on the crystallite.

Chapter 6

DFT: Theory and Method

In this chapter we give an overview of the development of electronic density functional theory (DFT). Our presentation will differ from the conventional development in which improvement of the Hartree model leads to the Hartree Fock model which defines an important quantity known as the correlation energy, E_{corr}, which in turn helps define the basic terms of DFT [94, 95]. Our development will focus on the the key mathematical approach that facilitates the solution of real quantum mechanical problems: the calculus of variations. Knowledge of the calculus of variations is essential to understanding the most basic concepts and methods required for the application of quantum mechanics, and density functional theory, to the non-trivial problems of interest to us. For this reason we begin with a brief overview of variational calculus.

6.1 The Calculus of Variations

The mathematical physics reference literature describes a variety of different approaches to explain variational methods at differing levels of complexity and application. The calculus of variations was formalised by Lagrange in his 1788 work *Mécanique Analytique* [96]. It is concerned with finding the stationary values or extrema of definite integrals called *func-*

tionals. The term functional refers to a quantity that depends on a set of functions (a *function space*) rather than a finite set of independent variables (scalars). A functional *maps* functions to the real number line, and is therefore likened to a 'function of functions'. Functionals take the general form

$$I = \int_a^b F(y, y^1, y^2, ..., y^n, x)dx \quad \text{where } y^n = \frac{d^n y}{dx^n} \tag{6.1}$$

with

$$y(a) = \alpha \quad \text{and} \quad y(b) = \beta. \tag{6.2}$$

Here F is a function (not a functional) of the function y and its derivatives y^n, and x is the independent variable upon which we define our interval. In solving a variational problem we seek to find the unknown function $y = y(x)$ that minimises (or maximises) I on the interval $x \in [a, b]$. Such a function is called an *extremal*. As in ordinary calculus of functions the task is to find the stationary value of the functional.

6.1.1 The Stationary Value of a Functional

The stationary value of a functional can be defined in a variety of ways. The following development is based on that of Courant & Hilbert [97] and Gelfand & Fomin [98]. First we imagine that our integral I is made stationary by some unknown function $y = y(x)$. We introduce a family of test functions of the form $\overline{y(x)} = y(x) + \epsilon\eta(x)$ where $\eta(x)$ is an arbitrary function that conforms to the same requirements as $y(x)$ (continuous, differentiable, and has the same fixed endpoints), and ϵ is an arbitrarily small variable parameter that ensures the test functions ($\overline{y(x)}$) lie within an arbitrarily small neighbourhood of the extremal $y(x)$.

The *variation* of y is now defined as

$$\delta y = \overline{y(x)} - y(x) = \epsilon\eta(x)^1. \tag{6.3}$$

[1]This expressed more generally as $\{\frac{d}{d\epsilon}y(x, \epsilon)\}_{\epsilon=0}$.

At sufficiently small ϵ, the functional I can be regarded as a function of ϵ, i.e. the function $y(x)$ is static on such a scale and we have $I[y+\delta y] = I[\overline{y(x)}] = \phi(\epsilon)$. We know that $\phi(\epsilon)$ must have a minimum at $\epsilon = 0$ and that $\phi'(\epsilon)$ at this point must equal zero, thus $\phi'(0) = 0$. Writing out $\phi(\epsilon)$ for the simplest variational problem, $I = \int_a^b F(x, y, y')dx$,

$$\phi(\epsilon) = \int_a^b F(x, y + \epsilon\eta, y' + \epsilon\eta')dx \tag{6.4}$$

and taking the derivative with respect to ϵ yields

$$\phi'(\epsilon) = \int_a^b \frac{d}{d\epsilon} F(x, y + \epsilon\eta, y' + \epsilon\eta')dx \tag{6.5}$$

$$= \int_a^b \lim_{\epsilon \to 0} \frac{F(x, y + \epsilon\eta, y' + \epsilon\eta') - F(x, y, y')}{\epsilon} dx. \tag{6.6}$$

When expressed as a Taylor series [2]

$$\phi'(\epsilon) = \lim_{\epsilon \to 0} \int_a^b \left\{ \left[\frac{\partial F}{\partial y} - \frac{d}{dx}\left(\frac{\partial F}{\partial y'}\right) \right] \eta + O(\epsilon) \right\} dx \tag{6.7}$$

it is clear that

$$\phi'(0) = \int_a^b \left[\frac{\partial F}{\partial y} - \frac{d}{dx}\left(\frac{\partial F}{\partial y'}\right) \right] \eta(x) dx. \tag{6.8}$$

According to a fundamental lemma of variational calculus [3] $\phi'(0) = 0$ if and only if

$$\frac{\partial F}{\partial y} - \frac{d}{dx}\left(\frac{\partial F}{\partial y'}\right) = 0. \tag{6.9}$$

[2] Here partial integration was used to change multiplication of the second bracketed term by η' into the sum of a boundary term which is dropped on account of fixed boundary and a term multiplied by η i.e. $\int_a^b \frac{\partial F}{\partial y'}\eta' dx = [\frac{\partial F}{\partial y'}\eta]_a^b - \int_a^b \frac{d}{dx}\left(\frac{\partial F}{\partial y'}\right)\eta dx$ where due to fixed endpoints $\frac{\partial F(a)}{\partial y'} = \frac{\partial F(b)}{\partial y'} = 0$.

[3] If $\int_a^b E(x)\eta(x)dx = 0$ for every continous function $\eta(x)$ that vanishes on the boundaries a and b then $E(x) = 0$.

This ordinary differential equation is known as the Euler-Lagrange equation, to which solutions yield stationary values of the functional I. In analogy to our definition of the variation of y, $\delta y = \epsilon\eta$, we can define the variation of our functional δI as

$$\delta I = \epsilon\phi'(0) \tag{6.10}$$

where $\phi'(0)$ is the left hand side of the differential equation - Equation 6.9 - obtained above. This is the *indirect* approach of Euler and Lagrange which has facilitated the development of the variational formalism used in mathematical analysis. The *direct* method consists of converting the variational problem into an approximate finite sum which can be treated in the same way as ordinary functions, by taking the limit $\Delta x \to 0$. The result is a 'minimising series' [97], of which the convergence must be investigated independently. Finally, analogous to ordinary calculus the *functional derivative* $\frac{\delta I}{\delta y}$ is defined

$$\delta I = \int_a^b \frac{\delta I}{\delta y}\delta y dx. \tag{6.11}$$

From Equations 6.8, 6.10 and 6.11 above it can be seen that the functional derivative is the left hand side of the Euler-Langrage equation,

$$\frac{\delta I}{\delta y} = \frac{\partial F}{\partial y} - \frac{d}{dx}\left(\frac{\partial F}{\partial y'}\right), \tag{6.12}$$

and therefore, as with the ordinary search for extrema, yields a stationary point when $\delta I/\delta y = 0$. Gelfand and Fomin's [98, p. 14] method of identifying a part of the difference $\Delta I[\delta y] = I[\overline{y}] - I[y]$ that varies linearly with δy is also valuable, in that it emphasises the linearity of the definition, which provides a concise goal with which to obtain the Euler-Lagrange equation. The derivation of Lanczos is worth noting for its originality. Lanczos first identifies the commutation of the variational operator with the integral in the following way

$$\delta I = \delta \int_a^b F(x)dx = \int_a^b [\overline{F(x)} - F(x)]dx = \int_a^b \delta F(x)dx. \tag{6.13}$$

Implicit in the last rearrangement is the statement $\overline{F(x)} - F(x) = \delta F(x)$, which presumes that the linear part of the difference is taken, to wit, δ is linear. Such is the case for very small variation (very small ϵ), and thus consistent with the above.

Finally, the solution to the general case

$$I[y] = \int_a^b F(x, y, y', y'', ..., y^{(n)})dx, \quad \text{where } y^{(n)} = \frac{\partial^n y}{\partial x^n} \tag{6.14}$$

is found to be [98, p. 42]

$$\frac{\partial F}{\partial y} - \frac{d}{dx}\left(\frac{\partial F}{\partial y'}\right) + \frac{d^2}{dx^2}\left(\frac{\partial F}{\partial y''}\right) - \cdots + (-1)^n \frac{d^n}{dx^n}\left(\frac{\partial F}{\partial y^{(n)}}\right) = 0. \tag{6.15}$$

6.1.2 Variational Calculus with Constraints

It is possible to apply more constraints than simple boundary conditions as in the previous section (Section 6.1). Restrictions can be applied to the allowed set of curves that satisfy the variational problem. When confronted with such constraints there are two methods of solution. Firstly, one might try to eliminate variables. For example, if there are m constraints and n variables one could eliminate the m variables leaving $m - n$ degrees of freedom. The drawback of this *method of elimination* is that it can be tedious to perform the elimination, and, more importantly, it may introduce unphysical restrictions on the system symmetry. The method of Lagrange overcomes such difficulties. The method is based on the reasoning that if we wish our functional I, subject to constraints J, to be stationary then we require both the variation of I, δI, and the constraint δJ to be zero. Therefore addition of δJ to δI does not modify it.

To illustrate the method of Lagrange consider a function $F = F(u_1, ..., u_n)$ constrained by $G = G(u_1, ..., u_n) = c$, where c is a constant. We require both functions to be stationary at the extremum,

$$dF = \sum_{k=1}^{n} \frac{\partial F}{\partial u_k} du_k = 0 \quad \text{and} \quad dG = \sum_{k=1}^{n} \frac{\partial G}{\partial u_k} du_k = 0. \tag{6.16}$$

Because F is constrained du_k is not arbitrary and the condition $\frac{\partial F}{\partial u_k} = 0$ for $k = 1, ..., n$ is not sufficient. However, since $dG = 0$ is satisfied everywhere (because c is constant) the equation

$$dF + \lambda dG = 0 \tag{6.17}$$

is true. Where λ is a *Langrange undetermined multiplier*. The ingenious method of Lagrange is to 'eliminate' the dependence on, for example, u_n, indirectly by setting λ such that

$$dF_n + \lambda dG_n = 0. \tag{6.18}$$

Here

$$dF_n = \frac{\partial F}{\partial u_n} du_n \quad \text{and} \quad dG_n = \frac{\partial G}{\partial u_n} du_n. \tag{6.19}$$

Now the system consists of $n + 1$ equations

$$dF_k + \lambda dG_k = 0 \quad \text{for} \quad k = 1, ..., n \tag{6.20}$$

and

$$G = c. \tag{6.21}$$

The variational problem has retained n dependent variables u_k all of which can be chosen arbitrarily (and are therefore still free), but we also have 1 extra degree of freedom λ. The concept is easily generalised to many constraints and results in a free variational problem of $n + m$ degrees of freedom. Instead of solving $\delta F = 0$, the procedure is to solve the equivalent $\delta F^* = 0$ where $F^* = F + \lambda f$. It is not necessary but often the Lagrange multiplier λ has physical meaning.

The use of Lagrange multipliers is demonstrated with the simplest system of a constrained functional,

$$I = \int_a^b F(x, y, y')dx, \tag{6.22}$$

with constraints on possible solution curves y

$$y(a) = \alpha, \quad y(b) = \beta, \quad J = \int_a^b G(x, y, y')dx. \tag{6.23}$$

We can apply a constant λ such that the curve $y = y(x)$ yields a stationary point of the functional,

$$I^* = \int_a^b F(x, y, y')dx + \lambda \int_a^b G(x, y, y')dx \tag{6.24}$$

because (using commutation of the variation with the integral)

$$\int_a^b (\delta F(x, y, y') + \lambda \delta G(x, y, y')dx) = 0, \tag{6.25}$$

that is to say, using the general solution (Equation 6.15)

$$\left\{ \frac{\partial F}{\partial y} - \frac{d}{dx}\left(\frac{\partial F}{\partial y'}\right) + \lambda \left[\frac{\partial G}{\partial y} - \frac{d}{dx}\left(\frac{\partial G}{\partial y'}\right) \right] \right\} = 0. \tag{6.26}$$

Such problems with auxiliary constraints that are definite integrals are called *isoperimetric* problems [99, chap. 4] and are the most commonly encountered in quantum mechanics.

6.2 Quantum Mechanics

The calculus of variations have found wide use across many areas, in many regards the calculus of variations is a "unifying mathematics" [96]. As we shall see, the field of quantum mechanics has benefited greatly from the developments in the calculus of variations.

6.2.1 Schrödinger's Wave Equation

We start our discussion of quantum mechanics with the famous Schrödinger equation

$$H\Psi = E\Psi \tag{6.27}$$

where

$$H = \sum_{i=1}^{N}(-\frac{1}{2}\nabla_i^2) + \sum_{i<j}^{N}\frac{1}{r_{ij}} + \sum_{i=1}^{N} v(\mathbf{r}_i) \quad \text{with} \quad v(\mathbf{r}_i) = \frac{Z_\alpha}{r_{i\alpha}} \tag{6.28}$$

is the total energy operator, the Hamiltonian for the electronic system, and $\Psi = \Psi(\mathbf{x_1}, \mathbf{x_2}, ..., \mathbf{x_N})$ is the *wave function* on account of it being a solution to a second order linear *wave equation* (an equation of the form $\partial u/\partial t = \partial^2 u/\partial x^2$), and E is the electronic energy. More concisely,

$$H = T + U + V \tag{6.29}$$

where

$$T = \sum_{i=1}^{N}(-\frac{1}{2}\nabla_i^2) \tag{6.30}$$

is the electron kinetic energy operator,

$$U = \sum_{i<j}^{N}\frac{1}{r_{ij}} \tag{6.31}$$

is the electrostatic repulsion potential energy function, and

$$V = \sum_{i=1}^{N} v(\mathbf{r}_i) \tag{6.32}$$

is the electron-nucleus potential energy function (usually referred to as the 'external potential'). Here, and throughout this Chapter we have used atomic units to describe the Hamiltonian system[4].

6.2.2 The Variational Principle of Quantum Mechanics

The most prevalent physical result used in conjunction with the methods of variation described above is the *Variational Principle* of quantum mechanics. It establishes a lower bound on the energy - a result that will be

[4]Specifically, we have used *Hartree atomic units* in which the mass of an electron, the charge of an electron, the Bohr radius, and the unit of atomic energy (au) are all normalised to 1.

used many times in the following work and therefore treated here. From the elementary theorem of linear differential equations [100, chapter 3, p 85] that the general solution of an linear differential equation may be written as a linear combination of the complete set of all particular solutions - "the superposition of solutions" , thus the *total* wave function may be written

$$\Psi = \sum_n c_n \psi_n \tag{6.33}$$

where each ψ_n is a solution (eigenstate) to Equation 6.27, and for normalised wavefunction

$$\sum_n |c_n|^2 = 1. \tag{6.34}$$

The expection value is now re-written

$$\langle \hat{H} \rangle = \langle \psi | \hat{H} | \psi \rangle \tag{6.35}$$

$$= \langle \sum_m c_m \psi_m | \hat{H} | \sum_n c_n \psi_n \rangle \tag{6.36}$$

$$= \langle \sum_m c_m \psi_m | \sum_n c_n H \psi_n \rangle \tag{6.37}$$

$$= \langle \sum_m c_m \psi_m | \sum_n c_n E_n \psi_n \rangle \tag{6.38}$$

$$= \sum_m \sum_n c_m^* c_n E_n \langle \psi_m | \psi_n \rangle \tag{6.39}$$

using orthonormality $\langle \psi_m | \psi_n \rangle = \delta_{mn}$

$$\langle \hat{H} \rangle = \sum_n |c_n|^2 E_n \tag{6.40}$$

If the eigenvalue E_n is replaced by the ground state eigenvalue $E_\circ$, the inequality

$$\langle \hat{H} \rangle \geq \sum_n |c_n|^2 E_\circ = E_\circ \sum_n |c_n|^2 \tag{6.41}$$

is produced. Finally, using normalisation [101]

$$\langle \hat{H} \rangle \geq \sum_n |c_n|^2 E_\circ = E_\circ. \tag{6.42}$$

In other words,

$$E_\circ \leq \int \psi \hat{H} \psi d\mathbf{r} \tag{6.43}$$

Equation 6.43 defines a lower limit for the energy, and any trial wavefunction can itself be used as the upper bound. Thus a variational search can be undertaken by varying the wavefunction ψ until we reach a minimum energy. This result would be more aptly named the *minimum energy principle*.

6.2.3 A First Application of Calculus of Variations

The power of the calculus of variations described in the previous sections is first illustrated by finding the curves (in this case wavefunctions) that correspond to the minimum ground state energy of a quantum mechanical system described by Equation 6.27 with Hamiltonian Equation 6.29. The functional quantity we seek to minimise is the expectation value, $E = \langle\psi|\hat{H}|\psi\rangle$, from elementary quantum mechanics. We must constrain our solutions (wavefunctions) to be to be linearly independent to correctly satisfy superposition [100], and for convenience we use normalised solutions (especially useful in the statistical interpretation of a wavefunction where $\int |\phi|^2 d\tau = 1$). These two constraints are collected by the equation, $F = \langle\psi_m|\psi_n\rangle = \delta_{mn}$, where $\delta_{mn} = 0$ and $\delta_{mm} = \delta_{nn} = 1$.

The problem is clearly isoperimetric and is treated as follows. We define a constrained energy functional $I = E + \lambda F$

$$I[\psi] = \langle\psi|\hat{H}|\psi\rangle + \lambda\langle\psi_m|\psi_n\rangle \tag{6.44}$$

and apply a variation to the wavefunction conjugate ψ^*

$$I[(\psi + \delta\psi)^*] = \langle\psi + \delta\psi|\hat{H}|\psi\rangle + \lambda\langle\psi + \delta\psi|\psi\rangle \tag{6.45}$$

which when expanded gives

$$I[(\psi + \delta\psi)^*] = \langle\psi|\hat{H}|\psi\rangle + \lambda\langle\psi_m|\psi_n\rangle + \langle\delta\psi|\hat{H}|\psi\rangle + \lambda\langle\delta\psi_m|\psi_n\rangle \tag{6.46}$$

$$= I[\psi^*] + \langle\delta\psi|\hat{H}|\psi\rangle + \lambda\langle\delta\psi_m|\psi_n\rangle. \tag{6.47}$$

Using $\delta I[\delta\psi^*] = I[\psi + \delta\psi)^*] - I[\psi^*]$ we have

$$\delta I[\delta\psi^*] = \langle\delta\psi|\hat{H}|\psi\rangle + \lambda\langle\delta\psi_m|\psi_n\rangle \tag{6.48}$$

$$= \int \delta\psi^*\hat{H}\psi + \lambda\delta\psi^*\psi d\tau \tag{6.49}$$

$$= \int (\hat{H}\psi + \lambda\psi)\delta\psi^* d\tau. \tag{6.50}$$

Finally, using the definition of a functional derivative (6.11) we obtain,

$$\frac{\delta I}{\delta\psi^*} = \hat{H}\psi + \lambda\psi. \tag{6.51}$$

Recalling that the functional derivative vanishes at extrema we arrive at the Schrödinger equation $H\psi = -\lambda\psi$ where $-\lambda = E$, thus we can compactly write the Schrödinger equation as $\delta I = 0$. Each λ corresponds to an eigenstate of the system and by the minimum-energy principle [102, p.6], the curve that yields the minimum Lagrange multiplier is the ground state wavefunction and the Lagrange multiplier itself is the negative of the ground state energy. Thus, Equation 6.44, for a given number of electrons N and external potential $v(r)$, provides a way of obtaining the ground-state wavefunction $\overline{\Psi_\circ}$ from an initial guess $\overline{\Psi}$. The accuracy of the final solution is limited by the span of the function space from which the trial curves are selected - a larger set of trial wavefunctions will give better convergence to the true ground state wavefunction.

Asking how the trial wave function looks and how to vary it leads us to a brief discussion of the wave function methods, often referred to as Hartree/Hartree Fock (H/HF) methods.

6.2.4 The Wave Function Method(s)

The Hartree Fock method has been developed to very high level of complexity, however the basic concepts of the H/HF method is useful to understand as they introduce some of the general methodology, and also the

concept of correlation energy (E_{corr}). In following sections the wavefunction coordinates are denoted $\mathbf{x_i} = (\mathbf{r_i}, s_i)$ where $\mathbf{r_i}$ is the spatial coordinate in 3 dimensions and s_i is the spin coordinate which spans only two states, "spin-up" (α) and "spin-down" (β). The corresponding wavefunctions known as *molecular spin orbitals* [103] are assumed to be separable

$$\Psi(\mathbf{x_i}) = \Psi(\mathbf{r_i}, s_i) = \phi(\mathbf{r_i})\sigma(s_i). \tag{6.52}$$

The H/HF method aims to solve the many-body Hamiltonian by treating the electron-electron repulsion in a *mean field* fashion. It extends the elementary treatment of an independent electron to that of N independent electrons interacting with each other through only the average of electric fields produced by the other electrons. The distinction between the Hartree and the Hartree-Fock method is the latter's fulfilment of the anti-symmetry requirement

$$\Psi(\mathbf{x_1}, ..., \mathbf{x_i}, ..., \mathbf{x_j}, .., \mathbf{x_N}) = -\Psi(\mathbf{x_1}, ..., \mathbf{x_j}, ..., \mathbf{x_i}, ...\mathbf{x_N}) \tag{6.53}$$

of wavefunctions (the Pauli Principle [104, Chapter 17, p.332]) by exploiting the properties of a determinant to change sign if any two columns are interchanged, and to vanish if any two columns are the same. The resulting wavefunction is the anti-symmetrised product of the molecular spin orbitals. The drawback here is that an $N \times N$ matrix is required to hold the wavefunction.

The energy of the system composed of HF wavefunctions is obtained by taking the expectation value [102, p.7],[105, p.30],

$$E_{HF} = \langle \Psi_{HF} | \hat{H} | \Psi_{HF} \rangle = \underbrace{\sum_{k=1}^{N} H_k}_{electron-nulei} + \frac{1}{2} \underbrace{\sum_{i,j=1}^{N} (J_{ij} - K_{ij})}_{electron-electron} \tag{6.54}$$

where

$$H_k = \int d\mathbf{x} \psi_k^*(\mathbf{x}_1)[\tfrac{1}{2}\nabla^2 + v(\mathbf{x}_1)]\psi_k(\mathbf{x}_1) \tag{6.55}$$

describes independent electron interaction with the external field (generally due to the nuclei), and the *Coulomb integrals*

$$J_{ij} = \int d\mathbf{x_1} d\mathbf{x_2} \frac{1}{r_{12}} |\psi_i(\mathbf{x}_1)|^2 |\psi_j(\mathbf{x}_1)|^2 \tag{6.56}$$

describe the electron-electron repulsion that results from the mean field treatment. Finally the *exchange integrals*

$$K_{ij} = \int d\mathbf{x_1} d\mathbf{x_2} \frac{1}{r_{12}} \psi_i(\mathbf{x}_1)^* \psi_j(\mathbf{x}_1) \psi_i(\mathbf{x}_2)^* \psi_j(\mathbf{x}_2) \tag{6.57}$$

result from the antisymmetric nature of the Slater determinant. That is, they represent the cost of bringing electrons of parallel spin together. Application of the variational calculus to Equation 6.54 proceeds as described for the simple case with a few minor additional requirements such as the summation over all electrons. The variation of the unconstrained expectation integral E_{HF} is written [103] [5]

$$\delta E = \sum_i^N \int \delta\psi_i^* \left[H_i + \frac{1}{2} \sum_j (J_j - K_j)\psi_i \right] d\mathbf{x}. \tag{6.58}$$

The summation of the orthonormality constraints times the Lagrange multiplier is

$$\sum_{ij}^N \lambda_{ij} \int \delta\phi_i^* \phi_j. \tag{6.59}$$

Now the variation of the sum of the two functionals is

$$\delta I = \sum_i \int \delta\psi_i^* \left[H_i + \frac{1}{2} \sum_j (J_j - K_j)\psi_i - \sum_j \psi_j \lambda_{ij} \right] d\mathbf{x}, \tag{6.60}$$

from which it is clear that the stationarity condition $\delta I = 0$ is satisfied if

$$H_i + \frac{1}{2} \sum_j (J_j - K_j)\psi_i = \sum_i \psi_j \lambda_{ji}. \tag{6.61}$$

[5] As the electronic systems become more complex a more powerful formulation using *density martrices* is used (see [102, Chapter 2]).

This set of Euler-Lagrange equations are known as the Fock differential equations and are usually written

$$F\psi_i = \sum_j \psi_i \epsilon_{ji} \tag{6.62}$$

where F is the Fock operator (and $\epsilon_{ij} = \lambda_{ij}$)

$$F = H_i + \frac{1}{2}\sum_j (J_j - K_j). \tag{6.63}$$

The Fock differential equations require iterative solution since the operator, F, itself contains the wavefunctions ψ_i and ψ_j. The iterative method proceeds first by proposing a starting wavefunction that is used to calculate the electron interaction terms required to construct the Fock operator. The Fock differential equations are then diagonalised and solved. The resulting wavefunctions are used to update the Fock operator and solve the Fock equations until the wavefunctions cease to change. In this way self-consistency is reached.

The Hartree-Fock method captures exchange and Coulombic correlation, but due to the mean field approximation, error arises due to spontaneous interaction between electrons. This neglected correlation is called the correlation energy and can now be defined with respect to the HF energy

$$E_{corr} = E_{HF} - E_{exact} \tag{6.64}$$

where E_{corr} is the correlation energy, E_{HF} is the Hartree energy, and E_{exact} is the exact (unknown) electronic energy.

6.3 Electronic Density Functional Theory (DFT)

The density functional theory approach replaces the many variable wavefunction $\Psi(\mathbf{x_1}, \mathbf{x_2}, ..., \mathbf{x_N})$ where $\mathbf{x_i} = (\mathbf{r_i}, s_i)$ as the basic quantity with the 3 variable quantity, the electron density $\rho(\mathbf{r})$, and an associated calculational

scheme. The idea of using density was not new at the time of the first DFT breakthrough: the 1964 paper of Pierre Hohenberg and Walter Kohn. In a 1927 paper Llewellyn Thomas wrote [102, p. 47],[106]

> "Electrons are distributed uniformly in the six-dimensional phase space for the motion of an electron at the rate of two per h^3 of volume" and that there is an effective potential field that "is itself determined by the nuclear charge and the distribution of electrons"

This contains the most essential principle of DFT, that the electron density and external potential determine the electronic system. Thomas and Fermi established the following system to calculate the ground state energy of the electronic system [102]:

$$E_{TF}[\rho] = C_F \int \rho(\mathbf{r})^{5/3} d\mathbf{r} - \frac{1}{2}\int \frac{\rho(\mathbf{r})}{r} d\mathbf{r} + \frac{1}{2}\int\int \frac{\rho(\mathbf{r_1})\rho(\mathbf{r_2})}{|\mathbf{r_1} - \mathbf{r_2}|} d\mathbf{r_1} d\mathbf{r_2} \quad (6.65)$$

where $C_F \approx 2.871$

$$= T + V_{ne} + U_{ee}. \quad (6.66)$$

Here the first term is the kinetic energy functional written explicitly in terms of the density, the second term is a classical form for the electron-nuclear attraction, and the third term approximates the electron-electron repulsion. The minimum energy variation is contrained by the number of electrons with,

$$F = \int \rho(\mathbf{r}) d\mathbf{r} - N, \quad (6.67)$$

which ensures the electron density is consistent with the number of electrons. Now,

$$\delta \left\{ E_{TF} - \mu \left(\int \rho(\mathbf{r}) d\mathbf{r} - N \right) \right\} = 0 \quad (6.68)$$

which yields the Euler-Lagrange equation

$$\mu_{TF} + \frac{\delta E_{TF}}{\delta \rho(\mathbf{r})} = 0. \quad (6.69)$$

Because each term in the Thomas-Fermi energy functional E_{TF} is written explicitly in terms of the density, using the functional derivative definition (Equation 6.11) and its linearity (Equation 6.13), we can write the stationarity condition explicitly

$$\mu_{TF} = \frac{5}{3}\rho(\mathbf{r})^{2/3} + \frac{1}{r} - \int \frac{\rho(\mathbf{r}_2)}{\mathbf{r} - \mathbf{r}_2} d\mathbf{r}_2, \tag{6.70}$$

or where $v(\mathbf{r})$ is the electrostatic interaction associated with all electrons and nuclei,

$$\mu_{TF} = \frac{5}{3}\rho(\mathbf{r})^{2/3} + v(\mathbf{r}). \tag{6.71}$$

The formulation of Thomas and Fermi is drastically simplified and results in irreconcilable shortcomings such as an inability to describe chemical bonding [107] or to reproduce the density fluctuations about a nucleus due to electron shells [95]. The greatest amount of error comes from the approximate form of the kinetic energy functional, followed by the neglect of electron correlation and exchange.

Hohenberg and Kohn showed that the Thomas-Fermi functional is an approximation to an exact functional of an exact theory in which density is valid as the basic quantity. They did so using proof by *reductio ad absurdum* to show a one to one correspondence between the external potential $v(\mathbf{r})$ and the ground state density $\rho(\mathbf{r})$ [94]. Such a correspondence is sufficient because the number of electrons, N (a simple functional of the density), and the external potential $v(\mathbf{r})$ completely determine the electronic Hamiltonian and therefore the groundstate wavefunction Ψ (by the variational principle). Using the 1:1 correspondence, referred to as the first Hohenberg-Kohn Theorem (HK1), they recast the Thomas-Fermi energy functional into an exact form, illustrated by the following

$$E[\rho] = T[\rho] + U[\rho] + V[\rho] \tag{6.72}$$

or

$$E[\rho] = \int \rho(\mathbf{r})v(\mathbf{r})d\mathbf{r} + T[\rho] + U[\rho] \tag{6.73}$$

$$= \int \rho(\mathbf{r})v(\mathbf{r})d\mathbf{r} + F_{HK}[\rho] \tag{6.74}$$

where

$$F_{HK}[\rho] = T[\rho] + U[\rho] \tag{6.75}$$

is the Hohenberg-Kohn energy functional in which $U = J[\rho]$ plus an unknown non-classical term. All error has been collected in the *universal functional* (depends only on ρ) $F_{HK}[\rho]$, and we see that the Thomas-Fermi approximates this functional as $F_{TF}[\rho] = T_{TF}[\rho] + U_{TF}[\rho]$. Next, what is called the second Hohenberg-Kohn Theorem (HK2) is simply the statement of the variational principle for the density (rather than the wavefunction)

$$E_{HK}[\rho] = \int \rho(\mathbf{r})v(\mathbf{r})d\mathbf{r} + F_{HK}[\rho] \geq E[\rho_\circ] \tag{6.76}$$

with the stationarity condition

$$\delta \left\{ E_{HK}[\rho] + \mu \left(\int \rho(\mathbf{r}) - N \right) \right\} = 0 \tag{6.77}$$

yields the Euler-Lagrange equation

$$\mu = \frac{\delta E_{HK}[\rho]}{\delta \rho(\mathbf{r})} = \frac{\delta F_{HK}[\rho]}{\delta \rho(\mathbf{r})} + v(\mathbf{r}). \tag{6.78}$$

Not surprisingly there is strong resemblance to the form for the Thomas-Fermi variational condition except all inaccuracy has been moved to the HK functional F_{HK}.

The seminal work of HK had two limitations to its general employment. The first issue surrounded degeneracy of ground state wavefunctions - if they were degenerate the *reductio ad absurdum* proof (HK1) fails. The other limitation was associated with the variational scheme (HK2)

and was concerned with *v-representability*. A density is v-representable if it is associated with the groundstate anti-symmetric wavefunction of the Hamiltonian $H = T + U + V$ with an external potential $v(\mathbf{r})$ [102]. Such a condition is difficult to meet for a variational trial density. Both these limitations are overcome using Levy's constrained search method [108, 109].

If, having established a 1:1 correspondence between $\rho_\circ$ and $v(\mathbf{r})$, we wish to obtain $\Psi_\circ$ from $\rho_\circ$, another more robust and powerful justification for density as basic variable (the HK theorems) can be devised. Firstly, it is trivial to obtain $\rho_\circ$ from $\Psi_\circ$ by quadrature

$$\rho = \int |\Psi|^2 dr. \tag{6.79}$$

However, the reverse is certainly non-trivial because an infinite number of (non-ground state) wavefunctions could be combined to produce the ground state density. The Levy constrained search uses the minimum energy (variational) principle by noting that any wavefunction obtained from the ground state density must, like the density, conform to the variational principle,

$$E_{HK}[\rho_\circ] = \langle \Psi_{\rho_\circ} | \hat{H} | \Psi_{\rho_\circ} \rangle \geq \langle \Psi_\circ | \hat{H} | \Psi_\circ \rangle = E_\circ. \tag{6.80}$$

The external potential can be separated and disposed because it is a simple functional of the density yielding

$$\langle \Psi_{\rho_\circ} | \hat{T} + U | \Psi_{\rho_\circ} \rangle \geq \langle \Psi_\circ | \hat{T} + U | \Psi_\circ \rangle. \tag{6.81}$$

Thus, of the set of wavefunctions that give the ground state density $\rho_\circ(\mathbf{r})$, the ground state wavefunction is that which minimises $\langle T + U \rangle$. From Equation 6.75 we see that Levy devised a variational definition to acquire the Hohenberg-Kohn functional

$$F[\rho_\circ] = \langle \Psi_{\rho_\circ} | \hat{T} + U | \Psi_{\rho_\circ} \rangle = \min_{\Psi \to \rho_\circ} \langle \Psi | \hat{T} + U | \Psi \rangle = F_{HK}[\rho]. \tag{6.82}$$

This new density-wavefunction search is written

$$E_\circ = \min_\rho \left[F[\rho] + \int v(\mathbf{r}) \rho(\mathbf{r}) d\mathbf{r} \right] \tag{6.83}$$

in which there is an inner minimisation to obtain F as shown in Equation 6.82 and an outer one to obtain the ground state energy. The outer minimisation only need be done on N-representable densities, which need only be obtainable from an anti-symmetric wavefunction (c.f. v-representation requires association with the Hamiltonian and external potential also). Thus, a one to one mapping between the ground state wavefunction $\psi_\circ$ and the ground state density $\rho_\circ$ is achieved by selecting the wavefunction that delivers the energy minimising density by Equation 6.79. The v-representability condition is satisfied because the density is obtained from an anti-symmetric wavefunction, and the degeneracy problem is overcome as the variational method selects the wavefunction that yields the energy-minimising density.

The re-introduction of the wavefunction foreshadows the second great advance in the theory: the DFT of Kohn-Sham (KS) non-interacting *orbitals*. At the time of the Levy constrained search publication, the use of wave functions was well established in the KS DFT.

It is worth noting that the universal functional is universal because it is system independent. The system dependence arises exclusively from the external potential $\int \rho(\mathbf{r})v(\mathbf{r})d\mathbf{r}$. The precise form of the functional is non-trivial and remains the most challenging aspect of the development of the theory - perhaps not surprisingly as it can be thought to contain all the complexity associated with going from an N-variable problem to a 3 variable problem. More detail regarding the universal functional is given in Section 6.3.2.

6.3.1 Kohn-Sham DFT

Unfortunately, the DFT thus far has very little practical use as the form of the HK functional is unknown. In particular the form of the kinetic energy functional is still unknown. The celebrated work of Kohn and Sham overcame this limitation ingeniously and paved the way for DFT to be-

come a highly competitive quantum mechanics method when both accuracy and computational cost are at a premium. That the three most cited papers[95, 94, 110] in the Physical Review journal family are the DFT papers is testament to the importance of DFT. Like the HK theorems, the basis is surprisingly simple. The total energy functional is further decomposed in the following way

$$E = T_s + J + E_{xc} + \int \rho(\mathbf{r}) v(\mathbf{r}) d\mathbf{r} \tag{6.84}$$

where T_s is the kinetic energy operator for N *non-interacting* electrons, J is the electron-electron Coulombic repulsion (the fully classical Coulomb integral, Equation 6.56, defined earlier in the Hartree-Fock treatment), and E_{xc} is the error or remainder of the two approximations:

$$E_{xc} = T - T_s + U - J. \tag{6.85}$$

Where $T - T_s$ is the *correlation* and $U - J$ is the *exchange*. Such a decomposition helps to clarify the critical importance of the validity of the exchange correlation functional [6]. Seeking the minimum of this new total energy functional delivers an Euler-Lagrange equation in the now very familiar form

$$\mu = v_{eff}(\mathbf{r}) + \frac{\delta T_s}{\delta \rho(\mathbf{r})}. \tag{6.86}$$

where

$$v_{eff}(\mathbf{r}) = v(\mathbf{r}) + \int \frac{\rho(\mathbf{r}')}{|\mathbf{r} - \mathbf{r}'|} d\mathbf{r}' + \frac{\delta E_{xc}[\rho]}{\delta \rho(\mathbf{r})} \tag{6.87}$$

Kohn and Sham recognised that this is precisely the Euler-Lagrange equation expected for a system of N independent electrons acting in a potential $v_{eff}(\mathbf{r})$ rather than the single electron potential $v_s(\mathbf{r})$. As such, Equation 6.86 is satisfied by solving the single electron Hamiltonian

$$[-\tfrac{1}{2}\nabla^2 + v_{eff}(\mathbf{r})]\psi_i = \epsilon_i \psi_i \tag{6.88}$$

[6] However, in systems that are not highly correlated (e.g. non-magnetic systems) the influence of the E_{xc} is small.

for the N lowest energy eigenstates and evaluating the density from

$$\rho(\mathbf{r}) = \sum_{i}^{N} \sum_{s} |\psi_i(\mathbf{r}, s)|^2. \tag{6.89}$$

Because $v_{eff}(\mathbf{r})$ depends on the density through the exchange correlation term in equation 6.87 the system must be solved self-consistently. Equations 6.87, 6.88 and 6.89 are the Kohn-Sham orbital equations. The system closely resembles the Hartree-Fock system, but is computationally far less demanding (only N equations need to be solved) and is, in principle, exact.

6.3.2 The Exchange-Correlation Functional(s)

The approach of the last two sections - the HK and KS methods - has been to subtract out the easily computed terms and collect the remaining complexity in the exchange-correlation energy functional. We now address this aspect of the theory. In their 1965 paper, Kohn and Sham used what is now known as the local density approximation (LDA). The approximation is *local* in the sense that it uses a function to approximate the functional locally (at the coordinate of functional evaluation), in analogy to the Slater approximation to the difficult to compute *non-local* exchange functional: $(Vf)(\mathbf{r}) \rightarrow V(\mathbf{r})f(\mathbf{r})$. Thus the KS-LDA functional is

$$E_{xc}^{LDA}[\rho] = \int \rho(\mathbf{r})\epsilon_{xc}(\rho)d\mathbf{r} \tag{6.90}$$

which is entered into the KS scheme (Equation 6.88) by setting $v_{xc} = v_{LDA}$ from Equation 6.87 , where

$$v_{LDA} = \frac{\delta E_{xc}^{LDA}}{\delta \rho} = \left(\epsilon_{xc}(\rho) + \rho \frac{\delta \epsilon_{xc}(\rho)}{\delta \rho} \right)_{\rho=(\rho(\mathbf{r}))}. \tag{6.91}$$

Here exchange-correlation function $\epsilon_{xc}(\rho)$ used was that of the homogeneous electron gas [94]. The approach has been successful in practice

(especially for solids) despite treating exchange-correlation as if the density dependence is the same as for a homogeneous electron gas. The reason for this unexpected success is associated with a cancelling of error associated with exchange and correlation - the exchange-correlation hole due to Pauli's antisymmetry [102, 111]. Improvements to the treatment of molecules were found [112] by including a dependence on the density gradients also:

$$E_{xc}^{GGA}[\rho] = \int \rho(\mathbf{r})\epsilon_{xc}(\rho, \nabla\rho)d\mathbf{r}. \tag{6.92}$$

These (still local) functionals are called generalised gradient functionals (GGA) [110, 113, 114] and are now the most commonly used functionals. The GGA functionals are constructed by *constraint satisfaction* of the electron-hole exchange description [110],[113],[114], and the level of constraint applied to derive the function usually translates to greater computational cost and accuracy. The GGA constrain the density gradient, the meta-GGA [112] constrain the curvature, and higher level functionals use non-local approximations [112, 111]. The best results in terms of accuracy and computational efficiency require careful selection of an exchange correlation functional best suited to the problem of interest.

Finally, the most cutting edge work includes the development of fully *ab initio*, highly accurate orbital dependent random phase approximations (RPA) functionals [111] that capture long range Van der Wals interaction. However the computational cost due to the enormous basis sets (see Section 6.4.1) make such functionals impractical for present general use [112].

6.4 DFT Techniques

The previous section described the key theoretical concepts and quantities of DFT. In this section we introduce quantities that arise from an applied or computational focus.

6.4.1 Plane Waves

The first calculational development addresses the representation of the Kohn-Sham non-interacting orbitals from which the non-interacting wavefunction is constructed. DFT has been successfully applied - although is not limited to - solid or condensed systems. Solution of such problems requires resolution of the issues surrounding an infinite number of electrons extending over the entire system, and hence an infinite wavefunction basis set. These difficulties are overcome by applying Bloch's Theorem to periodic boundary conditions to yield wavefunctions defined by a discrete set of plane waves (PW),

$$u(\mathbf{r}, \mathbf{k}) = ae^{i\mathbf{k}\cdot\mathbf{r}}. \tag{6.93}$$

So successful is this method that DFT is now synonymous with the use of plane waves - the "Plane Wave Methods".

Bloch's theorem states [104] that the eigenstates of a one electron Hamiltonian, such as the KS Hamiltonian H_{KS}, where the external potential is periodic $V(\mathbf{r} + \mathbf{R}) = V(\mathbf{r})$ for all $\mathbf{R}$ in a Bravais lattice can be expressed as the product of a plane wave and a function, $f(\mathbf{r})$, possessing the periodicity of the Bravais lattice,

$$\psi_{m\mathbf{k}} = e^{i\mathbf{k}\cdot\mathbf{r}} f_{m\mathbf{k}}(\mathbf{r}). \tag{6.94}$$

Here the subscript m denotes the particular eigenstate, the wavevector $\mathbf{k}$ the position in reciprocal space, and $\mathbf{r}$ the real space coordinate.

Application of Bloch's theorem to the Born-Von Karman boundary condition [104] for 3-dimensional periodicity

$$\psi(\mathbf{r} + \mathbf{R}) = \psi(\mathbf{r}), \tag{6.95}$$

gives

$$\psi_{n\mathbf{k}}(\mathbf{r} + \mathbf{R}) = e^{i\mathbf{k}\cdot\mathbf{R}}\psi_{n\mathbf{k}}(\mathbf{r}). \tag{6.96}$$

Here

$$\mathbf{R} = \mathbf{a}_i N_i \quad i = 1, 2, 3 \tag{6.97}$$

$\mathbf{a}_i$ are the primitive cell lattice vectors and N_i are integers. Equation 6.96 provides the condition[7], $e^{i\mathbf{k}\cdot\mathbf{R}} = 1$, that determines the set of reciprocal lattice vectors $\{\mathbf{G}\}$ from the Bravais lattice vectors $\mathbf{R}$. The condition is satisfied when $\mathbf{G}\cdot\mathbf{R} = 2\pi n$ for integer n.

Because $f_{m\mathbf{k}}(\mathbf{r})$ is periodic it can be expanded as a set of plane waves

$$f_{m\mathbf{k}}(\mathbf{r}) = \sum_{\mathbf{G}} c_{m,\mathbf{k}+\mathbf{G}} e^{i\mathbf{G}\cdot\mathbf{r}} \tag{6.98}$$

The discrete nature is conferred to the wavefunction $\psi_{m\mathbf{k}}(\mathbf{r})$ by substituting Equation 6.98 into Equation 6.94

$$\psi_{m\mathbf{k}}(\mathbf{r}) = \sum_{\mathbf{G}} c_{m,\mathbf{k}+\mathbf{G}} e^{i(\mathbf{k}+\mathbf{G})\cdot\mathbf{r}}. \tag{6.99}$$

An infinite number of electrons is represented by an infinite number of k-points with finite wavefunction occupation. Thus Bloch's theorem changes the problem from one of calculating an infinite number of wavefunctions to that of calculating a finite number of wavefunctions over an infinite number of points. An infinite number of plane wave basis functions is required to exactly represent the true wavefunction, however, it turns out [115] that the coefficients $c_{m\mathbf{kG}}$ for the plane waves with low kinetic energy $\frac{1}{2}|\mathbf{k}+\mathbf{G}|^2$ are more important than those for high kinetic energy. The discrete nature of the plane wave wavefunction means that truncation of the high kinetic energy plane waves yields a finite basis set. Thus Bloch's theorem allows accurate representation of wavefunctions using a finite basis set. Finally, certain sets of k-points within the Brillouin zone make a greater contribution to the wavefunction and special schemes [116, 115] have been developed to identify such sets [8]. The kinetic energy cut-off, usually referred to simply as the *energy cut-off* must, along with the number of k-points (k-point grid), be converged with respect to the quantity of interest (e.g. the ground state energy).

[7] Using R to denote the set of $N_i a_i$ where $\{a_i\}$ constitute the Bravais lattice.

[8] The choice of scheme generally requires prior knowledge of electronic behaviour of the material.

Now, like the single electron Schrödinger equation in Bloch form, the KS equation takes the simple form called a *secular equation*

$$\sum_{\mathbf{G}'} \left\{ \tfrac{1}{2}|k+G|^2 \delta_{\mathbf{G}\mathbf{G}'} + V_{KS}(\mathbf{G}-\mathbf{G}') \right\} c_{m,\mathbf{k}+\mathbf{G}'} = c_{m,\mathbf{k}+\mathbf{G}} \epsilon_i \tag{6.100}$$

where $V_{KS}(\mathbf{G}-\mathbf{G}')$ is the Fourier transform of the Kohn-Sham effective potential Equation 6.87.

The exposition of the KS-DFT provided in the previous sections described an *indirect* minimisation of the total energy functional 6.86 using SCF iterative diagonalisation methods. The use of a plane wave basis for the wavefunction permits a *direct* minimisation of the Kohn-Sham energy functional by variation of the plane wave coefficients $c_{m,k+G'}$. The direct minimisation of the KS total energy functional has improved stability [115] because, unlike the system Hamiltonian, it usually has a single well-defined minimum. The Hamiltonian problem of multiple minima increases with system size.

Having established the ability to overcome the issues surrounding infinite system size, we can note other advantages of the plane wave basis set over a localised basis set (such as Slater or Gaussian functions): (i) the same basis set can be used for all atomic species, (ii) convergence is easily tested, and (iii) plane waves are independent of nuclear positions and hence need not be corrected for force calculation (see Section 6.4.3). There is however, a major drawback to the use of a plane wave basis set to represent the electronic wavefunctions; a plane wave basis set must be very large to accurately represent the fluctuations of the core shell electrons. This problem can be ameliorated by the use of *pseudopotentials*.

6.4.2 Pseudopotentials

The oscillations of core electrons require a large plane wave basis set to be represented accurately, yet play little role in chemical bonding and solid state properties. The pseudopotential approximation alleviates the cost associated with the core by replacing the strong ionic potential with a weak

pseudopotential and the core electrons with a smoothly varying pseudo-wavefunction as shown in Figure 6.1.

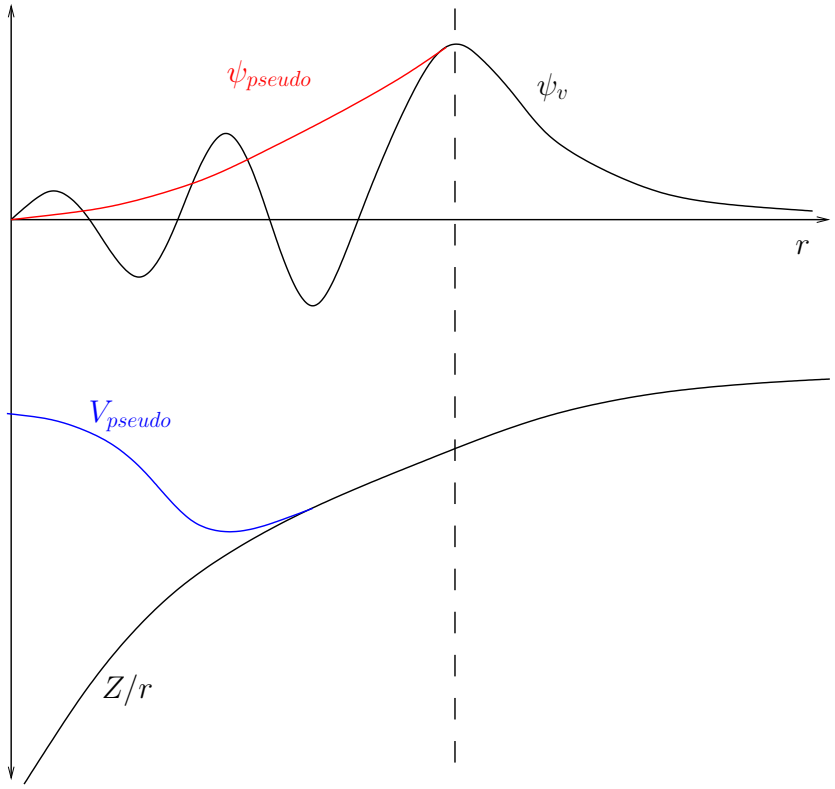

Figure 6.1: Schematic of the pseudo wavefunction (upper), and the pseudopotential (lower).

A suitable pseudopotential must [117] yield the same energy as the all electron KS-DFT result, and the pseudopotential wavefunction must be identical, within acceptable error, to the all-electron wavefunction above the core radius. Finally, the pseudo charge and the true core charge must be the same - a condition known as *norm-conservation*. Pseudopotentials are usually constructed so that the scattering properties of the pseudo wavefunctions are the same as the ion and the core part of the true valence wavefunction, yet also have no radial nodes within the core region. The ultrasoft-pseudopotential [115] and projector augmented wave (PAW)

[115] methods are related methods.

6.4.3 Structure Optimisation

One of the most fundamental applications of DFT is to find an optimised (lowest energy) structure for a solid, molecule, or surface. To find optimal structure a method of moving the ions must be used. It is a problem of finding a minimum on a $3N$ dimensional space. The method of conjugate gradients and the method of direct inversion of iterative subspace (DIIS) are the most robust [115, 102] methods. Structure optimisation using forces is less likely to find the global minimum compared to energy [117]. However, in our experience, the success and speed of the structure optimisation is often greater. To move the ions we consider the forces that arise from the derivative of the total energy with respect to the ion positions - these are the Hellmann-Feyman forces. The motion of the ions is separable from that of the electrons according to the Born-Oppenheimer principle, thus the electronic and atomic relaxations are alternated until the Hellmann-Feynman forces vanish.

6.4.4 Supercells

The supercell method was devised for simulation of surfaces, defects, and molecules or finite solids. The use of plane waves is ideally suited to materials that possess periodic structure such as crystals, however, the benefits are not limited to structures with implicit periodicity. By setting up the structure of the unit cell the advantages of a plane wave basis set can be applied to non-periodic or finite structures such as surfaces, melts, crystal defects, and even molecules which possess no periodicity. The method is to build the structure of interest as a *supercell* (see Figure 6.2).

When using supercells we must ensure that the artificial periodicity is not influencing the result - we must ensure that the quantity of interest is converged with respect to the non-periodic parameters. For example

in the case of a surface (see Figure 6.2a), the supercell is constructed by repetition of the bulk unit cell and addition of an empty space adjacent to the surface of interest. The size of the empty space must be great enough to minimise the interaction between the periodic images of the truncated surface, and the thickness of the slab must be great enough that the core experiences a bulk like environment.

There is some efficiency cost associated with evaluating the wavefunction in the empty space, however such cost can be minimised by using minimal k-points in the aperiodic region, and is usually outweighed by the effecincy gains of the plane wave method.

6.4.5 VASP DFT Code

Throughout this work we have used the Vienna Ab initio Simulation Package (VASP) [118, 119, 120, 121] with ultrasoft pseudo potentials [122], as supplied by G. Kresse and J. Hafner [123] to perform quantum mechanical calculations using the DFT formalism.

6.4.6 Computing

Execution of DFT calculations is almost always done using parallel computation. The reason being that a single computer has insufficient memory and processor speed to solve the KS equations of a system in a reasonable time. Parallelisation require the calculation to be decomposed into smaller parts (e.g. bands of planes waves) which are passed out to individual computers (nodes). Each node works on its part and communicates its results, either directly or through a central node, to the others via a message passing protocol.

A very common platform is the Beowulf cluster in which standard personal computers using a UNIX based operating system are connected to a central master computer. The performance of the cluster depends on the computer specifications (CPU and memory), and the communication

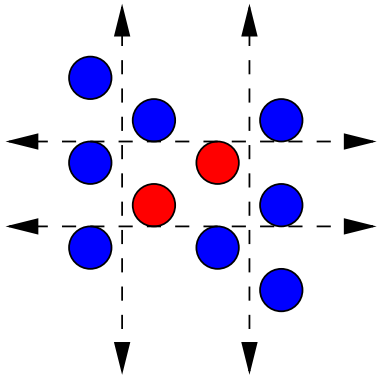

(a) Periodic boundaries applied to a single bulk unit cell.

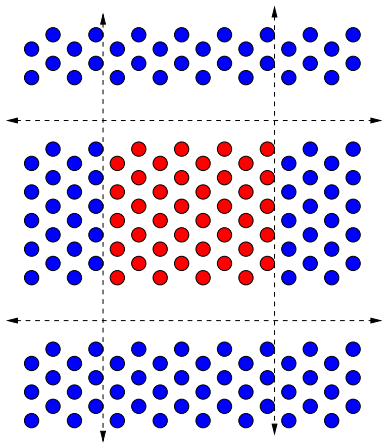

(b) A supercell used to represent a surface constructed by repetition of the bulk unit cell and addition of empty space to produce a truncated surface.

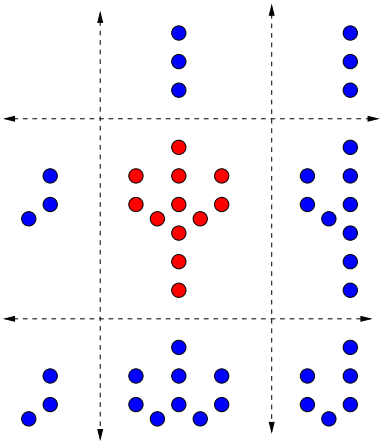

(c) A molecular supercell 'psianide' which itself has no periodicity

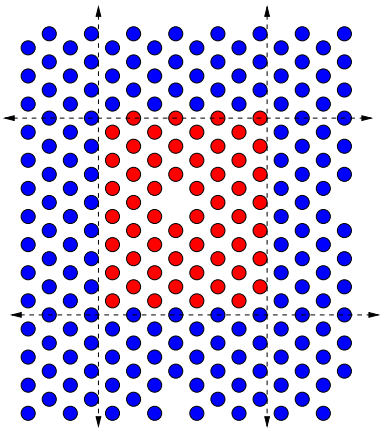

(d) Supercell representation of a point defect in a crystal.

Figure 6.2: Aperiodic structures can be expressed as a 'crystal' of supercells containing empty space in the aperiodic directions.

speed (ethernet speed). Much of the work presented here was performed on this kind on machine.

Some of our calculations were also carried out on an IBM BlueGene (BG/L) machine. The BlueGene series of machines are said to represent a new paradigm in supercomputing. BlueGene machines are 'massively parallel', they consist of a central control node, and thousands of astonishingly low-specification work nodes. By low spec we mean dualcore 700 MHz PowerPC processors, and 512 MB/2cpu in memory, compared with a generic office desktop machine in early 2008 with dual-core 3.06 GHz processors, and 2 GB/2cpu in memory. The use of low specification nodes is balanced by the use of incredibly fast communication. The BG/L uses a high performance, low latency bi-directional serial computer-bus interconnect called 'Infiniband' which provides a theoretical maximum data rate of nearly 10 times that of GigaBit ethernet.

6.5 Summary

The material described in the preceding sections is sufficient to understand the key methods and quantities of DFT, and provides a satisfactory basis to begin using DFT. Variational techniques feature very strongly in all aspects of the development of the theory and also in the techniques used to optimise the application of the theory. The use of DFT is especially widespread in the scientific literature due to its superior speed in tackling large systems. DFT is interesting in that it has the potential to be exact, however, devising or discovering the exact exchange-correlation functional is very difficult.

Chapter 7

A Study of ZnO Using DFT

7.1 Introduction

In this chapter we investigate the nature of the crystal faces that make up the hexagonal nanorods which compose the electrochemically grown ZnO films using quantum mechanical calculations. This work represents a first treatment of the very difficult problem of predicting macroscopic materials behaviour from first principles, on a very complicated experimental electrochemical system. Nonetheless, we have developed a method that uses total energies calculated using DFT to parameterise both equilibrium and kinetic crystal growth models, to predict growth trends as a function of constituent chemical potentials. We first develop the model, then illustrate how the surface free energies are obtained, and finally use the model to predict the dependence of the growth morphology of ZnO crystals on the chemical environment, from these calculations.

The DFT-thermodynamic formalism and crystal growth theory are expounded in Sections 7.3 and 7.4, respectively. The key crystal growth parameters and their relation to a the kink free energy and DFT-thermodynamic formalism is discussed in the later part of Section 7.4.2. The remaining sections contain the calculations and procedures required to paramterise the DFT-thermodynamic-crystal growth formulation. The bulk unit cell

is converged and studied in Section 7.5. The bare polar and non-polar surface energies are studied in Section 7.6, and the hydrated surfaces in 7.7. Section 7.7 culminates in a series of surface stability, and equilibrium growth shape analyses, using the DFT-thermodynamic formalism introduced in Section 7.3. Finally, the DFT calculations, and thermodynamic analyses are extended to kinetic growth shapes in Section 7.8.

7.2 Zinc Oxide

Zinc oxide (ZnO) has a hexagonal crystal structure and belongs to the $P6_3mc$ (B4, #186) point group[1] commonly called *wurtzite*. X-ray measurements confirm that the ZnO nano-rod crystallites grown electrochemically possess the wurtzite crystal structure [6]. The ZnO wurtzite cell is characterised by the primitive cell vectors

$$\vec{a}_1 = \tfrac{1}{2}a\hat{x} - \tfrac{\sqrt{3}}{2}a\hat{y} \tag{7.1}$$

$$\vec{a}_2 = \tfrac{1}{2}a\hat{x} + \tfrac{\sqrt{3}}{2}a\hat{y} \tag{7.2}$$

$$\vec{a}_3 = c\hat{z} \tag{7.3}$$

where $a = 3.250$ Å, $c = 5.207$ Å[124]. The primitive cell contains two ZnO units with atomic positions

$$\text{Zn(1), Zn(2)} \quad (1/3, 2/3, 0), (2/3, 1/3, 1/2) \quad z = 0 \tag{7.4}$$

$$\text{O(1), O(2)} \quad (1/3, 2/3, u), (2/3, 1/3, u + 1/2) \quad \text{where } u = 0.3825 \tag{7.5}$$

as shown in Figure 7.1a. The key parameters when discussing hexagonal crystals are a, c, and u. A useful way to view the wurtzite structure is to observe its layered arrangement along the c-axis. When viewed this way we see that the structure consists of alternating layers of four-fold coordinated

[1] Pearson m: monoclinic, c: cubic, denotation indicates a screw axis with 6 nodes and 3-fold symmetry. Rotation by 30° followed by translation to next layer yields an equivalent position.

Zn^{2+} and O^{2-}. The inter-layer distance also alternates with $R_1 = 0.61$ Å and $R_2 = 1.99$ Å as shown in Figure 7.1b. Ball and stick models, shown in

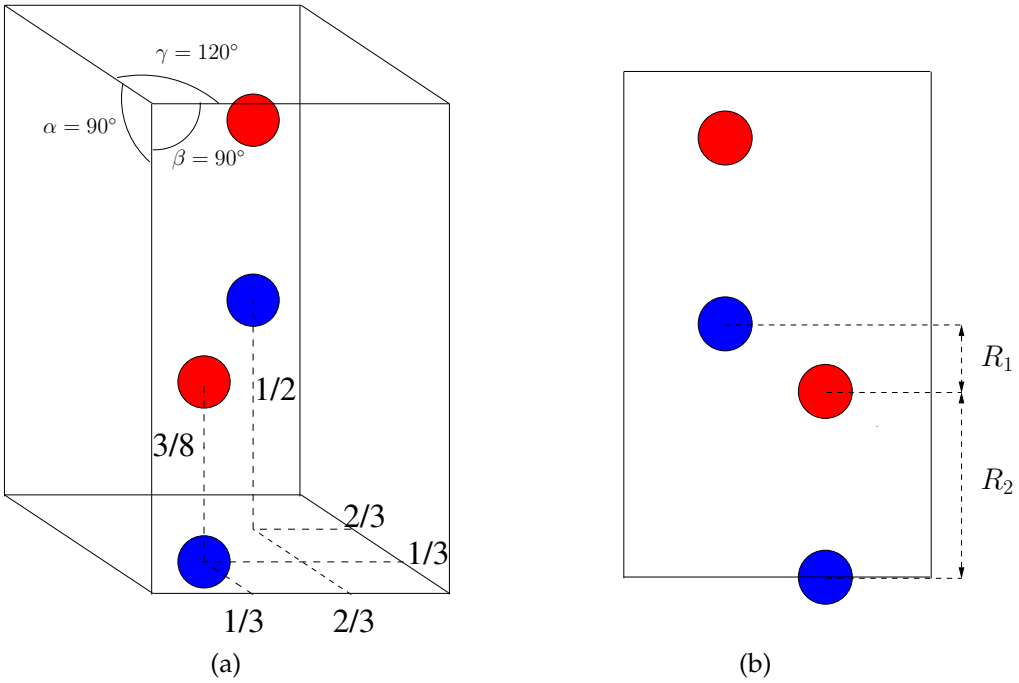

Figure 7.1: Schematics showing the typical parameters used to characterise the ZnO wurtzite crystal structure. (a) ZnO wurtzite unit cell in terms of fractional coordinates and angles α,β,γ. Red - oxygen, blue - zinc. (b) ZnO wurtzite unit cell showing R_1 and R_2.

Figure 7.2, give a clearer view of the geometric arrangement of the atoms in the two lowest index facets of ZnO wurtzite.

Crystal growth shape depends on which crystal facets control growth and which predominate in the final crystallite. In the case of electrochemically formed ZnO crystallites [6, 9] only hexagonal prismatic (hexagonal columns) crystallites with sharp edges are formed. The two extreme cases of very large aspect ratio and very small aspect ratio have been observed as shown in Figure 7.3. With such a morphology it is trivial to determine the identity of the crystallite facets exposed by the electrochemically formed

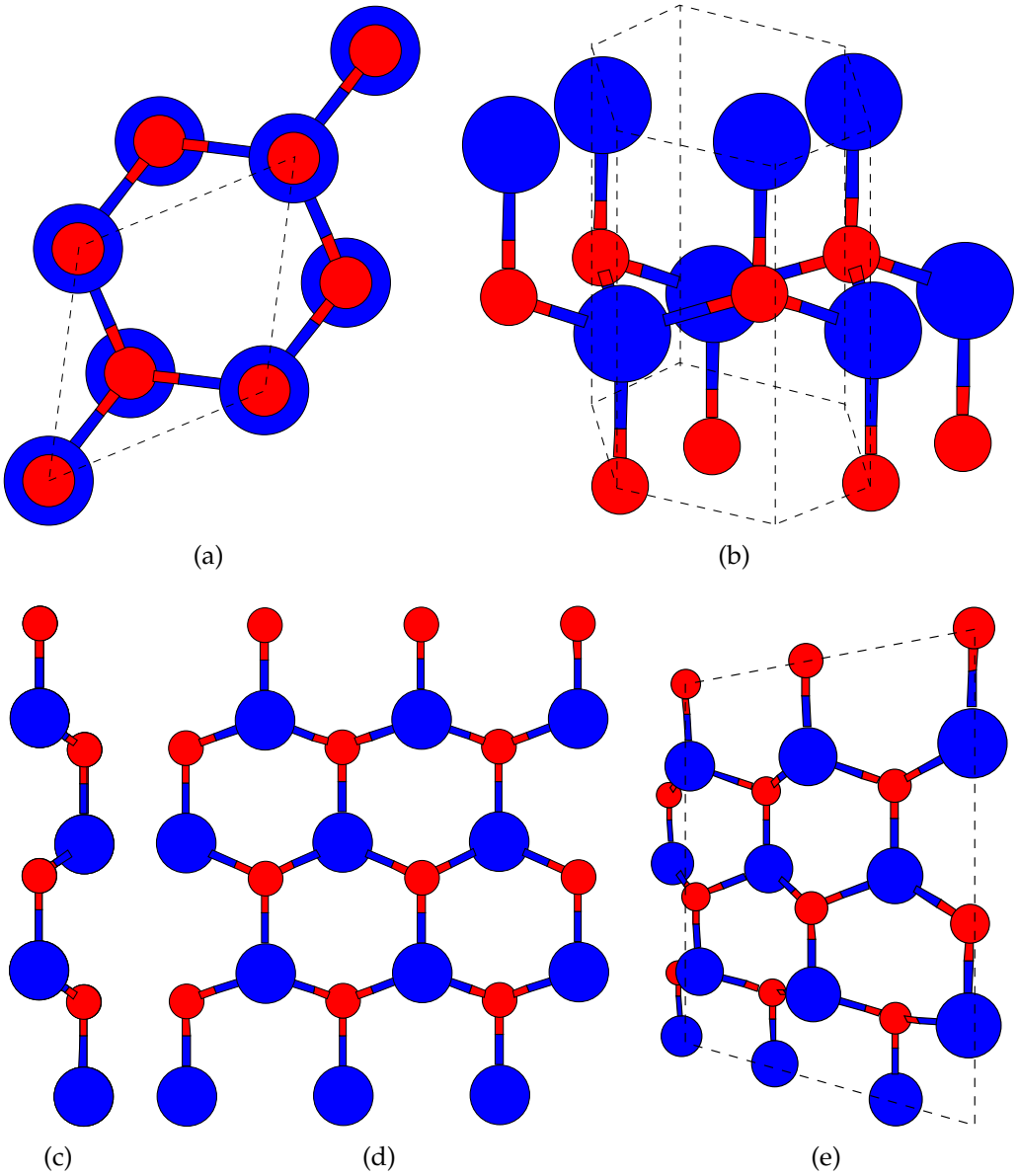

Figure 7.2: Ball and stick representations of the wurtzite low index facets (here the small red circles represent O and the larger blue circles represent Zn): (a) Top view where dashed line indicates the unit cell, (b) perspective view illustrating the hexagonal prism structure, (c) profile view of a lateral facet, (d) planar view of a lateral facet, (e) perspective of lateral facet (here the dashed line is used to emphasise perspective).

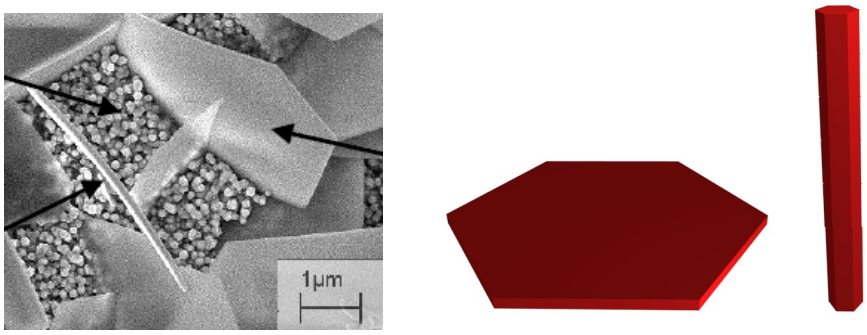

(a) (b) (c)

Figure 7.3: Morphological difference observed in electrochemical deposition: (a) An SEM image showing the two extreme morphologies (b) the large aspect ratio, and (c) the small aspect ratio.

crystallites. The lateral planes of the hexagonal nano-rods are identified as the $\{10\bar{1}0\}$ facets[2]. The non-polar nature and symmetrical equivalence can be seen by looking at the arrangement of atoms on the surface of a unit hexagonal prism shown in Figure 7.4. It can also be seen from Figure 7.4 that the basal planes (the top and bottom planes) are polar and not chemically equivalent.

Cleavage of ZnO wurtzite normal to the c axis exposes the two chemically and physically distinct surfaces [125, p. 146]). A positively charged $(0001) - \text{Zn}$ surface is exposed on one side, and a negatively charged $(0001) - \text{O}$ on the other. Thus ZnO wurtzite is referred to as a *polar* crystal. The finite truncated crystal consists of a repeated stack of layers with non-zero dipole parallel to the surface normal. Such a surface is often called a Tasker type 3 surface [126]. The stacking of dipole layers in type 3 surfaces leads to a non-zero electric field[3] and the electrostatic potential increases

[2]Hexagonal crystals are usually denoted using 4 indices, $(h, k, -(h+k), l)$. Equivalent facets are denoted with curly braces '{}'

[3]the mean electric field is $\bar{\mathscr{E}} = 2\pi\sigma$, where σ is the layer charge density.

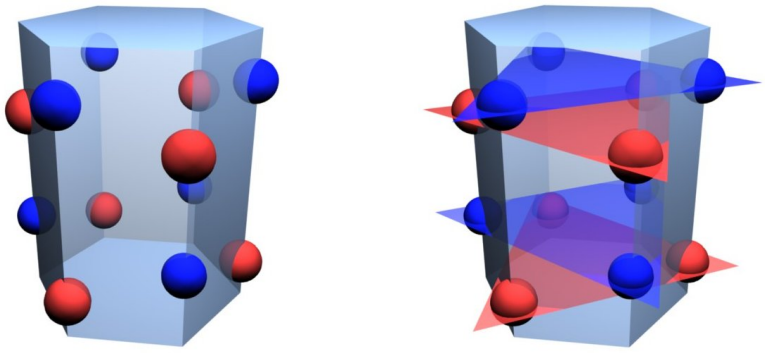

(a) (b)

Figure 7.4: Schematic representations of atom arrangement in ZnO wurtzite. Zn - blue, O - red. (a) illustrates the atom arrangement in terms of the hexagonal prism, (b) emphasises high index polar planes (b) indicates the polar nature of the basal planes.

monotonically with increasing slab thickness[4] [127]. In the absence of any charge compensation the electrostatic energy that contributes to the surface energy,

$$E_{surface} = 2\pi\sigma^2 R_1 N, \tag{7.6}$$

where σ is the layer charge density, diverges to infinity in the macroscopic limit. The concept of a surface Madelung constant is not applicable as the electrostatic potential varies from layer to layer for all layers [128]. However, polar surfaces are abundant in nature, and hence some stabilisation process is at play. Electrostatic arguments [127] show that the formation of a counter-field can stabilise the surfaces by cancellation of the macroscopic dipole. The counter-field is produced[5] if the Zn-terminated surface is less positive and the O-terminated surface is less negative by a factor of $R_2/(R_1 + R_2) \sim 0.75$ or $R_1/(R_1 + R_2) \sim 0.25$, illustrated in Figure 7.5.

[4] $\delta V = 4\pi\mu = 4\pi\sigma R_1$, thus $V = 4\pi\sigma R_1 N$

[5] Total dipole moment $M = N\sigma R_1$, and the condition for cancellation of macroscopic dipole $\sum_{j=1}^{m} \sigma_j = -\frac{\sigma_{m+1}}{2}\left[(-1)^m - \frac{R_2 - R_1}{R_2 + R_1}\right]$, i.e. $\sigma' = \sigma R_1/(R_1 + R_2)$

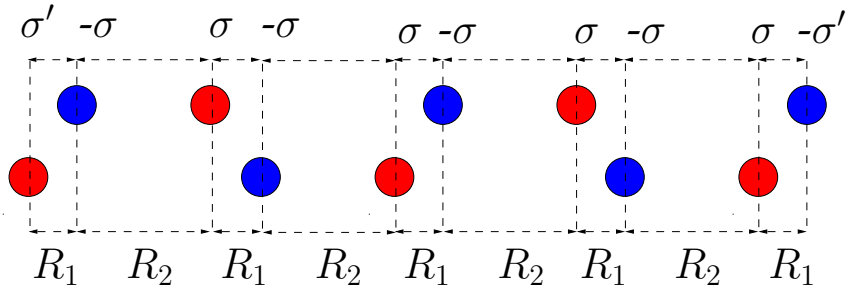

Figure 7.5: Schematic showing layered structure and surface charge modification required to cancel macroscopic dipole. Here $\sigma' = 0.25\sigma$.

There are three main classes of charge compensation identified in the surface science literature [127], [129]: charge transfer from the negative to the positive surface, surface reconstruction (including vacancy formation by desorption of surface atoms), and chemical interaction with adsorbates. The predominant stabilisation mechanism depends strongly on the physical-chemical environment of the crystal [129].

7.3 DFT and Thermodynamics

In 2001 Scheffler and Reuter published a seminal paper [130] outlining a method to relate thermodynamics to DFT total-energy calculations and coined the phrase 'First Principle Statistical Mechanics'. It is this method we have adopted to our analysis of the ZnO surfaces. The approach was described for RuO_2 in an oxygen atmosphere, but is easily generalised to any M_xO_y in a heterogeneous vapour environment.

The surface free energy is defined

$$\gamma_{hkl}(T,p) = \frac{1}{A}\left[G(T,p,\{N_i\}) - \sum_i N_i\mu_i(T,p)\right] \tag{7.7}$$

where $G(T,p,\{N_i\})$ is the Gibbs free energy of a truncated crystal at pressure p, the second term is the stoichiometric sum of the chemical potentials

per atom of the elements that make up the truncated crystal, or 'slab', at their given partial pressures (i.e. N_i is the number of atom i in the slab), and A is the area of the truncated face. Throughout this work we define the chemical potential, μ_i, per atom rather than per mole. The Gibbs free energy of the slab is defined as the sum of the internal energy, an entropy term, and a pressure-volume term.

$$G(T, p, \{N_i\}) = E(\{N_i\}) - TS + pV \tag{7.8}$$

The internal energy , $E(\{N_i\})$, is easily calculated using DFT as a total energy calculation, and is equal to the Gibbs free energy at zero temperature and pressure. For low temperatures the entropy S can be estimated by calculating the phonon spectrum and using the quasi-harmonic approximation for the free energy [131]. Scheffler *et al* [130] did exactly that and found the $-TS$ and pV terms to be very small ($O(\text{meV}/\text{Å}^2)$) compared to the difference between surface reconstructions ($>$ meV/Å^2).

Having established the validity of the internal energy as a representation of the Gibbs free energy it is possible to use DFT total energies in a thermodynamic equilibrium description of the crystal surface. For the case of hydrated ZnO we expand the summation in Equation 7.7 and write the surface free energy of the hydrated surface as

$$\gamma_{hkl} = E_{slab}(N_{Zn}, N_O, N_H) - N_{Zn}\mu_{Zn} - N_O\mu_O - N_H\mu_H. \tag{7.9}$$

Under this approximation, the slab structure that minimises the surface free energy for the given constituent chemical potentials μ_{Zn}, μ_O and μ_H is the most stable configuration, and in this way a phase diagram can be constructed from first principles calculations. Equilibrium constraints are applied to reduce the degrees of freedom. For a large enough slab the oxide acts as a reservoir, thus

$$\mu_{Zn} + \mu_O = g^{bulk}_{ZnO}(T, p) = E_{ZnO}. \tag{7.10}$$

This allows Equation 7.9 to be written in terms of the experimental vari-

ables μ_H and μ_O or μ_{Zn},

$$\gamma_{hkl} = E_{slab}(N_{Zn}, N_O, N_H) - N_{Zn}E_{ZnO} - (N_O - N_{Zn})\mu_O + N_H\mu_H, \quad (7.11)$$

which in the absence of H, and when $N_{Zn} = N_O$, is simply

$$\gamma_{hkl} = E_{slab}(N_{Zn}, N_O) - N_{Zn}E_{ZnO}. \quad (7.12)$$

If the slab is not permitted to relax structurally, then γ_{hkl} is the cleavage energy.

The chemical potential of O and H are related to the macroscopic experimental variables of the molecular gases by,

$$\mu_H = \tfrac{1}{2}\mu_{H_2}; \quad \mu_O = \tfrac{1}{2}\mu_{O_2}. \quad (7.13)$$

We are interested in the aqueous system and ensure the presence of water by applying the equilibrium relation,

$$\mu_{H_2} + \tfrac{1}{2}\mu_{O_2} = \mu_{H_2O}, . \quad (7.14)$$

Thus, the vapour consists of molecular hydrogen, oxygen, and water, in equilibrium with one another. The equilibrium (7.14) is used to eliminate the O dependence in Equation (7.11) giving,

$$\begin{aligned}\gamma^{hyd}_{hkl}(\{N_i\}, \mu_{H_2O}, \mu_H) = E_{slab} - N_{Zn}E_{ZnO} + (N_{Zn} - N_O)\mu_{H_2O} \\ + (2N_O - 2N_{Zn} - N_H)\mu_H.\end{aligned} \quad (7.15)$$

Equation 7.15 describes the surface free energy in a heterogeneous gas environment containing H_2, O_2, and H_2O.

Construction of a valid phase diagram (here in terms of μ_H and μ_{H_2O}) requires application of some thermodynamic constraints. We restrict ourselves to the chemical potentials where the surface is stable, thus, we investigate the chemical potentials below that of the ideal gases using

$$\Delta\mu_H = \mu_H - \tfrac{1}{2}E_{H_2} \quad \text{where} \quad \Delta\mu_H < 0, \quad (7.16)$$

and

$$\Delta\mu_{H_2O} = \mu_{H_2O} - E_{H_2O} \quad \text{where} \quad \Delta\mu_{H_2O} < 0, \tag{7.17}$$

to map the phase diagram domain. In this work the chemical potential of the ideal gases are represented by the internal energy calculated using DFT.

Finally, we note some features of the surface free energy defined by Equation (7.15). The situation in which $N_{Zn} - N_O = 0$ and $N_H \neq 0$, corresponds to a protonated surface. In our studies we have only permitted such surfaces to be made by protonation of the terminal O atoms. Neutral surfaces are those in which the net charge represented by $2N_O - 2N_{Zn} - N_H$ [6] is zero. The free energy of such surfaces depends only on the water chemical potential through,

$$\gamma^{hyd}_{hkl}(\{N_i\}, \mu_H) = E_{slab} - N_{Zn}E_{ZnO} + (N_{Zn} - N_O)\mu_{H_2O}. \tag{7.18}$$

Surfaces in which $2N_O - 2N_{Zn} - N_H \neq 0$ are charged. Those with $2N_O - 2N_{Zn} - N_H > 0$ possess a net positive charge, that in the context of our tri-vapour system correspond to protonated surfaces. Conversely, slabs in which $2N_O - 2N_{Zn} - N_H < 0$ correspond to negatively charged surfaces resulting from hydroxylation.

Given that our greatest interest lies in the aqueous system, we make inferences to the aqueous system thoughout our analysis of the vapour system. In the aqueous system water is condensed on the surface, thus the region of our vapour system where the resemblance to the aqueous system is greatest is when $\mu_{H_2O} = E_{H_2O}$, i.e. $\delta\mu = 0$. Taking the surface H atoms to be effectively protons, H^+, and using $\mu_H = \mu^{\ominus}_H + \frac{RT}{2.718}p\mathrm{H}$ to describe the chemical potential, allows construction of a relation between pH and surface free energy,

$$\begin{aligned}\gamma^{hyd}_{hkl}(\{N_i\}, pH) = E_{slab} - N_{Zn}E_{ZnO} + (N_{Zn} - N_O)E_{H_2O} \\ + (2N_O - 2N_{Zn} - N_H)(\tfrac{RT}{2.718}\mathrm{pH}).\end{aligned} \tag{7.19}$$

[6] i.e. $\sum_i z_i N_i$, where z_i is the valence of species i

Further connections to the electrochemical system responsible for our interest in the ZnO-aqueous interface are made by considering the *electrochemical* potential $\bar{\mu}_i = \mu_i + zF\phi$, where $\phi = V_{surf} - V_\circ$, in place of μ_i. Thus for the dependence on pH, and ϕ we have,

$$\begin{aligned}\gamma^{hyd}_{hkl}(\{N_i\}, \mu_H, \phi) &= E_{slab} - N_{Zn}E_{ZnO} + (N_{Zn} - N_O)E_{H_2O} \\ &\quad + (2N_O - 2N_{Zn} - N_H)\bar{\mu}_H \\ &= E_{slab} - N_{Zn}E_{ZnO} + (N_{Zn} - N_O)E_{H_2O} \\ &\quad + (2N_O - 2N_{Zn} - N_H)(\tfrac{RT}{2.718}\mathrm{pH}) \\ &\quad + (2N_O - 2N_{Zn} - N_H)z_H F\phi,\end{aligned} \tag{7.20}$$

where $\phi = V_{surf} - V_\infty$, z_H is the valence of aqueous H^+, usually taken as +1, and F is Faraday's number. The corresponding surface energy dependence on Zn^{2+}, pH, ϕ is written,

$$\gamma^{hyd}_{hkl}(\{N_i\}, c_{Zn^{2+}}, pH, \phi) = E_{slab} - N_{Zn}\mu_{Zn} - N_O E_{H_2O} + (2N_O - N_H)\bar{\mu}_H. \tag{7.21}$$

Alternatively, the free energy of hydration, or more commonly, the binding energy,

$$\Delta G^b_{hkl}(N_i, \mu_{H_2O}) = E^{hyd}_{hkl} - N_{bare}E^{bare}_{hkl} - N_{H_2O}\mu_{H_2O} \tag{7.22}$$

may be calculated. The binding energy is more computationally intensive as it involves the calculation of two slab structures: one to represent the bare surface and another to represent the hydrated surface. The dependence of both the hydration energy and the hydrated surface energy on the chemical environment (e.g. pH) can be investigated using the method outlined above for the surface free energy.

Two groups [132, 129] have performed calculations on a variety of supercells with O and OH terminations in order to calculate the phase diagram in the vapour environment. However, neither group considers the implications for the aqueous situation. The situation is more complex in the aqueous situation as many more factors influence the surface state.

The studies of Meyer [133, 129, 134] and Kresse [135, 132] provide valuable insight into the ZnO surface despite having a different focus to our work. The focus of our work differs not only because we are most interested in the aqueous system, but also in that we are interested in structures thought to facilitate crystal growth.

7.4 DFT and Crystal Growth

The preceding section described how total energy calculations can be applied to realistic treatment of oxide surfaces in a chemical (vapour) environment. In this section we outline our motives with regard to the use of DFT to aid our modelling of ZnO crystal growth. As mentioned earlier, there are two features of our work that are not treated in the literature: the effect of bulk water on the zinc oxide surfaces, and energies associated with the surface features that are required for crystal growth. Due to the shortcomings of DFT in treating Van der Waals interaction [136, 137, 138] and therefore aqueous systems, we focused on the investigation of surface features that are required for crystal growth, rather than direct investigation using ZnO/H_2O supercells, due to limited computing power. As a compromise we have investigated the effect of surface hydration of features required for crystal growth, to give an indication of the effect of the aqueous environment. Here we give an overview of the fundamentals of crystal growth and propose a method through which DFT calculations can be used to determine parameters upon which crystal growth theory depends.

7.4.1 The Equilibrium Shape

The most fundamental idea of crystal shape and growth prediction is that of the Wulff shape. The Wulff shape can be thought to arise from the notion that at equilibrium the most stable crystal shape is that which min-

imises its total surface free energy for a given volume, V [55, p. 45],

$$\delta(\gamma + \lambda V) = 0, \tag{7.23}$$

where γ is the surface free energy and λ is a Lagrange multiplier. The solution of Equation 7.23 for a faceted crystal is commonly expressed as,

$$\gamma_i A_i = \gamma_j A_j, \tag{7.24}$$

where A is the facet area, and the subscripts denote different crystal faces.

7.4.2 The Kinetic Models

The kinetic models are based on the development of a detailed mechanistic description of the structures and processes that exist at the crystal surface and surrounding medium. Here we briefly review the basics of kinetic growth models.

Supersaturation

We first review the notion of supersaturation, $\Delta\mu$, the driving force for crystal growth, and introduce the relative supersaturation. The relative supersaturation σ is defined by

$$\sigma = \frac{c - c_\circ}{c_\circ}, \tag{7.25}$$

where c is the concentration of the crystal growth unit, and $c_\circ$ is the equilibrium concentration of the crystal growth unit. The equilibrium concentration is the concentration at which the surface growth units have the same chemical potential as the solution growth units, and is therefore sometimes called the saturation concentration. The concentration can be expanded using Gibb's equation, $c_\circ = \exp(+\mu_\circ/kT)$ [55], and since $\Delta\mu = \mu - \mu_\circ$ we can write (7.25) in terms of the equilibrium concentration and the difference in chemical potential (the supersaturation), using

$$c = c_\circ \exp(\Delta\mu/kT). \tag{7.26}$$

Now the relative supersaturation is written,

$$\sigma = \frac{c_\circ \exp(\Delta\mu/kT) - c_\circ}{c_\circ} \tag{7.27}$$

$$= \exp(\Delta\mu/kT) - 1. \tag{7.28}$$

Provided $\Delta\mu \ll 1$ holds, we have

$$\sigma = \frac{c - c_\circ}{c_\circ} = \Delta\mu/kT, \tag{7.29}$$

a linear relation between the relative supersaturation and the excess chemical potential $\Delta\mu$ (the supersaturation).

Normal Growth

The simplest kinetic growth model is that of normal growth. Such growth occurs on rough, highly kinked surfaces, upon which attachment can occur anywhere on the surface. The kinetic model is developed by considering the free energy profile of the solid-medium system.

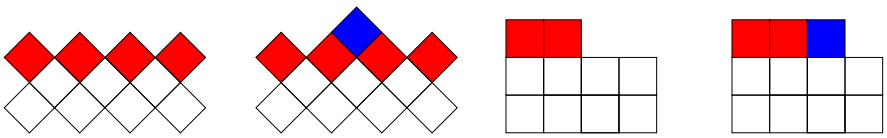

Figure 7.6: A two dimensional depiction of surface (red blocks) growth by incorporation of growth unit (blue) into a kink site on a (a) rough surface, and a (b) Smooth surface.

The rate of crystal growth from solution is limited by the incorporation of growth material into the surface at kink sites [44], shown schematically in Figure 7.6. The rate of normal growth is simply the probability a growth unit approaching the surface encountering an entrance site (a kink), times the net flux into the kink, times the distance propagated due to inclusion

of a growth unit [44, 53],

$$R = a(a/\lambda_K)^2(j_+ - j_-). \tag{7.30}$$

Here a is the dimension of a growth unit (ZnO in our case) and λ_K is the mean inter-kink distance, thus $(a/\lambda_K)^2$ is the (geometric) probability of a growth unit encountering a kink on the surface, i.e. the likelihood of a lattice site being kinked. The flux into the kink is j_+ and the flux out is j_-, and the net flux per kink site is the difference $(j_+ - j_-)$.

The kinetic barrier to kink entrance, associated with monomer rearrangement (especially for large molecules), and de-solvation, is additively collected as E, which is considered to be essentially isotropic between surfaces. The kink entrance flux is derived from simple transition state theory (Arrhenius kinetics) and is taken as [44]

$$j_+ = Xa^3\nu\text{exp}(-E/kT), \tag{7.31}$$

where ν is the attempt frequency (assumed equal for lattice and interface), X is the interfacial concentration of monomer, and Xa^3 is therefore the probability a growth unit occupying an interfacial site. This expression is valid when the attachment is single stepped and each occurrence is statistically independent. The dissolution flux is

$$j_- = (1 - Xa^3)\nu\text{exp}(-(\Delta H + E)/kT), \tag{7.32}$$

where $(1 - Xa^3)$ represents the probability of a vacant solute (growth unit) shell occurring at an interfacial site, and ΔH is the enthalpy of dissolution.

At equilibrium the growth rate is zero, and the fluxes are balanced, $j_+ = j_-$, and thus

$$\text{exp}(-\Delta H/kT) = \frac{X_\circ a^3}{1 - X_\circ a^3} \tag{7.33}$$

where $X_\circ$ is the equilibrium concentration of monomer. We now write the growth rate

$$R = a(a/\lambda)^2\nu\text{exp}(-E/kT)\left[Xa^3 - (1 - Xa^3)\left(\frac{X_\circ a^3}{1 - X_\circ a^3}\right)\right], \tag{7.34}$$

which under dilute conditions, $X_\circ a^3 \ll 1$, is

$$R = a(a/\lambda)^2 \nu \text{exp}(-E/kT) \left[a^3(X - X_\circ)\right]. \tag{7.35}$$

The term outside the square brackets is the kinetic factor,

$$\beta = a(a/\lambda_K)^2 \nu \text{exp}(-E/kT). \tag{7.36}$$

Finally the normal growth for a given facet, hkl, can be written succinctly in terms of the relative supersaturation,

$$R_{hkl} = \beta_{hkl} a^3 X_\circ^{hkl} \sigma_{hkl} = \beta_{hkl} a^3 X_\circ^{hkl} \Delta\mu_{hkl}/kT, \tag{7.37}$$

Here all the anisotropic terms are denoted with the subscript hkl, however, the kinetic factor is regarded as the principal anisotropic parameter [139].

Equation (7.37) exhibits a linear dependence on supersaturation. It is the kind of growth we might expect of an amorphous or rough surface, and closely resembles the type of equation we used to treat ZnO formation deposition (c.f. (3.9)),

$$R = \beta \left(1 - \frac{Q}{K}\right). \tag{7.38}$$

Here Q is a reaction quotient (equivalent to X above) and K is the equilibrium reaction quotient ($Q_\circ$), i.e.

$$R = \beta \left(\frac{Q_\circ - Q}{Q_\circ}\right), \tag{7.39}$$

or more concisely

$$R = \beta\sigma = \beta\Delta\mu/kT. \tag{7.40}$$

Finally we note that this description can be used to model two kinds of rough growth: growth onto a 'thermodynamically' rough surface as used in this derivation, or alternatively we may think of the surface as being 'kinetically' rough. A kinetically rough surface arises when the rate of island nucleation is so great that the surface is considered to be effectively rough and thus growth possesses the linear dependence on supersaturation as above. However, rudimentary crystal growth theory shows that an activation barrier of order $\gamma^2/\Delta\mu$ must be overcome, and thus such growth only occurs under conditions of large supersaturation.

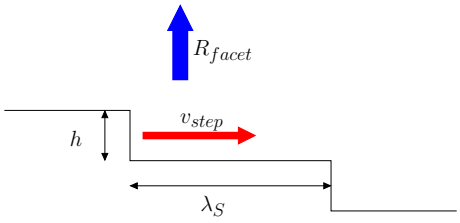

Figure 7.7: Schematics depicting facet growth by propagation of steps

Layer Growth

The alternative to rough growth is layer growth, which produces less defective crystals, and in fact, our experimental data (see Figure 2.5e) suggests the presence of layer growth (at least during the final stages of growth). Solution growth usually proceeds by a layerwise mechanism [44]; normal growth from solution is rare [44, p. 108]. This is because solubility is low ($K_s \sim 10^{-17}$), and therefore interfacial energy is high [44], which (especially at moderate temperature) yields low density of kinks on steps. Layerwise growth involves the formation and propagation, or *flow*, of steps as shown in Figure 7.7, requires the presence of steps on a flat surface, and proceeds by incorporation of material into the step front.

The flow of steps determines the overall facet growth rate (see Figure 7.7) according to

$$R = \left(\frac{h}{\lambda_S}\right) \times v \tag{7.41}$$

where λ_S is the mean distance between steps, h is the step height, and v is the step velocity. The step velocity term takes the same form as the growth rate described above for normal growth. Thus,

$$v_S = a(a/\lambda_K)(j_+ - j_-) \tag{7.42}$$

$$= \beta_S a^3 X_\circ \sigma. \tag{7.43}$$

Aside from the geometric factor, h/λ_S, the only difference is that the monomer incorporation is occurring along a line (step edge) rather than at a surface. The kinetic factor for layer growth is,

$$\beta_{step} = a\left(\frac{a}{\lambda_K}\right)\nu \exp\left(-\frac{E}{kT}\right). \tag{7.44}$$

Finally, we have for layer growth

$$R = \left(\frac{a}{\lambda_S}\right)\beta_S a^3 X_\circ \sigma = \left(\frac{a}{\lambda_S}\right)\beta a^3 X_\circ \left(\frac{\Delta\mu}{kT}\right). \tag{7.45}$$

The key quantities in (7.45) and (7.44) are the activation barrier, E, the mean inter-step distance, λ_S, and the mean interkink distance, λ_K.

The Terrace Length, λ_S

Burton, Cabrera and Frank [140] (BCF) realised that screw dislocations provide a perpetual step source, thus bypassing the need to overcome a critical supersaturation for layer growth. Layer growth can occur at low supersaturations and can therefore be modelled without needing to consider complex cooperative effects associated with high adatom density[7]. BCF [140] found an approximate relation between the critical radius, r_c, the radius above which it is favourable for a disc shaped seed to grow, and the distance between concentric rings of a growth spiral, λ_S. The relation is [44]

$$\lambda_S \approx 19 r_c. \tag{7.46}$$

The critical radius arises from consideration of the free energy of formation of a circular disc and is expressed,

$$r_c = \frac{V\sigma}{\Delta\mu}, \tag{7.47}$$

where V is the growth unit volume, σ is the surface energy of the circular disc face (the step face), and $\Delta\mu$ represents the supersaturation.

Utilisation of the layer growth kinetic model relies on being able to estimate the anisotropic parameters, λ_S, the mean inter-step distance, and λ_K, the mean inter-kink distance. It has been shown [141, 142] that both parameters are strongly related to the average kink free energy, $\bar{\phi}_{hkl}$.

[7] Today many numerical and atomistic simulations focus on the dynamics of cooperative entities such as small islands (dimers, trimers, etc).

(a) (b)

Figure 7.8: Schematic showing how a kink can be formed from a step. (a) Shows a step with energy ϕ_S^1 per characteristic area (yellow), while (b) shows a kink forms by extrusion of part of the step with energy $2\phi_K \approx \phi_S^1 + \phi_S^2$ (red). At the kink two differently oriented step fronts meet.

The Kink Energy

Here we look more closely at what the kink energy means in the context of circular step propagation. The step energy, γ_S^{hkl} is the work per unit length, a, to form a step on a flat surface. Likewise, the kink energy is the work required, per unit length, to form a step on an existing step, illustrated in Figure 7.8. The case illustrated in Figure 7.8 illustrates the formation of a kink (with energy ϕ_K^{xy}), by formation of a y-oriented step on an x-oriented step. The energy of the construction per unit length can be decomposed into steps (S) and edges (E)

$$2\phi_K^{xy} = \phi_S^x + \phi_S^y + \phi_E^+ + \phi_E^-, \tag{7.48}$$

where ϕ_S^x is the step with front facing toward the x-direction, ϕ_S^x is the step with front facing toward the x-direction, ϕ_E^+ is the convex edge, and ϕ_E^- is the concave edge. The contribution of edges per unit length is small compared to the step faces, and are therefore neglected, giving

$$2\phi_K^{xy} = \phi_{hkl}^x + \phi_{hkl}^y = \sum_{i\in\Gamma} \phi_{hkl}^i \quad \text{where } \Gamma = \{\vec{x}, \vec{y}\}. \tag{7.49}$$

Spiral growth requires the formation and transit of kinks around the entire circumference of the spiral, which allows us to consider the average kink

energy of a crystal facet, $\bar{\phi}_K^{hkl}$. Repetition of the operation of step formation on an existing step over a single revolution yields,

$$n\bar{\phi}_K^{hkl} = \sum_{i\in\Gamma} \phi_{hkl}^i, \quad \text{where } \Gamma = \{\vec{n}_{theta}\}, -\pi \leq \theta \leq \pi \ , \tag{7.50}$$

and $\vec{n}_\theta$ is the step front normal at angle θ. In other words, the average kink energy equals the average step energy, $\bar{\phi}_K^{hkl} = \bar{\phi}_S^{hkl} = \bar{\phi}$.

Key Parameters: $\lambda_S, \lambda_K, \bar{\phi}$

Having defined the average kink energy, and its relation to the step energy we investigate how it relates to the anisotropic kinetic parameters, λ_S, and λ_K.

First we consider the inter-step distance λ_S, which, under spiral growth is proportional to the critical seed radius, Equation (7.46). In turn, the critical radius is really an effective critical radius that depends on the average free energy of the step front per unit area, $\bar{\phi}/a^2$. Thus from (7.47)

$$r_c = \frac{a^3\bar{\phi}}{\Delta\mu a^2} = \frac{a\bar{\phi}}{\Delta\mu}, \tag{7.51}$$

and,

$$\lambda_S \approx \frac{19a\bar{\phi}}{\Delta\mu}. \tag{7.52}$$

The critical radius, and hence the interstep distance, is proportional to the average kink energy.

Next, we consider the inter-kink distance λ_K^{hkl}. The average distance between kinks on a step is [140],[44, p. 24]

$$\lambda_K = a\left[1 + \tfrac{1}{2}\text{exp}\left(\frac{\bar{\phi}}{kT}\right)\right], \tag{7.53}$$

which in the limit $\lambda_K \gg a$ reduces to

$$a/\lambda_K \approx 2\text{exp}\left(-\frac{\bar{\phi}}{kT}\right). \tag{7.54}$$

The probability of a kink along a step is the Gibbs function for the average kink energy.

Substitution of 7.52 and 7.54 into the surface growth rate equation for layer growth (7.45) gives,

$$R = \frac{a^3 X_\circ \beta \Delta\mu^2}{9.5kT\bar{\phi}} \tag{7.55}$$

where

$$\beta_{hkl} = a\nu \exp\left(-\frac{\bar{\phi} + E}{kT}\right). \tag{7.56}$$

Thus layer growth exhibits a quadratic dependence on supersaturation.

Acquisition of the average step energy is crucial to parameterise the step velocity equations ((7.55) and (7.56)). The aim of this study is to attempt, for the first time, to acquire them directly using DFT total energy calculations using supercell models (c.f. Section 6.4.4). Due to the computational expense of quantum mechanical calculations, although DFT is relatively cheap, we use the minimum possible number of step orientations to calculate the average kink (step) energy. The steps used to approximate the kink energy are constructed solely from the low index facets and are illustrated in Figure 7.9.

Despite investigating the minimum set of steps, this study requires a great deal of calculation and analysis before step energies can be obtained. Analysis requires calculation of both bare and hydrated surfaces, both flat and stepped. The surfaces must be converged with respect to the parameters used for a typical surface: the slab thickness, large enough planar area, but also the lower and upper step length, and the length of the step rise (the step face), as well as conventional parameters such as k-points and energy cut-offs.

7.5 ZnO Bulk Structure Convergence

For consistency we must represent the ground state bulk energy as best we can within the bounds of our calculational set-up. The first step in doing

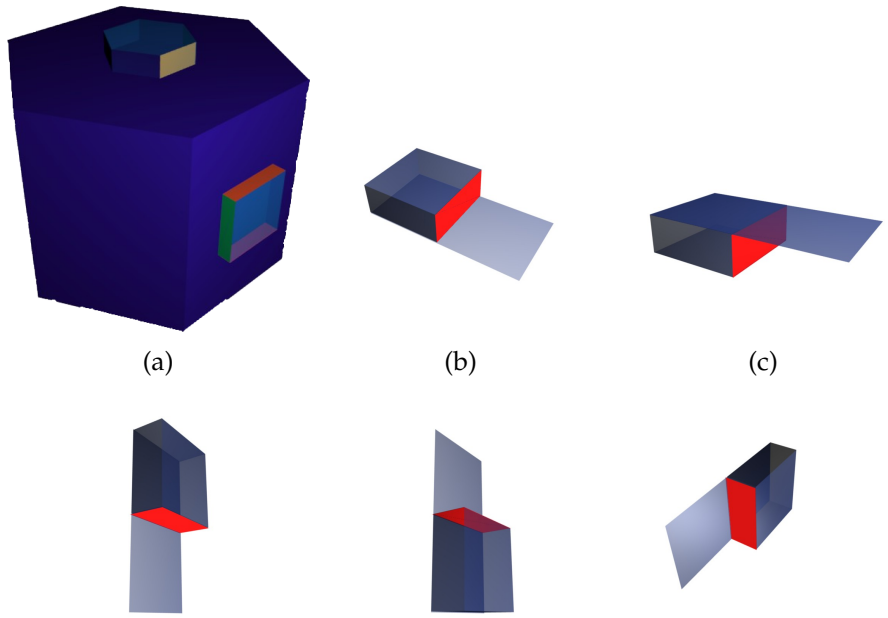

Figure 7.9: (a) Illustration of the symmetrically independent faces required to describe a coarse average kink energy on hexagonal columnar ZnO. The beige face is the only symmetrically independent step on the $\{0001\}$ faces, whilst the $\{10\bar{1}0\}$ require three steps due to the polar nature of ZnO in the $\vec{c}$ direction. The green step points in the $[10\bar{1}0]$ direction, red in the $[0001]$, and purple in the $[000\bar{1}]$ direction. Sections of the unique steps considered in our studies to calculate the average kink energy from the lowest index step orientations are represented in (b)-(f), in which the first indice is denotes the facet whilst the second denotes the step rise direction. The basal steps (b) $(0001) - (10\bar{1}0)$, and (c) $(000\bar{1}) - (10\bar{1}0)$, and the lateral steps (d) $(10\bar{1}0) - (000\bar{1})$, (e) $(10\bar{1}0) - (0001)$, and (f) $(10\bar{1}0) - (10\bar{1}0)$.

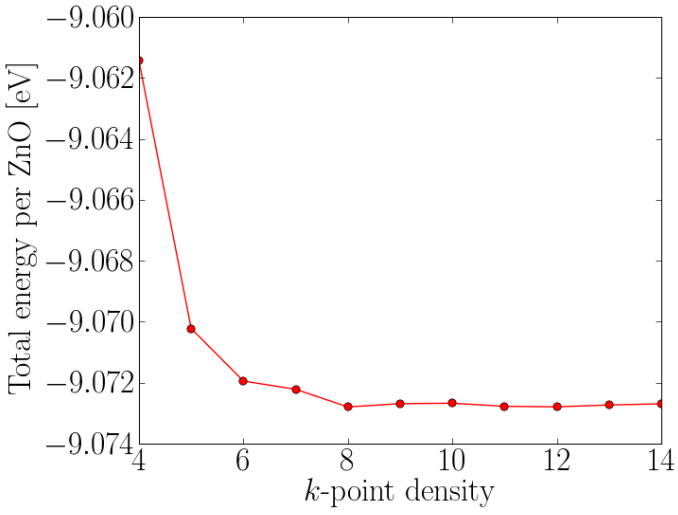

Figure 7.10: k-point convergence for ZnO

DFT calculations is to ensure that the quantity of interest (in our case the energy) is invariant with the k-point grid [115, 143]. Using a converged energy cut off (396.0 eV) we found energy-k-point convergence (Figure 7.10) was reached using an automatically generated gamma centred mesh with a density of $11 \times 11 \times 11$ which corresponds to 216 k-points in the first Brillouin zone.

The convergence procedure for the bulk cell dimensions is very important for the calculation of surface energies. The importance can be illustrated using the relation used for calculating the surface energy σ using slab models,

$$\sigma = \frac{E_{surf}}{2A} \quad \text{where} \quad E_{surf} = E_{slab} - NE_{bulk}. \tag{7.57}$$

We see that the error associated with the bulk calculation is multiplied by the slab size N, and because the surface total energy is a small number obtained from two large numbers, the absolute error is large. Also, in cases where the cell dimensions do not greatly influence the total energies (shallow energy volume surface), significant uncertainty in the surface free energy can result from small variations in the cell dimensions that define the

surface area. It is therefore very important that the bulk cell dimensions are as accurate and consistent as possible. The type of functional used also makes a difference, as shown in Figure 7.11. We see that the LDA underestimates the lattice constant $\vec{a}$ by c.a. 1.5 % whereas the GGA overestimates it by a similar amount. However, in most cases we are interested in quantities obtained from the differences between two or more calculations, so the discrepancy between functionals is much more subtle.

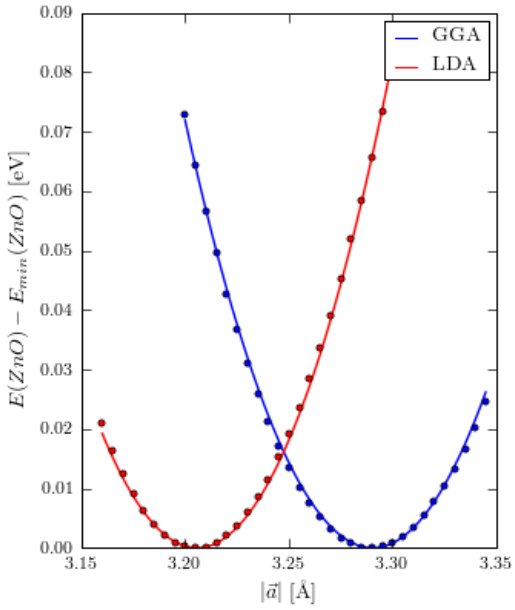

Figure 7.11: Isotropic volume scan with structural relaxation at each volume using LDA (Ceperley-Alder [144]), and GGA functionals (Perdew-Wang 91 [145]). The curves are offset by their respective minimum total energies: E_{min}(ZnO), -10.63 eV for the LDA, and -9.087 eV for the GGA.

The conventional way to converge the bulk cell dimensions is to isotropically vary the bulk cell volume, and relax the wavefunction only [143]. The cell corresponding to the volume-energy minimum is then structurally relaxed to obtain the converged bulk structure. Alternatively, provided the unit cell is not prohibitively large, the structural relaxation may be per-

formed at each volume. Figure 7.11 was produced using the latter method.

For calculations on hexagonal cells, Pulay stress, stress arising from anisotropic change in the cut-off energy due to change in cell volume, can be problematic. The problem is avoided if the unit cell volume is kept fixed, but change in the atom positions and cell shape are permitted. The minimum energy structure is found by performing a set of fixed volume relaxations. Because of the cell anisotropy ($a \neq c$) it is necessary to converge the energy with respect to the (a, c) coordinate rather than simply the a parameter with fixed ratio, c/a.

We performed relaxations over a range of c and a values. The conventional procedure is to vary the structural parameter, then relax the wavefunction only, to find the minimum energy cell parameters [143]. Once this is done an accurate full relaxation is performed to determine the ground state structure and properties. We compared the conventional procedure with a more rigorous convergence strategy in which the full relaxation was performed at each coordinate. Indeed, the need for such care is supported by recent work on hexagonal Zn metal in which three minima were found on the c-a surface [146]. We performed the calculations using the atom positions found in the literature, as well as those determined from the isotropic minimisation mentioned earlier (Figure 7.11).

The electron-only relaxations of the literature cell suggested a structure with relatively large c/a ratio (Figure 7.12a). However, we found that when full relaxation was performed at each (a, c) coordinate, instead of mapping an energy well, an energy valley was obtained, shown in Figure 7.12b. The valley topology is accompanied by significant compression along the c-axis. Replication of the conventional c-a convergence using the energy-volume minimised structure (see Figure 7.11) with electron-only relaxation suggested a moderate to low c/a ratio, as shown in Figure 7.12c. However, as with the previous case, full relaxation resulted in a valley energy-cell vector topology, and c-axis compression (Figure 7.12d).

Given that the volume at each coordinate is fixed, and there is little

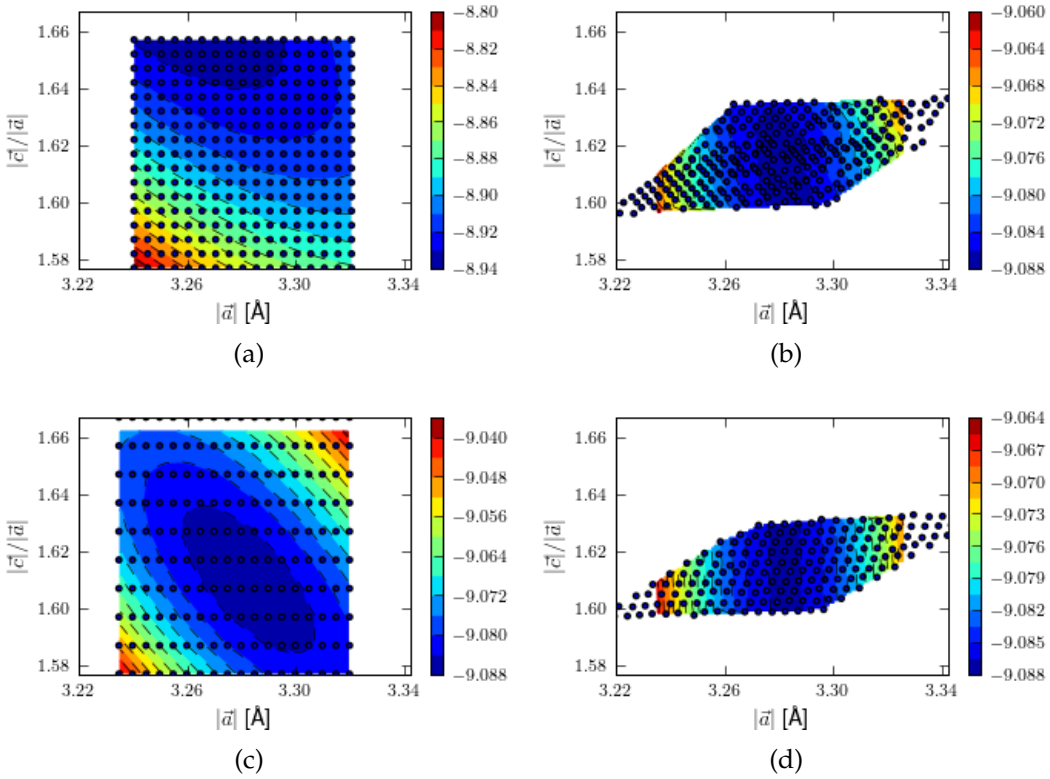

Figure 7.12: Contour plots (in eV) showing the various (c, a) convergence tests performed using either electron-only relaxation or fixed volume, free shape atom position, structural relaxation (ISIF=4) at each (c, a). (a) Electron-only using literature cell. (b) Structural relaxation of literature cell (c) Electron-only relaxation of the unit cell obtained using the conventional isotropic energy-volume convergence, and (c) Structural relaxation executed at each (c, a).

change in the magnitude of the $\vec{a}$ vector, the only way volume can be conserved is if the angle γ, which subtends $\vec{a}$ and $\vec{b}$, varies. Thus we expected a unique γ for each c-a structure. Indeed this was found to be the case, as shown in Figure 7.13, which shows increasing c/a ratio accompanied by an increased γ, which produces a diminished basal area.

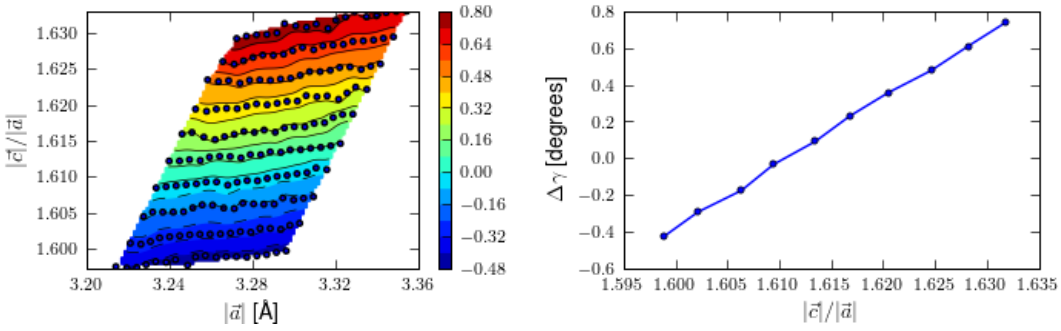

(a) (b)

Figure 7.13: (a) Contour map of $\gamma_{relax} - \gamma_{\circ}$, the γ angle in the relaxed structure versus the un-relaxed cell. (b) A plot of $\gamma_{relax} - \gamma_{\circ}$, the γ angle in the relaxed structure versus the un-relaxed cell, against the cell anisotropy for a specific $|a|$.

Ultimately, for use in further studies of surface energies, we chose the structure obtained from full relaxation of the minimum determined by Figure 7.12c, which yielded, $a = 3.283$ Å, $c = 5.309$ Å, $u = 0.379$ Å, and $E_{Zn_2O_2} = -18.17$ eV (-9.087 eV per formula unit). Table 7.1 shows our structural results to be consistent with the latest published results [132, 133]. We can calculate the free energy (heat) of formation of ZnO using

$$\Delta G = E^f_{ZnO} = E_{ZnO} - E_{Zn} - \tfrac{1}{2}E_{O_2}. \tag{7.58}$$

After performing structural relaxations on both hexagonal Zn (eV) and face centred cubic Zn (eV), and a supercell relaxation on O_2 (eV), we calculate the free energy of formation to be -3.06214 eV (-295.412 kJ/mol),

which compares well with the result of Kresse *et al* [132] (-3.04 eV) and reasonably well with the experimental value of 318 kJ/mol [40] (7 % error).

Table 7.1: ZnO data found in the literature. The percent deviation from experiment [124] is bracketed.

Author	Data Type	a (Å)	c (Å)	u (Å)	$\|c\|/\|a\|$	tot. err. (%)
Cooke	LDA [147]	3.2(1.5)	5.16(0.9)	—	1.6125(0.7)	—
Meyer	LDA [133]	3.193(1.8)	5.163(0.8)	0.3783(1.1)	1.617(0.9)	4.6
	PBE [133]	3.282(1.0)	5.291(1.6)	0.3792(0.9)	1.612(0.6)	5.2
Kresse	PW91 [135]	3.282(1.0)	5.309(2.0)	0.378(1.2)	1.618(1.0)	5.2
	PW91 [132]	3.250(0.0)	5.207(0.0)	0.375(2.0)	1.602(0.0)	2.0
Claeyssons	PW91 [148]	3.270(0.6)	5.218(0.2)	0.3822(0.1)	1.596(0.4)	2.2
	EXPT [148]	3.253(0.1)	5.213(0.1)	0.3820(0.1)	1.603(0.1)	0.3
Mackay	PW91	3.283(1.0)	5.309(2.0)	0.379(1.2)	1.617(1.0)	5.2
	LDA	3.2(1.5)	5.16(0.9)	0.378(1.2)	1.6125(0.7)	4.3
Abrahams	Measured [124]	3.250(0.0)	5.207(0.0)	0.3825(0.0)	1.602(0.0)	0.0

7.6 Surface Energy calculations

Surface energy calculations are particularly challenging due to the large cell size required to emulate bulk material and surface structures. High accuracy is required to minimise the error associated with calculating surface energy, a small quantity, from summation of large quantities, bulk and supercell energies. Before we can begin to look at, and compare, the energies of surface structures necessary for growth, such as kinks and steps, we must determine the supercell dimensions suitable to use as a basis for further calculations. The surface must be converged with respect to the vacuum spacing and the slab thickness. In the case of polar surfaces, full convergence using standard techniques (without customised pseudopotentials[8]) requires larger supercells than we can reasonably calculate with

[8]Pseudopotential customisation is an involved process as much validation work must be done before the pseudopotential can be used. The widely used pseudopotentials have a reliability and consistency due to their widespread use.

our computational resources. We consider an acceptable criterion for surface energy convergence to be a variation of less than approximately 10% from our most accurate calculation of a given surface energy.

Flat surfaces are the simplest type of surface, and provide a good basis to look at surface energies and surface stabilisation effects. In the following sections we present our investigation of the surface energies of the lowest index polar and non-polar surfaces in the bare and hydrated states. Much of the work involves finding the minimum acceptable supercell dimensions. Unlike the calculations for the bulk, it is essential to relax the ionic positions at each (N_{cell}, N_{vacuum}) coordinate. The reason for this is that when considering the polar surfaces the surface rearrangement can play a large part in the surface stabilisation [133, 131], and thus if relaxation is permitted smaller supercells can satisfy the convergence criteria.

Investigation of more complex surface reconstructions such as those that include vacancy or island formation requires very large supercells to model [132]. However, under conditions of abundant H and O it was found that the flat hydrated surface was more stable [132]. Given that we are interested in such a system (the aqueous system) we need not investigate the effect of massive surface reconstruction. The flat supercell convergence calculations were repeated with H and OH, attached to the terminal $(000\bar{1})$-O, and terminal (0001)-Zn respectively.

7.6.1 Bare Non-Polar Surfaces

We begin with the simplest case of a bare, non-polar ZnO surface (Figure 7.14). We found the non-polar $(10\bar{1}0)$ surface to be insensitive to the changes in N_{cell} and N_{vacuum}. The convergence behaviour shown in Figure 7.15 exhibits variation of 1.8 % (55.1 - 56.1 meV/Å^2, 0.883 - 0.899 J/m^2) from the largest supercell (Figure 7.14a) with thickness of 10 unit cells and vacuum spacing equivalent to 8 unit cells, to the smallest supercell (Figure 7.14b) with thickness four and vacuum spacing of only four cell

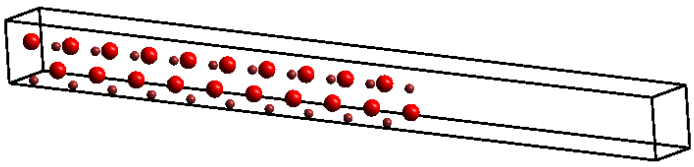

(a) The largest non-polar supercell, $(N_c = 10, N_v = 8)$

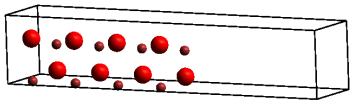

(b) The smallest non-polar supercell, $(N_c = 4, N_v = 4)$

Figure 7.14: The largest and smallest supercells used to investigate convergence of supercell parameters for the non-polar $(10\bar{1}0)$ surface.

equivalents. The results compare well with other work, using the GGA functional [133, 149].

The surface is completely unresponsive to changes in the vacuum spacing, as expected, due to the surface possessing no dipole and net zero charge (Tasker type 1) and thus the surface periodic images do not interact. The surface displays a very small dependence on supercell thickness, because as the slab thickens the inner core atoms become more fixed in the bulk-like geometry which limits their ability to contribute to stabilising the under-coordinated surface.

7.6.2 Bare Polar Surfaces

The polar surface calculations proved more interesting than the non-polar surfaces, as one might expect given that polar surfaces are commonly used as catalysts and sensors, and have greater reactivity than non-polar surfaces [127]. By looking at the supercell convergence behaviour and comparing electron-only (wavefunction) relaxations to electron and atomic (struc-

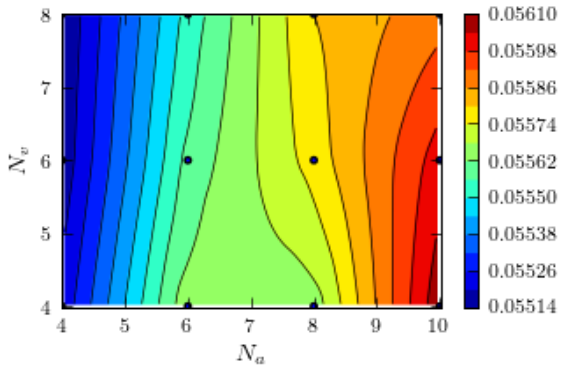

Figure 7.15: Non-polar bare surface supercell convergence using full relaxations (electron and atom), displayed as a surface energy (eV/Å^2) contour plot.

tural) relaxations, effects arising from the polar nature of the surface are encountered.

In the electron-only relaxations, we found the surface energy to be significantly stabilised by low vacuum spacing (2-4 bilayer equivalents) for all supercell thicknesses (Figure 7.16). This indicates that at low vacuum spacing, through space charge transfer is the dominant relaxation mechanism. At larger vacuum spacing (>4 bilayer equivalents) the vacuum spacing dependence is diminished and a linear dependence on slab thickness is observed. The larger supercells experienced a steeper and prolonged energy destabilisation associated with increased vacuum spacing. This is most probably due to a reduced ability to compensate the divergent electric field by transfer of charge through the core in the thicker supercells. In other words, for larger slabs, through-vacuum stabilisation plays a greater role than for small slabs in which through core stabilisation is facile. The surface energy deviation from the largest supercell to the smallest is 5.5 %, and about 2 % if the close ($N_v < 4$) supercells are neglected.

The full structural relaxation (electronic and atomic relaxation) convergence (Figure 7.17) results in a reversal in behaviour and the slab thickness dominates the energy variation. The vacuum spacing has little influence on the surface energy, suggestive of stabilisation dominated by atomic rearrangement rather than through core or space mechanisms. Structural

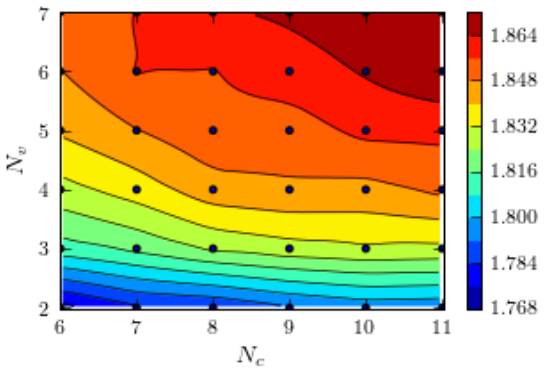

(a) No structural relaxation

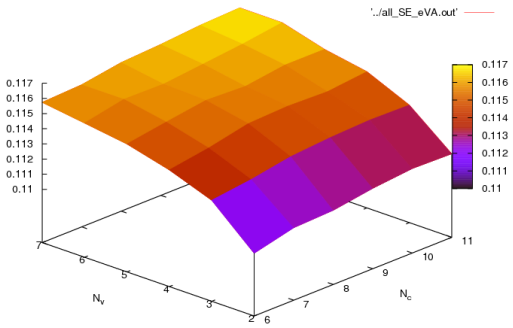

(b) No structural relaxation

Figure 7.16: Supercell parameter electron-only convergence behaviour (in eV/Å^2) of the polar $\{0001\}$ surfaces, surface energy, $E_{\{0001\}} = (E_{slab} - N_{Zn}E_{ZnO})/2A_{\{0001\}}$, versus $N_c = N_{Zn}$ and N_v

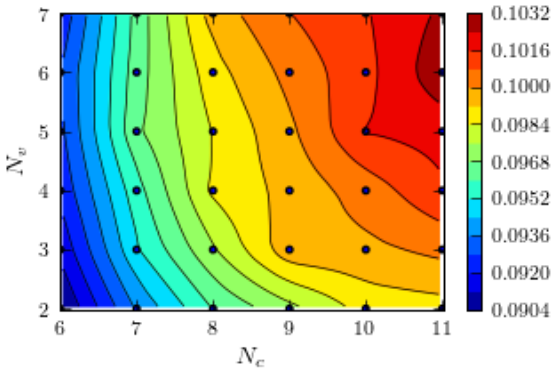

(a) Structural relaxation permitted.

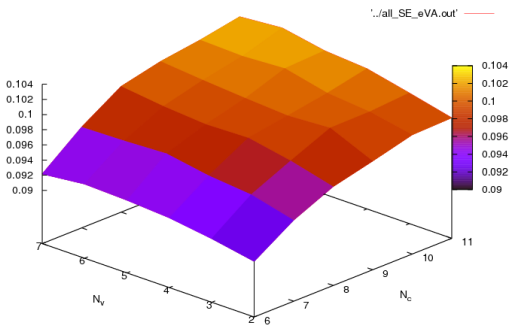

(b) Structural relaxation permitted.

Figure 7.17: Supercell parameter electron and all atom convergence behaviour (in eV/Å^2) of the polar $\{0001\}$ surfaces, surface energy, $E_{\{0001\}} = (E_{slab} - N_{Zn}E_{ZnO})/2A_{\{0001\}}$, versus $N_c = N_{Zn}$ and N_v

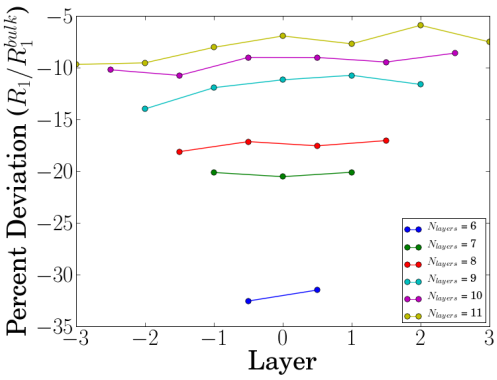

Figure 7.18: The deviation from bulk of the core R_1's plotted against the slab centre for ZnO layers from 6 to 11.

relaxation clearly allows more effective dipole cancellation. At large slab thickness there is some effect at very small vacuum spacing, similar to the electron-only relaxation. Thus even with very large cells some through core relaxation occurs. In other words, because energy increases when vacuum spacing increases some through space must have been occurring, although it is very small vacuum - only 2-3 layers. The surface energy varies 12.5% from the largest cell, twice that of the electron only case, however the absolute energy is lower, in agreement with improved stabilisation illustrated by diminished vacuum dependence above. The larger variation is associated with the smaller slabs being able to rearrange to a greater extent than the larger cells in which the core atoms experience a more rigid bulk-like environment, demonstrated in terms of the small layer spacing (c.f. Figure 7.5), R_1, in Figure 7.18.

The contribution of core atoms to the (N_c,N_v) convergence was investigated by comparison of convergence surfaces using (9,5) slabs with core atom movement forbidden. Three illustrative scenarios are shown in Figure 7.19: slabs with all atoms fixed, the outer 2 layers free (fixed core), and all atoms free. The fixed core free surface exhibits convergence behaviour intermediate to the totally fixed and totally free. For investigation of surfaces, in which surface reconstruction only effects the outermost layers, fixed core slabs better mimic the experimentally observed behaviour than the all free case, which is better suited to finite or molecular sized

crystals. In the macroscopic limit the core atoms have very limited ability to rearrange, thus the greatest error arises from the electronic interaction between the two surfaces.

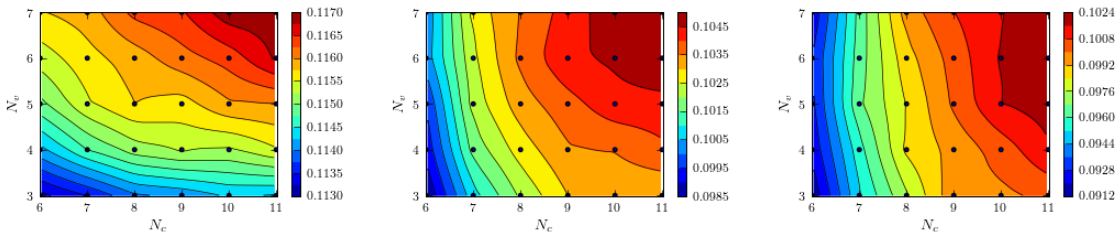

(a) (b) (c)

Figure 7.19: (N_a, N_c) convergence surfaces (in eV/Å^2) for (a) fixed atoms (cleavage), (b) fixed core, free outer two layers, and (c) all atoms free to move.

The relaxation energy ΔE_{rel}, defined by

$$E_{surf} A_{surf} = E_{slab} - N E_{bulk} + \Delta E_{rel} \tag{7.59}$$

where E_{slab} is the total energy of the unrelaxed truncated crystal, shows how structural modification contributes to surface stabilisation. Figure 7.20 shows the relaxation energy for three supercells: full relaxation, outer three layer relaxation, and outer two layer relaxation. The relaxation surfaces are insensitive to vacuum thickness, justified above by more effective dipole compensation and hence less through space interaction. Secondly, they show that the smaller slabs benefit the most from the allowance of atomic rearrangement.

Fixing the core atoms and relaxing the outer two layers yielded slightly higher surface energy than the full relaxation. However, the fixed atom case is probably more realistic because in the macroscopic limit the bulk is rigid and unable to contribute to surface relaxation. The validity of relaxing only the outer two layers is supported by the confluence of all the surface energies at higher (N_c or N_v) (shown in Figure 7.21). Although

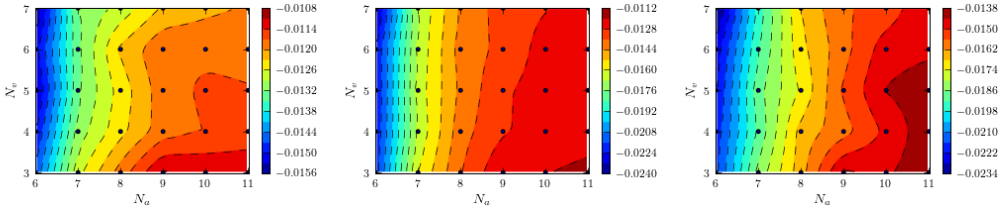

(a) (b) (c)

Figure 7.20: Relaxation energies per surface area (eV/Å^2).

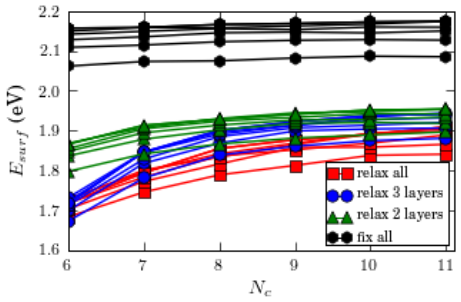

Figure 7.21: Surface total energy (eV), $E_{surf}(N_c)$, as a function of N_c for the $9,5$-slab using fixed and non-fixed core slabs.

it is possible that the fixed core may introduce some artificial effects not present in the real system, e.g. elastic strain.

As a compromise between accuracy and computational time, we chose the 9-5 supercell (9 ZnO bilayers and 5 bilayer equivalents of empty space), with the outer two layers fixed, as the basis for further, and more complicated surface structures. The cleavage energy is 222.0 meV/Å^2 (3.56 J/m^2), the relaxation energy is -23.6 meV/Å^2 (-0.38 J/m^2), and the surface free energy is 199.2 meV/Å^2 (3.30 J/m^2, which varies by 1 % from the largest supercell investigated (11-7)). The result compares very well with recent studies using GGA functional [133], which found a cleavage energy of 212.0 meV/Å^2 (3.4 J/m^2), with a relaxation energy of -17 meV/Å^2 (-0.25 J/m^2).

Structural Analysis

From the energy convergence study in the previous section we concluded that the $(9, 5)$ slab is a suitable basis for the construction of hydration and step models. Now we take a closer look at the geometric changes associated with relaxation, using the $(9, 5)$ as the representative case. Structural relaxation of the supercell models resulted in a decrease in the bilayer thickness (R_1 decrease) and an increase in the bilayer spacing (R_2 increase). The structural relaxation is essentially a 'graphitisation', and works to decrease the layer dipole (rearrangement to a Tasker type 1 surface).

It is clear from Figure 7.22a that most of the relaxation occurs in the outer two layers. Figure 7.22b shows that the behaviour of the outer two layers where most relaxation occurs is very similar irrespective of whether the core is fixed or free. The extent of relaxation in the outer layers is comparable regardless of slab size. In other words, the outer two layers behave the same regardless of slab size for given number of free surface layers (Figure 7.23).

The structural analysis indicates that the structural variation of the $(9, 5)$-slab is sufficiently converged, and that fixing the core atoms produces more realistic results.

7.7 Hydrated Surfaces

Having determined the bare supercell dimensions required for consistent results, we turn our attention to the energetics of the low index surfaces in a chemical environment. We investigate the effect of hydration from a thermodynamic perspective on the non-polar and polar surfaces using the Equations (7.15) (7.19) and (7.22) derived in Section 7.3.

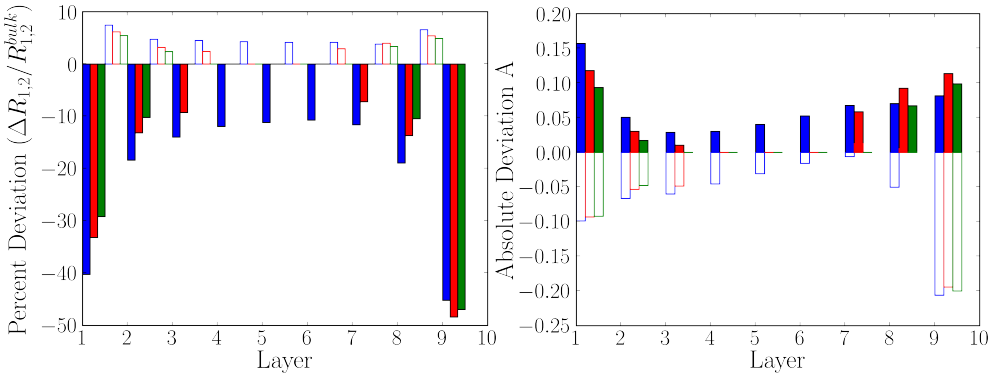

(a) Full bars are R_1, no-fill bars are R_2

(b) Atom movement, filled is Zn, non-filled is O.

Figure 7.22: Bar plots showing the deviation from bulk structure upon relaxation of the (9,5)-slab, in terms of R_1 and R_2 (a), and atom position (b). Full, all atoms realxations are coloured blue, outer 3 layer relaxations are red, and outer 2 layer relaxations are coloured green.

7.7.1 Hydrated Non-Polar Surfaces

Our interest in the aqueous growth of ZnO crystallites encouraged us to look at the effect of hydration on the ZnO surfaces. The ZnO non-polar $(10\bar{1}0)$ surfaces were hydrated by replacement of a terminal Zn with H and the complementary O with OH (see Figure 7.24). The attachment of cleaved water onto the $(10\bar{1}0)$-ZnO surface, has been observed under humid vapour conditions using STM, and recently found to be more stable using DFT [134].

The convergence study was done by performing relaxations on supercells constructed from repetition of four to seven unit cells in the $\vec{a}$ direction, each with a vacuum spacing equivalent to two, three, four, and five unit cell equivalents of empty space, a total of sixteen relaxations. The variation of the surface free energy, calculated using Equation (7.18) at $\mu_{H_2O} = E_{H_2O}$, was 6.4 % (-12.7 to -11.9 meV/Å^2, -0.204 to -0.190 J/m^2). A second kind of hydration in which a single water molecule is split between

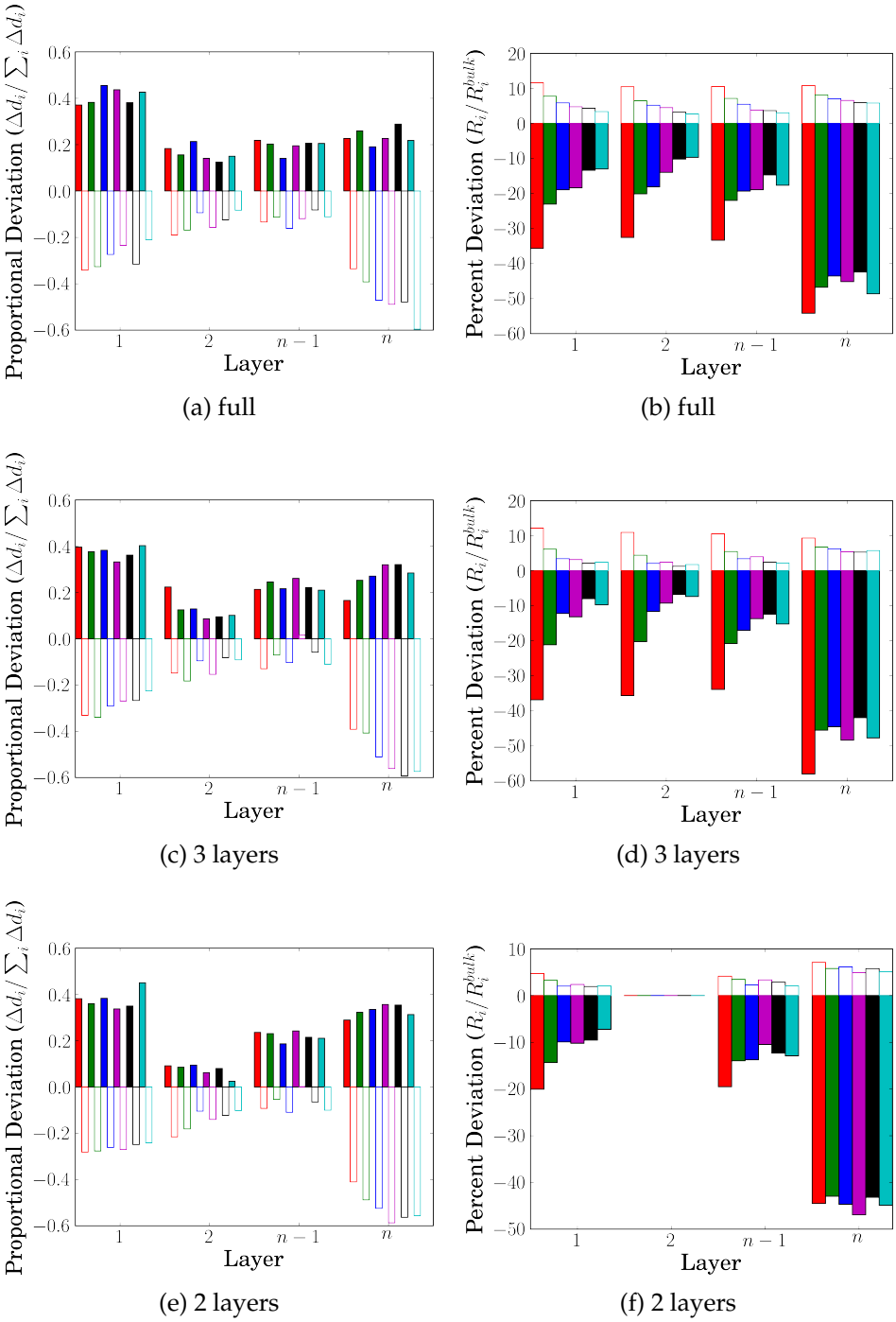

(a) full (b) full

(c) 3 layers (d) 3 layers

(e) 2 layers (f) 2 layers

Figure 7.23: $N_v = 5$ series, $(6,5)$-slab (red), $(7,5)$-slab (green), $(8,5)$-slab (blue), $(9,5)$-slab (purple), $(10,5)$-slab (black), $(11,5)$-slab (cyan). The left column (a, c, e) shows the movement of the individual atoms (Zn = filled, O = non-filled), and the right column shows the change in the layer distance (R_1 = filled, and R_2 = non-filled).

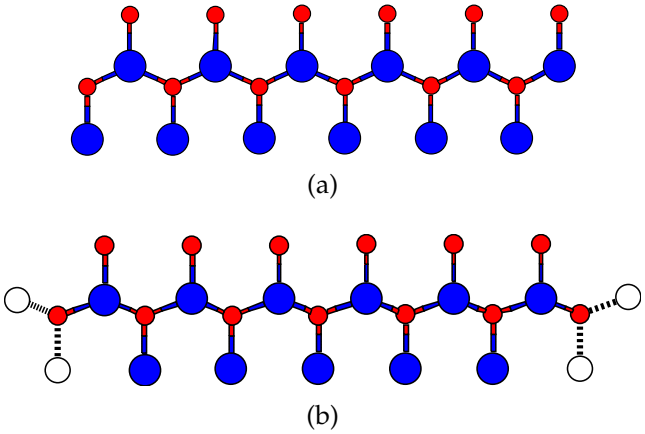

Figure 7.24: Ball and stick models of the $(10\bar{1}0)$ supercells where Zn is blue, O is red, and H is white. (a) The bare supercell, and (b) the hydrated supercell created by replacement of a terminal Zn with H and the complementary O with OH.

the two surfaces, resulting in partially hydrated surfaces, as shown in Figure 7.25, was also investigated. The typical surface free energy (again using $\mu_{H_2O} = E_{H_2O}$) was found to be 106.5 meV/Å^2 (1.75 J/m^2), significantly different to the fully hydrated case.

The surface free energy dependence of the two apparently very different hydrations on the chemical potential of the water containing phase is shown in Figure 7.26a. We see that the less hydrated surface becomes more favourable at more negative $\Delta\mu_{H_2O}$, where water molecules prefer the vapour to the surface. Conversely, at higher vapour potential, the more hydrated surface is preferred. At some point of high vapour chemical potential, the surface free energy becomes negative, which would drive hydroxide formation. Investigation of the 'dissolution' of the surface would require a bulk hydroxide model, rather than the surface hydroxylated surfaces used in this study, to accurately represent the energetics. The behaviour is repeated in the plot of binding energy against water chemical potential Figure 7.26b, which shows movement towards negative binding

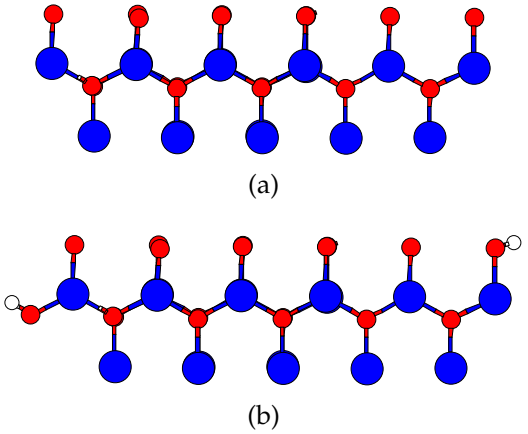

(a)

(b)

Figure 7.25: Ball and stick models of the $(10\bar{1}0)$ supercells where Zn is blue, O is red, and H is white. (a) The bare supercell, and (b) the hydrated supercell created by addition of H on one face and OH on the other.

energy free energy at higher chemical potential.

7.7.2 Hydrated Polar Surfaces

In this section we look at the effect of surface hydration on the polar Surfaces. To investigate partial coverages we used (9,5) basis slabs with a 2×2 surface. First we compare the effect of surface hydration such that the sum of standard reference valancies is zero. The stoichiometry of such structures (shown in Figures 7.27a-7.27c) is constrained by $2N_O - 2N_{Zn} - N_H = 0$, and according to Equation (7.15), the free energies of these model structures are independent of μ_H. We call such surfaces 'neutral' surfaces. We also look at the surface free energy as a function of μ_H and μ_{H_2O}, for all surface types, to map out a stability diagram. Finally, we look at the pH dependence of both the positively and negatively charged surfaces in which $2N_O - 2N_{Zn} - N_H \neq 0$ using Equation 7.19. Examples of charged and neutral polar surfaces are shown in in Figure 7.27.

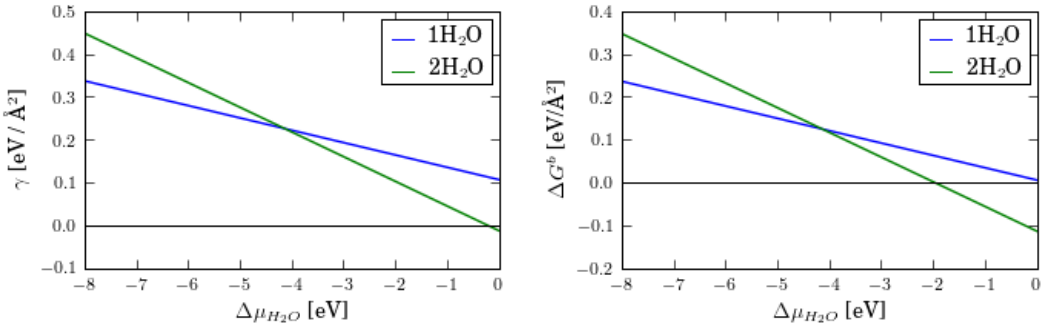

(a) (b)

Figure 7.26: (a) The surface free energy and, (b) the water binding energy, of singly (blue) and doubly (green) hydrated non-polar slabs in the vicinity of the ideal gas state of H_2O.

Neutrally Hydrated Polar Surfaces

We begin our discussion by commenting on the convergence of the slab models. The full relaxation over N_c:6-11, N_v: 3-7, has variation of 1.5 % (-10.8– -10.9 eV/Å^2), and the fixed core convergence has 1.8 % (-10.7– -10.5 eV/Å^2), thus, we continued using the (9,5)-slab as our standard reference structure.

As with neutrally hydrated non-polar surfaces we consider the surface free energy as a function of the water chemical potential in the vicinity of the ideal gas environment. The free energy plot (Figure 7.28a), shows a preference for sparsely hydrated surfaces at lower water chemical potential, and indicates an eventual preference for denser hydration at higher potentials. Unlike the non-polar case, the plots show a preference for the 50% coverage surface over the 25% surface coverage at higher water chemical potential. The behaviour is repeated if we consider the binding energy described by Equation 7.22, and shown in Figure 7.28b. Negative binding energy indicates a preference for water attachment. The preference for 50 % hydration can be understood by recalling that the surface is polar, and particular reconstructions or chemical reactions are optimum for cancella-

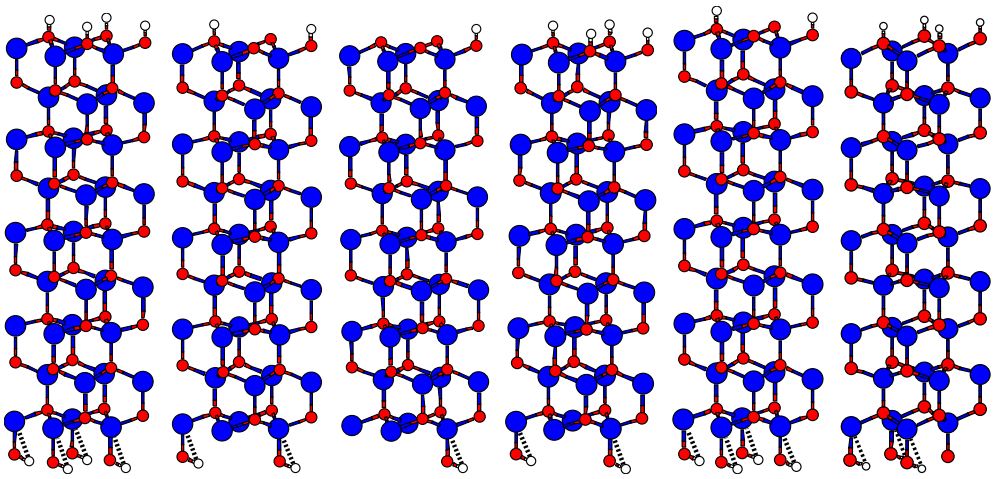

Figure 7.27: Ball and stick (Zn=blue, O=red, H=white) models of the supercells used to study the energetic influence of surface hydration. (a) Full hydration, (b) 50% hydration, (c) 25% hydration, (d) 50% hydration on (0001)-Zn and full hydration of $(000\bar{1})$-O, (e) 50% hydration on $(000\bar{1})$-O and full hydration of (0001)-Zn, and (f) full protonation of $(000\bar{1})$-O and 75% protonation of the oxylated (0001)-Zn surface. Slabs (a)-(c) are neutral and (d)-(f) are charged.

tion of surface charge. Each terminal Zn possesses a net positive charge of $0.5e$, therefore a (2×2) surface possesses a net charge corresponding to 2 electrons, $2e$. Attachment of two OH groups is sufficient to neutralise the excess charge and hence stabilise the surface. An equivalent argument can be made for the terminal O atoms, and their interaction with two H groups.

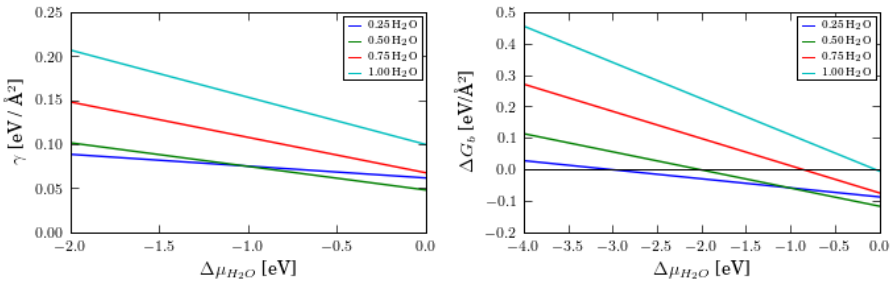

(a) (b)

Figure 7.28: (a) Surface free energy, and (b) water binding energy, of the neutrally hydrated polar surface.

Comparison of the free energy of the hydrated polar and neutral surfaces is shown in Figure 7.29a. The plot indicates a preference for the minimally hydrated polar surface at low water potential, however, as the water potential increases, the non-polar surface has greatest stability. From the greater stability of the non-polar surfaces in the more hydrous environment we infer greater stability in the aqueous environment, which is consistent with the formation of rods, which maximise the area of the non-polar faces.

Consideration of the equilibrium Wulff shape, characterised by,

$$\gamma_P A_P = \gamma_{NP} A_{NP} \tag{7.60}$$

where γ is the surface free energy, A is the area, and the subscripts P and NP denote the polar and non-polar surfaces respectively, quantifies the

prediction of large aspect ratio. Using Equation 7.60 we can calculate the aspect ratio,

$$a_r = \frac{l}{2r}, \tag{7.61}$$

of a hexagonal prism as a function of the water chemical potential. Setting the 6 lateral planes to be non-polar,

$$A_{NP} = 6rl, \tag{7.62}$$

and the 2 basal planes to be polar,

$$A_P = 3\sqrt{3}r^2, \tag{7.63}$$

permits the aspect ratio of the equilibrium Wulff shape to be calculated as a function of water chemical potential by,

$$a_r = \frac{\sqrt{3}}{4}\left(\frac{\gamma_P}{\gamma_N P}\right), \tag{7.64}$$

were l is the rod height, and r is the hexagonal 'radius' (the distance from the hexagonal centre to a vertex). Figure 7.29b shows the dependence of the aspect ratio ($a_r = l/2r$) on water chemical potential, of a hexagonal prism with non-polar lateral faces and polar hydrated basal faces. With increasing water chemical potential the high aspect ratio shape is dominant. We observe that excess water favours the exhibition of non-polar faces, and thus infer that in the aqueous environment acicular crystals are the preferred equilibrium shape.

However, it is more likely that the observed growth shape behaviour is determined by the growth kinetics not the equilibrium Wulff shape [44]. The kinetic growth shape depends on the parameters outlined in Section 7.4, the determination of which are the goal of this study. As yet we have not mentioned the effect of other ions, or even impurity, on the surface energetics, and therefore growth. Effects of impurity are known to influence both electrode reactions [48], and crystal growth [44]. Impurities usually inhibit electrode reactions and crystal growth by forming stable surface

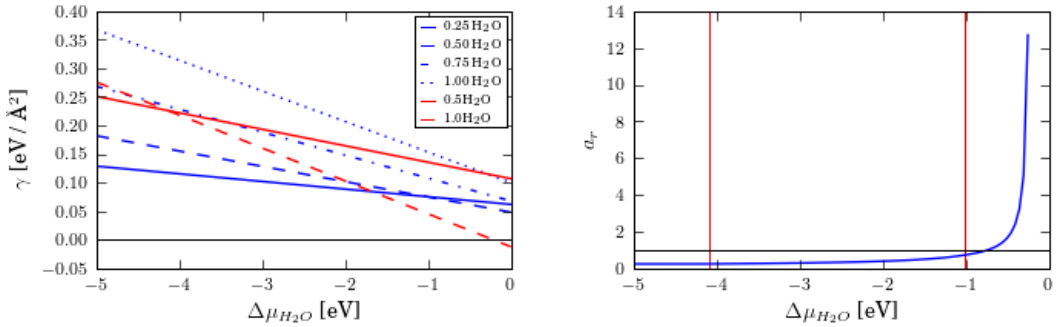

(a) (b)

Figure 7.29: (a) Surface free energy, plotted against the deviation from the chemical potential of the ideal gas state of water, of the hydrated non-polar surface (red), and the hydrated polar surface (blue). (b) The expected aspect ratio of a hexagonal prism shape rod based on the minimum surface free energies of the non-polar and polar surface models. The vertical red lines indicate changes in minimum energy surface termination.

structures or chemical species. Although it would be possible, and interesting, to consider the effect of other growth units (e.g. impurity, or buffer ions) on the surface, step, and kink energies used in our model, it is beyond the scope of this study.

Polar Surface Stability Diagrams

The free energy surface diagrams for the polar surfaces exposed to an environment containing H_2, O_2, and H_2O were calculated for a set of 25 different H/OH surface terminations. Of these, 4 were neutral, 6 were 'positively charged' $(3 \times (^{+1}), 2 \times (^{+2}), 1 \times (^{+3}))$, and 21 were negative $(5 \times (^{-1}), 5 \times (^{-2}), 5 \times (^{-3}), 3 \times (^{-4}), 2 \times (^{-5}), 1 \times (^{-6}))$. The charged slabs were constructed in two ways. The first method ('method 1'), begins with the neutral bare slab and involved protonation of the $(000\bar{1})$-O surface, and hydroxylation of the (0001)-Zn surface ('water splitting'). Surfaces constructed this way can have terminal Zn exposed to the vapour envi-

ronment (see Figure 7.27d for an example). We investigated charge from +3 to -3 using this method. The alternative method ('method 2') begins with a slab in which the (0001)-Zn face is 'oxylated' by attaching O to each terminal Zn, resulting in a negatively charged (-8) basis slab. The O terminated surfaces are protonated stoichiometrically, and can have charge from -8 to 0 (See Figure 7.27f for an example). In the following discussion each model surface is denoted by a tag of the form nXXXX_sXXXX. The 'n' denotes the $(000\bar{1})$-O face, and the 's' denotes the (0001)-Zn face. Each of the four X's refer to whether a particular quarter of the surface is hydrated: a '1' is hydrated, and a '0' is bare. Additionally, the method 1 models have an 'a' suffix, method 2 have a 'b' suffix, and neutral have a 'o' suffix. Because the tag counts the amount of H/OH on the basis slab it can be used to calculate the net charge of each model. The 6 models shown in Figures 7.27a-f are denoted as: [n1111_s1111o], [n1010_s1010o], [n0001_s0001o], [n1010_s1111a]$^{-2}$, and [n1111_s1101b]$^{-1}$.

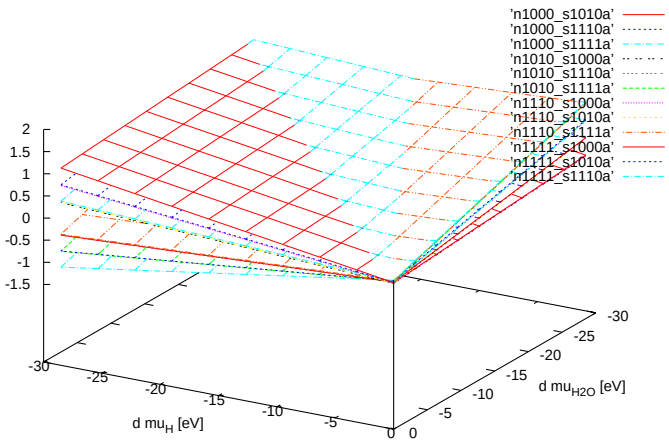

Figure 7.30: Surface free energy against μ_{H_2O} and μ_H of method 1 hydration of the polar surface.

The thermodynamic stability surfaces obtained from the model surface

constructed by the first method are shown in Figure 7.30. The minimum energy surface is represented in Figure 7.31a, in which three surface terminations are represented. The coloured squares denote the slab model, and the surface free energy is indicated by the free energy surface upon which the coloured squares are projected. The minimum energy surface consists of contributions from 2 negatively charged surfaces [n1000_s1010a]$^{-1}$, [n1000_s1111a]$^{-3}$, and 1 positively charged surface, [n1010_s1000a]$^{+1}$, which dominates at high μ_H. The lowest energy surface is that of the fully hydroxylated (0001)-Zn surface. The surfaces with a negative free energy represent surfaces in which formation of the bulk hydroxide may be preferable. However, investigation of such species in beyond the scope of this study. Omission of the negative surface energy models results in the stability map shown in Figure 7.31b

The modified stability map consists of contributions from 7 surface terminations, only one of which bears a positive charge. The lowest surface free energy region is that of higher water chemical potential, and lower hydrogen chemical potential. The terminations in this region are dominated by a high degree of (0001)-Zn hydroxylation, indicating that the hydration of Zn makes a significant contribution to stability. Conversely, coordinatively unsaturated Zn on the surface is energetically unfavourable.

The thermodynamic stability maps obtained by protonating the fully oxylated basis slab (method 2) are shown in Figure 7.32a, from which we can see that all terminations have negative surface free energy in much of the μ_{H_2O}, μ_{H_2} domain. The lowest energy surface has the greatest negative charge ([n1000_s1000b]$^{-6}$) whilst the highest has the least negative charge ([n1010_s1111b]$^{-2}$) and exists only at high μ_H. Clearly, the negatively charged surface provide the greatest stability.

Finally, we collect the method 1 and 2 stability maps together in Figure 7.33a. The minimum energy surface consists mostly of the minimally protonated surface ([n1000_s1000b]$^{-6}$), and the neutral surface ([n1000_s1000o]), with the positive (n1010_s1000a^{+1}) surface prevailing only at high μ_H. The

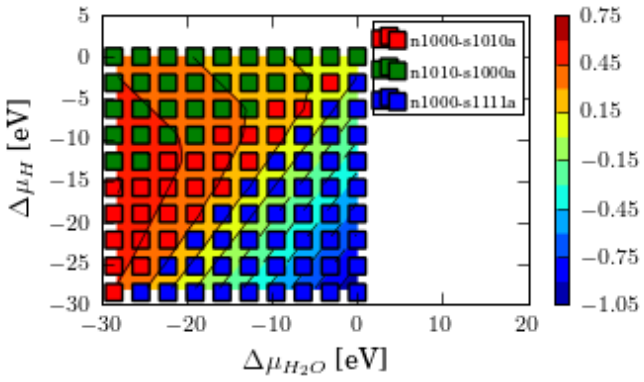

(a)

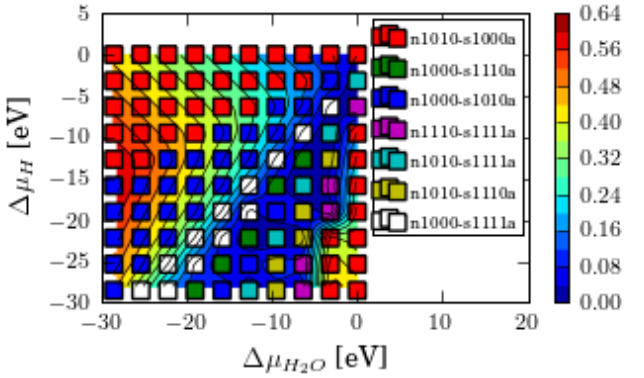

(b)

Figure 7.31: The minimum surface free energy against μ_{H_2O} and μ_H of method 1 hydration of the polar surface: (a) The complete method 1 set, and (b) only the positive surfaces.

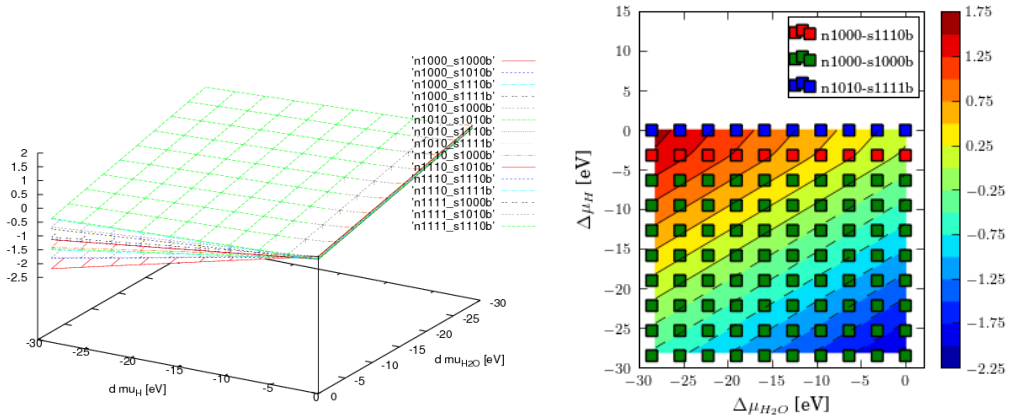

(a) (b)

Figure 7.32: The minimum surface free energy against μ_{H_2O} and μ_H of method 2 hydration of the polar surface: (a) 3d plots (b) scatter plot. All slab models have negative free energy in some part of the domain.

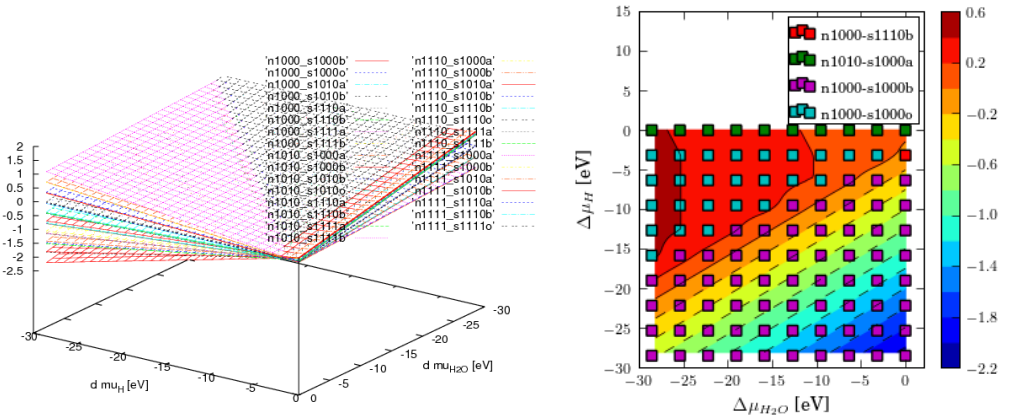

(a) (b)

Figure 7.33: (a) The minimum surface free energy surfaces of all (method 1 & 2) hydrated slab models against μ_{H_2O} and μ_{H_2}, and (b) the resulting minimum energy surface.

stability map constructed by restricting the surface energy to positive-only values is highly varied (Figure 7.34), and consists of 19 different surface terminations, of which the majority are derived from the oxylate basis slab (11). The greatest single contributer is the neutral slab, [n1000_s1000o] which possesses the second highest free energy after the only positively charged termination, [n1010_s1000a]$^{+1}$ which occupies the high μ_H boundary. The neutral surface with 50 % coverage ([n1010_s1010o]), makes an appearance, due to the extra stability associated with dipole cancellation, at high μ_{H2O}. It is difficult to resolve any clear trends about the state of protonation, although, as with above analyses, the lowest energy surfaces are those in which terminal Zn exposure is minimised. All surface terminations are within 0.4 eV/Å^2 of one another, and the negatively charged terminations are all within 0.12 eV/Å^2 of one another.

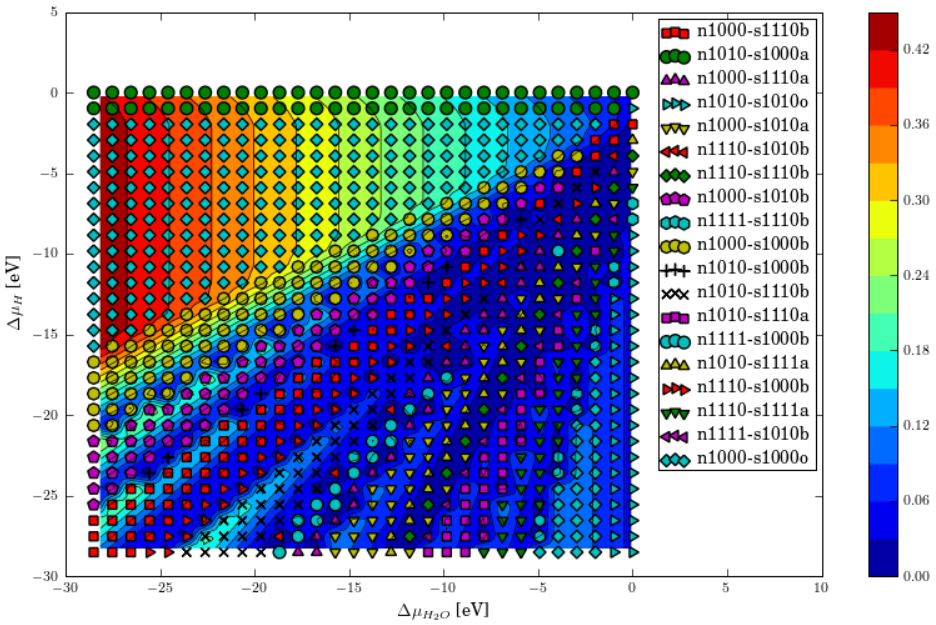

(a)

Figure 7.34: The minimum positive surface free energy against μ_{H_2O} and μ_{H_2} of method 1 & 2 hydration of the polar surface.

pH Stability Plots

We have used Equation 7.19 to calculate the dependence on a given surface model on the pH, shown in Figure 7.35, from which we can see that there are more stable structures at basic pH. It is interesting to note that ZnO has a basic isoelectric point (9.5) which indicates greatest ZnO stability (insolubility) at basic pH. The result cannot be directly related to the formal charge possessed by the surface model, as when the magnitude of the charge is limited to 3 or less (Figures 7.35c and 7.35d), the negatively charged models still yield lower surface free energies on the pH domain.

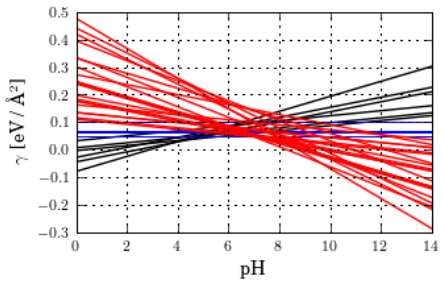

(a) Positively charged slabs ($2N_{Zn} + N_H - 2N_O > 0$) are colored black, and negatively charged slabs ($2N_{Zn} + N_H - 2N_O < 0$) are coloured red.

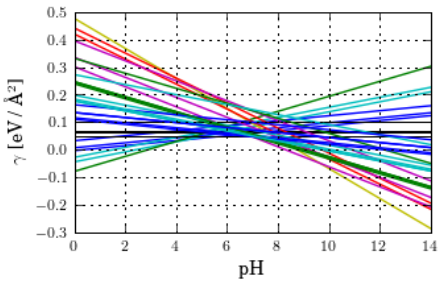

(b) All slabs with charges: neutral (black), $|1|$ (blue), $|2|$ (cyan), $|3|$ (green), $|4|$ (magenta), $|5|$ (red), $|6|$ (yellow).

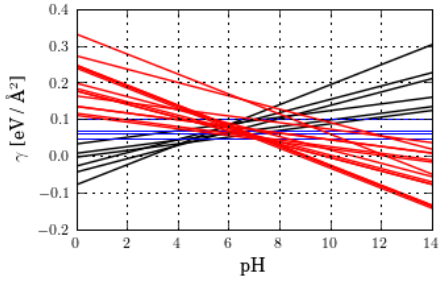

(c) $|\rho| \leq 3$.

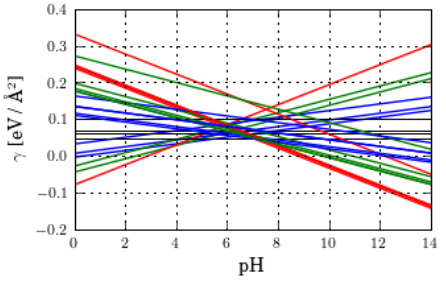

(d) $|\rho| \leq 3$, blue: $|\rho| = 1$, green: $|\rho| = 2$, red: $|\rho| = 3$.

Figure 7.35: Surface free energy, γ versus pH for the surface hydration states.

7.7.3 Summary of Hydrated Polar and Non-Polar Surface Studies

We have performed a detailed thermodynamic analysis on a comprehensive set of surface terminations. We found that generally the most significant stabilisation occurred when the Zn surface was either oxylated or hydroxylated. Comparison of the neutrally hydrated polar surfaces with the neutrally hydrated non-polar surfaces suggested that high aspect ratio rods are the favoured equilibrium shape at high water chemical potential, and therefore we infer that rods will be preferred in the aqueous environment. Investigation of charged polar slabs found the surface stability to favour negatively charged slabs, and such slabs were found to be predominant at basic pH, consistent with the basic isoelectric point of ZnO. A detailed study of the effect of surface charging on the equilibrium shape was not undertaken, nor was the effect of other ions considered. However, the pH plots suggest that the polar surface is more stable at higher pH, and therefore rod growth might be less favourable than plate growth in such conditions.

7.8 Stepped Surfaces

In the preceding sections we determined the dimensions of the slabs used to build steps that we expect to give consistent results, and studied the thermodynamic stability of the hydrooxylated surfaces. We found that chemical modification of terminal Zn produced the most stable structures. Due to the size of the step models (up to 224 atoms and 3504 electrons), it is beyond current computational capabilities to perform detailed convergence studies on such large structures. It is also impractical to investigate all surface terminations, so in the study of steps we consider only the neutral hydration produced by full coverage of (0001)-Zn with OH, and $(000\bar{1})$-O with H. Note that this is the very beginning of a step analysis in

which there are many hydrations and defects that could be investigated, however, similarly to the hydration of the flat surfaces, they will probably be very close in energy. We present the results of thermodynamic analysis on the structures that are the ultimate goal of this work due to their importance with regard to crystal growth. We performed structural relaxations on slab models representing the five steps types illustrated in Figure 7.9, in bare and fully hydrated states.

Due to the inequivalence of the $\{0001\}$ surfaces, the steps depicted by Figures 7.9a and 7.9b were treated by a single step model, giving the average values, as was done for the flat surface analogues. Also due to the inequivalence of the $\{0001\}$ surfaces it is not possible to resolve the steps depicted in Figures 7.9d and 7.9e. The three bare and hydrated surface steps used to estimate the steps energies are shown in Figure 7.36.

Table 7.2: Table summarising step free energies at $\mu_{H_2O} = E_{H_2O}$.

	Surface Free Energy eV/Å^2	
Step Orientation	Bare	Hydrated
ba	71.2396	-0.00171
bc	69.6378	-0.00303
ca	105.5656	0.0809

The free energy of the step models, calculated using equation 7.18 at $\mu_{H_2O} = E_{H_2O}$, is displayed in Table 7.2. We can also now perform analysis of morphology, in terms of aspect ratio (as earlier for flat surfaces), associated with layer growth whose parameters are determined by the *step* free energies of the facets involved. More precisely we look at the ratio of the surface growth rates described by Equation 7.55 and Figure 7.7 . Using the same constraints used to obtain Equation 7.64, we define the rate 'aspect' ratio as

$$\alpha_r = \frac{\sqrt{3}}{4}\left(\frac{R_P}{R_{NP}}\right). \tag{7.65}$$

Using Equation 7.55 we expand as,

$$\alpha_r = \frac{\sqrt{3}}{4}\left(\frac{a_{NP}}{a_P}\right)\left(\frac{X^{\circ}_{NP}}{X^{\circ}_{P}}\right)\left(\frac{\Delta\mu_{NP}}{\Delta\mu_P}\right)^2\left(\frac{\bar{\phi}_P}{\bar{\phi}_{NP}}\right)\exp\left(\frac{\bar{\phi}_P - \bar{\phi}_{NP}}{kT}\right). \tag{7.66}$$

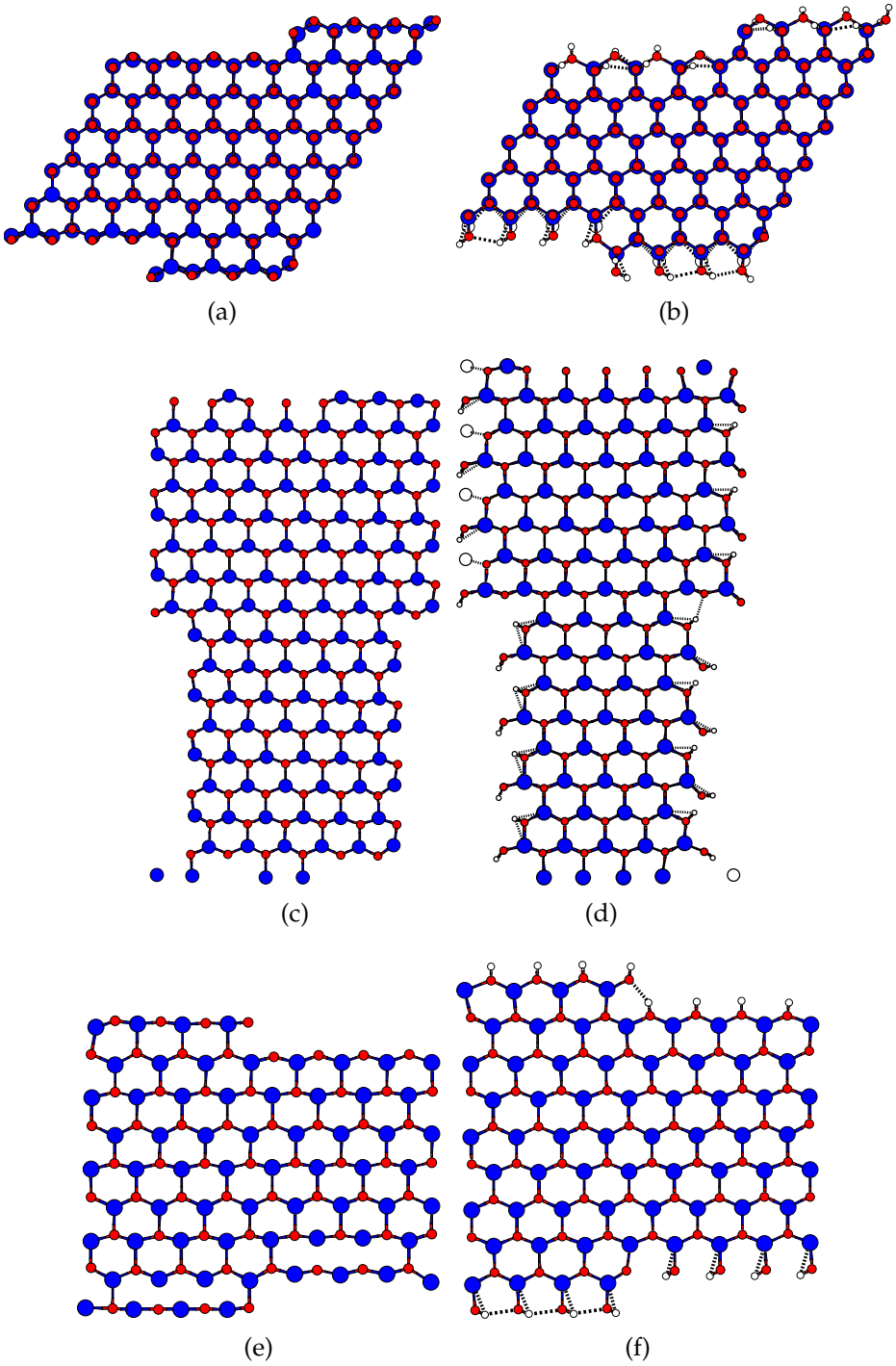

Figure 7.36: The step models used to model the the lowest-index steps on the polar and non-polar surfaces illustrated in Figure 7.9. (a) $(10\bar{1}0) - (10\bar{1}0)$ and (b) hydrated, (c) The average of $(10\bar{1}0) - (0001)$ and $(10\bar{1}0) - (000\bar{1})$, and (d) hydrated, (e) the average of $(0001) - (10\bar{1}0)$ and $(000\bar{1}) - (10\bar{1}0)$, and (f) hydrated.

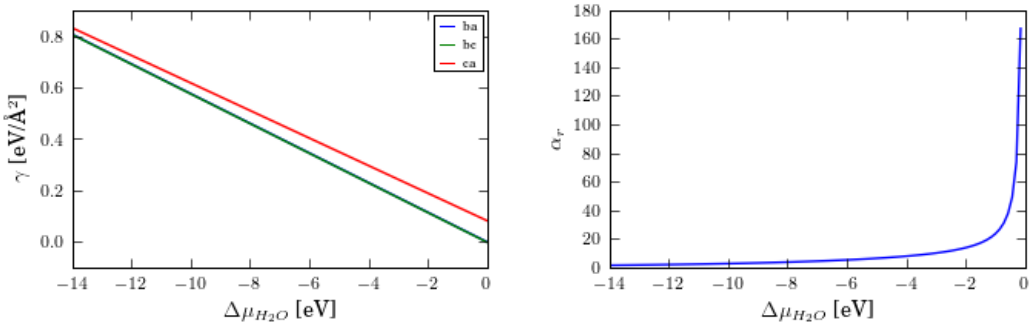

(a) (b)

Figure 7.37: (a) Step free energy, plotted against the deviation from the chemical potential of the ideal gas state of water, of the hydrated non-polar surface (red), and the hydrated polar surface (blue). (b) The ratio of non-polar to polar growth rates based on a layer growth mechanism.

Now if we consider the ZnO growth units to be more or less symmetric, the equilibrium surface concentrations to be similar, and the driving force for deposition to all be similar, then we can write,

$$\alpha_r = \frac{\sqrt{3}}{4}\left(\frac{\bar{\phi}_P}{\bar{\phi}_{NP}}\right)\exp\left(\frac{\bar{\phi}_P - \bar{\phi}_{NP}}{kT}\right), \tag{7.67}$$

from which we see the effect of the layer growth mechanism on the aspect ratio is to add an exponential dependence on the difference in step free energies of the surfaces. The aspect ratio as a function of μ_{H_2O} is shown in Figure 7.37b. It shows a behaviour similar to Figure 7.29b, obtained using the equilibrium Wulff structure, except the extent of the preference for high aspect ratio towards the more hydrous environment is much greater.

7.9 Summary

In this chapter we have used DFT calculations to look at the macroscopic phenomena associated with ZnO crystallites. We proposed two ways in

which the preferred shape of a hexagonal ZnO crystal might be approximated using DFT, based on surface energies (Wulff) or step energies (kinetic). The surface energies of the prevalent faces were calculated and their dependence on the chemical environment was investigated. The surface free energy dependence on the chemical environment was used to predict the equilibrium crystal shape as a function of the water chemical potential, the humidity. It was predicted that a high aspect ratio would be preferred, consistent with rod formation. A comprehensive set of polar surface hydration states was investigated, and their dependence on the environment studied. A μ_H, μ_{H_2O} stability diagram was constructed from which we concluded that the exposed terminal Zn was particularly unstable, and that generally the negatively charged slabs were more stable. The stability of the negatively charged slabs was demonstrated again in the context of 'pH' studies, which found that the basic (negatively charged) surfaces dominate at high pH and are most stable overall. Next in terms of pH-stability the acidic (positively charged) structures which are predominant at low pH, and finally the neutral slabs, which prevail around pH7 are found to be the overall least stable. Thus, we expect the needle-like growth to be tempered at basic pH, exacerbated at neutral, and to be moderate at acidic pH. Encouragingly, our prediction is consistent with experimental results obtained under aqueous conditions [150, 151] in which rod- and needle-like crystals are formed at neutral rather than basic pH conditions.

We calculated the step free energies for the low index faces, and used the results with our thermodynamic treatment and a model of crystal growth kinetics to predict the shape dependence, in terms of a hexagonal prism aspect ratio, on the water chemical potential. The result was a far greater preference, exponential in fact, for the high aspect shape in a more hydrous environment. Thus in the non-equilibrium growth regime we predict a preference for rod growth. However, layer growth usually occurs at lower supersaturation (of growth unit, ZnO), and is therefore more likely

in the later stages of growth when concentration gradients have settled.

To perform these analyses, we had to carry out convergence tests on the ZnO bulk unit cell, the non-polar $(10\bar{1}0)$, and polar $\{0001\}$ surface models in both the bare and hydrated states. The stability diagrams and plots required calculation of numerous different surface terminations, and the steps required coercing very large and initially unstable supercells to converge without exceeding the code's ability to reach a finite and reasonable result.

We have developed a model to predict the morphological behaviour of hexagonal prismatic crystals as a function of the multi-component chemical environment, from first principles. However, the work could be refined both in terms of the DFT calculations, and the details of the crystal growth model. The accuracy of the morphological predictions could be improved by performing calculations on a larger set of step orientations, and by using step models with larger terrace length, and slab width. The model was demonstrated using only two unique facets, and a fixed crystal shape (hexagonal prism), however, consideration of more facets could allow prediction of and evolution of the crystal shape.

From a crystal growth theory perspective, the trend in crystal growth theory is away from the sharp interface models, such as that used here, to diffuse interface models [152, 153] known as phase field models. Phase field models implicitly include corrections for surface curvature (via the Gibbs Thomson equation), anisotropy and departures from local equilibrium (interface kinetics) within the diffuse interface [153]. Such methods are advantageous in that the coupling between regimes, such as macroscopic transport, and surface processes are treated implicitly. The treatment of complicated surface features such as islands, small surface ensembles, vacancies, and the various modes of interaction between these features is also studied using simulation with kinetic Monte Carlo, and molecular dynamics methods. The coupling of such atomistic simulations with larger scale continuum models - multiscale models - permits the for-

mulation of continuum scale models with atomic level accuracy.

Chapter 8

Conclusions

Our results fall into two main categories: macroscopic transport modelling, and microscopic crystal growth. The macroscopic transport model, electrolytic transport in combination with surface chemistry boundary conditions, was successful in qualitatively replicating the experimentally measured dependence on applied potential. The transport modelling produced a number of interesting results. The growth is limited by OH^- concentration, not Zn^{2+}. Rapid OH^- production results in lower growth rates due to less efficient use of O_2 stemming from loss of OH^- to the upper boundary. The ORR reaction appears to proceed on both the electrode and the crystallite, with an applied potential rate dependence in both cases. It is likely the crystallite and electrode possess varying dependence on potential. In this work, the abrupt growth transition is attributed to the cessation of lateral growth, and the sharpness of the transition depends on the rate of vertical growth at transition time. The notion that increased concentration results in lower density is supported, albeit weakly, by our simulations, rather than the converse in which increased concentration produces an increase in seed density. An analysis of the nucleation and early growth would benefit our understanding of this aspect of the crystallite growth.

The microscopic crystal growth model, based on quantum mechanical calculations of the total energies of the low index surfaces and surface

features, predicted a preference for nanorod over nanoplate growth. For growth close to equilibrium (where the crystal maintains its Wulff shape), at low humidity an aspect ratio less than one is energetically preferred, however, at higher humidity, very large aspect ratio is preferred. Thus, the model to some extent predicts the presence of nanorods and nanoplates, both of which are observed experimentally. The preference for high aspect ratio was exacerbated for the kinetic growth model. We interpret higher humidity to be more like the aqueous case, however, this is not necessarily the case and the model would benefit from a more detailed treatment of the effect of bulk water at the surface.

The results of our computational study of the ZnO nanorod film electrodeposition system are promising in that both the macroscopic electrolytic transport based, and the microscopic DFT based approaches yielded results consistent with the experimental observations. The transport results are particularly gratifying in that we were able to qualitatively replicate the experimental dependence on concentration and applied potential within the ranges that produce the preferred nanorod films. The outcome of the DFT results was also very rewarding, given the clearly ambitious nature of extrapolation from the electronic regime to the macroscopic one.

The work presented here represents the first steps of a multi-scale approach to electrochemical crystal formation, and much work is still required to produce a consistent robust system. However, we have made significant inroads in terms of both methodology, and code implementation. Our code has many desirable characteristics, not least due to its object-oriented structure, and features implemented to maximise efficiency such as system compression and sparse solving. One of the most difficult parts of modelling is the development and testing of a computational problem solving environment. Our code was devised with the extension by incorporation of detailed boundary models that feed parameters directly to the transport model in mind.

The transport model did little to accommodate the growth shape of the

ZnO crystals. Throughout the simulations the aspect ratio of the crystallite was free to change but its shape was constrained to be rectangular. In other words, we neglected to treat the effect of surface inhomogeneity, such as roughness, and curvature within the boundaries of the electrolytic transport model. In the context of a multi-scale system, the work presented here lacks an investigation of a linking regime, a 'hand-shake' model. The Kinetic Monte Carlo approach has been successful for a similar system, the electrodeposition of copper [85, 84, 50], and thus we suggest future development along a similar vein.

In terms of the work presented here, there is much room for improvement, especially in the treatment of the the solid-electrolyte boundaries. Two improvements would greatly improve the validity of the inferences made in this work. First is associated with the determination of a relationship between applied potential, surface coverage, and crystal size. Effectively a way to capture the way charge and polarisation are distributed in the system. On this front, a relation between the applied potential and the surface capacitance of both the electrode, and the crystal surfaces that are moving away from the electrode, would be useful. Also, inclusion of more detailed electrode treatment, such as the relation between the ORR current, overpotential and Zn^{2+} concentration, and possibly even the ZnO formation and inclusion processes could benefit our understanding of the system.

Within the transport region there is a complicated solution chemistry [47] involving many different zinc hydroxylates ($[Zn_m(OH)_n]^{(m-n)}$). The presence and effect on the local solution electrolytic environment could influence the growth or nucleation of new crystals. The validity of the electrolytic transport equations also could be improved by using corrections for the Debye interactions between ions, neglected in this work though the use of the ideal solution assumption.

The use of two dimensions instead of three, and therefore crystallite planes instead of columns could also affect the model results. For exam-

ple, a three dimensional system could capture effects associated with non-uniform orientration of the crystals, which as well as its potential influence on transport, would produce a more natural treatment of the film porosity.

Further work could also be done on the microscopic model. In this work the crystal was constrained to be hexagonal columnar, investigation of more surfaces could provide a way in which the actual shape is predicted from first principles. Likewise calculation of more step orientations would give a truer indication of the step and kink energies of the respective surfaces. As computing becomes more powerful, the direct investigation of kink structures and even their interaction with water molecules could be investigated.

Computational studies which aim to replicate and simulate physical processes on a multitude of scales simultaneously is not only ambitious, but very interesting and gratifying for the researcher, as it gives, indeed requires, interest in a wide range of ideas: mathematical, physical and computational. Further work is required in model development, physical description, and computational manifestation.

Bibliography

[1] Z. L. Wang, J. Song, and X. Wang, "Zinc oxide nanostructures: growth, properties and applications," *Journal of Materials Chemistry*, vol. 17, pp. 711 – 720, 2007.

[2] U. Ozgur, Y. Alivov, C. Liu, A. Teke, M. Reshchikov, S. Dogan, V. Avrutin, S. Cho, and H. Morkoc, "A comprehensive review of ZnO materials and devices," *Journal of Applied Physics*, vol. 98, 2005.

[3] Z. L. Wang and J. Song, "Piezoelectric nanogenerators based on zinc oxide nanowire arrays," *Science*, vol. 312, pp. 242 – 246, 2006.

[4] Z. L. Wang, "The new field of nanopiezotronics," *Materials Today*, vol. 10, pp. 20 – 28, 2007.

[5] Z. L. Wang, "Nanostructures of zinc oxide," *Materials Today*, vol. 7, pp. 26 – 33, 2004.

[6] M. H. Wong, A. Berenov, X. Qi, M. J. Kappers, Z. H. Barber, B. Illy, Z. Lockman, M. P. Ryan, and J. L. MacManus-Driscoll, "Electrochemical growth of ZnO nano-rods on polycrystalline Zn foil," *Nanotechnology*, vol. 14, pp. 968 – 973, 2003.

[7] X. Chen, Z. Zhou, K. Wang, X. Fan, S. Hu, Y. Wang, and Y. Huang, "Ferromagnetism in Fe-doped tetra-needle like ZnO whiskers," *Materials Research Bulletin*, vol. 44, pp. 799 – 802, 2009.

[8] S. Cho, D.-S. Shim, S.-H. Jung, E. Oh, B. R. Lee, and K.-H. Lee, "Fabrication of ZnO nanoneedle arrays by direct microwave irradiation," *Materials Letters*, vol. 63, pp. 739 – 741, 2009.

[9] B. Illy, B. A. Shollock, J. L. MacManus-Driscoll, and M. P. Ryan, "Electrochemical growth of ZnO nanoplates," *Nanotechnology*, vol. 16, pp. 320 – 324, 2005.

[10] M. Wen, B. Yang, H. Yan, Z. Fu, C. Cai, K. Liu, Y. Chen, J. Xu, S. Fu, and S. Zhang, "Morphology-controlled synthesis of flowerlike ZnO nano/microstructures and their photocatalytic property," *Journal of Nanoscience and Nanotechnology*, vol. 9, pp. 2038 – 2044, 2009.

[11] X. Y. Kong and Z. L. Wang, "Polar-surface dominated ZnO nanobelts and the electrostatic energy induced nanohelixes, nanosprings, and nanospirals," *Applied Physics Letters*, vol. 84, pp. 975 – 977, 2004.

[12] A. Urnar, Y. K. Park, and Y. B. Hahn, "High aspect-ratio ZnO nanowires based nanoscale field effect transistors," *Journal of Nanoscience and Nanotechnology*, vol. 9, pp. 2692 – 2697, 2009.

[13] L. Ming, Z. Hai-Ying, G. Chang-Xin, X. Jing-Bo, and F. Xiao-Jun, "The research on suspended ZnO nanowire field-effect transistor," *Chinese Physics B*, vol. 18, pp. 1594 – 1597, 2009.

[14] M. Arnold, P. Avouris, Z. Pan, and Z. Wang, "Field-effect transistors based on single semiconducting oxide nanobelts," *Journal of Physical Chemistry B*, vol. 107, pp. 659 – 663, 2003.

[15] S. Barth, C. Harnagea, S. Mathur, and F. Rosei, "The elastic moduli of oriented tin oxide nanowires," *Nanotechnology*, vol. 20, pp. 115705 – 115710, 2009.

[16] Y. Yoshino, "Piezoelectric thin films and their applications for electronics," *Journal of Applied Physics*, vol. 105, no. 6, pp. 061623 – 061630, 2009.

[17] L. Mai, V.-S. Pham, and G. Yoon, "Second-order resonant ZnO-based film bulk acoustic resonator devices and thermal techniques to improve their resonant characteristics," *Journal of Vacuum Science & Technology A*, vol. 27, pp. 67 – 72, 2009.

[18] C.-C. Ma, T.-J. Huang, and J.-M. Yu, "Application of slanted finger interdigital transducer surface acoustic wave devices to ultraviolet array photodetectors," *Journal of Applied Physics*, vol. 104, pp. 033528 – 033537, 2008.

[19] S. N. Mahmoodi and N. Jalili, "Piezoelectrically actuated microcantilevers: An experimental nonlinear vibration analysis," *Sensors and Actuators A-Physical*, vol. 150, pp. 131 – 136, 2009.

[20] A. Tsukazaki, M. Kubota, A. Ohtomo, T. Onuma, K. Ohtani, H. Ohno, S. F. Chichibu, and M. Kawasaki, "Blue light-emitting diode based on ZnO," *Japanese Journal of Applied Physics*, vol. 44, pp. L643 – L645, 2005.

[21] J. Fallert, R. J. B. Dietz, H. Zhou, J. Sartor, C. Klingshirn, and H. Kalt, "Lasing in single ZnO nanorods after fs- and ns-pulsed excitation," in *Physica Status Solidi C: Current Topics in Solid State Physics, Vol 6, No 2* (M. Stutzmann and H. Stolz, eds.), vol. 6 of *Physica Status Solidi C-Current Topics in Solid State Physics*, pp. 449 – 452, 2009.

[22] L. Liao, J. Li, D. Wang, C. Liu, and Q. Fu, "Electron field emission studies on ZnO nanowires," *Materials Letters*, vol. 59, pp. 2465 – 2467, 2005.

[23] R. Viswanatha, P. K. Santra, C. Dasgupta, and D. D. Sarma, "Growth mechanism of nanocrystals in solution: ZnO, a case study," *Physical Review Letters*, vol. 98, pp. 255501 – 255505, 2007.

[24] M. E. Coltrin, J. W. Hsu, D. A. Scrymgeour, J. R. Creighton, N. C. Simmons, and C. M. Matzke, "Chemical kinetics and mass transport

effects in solution-based selective-area growth of ZnO nanorods," *Journal of Crystal Growth*, vol. 310, pp. 584 – 593, 2008.

[25] A. Barnard, Y. Xiao, and Z. Cai, "Modelling the shape and orientation of ZnO nanobelts," *Chemical Physics Letters*, vol. 419, pp. 313 – 316, 2006.

[26] F. A. Reis, J. Badiali, T. Pauport, and D. Lincot, "Statistical modelling of electrochemical deposition of nanostructured hybrid films with ZnO-Eosin Y as a case example," *Journal of Electroanalytical Chemistry*, vol. 598, pp. 27 – 35, 2006.

[27] P. Mandin, J. Cense, C. Fabian, C. Gbado, and D. Lincot, "Electrodeposition process modeling using continuous and discrete scales," *Computers and Chemical Engineering*, vol. 31, pp. 980 – 992, 2007.

[28] M. Law, L. Greene, J. Johnson, R. Saykally, and P. Yang, "Nanowire dye-sensitized solar cells," *Nature Materials*, vol. 4, pp. 455 – 459, 2005.

[29] M. Kadota and T. Miura, "Shear bulk wave transducer made of (1120)-plane epitaxial ZnO film on R-sapphire," *Japanese Journal of Applied Physics*, vol. 41, pp. 3281 – 3284, 2002.

[30] R. Liu, A. A. Vertegel, E. W. Bohannan, T. A. Sorenson, and J. A. Switzer, "Epitaxial electrodeposition of zinc oxide nanopillars on single-crystal gold," *Chemistry Materials*, vol. 13, pp. 508 – 512, 2001.

[31] M. Izaki and T. Omi, "Transparent zinc oxide films prepared by electrochemical reaction," *Applied Physics Letters*, vol. 68, pp. 2439 – 2440, 1996.

[32] B. Canava and D. Lincot, "Nucleation effects on structural and optical properties of electrodeposited zinc oxide on tin oxide," *Journal of Applied Electrochemistry*, vol. 30, pp. 711 – 716, 2000.

[33] D. Gal, G. Hodes, D. Lincot, and H. W. Schock, "Electrochemical deposition of zinc oxide films from non-aqueous solution: a new buffer/window process for thin film solar cells," *Thin Solid Films*, vol. 361-362, pp. 79 – 83, 2000.

[34] J. Lee and Y. Tak, "Electrodeposition of ZnO on ITO electrode by potential modulation method," *Electrochemical and Solid State Letters*, vol. 4, pp. C63 – C65, 2001.

[35] B. O'Regan, V. Sklover, and M. Gratzel, "Electrochemical deposition of smooth and homogeneously mesoporous ZnO films from propylene carbonate electrolytes," *Journal of the Electrochemical Society*, vol. 148, pp. C498 – C505, 2001.

[36] R. Pandy, S. Sahu, and S. Chandra, *Handbook of Semiconductor Electrodeposition*. New York: Marcel Dekker Inc., 1996.

[37] A. Goux, T. Pauporte, and D. Lincot, "Oxygen reduction reaction on electrodeposited zinc oxide electrodes in KCl solution at 70°C," *Electrochimica Acta*, vol. 51, pp. 3168 – 3172, 2006.

[38] S. Hendy, B. Walker, N. Laycock, and M. Ryan, "Ab initio studies of the passive film formed on iron," *Physical Review B*, vol. 67, pp. 085407 – 085417, 2003.

[39] T. Pauporté and D. Lincot, "Heteroepitaxial electrodeposition of zinc oxide films on gallium nitride," *Applied Physics Letters*, vol. 75, pp. 3817 – 3819, 1999.

[40] G. Aylward and T. Findlay, *S I Chemical Data*. Brisbane: John Wiley and Sons, 3rd ed., 1994.

[41] B. Ingham, B. N. Illy, J. R. Mackay, S. P. White, S. C. Hendy, and M. P. Ryan, "In situ synchrotron x-ray absorption experiments and modelling of the growth rates of electrochemically deposited ZnO

nanostructures," *Mater. Res. Soc. Symp. Proc.*, vol. 1017, pp. DD12 – DD16, 2007.

[42] K. Kinoshita, *Electrochemical Oxygen Technology*. New York: Wiley-Interscience, 1992.

[43] A. P. Yadav, A. Nishikata, and T. Tsuru, "Oxygen reduction mechanism on corroded zinc," *Journal of Electroanalytical Chemistry*, vol. 585, pp. 142 – 149, 2005.

[44] A. A. Chernov, *Modern Crystallography III: Crystal Growth*. New York: Springer-Verlag, 1984.

[45] L. Yang, X. Wu, Y. Xionga, Y. Yanga, G. Huanga, P. K. Chub, and G. Siub, "Formation of zinc oxide micro-disks via layer-by-layer growth and growth mechanism of ZnO nanostructures," *Journal of Crystal Growth*, vol. 283, pp. 332 – 338, 2005.

[46] "Private communication with Benoît Illy."

[47] S. Peulon and D. Lincot, "Cathodic electrodeposition from aqueous solution of dense or open-structured zinc oxide films," *Advanced Materials*, vol. 8, pp. 166 – 170, 1996.

[48] A. J. Bard and L. R. Faulkner, *Electrochemical Methods*. New York: John Wiley and Sons, 1980.

[49] S. P. White and N. J. Laycock, "Computer simulation of single pit propagation in stainless steel under potentiostatic control," *Journal of the Electrochemical Society*, vol. 148, pp. B274 – B275, 2001.

[50] E. G. Webb and R. C. Alkire, "Pit initiation at single sulfide inclusion in stainless steel," *Journal of the Electrochemical Society*, vol. 149, pp. B286 – B295, 2002.

[51] S. M. Sharland, "A mathematical model of crevice and pitting corrosion II: The mathematical solution," *Corrosion Science*, vol. 28, pp. 621 – 630, 1988.

[52] J. C. Friedly and J. Rubin, "Solute transport with multiple equilibrium-controlled or kinetically controlled chemical reactions," *Water Resources Research*, vol. 28, pp. 1935 – 1953, 1992.

[53] I. V. Markov, *Crystal Growth for Beginners*. Singapore: World Scientific Publishing, 1998.

[54] M. Ohara and R. C. Reid, *Modeling Crystal Growth Rates from Solution*. New Jersey: Pretence-Hall, 1973.

[55] A. Pimpinelli and J. Villain, *Physics of Crystal Growth*. Cambridge: Cambridge University Press, 1998.

[56] C. Sweegers, W. van Enckevort, H. Meekes, P. Bennema, I. Hiralal, and A. Rijkeboer, "The impact of twinning on the morphology of γ-$Al(OH)_3$ crystals," *Journal of Crystal Growth*, vol. 197, pp. 244 – 253, 1999.

[57] T. F. Dirske, "The solubility product constant of ZnO," *Journal of the Electrochemical Society*, vol. 133, pp. 1656 – 1657, 1986.

[58] D. R. Lide, ed., *CRC Handbook of Chemistry and Physics*. Florida: CRC Press, 86th ed., 2004.

[59] J. N. Israelachvili, *Intermolecular and Surface Forces*. London: Academic Press, 1985.

[60] D. C. Grahame, "Diffuse double layer theory for electrolytes of unsymmetrical valence types," *Journal of Chemical Physics*, vol. 21, pp. 1054 – 1060, 1953.

[61] J. S. Newman, *Electrochemical Systems*. New Jersey: Prentice Hall, 1991.

[62] J. E. Guyer, W. J. Boettinger, J. A. Warren, and G. B. McFadden, "Phase field modeling of electrochemistry II: Kinetics," *Physical Review E*, vol. 69, pp. 021604 – 021616, 2004.

[63] M. Z. Bazant, K. Thornton, and A. Ajdari, "Diffuse-charge dynamics in electrochemical systems," *Physical Review E*, vol. 70, pp. 021506 – 021530, 2004.

[64] E. A. Guggenheim, *Thermodynamics: An advanced treatment for chemists and physicists*. Amsterdam: North-Holland Publishing Company, 5 ed., 1967.

[65] R. A. Alberty, "Use of legendre transforms in chemical thermodynamics (IUPAC technical report)," *Pure and Applied Chemistry*, vol. 73, pp. 1349 – 1380, 2001.

[66] J.-L. Barrat and J.-P. Hansen, *Basic Concepts for Simple and Complex Liquids*. Cambridge: Cambridge University Press, 2003.

[67] J. O. Bockris and A. K. N. Reddy, *Modern Electrochemistry 1: Ionics*. New York: Plenum Press, 2nd ed., 1998.

[68] Z. Schuss, B. Nadler, and R. S. Eisenberg, "Derivation of Poisson and Nernst-Planck equations in a bath and channel from a molecular model," *Physical Review E*, vol. 64, pp. 036116 – 036130, 2001.

[69] S. W. Feldberg, "On the dilemma of the use of the electroneutrality constraint in electroneutrality calculations," *Electrochemistry Communications*, vol. 2, pp. 453 – 456, 2000.

[70] A. D. MacGillivray, "Nernst-Planck equations and the electroneutrality and Donnan assumptions," *Journal of Chemical Physics*, vol. 48, pp. 2903 – 2907, 1968.

[71] S. P. White, G. J. Weir, and N. J. Laycock, "Calculating chemical concentrations during the initiation of crevice corrosion," *Corrosion Science*, vol. 42, pp. 605 – 629, 2000.

[72] J. Newman, "The polarised diffuse double layer," *Transactions of the Faraday Society*, vol. 61, pp. 2229 – 2237, 1965.

[73] W. H. Smeryl and J. Newman, "Double layer structure at the limiting current," *Transactions of the Faraday Society*, vol. 62, pp. 207 – 216, 1966.

[74] "Private communication with Dr S. White."

[75] R. M. Corless, G. H. Gonnet, D. E. G. Hare, D. J. Jeffrey, and D. E. Knuth, "On the Lambert W function," *Advances in Computational Mathematics*, vol. 42, pp. 329 – 359, 1996.

[76] J.-J. Chattot, *Computational Aerodynamics and Fluid Dynamics: An Introduction*. Berlin: Springer, 2002.

[77] J. Crank and P. Nicolson, "A practical method for numerical evaluation of solutions of partial differential equations of the heat conduction type," *Proceedings of the Cambridge Philosophical Society*, vol. 43, pp. 50 – 67, 1947.

[78] I. Fried, *Numerical Solutions of Differential Equations*. New York: Academic Press, 1979.

[79] E. Hairer and G. Wanner, *Solving Ordinary Differential Equations II: Stiff and Differential-Algebraic Problems*. Berlin: Springer, 2002.

[80] W. F. Ames, *Numerical Methods for Partial Differential Equations*. London: Academic Press, 3rd ed., 1992.

[81] J. M. Ortega and W. C. Rheinboldt, *Iterative Solution of Nonlinear Equations in Several Variables*. London: Academic Press, 1970.

[82] F. S. Acton, *Numerical Methods That Work*. New York: Harper and Row, 1970.

[83] J. M. Ortega and W. C. Rheinboldt, *Iterative solution of nonlinear equations in several variables*. Philadelphia, PA, USA: Society for Industrial and Applied Mathematics, 2000.

[84] Z. Zheng, R. M. Stephens, R. D. Braatz, R. C. Alkire, and L. R. Petzold, "A hybrid multiscale kinetic Monte Carlo method for simulation of copper electrodeposition," *Journal of Computational Physics*, vol. 227, pp. 5184 – 5199, 2008.

[85] M. Buoni and L. Petzold, "An efficient, scalable numerical algorithm for the simulation of electrochemical systems on irregular domains," *Journal of Computational Physics*, vol. 225, pp. 2320 – 2332, 2007.

[86] M. Buoni, *Multiscale Modeling and Simulation of Copper Electrodeposition*. PhD in mechanical engineering, University of California Santa Barbara (UCSB), 2008.

[87] "Routine for computation of the solution to a real system of linear equations." `http://www.netlib.org/lapack/double/dgesv.f`.

[88] T. A. Davis and I. S. Duff, "An unsymmetric-pattern multifrontal method for sparse LU factorization," *SIAM Journal on Matrix Analysis and Applications*, vol. 18, pp. 140 – 158, 1997.

[89] T. A. Davis and I. S. Duff, "A combined unifrontal/multifrontal method for unsymmetric sparse matrices," *ACM Transactions on Mathematical Software*, vol. 25, pp. 1 – 20, 1999.

[90] T. A. Davis, "Algorithm 832: Umfpack v4.3—an unsymmetric-pattern multifrontal method," *ACM Transactions on Mathematical Software*, vol. 30, pp. 196 – 199, 2004.

[91] T. A. Davis, "A column pre-ordering strategy for the unsymmetric-pattern multifrontal method," *ACM Transactions on Mathematical Software*, vol. 30, pp. 165 – 195, 2004.

[92] "Private communication with Benoît Illy."

[93] J. Lyklema, *Fundamentals of Interface and Colloid Science I*. San Diego: Academic Press, 1991.

[94] P. Hohenberg and W. Kohn, "Inhomegeous electron gas," *Physical Review*, vol. 136, pp. B864 – B871, 1964.

[95] W. Kohn and L. Sham, "Self-consistent equations including exchange and correation effects," *Physical Review*, vol. 140, pp. A1133 – A1138, 1965.

[96] C. Lanczos, *The Variational Principles of Mechanics*. Toronto: University of Toronto Press, 1970.

[97] R. Courant and D. Hilbert, *Methods of Mathematical Physics*. New York: Interscience Publishers, 1961.

[98] I. M. Gelfand and S. V. Fomin, *Calculus of Variations*. Englewood Cliffs, N.J., USA: Prentice-Hall, 1963.

[99] R. Weinstock, *Calculus of Variations: With Applications to Physics and Engineering*. New York: McGraw-Hill Book Company, 1952.

[100] M. D. Greenberg, *Advanced Engineering Mathematics*. New Jersey: Prentice Hall, 2 ed., 1998.

[101] L. I. Schiff, *Quantum Mechanics*. New York: McGraw-Hill, 1968.

[102] R. G. Parr and W. Yang, *Density-Functional Theory of Atoms and Molecules*. New York: Oxford University Press, 1989.

[103] C. C. J. Roothaan, "New developments in molecular orbital theory," *Reviews of Modern Physics*, vol. 23, pp. 69 – 89, 1951.

[104] N. W. Ashcroft and N. D. Mermin, *Solid State Physics*. New York: Harcourt College Publishers, 1976.

[105] R. G. Parr, *The Quantum Theory of Molecular Electronic Structure*. New York: W. A. Benjamin, 1964.

[106] L. H. Thomas, "The calculation of atomic fields," *Proceedings of the Cambridge Philosophical Society*, vol. 23, pp. 242 – 248, 1927.

[107] E. Teller, "On the stability of molecules in the Thomas-Fermi theory.," *Reviews of Modern Physics*, vol. 34, pp. 627 – 631, 1962.

[108] M. Levy, "Electron densities in search of Hamiltonians," *Physical Review A*, vol. 26, pp. 1200 – 1208, 1982.

[109] M. Levy and J. P. Perdew, *The constrained search formulation in density functional theory. In* Density Functional Methods in Physics. New York: Plenum, 1985.

[110] J. P. Perdew and A. Zunger, "Self-interaction correction to density-functional approximations for many-electron systems," *Physical Review B*, vol. 23, pp. 5048 – 5070, 1981.

[111] E. J. Baerends and O. V. Gritsenko, "Away from generalized gradient approximation: Orbital-dependent exchange-correlation functionals," *The Journal of Chemical Physics*, vol. 123, pp. 062202 – 062219, 2005.

[112] J. P. Perdew, A. Ruzsinszky, J. Tao, V. Staroverov, G. Scuseria, and G. Csonka, "Prescription for the design and selection of density functional approximations: More constraint satisfaction with fewer fits," *Journal of Chemical Physics*, vol. 123, pp. 062201 – 062210, 2005.

[113] J. P. Perdew, K. Burke, and Y. Wang, "Generalized gradient approximation for the exchange-correlation hole of a many-electron system," *Physical Review B*, vol. 54, pp. 16533 – 16539, 1996.

[114] J. P. Perdew, K. Burke, and M. Ernzerhof, "Generalized gradient approximations made simple," *Physical Review Letters*, vol. 77, pp. 3865 – 3868, 1996.

[115] M. C. Payne, M. P. Teter, D. C. Allan, T. A. Arias, and J. D. Joannopoulos, "Iterative minimization techniques for ab initio total-energy calculations: Molecular dynamics and conjugate gradients," *Reviews of Modern Physics*, vol. 64, pp. 1045 – 1097, 1992.

[116] H. J. Monkhurst and J. D. Pack, "Special points for Brillouin-zone integrations," *Physical Review B*, vol. 13, pp. 5188 – 5192, 1976.

[117] G. Paolo, "Metodi numerici in struttura elettronica," *A Course in Computational Physics*, 2006.

[118] G. Kresse and J. Hafner, "Ab initio molecular dynamics for liquid metals," *Physical Review B*, vol. 47, pp. 558 – 561, 1993.

[119] G. Kresse, *Ab initio Molekular Dynamik für flüssige Metalle*. PhD thesis, Technische Universität Wien, 1993.

[120] G. Kresse and J. Furthmüller, "Efficiency of ab-initio total energy calculations for metals and semiconductors using a plane-wave basis set," *Computational Materials Science*, vol. 6, pp. 15 – 50, 1996.

[121] G. Kresse and J. Furthmüller, "Efficient iterative schemes for ab initio total-energy calculations using a plane-wave basis set," *Physical Review B*, vol. 54, pp. 11169 – 11186, 1996.

[122] D. Vanderbilt, "Soft self-consistent pseudopotentials in a generalized eigenvalue formalism," *Physical Review B*, vol. 41, pp. 7892 – 7895, 1990.

[123] G. Kresse and J. Hafner, "Norm-conserving and ultrasoft pseudopotentials for first-row and transition elements," *Journal of Physics: Condensed Matter*, vol. 6, pp. 8245 – 8257, 1994.

[124] S. C. Abrahams and J. L. Bernstein, "Remeasurement of the structure of hexagonal ZnO," *Acta Crystallographica Section B*, vol. 25, pp. 1233 – 1236, 1969.

[125] V. E. Henrich and P. A. Cox, *The Surface Science of Metal Oxides*. Cambridge: Cambridge University Press, 1994.

[126] P. W. Tasker, "The stability of ionic crystal surfaces," *Journal of Physics C: Solid State Physics*, vol. 12, pp. 4977 – 4984, 1979.

[127] C. Noguera, "Polar metal oxides," *Journal of Physics: Condensed Matter*, vol. 12, pp. R367 – R410, 2000.

[128] C. Noguera, *Physics and Chemistry at Oxide Surfaces*. Cambridge: Cambridge University Press, 1996.

[129] B. Meyer, "First principles study of the polar O-terminated ZnO surface in thermodynamic equilibrium with oxygen and hydrogen," *Physical Review B*, vol. 69, pp. 045416 – 045426, 2004.

[130] K. Reuter and M. Scheffler, "Composition, structure, and stability of $RuO_2(110)$ as a function of oxygen pressure," *Physical Review B*, vol. 65, pp. 035406–1 – 035406–11, 2001.

[131] C. Noguera, F. Finocchi, and J. Goniakowski, "First principles studies of complex oxide surfaces and interfaces," *Journal of Physics: Condensed Matter*, vol. 16, pp. S2509 – S2537, 2004.

[132] G. Kresse, O. Dulub, and U. Diebold, "Competing stabilization mechanism for the polar $ZnO(0001)$-Zn surface," *Physical Review B*, vol. 68, pp. 245409 – 245424, 2003.

[133] B. Meyer and D. Marx, "Density-functional study of the stability of ZnO surfaces," *Physical Review B*, vol. 67, pp. 035403 – 035414, 2003.

[134] B. Meyer, H. Rabaa, and D. Marx, "Water adsorption on ZnO$(10\bar{1}0)$: From single molecules to partially dissociated monolayers," *Physical Chemistry Chemical Physics*, vol. 8, pp. 1513 – 1520, 2006.

[135] O. Dulub, U. Diebold, and G. Kresse, "Novel stabilization mechanism on polar surfaces: ZnO(0001)-Zn," *Physical Review Letters*, vol. 90, pp. 016102 – 016106, 2003.

[136] S. Kristyn and P. Pulay, "Can (semi)local density functional theory account for the london dispersion forces?," *Chemical Physics Letters*, vol. 229, pp. 175 – 180, 1994.

[137] J. Prez-Jord and A. D. Becke, "A density-functional study of Van der Waals forces: Rare gas diatomics," *Chemical Physics Letters*, vol. 233, pp. 134 – 137, 1995.

[138] J. Grafenstein and D. Cremer, "An efficient algorithm for the density-functional theory treatment of dispersion interactions," *Journal of Chemical Physics*, vol. 130, pp. 124105 – 124121, 2009.

[139] D. Winn and M. F. Doherty, "Modeling crystal shapes of organic materials grown from solution," *Separations*, vol. 46, pp. 1348 – 1366, 2000.

[140] W. K. Burton, N. Cabrera, and F. C. Frank, "The growth of crystals and the equilibrium structure of their surfaces," *Philosophical Transactions of the Royal Society of London, Series A, Mathematical and Physical Sciences*, vol. 243, pp. 299 – 358, 1951.

[141] X.-Y. Liu and P. Bennema, "Theoretical consideration of the growth morphology of crystals," *Physical Review B*, vol. 53, pp. 2314 – 2325, 1996.

[142] X. Y. Liu, E. S. Boek, W. J. Briels, and P. Bennema, "Prediction of crystal growth morphology based on structural analysis of the solid-fluid interface.," *Nature*, vol. 374, pp. 342 – 345, 1995.

[143] "Vasp manual." `http://cms.mpi.univie.ac.at/vasp/vasp/vasp.html`.

[144] D. M. Ceperley and B. J. Alder, "Ground state of the electron gas by a stochastic method," *Physical Review Letters*, vol. 45, pp. 566 – 569, 1980.

[145] Y. Wang and J. P. Perdew, "Correlation hole of the spin-polarized electron gas, with exact small-wave-vector and high-density scaling," *Physical Review B*, vol. 44, pp. 13298 – 13307, 1991.

[146] N. Gaston, B. Paulus, U. Wedig, and M. Jansen, "Multiple minima on the energy landscape of elemental zinc: A wave function based ab initio study," *Physical Review Letters*, vol. 100, pp. 226404 – 226408, 2008.

[147] D. J. Cooke, A. Mermier, and S. C. Parker, "Surface structure of $(10\bar{1}0)$ and $(11\bar{2}0)$ surfaces of ZnO with density functional theory and atomistic simulation," *Journal of Physical Chemistry B.*, vol. 110, pp. 7985 – 7991, 2006.

[148] F. Claeyssens, C. Freeman, N. Allan, Y. Sun, M. Ashfold, and J. Harding, "Growth of ZnO thin films - experiment and theory," *Journal of Materials Chemistry*, vol. 15, pp. 139 – 148, 2005. 10.

[149] U. Diebold, L. Koplitz, and O. Dulub, "Atomic-scale properties of low-index ZnO surfaces," *Applied Surface Science*, vol. 237, pp. 336 – 342, 2004.

[150] D. Vernardou, G. Kenanakis, S. Couris, E. Koudoumas, E. Kymakis, and N. Katsarakis, "pH effect on the morphology of ZnO nanos-

tructures grown with aqueous chemical growth," *Thin Solid Films*, vol. 515, pp. 8764 – 8767, 2007.

[151] K. Yu, Z. Jin, X. Liu, J. Zhao, and J. Feng, "Shape alterations of ZnO nanocrystal arrays fabricated from $NH_3 \cdot H_2O$ solutions," *Applied Surface Science*, vol. 253, pp. 4072 – 4078, 2007.

[152] A. A. Chernov, "Notes on interface growth kinetics 50 years after Burton Cabrera and Frank," *Journal of Crystal Growth*, vol. 264, pp. 499 – 518, 2004.

[153] R. F. Sekerka, "Morphology: From sharp interface to phase field models," *Journal of Crystal Growth*, vol. 264, pp. 530 – 540, 2004.